Coaxial laser wire additive manufacturing of Inconel 718

THÈSE

présentée et soutenue publiquement le 6 juillet 2022

pour l'obtention du titre de

Docteur de l'Université de Lorraine

Spécialité Sciences des Matériaux

par

Ivan Cazic

Composition du jury:

Rapporteurs :	María Teresa Pérez Prado	Directrice de recherche, IMDEA Materials, Madrid, Espagne
	Patrice Peyre (Président)	Directeur de recherche, PIMM, Paris, France
Examinateurs :	Güven Kurtuldu	Chargé de recherche, ETH, Zürich, Suisse
	Florence Pettinari Sturmel	Professeure, CEMES, Toulouse, France
Directeurs :	Benoît Appolaire	Professeur, IJL, Nancy, France
	Julien Zollinger	Maître de conférence, IJL, Nancy, France
Invités :	Maxime El Kandaoui	Ingénieur de recherche, Institut de Soudure, Yutz, France
	Ulrike Hecht	Directrice de recherche, RWTH, Aachen, Allemagne
	Michel Rappaz	Professeur émérite, EPFL, Lausanne, Suisse

Institut Jean Lamour, UMR CNRS-UL 7198, 54000 NANCY France

Remerciements

J'aimerai tout d'abord remercier María Teresa Pérez Prado et Patrice Peyre pour avoir accepté d'être rapporteurs de ce manuscrit, ainsi que Florence Pettinari Sturmel, Güven Kurtuldu, Michel Rappaz, Ulrike Hecht, les membres du jury pour avoir évalué ce travail. Je les remercie encore pour la qualité de leurs remarques ainsi que leur évaluation apportée à ce travail. J'ai été très honoré de leur présence.

Je tiens à remercier en tout premier lieu Benoit Appolaire et Julien Zollinger, mes directeurs de thèse, pour la patience et la confiance qu'ils m'ont toujours accordé. Je ne leur serai jamais assez reconnaissant pour leurs conseils, leur amitié, le regard critique qu'ils ont porté à mon travail et le savoir qu'ils transmettent avec passion.

Je remercie sincèrement Maxime El Kandaoui et Cécile Bernardi pour avoir fait en sorte que cette thèse soit possible et pour ces superbes années passées ensemble. J'aimerai également remercier Abdelkrim Chehaibou et Philippe Gressel, de m'avoir accueilli dans leur entreprise pour effectuer mes travaux, et d'avoir su créer un environnement agréable pour moi. Je tiens également à remercier les équipes à Yutz, surtout Daniel Knispel et Maxime Schmitt, pour ces nombreuses heures passées au laser. Je remercie l'ensemble des partenaires du projet FAFil pour les échanges et les collaborations autour du développement du procédé. Je remercie chaleureusement Flavio Soldera et Michael Engstler pour leur temps et l'intérêt qu'ils ont porté à ces travaux au cours de cette collaboration.

Je remercie également tout le département 3 à l'Institut Jean Lamour pour les nombreux échanges et la bonne ambiance qui y régnait. Je voudrais remercier plus particulièrement Julien Jourdan pour son aide sur la caméra rapide et la caméra thermique. Je remercie sincèrement Jaafar Ghanbaja, Sylvie Migot, Erwan Etienne, Mélanie Emo et Sandrine Mathieu du CC3M, pour leur sérieux et pour les nombreux accès au MET.

Je ne pourrais oublier de remercier mes collègues et amis, Mathias Lamari et Nazim Abdedou, qui m'ont rendu ces années au bureau plus faciles. Je remercie également tous les autres doctorants pour ces chaleureux moments et avec qui j'ai partagé un nombre incalculable de tasses de café. J'aimerais remercier toutes les personnes que j'ai pu rencontrer au cours de ces dernières années d'études.

J'aimerais remercier ma famille et mes amis proches malgré la distance qui nous sépare. Enfin je pense à Irmak, merci d'avoir été à mes côtés tant bien dans les moments difficiles que les meilleurs, et de ceux à venir.

Pour finir, je ne saurais comment assez remercier mes parents et mon frère pour leur amour et leur soutien sans faille au travers de toutes ces années. Rien n'aurait été possible sans eux, ce dont j'espère être digne.

Merci à tous,
Ivan

À mes parents,
à mon frère.

Résumé étendu en français

L'alliage Inconel 718 a fait l'objet de nombreuses études en fabrication additive au travers de ces dernières années. Développé pour ses hautes propriétés mécaniques et sa résistance à la corrosion jusqu'à 650 °C, cet alliage a été utilisé aussi bien dans l'industrie aéronautique que le nucléaire. La maîtrise de la morphologie de grain de croissance ainsi que la taille des microstructures ont été un challenge constant au fil des années à l'aide de nombreuses technologies de fabrication additive. La recherche s'est donc intensifiée particulièrement sur la transition colonnaire-équiaxe et la réduction de la taille des grains équiaxes, puisque ces dernières augmentent la tenue en fatigue ainsi que la résistance à la propagation de fissures pour les alliages de base Nickel.

Le procédé de fabrication additive par laser-fil coaxial est un procédé récent appartenant à la famille des procédés DED (Direct Energy Deposition). Celui-ci fait l'objet d'intérêt récent croissant pour les industriels car il permet de réduire les coûts de production liés à l'utilisation d'un fil par rapport aux technologies laser-poudres. Le projet INTERREG VA Grande Région de fabrication additive laser-fil (FAFil) a été entrepris dans l'objectif de développer la technologie laser-fil pour l'alliage Inconel 718 afin de l'amener vers l'échelle industrielle. La maîtrise du procédé a fait l'objet de plusieurs campagnes expérimentales, aboutissant à la fabrication d'un démonstrateur industriel. Le partenariat transfrontalier du projet (Région Grand Est, Wallonie, Sarre et Luxembourg) coordonné par l'Institut de Soudure, a su mettre en œuvre les compétences de chacun des 14 opérateurs pour mettre en place une synergie, sur les aspects techniques et scientifiques, conduisant à lever les verrous technologiques liés au procédé laser-fil. La phase finale des travaux a abouti à la fabrication, avec le procédé laser-fil, d'un démonstrateur selon une CAO fourni par Safran Aircraft Engines, permettant ainsi la comparaison de celui-ci avec les autres procédés de fabrication additive et le procédé de fabrication conventionnel dans le cadre d'une étude technico-économique.

Le travail de recherche présenté dans ce manuscrit est inscrit dans le cadre du projet FAFil et a pour objectif la compréhension de l'établissement des microstructures rencontrées lors de la fabrication de pièce en alliage d'Inconel 718 en utilisant la technologie laser-fil coaxial. Pour ce faire, la stabilité du procédé ainsi que les aspects thermiques ont été étudiés afin de faire le lien avec les mécanismes de solidification en jeu dans le bain de fusion lors du dépôt des couches successives.

De la technologie lit de poudre à celle de la projection directe de poudre, mais également du faisceau d'électron à l'arc-fil ; l'alliage Inconel 718 a fait l'objet d'un grand nombre de publications dans la littérature scientifique. Un intérêt particulier a été apporté à l'étude de la stabilité de dépôt et à la réduction des défauts présents dans les zones affectées thermiquement et fondues lors de l'opération de fabrication additive. Ces étapes permettent par la suite de s'intéresser à la transition colonnaire-équiaxe basée sur la modification du gradient thermique et de la vitesse d'interface de solidification à l'aide des paramètres du procédé. Des zones à grains équiaxes ont été rapportés avec l'utilisation d'une grande variété de procédé pour l'Inconel 718, mais

récemment des zones à grains très fins ont été observées avec le procédé laser-fil.

Le principe du procédé de fabrication est présenté sur la Figure 1. Le fil en Inconel 718 est dévidé afin d'être fondu par le faisceau laser annulaire lors du contact avec le bain de fusion. Le dépôt de matière est réalisé sous atmosphère inerte. Les principaux paramètres sont la puissance du laser (W), la vitesse d'avance (m/min) et la vitesse de dévidage du fil (m/min).

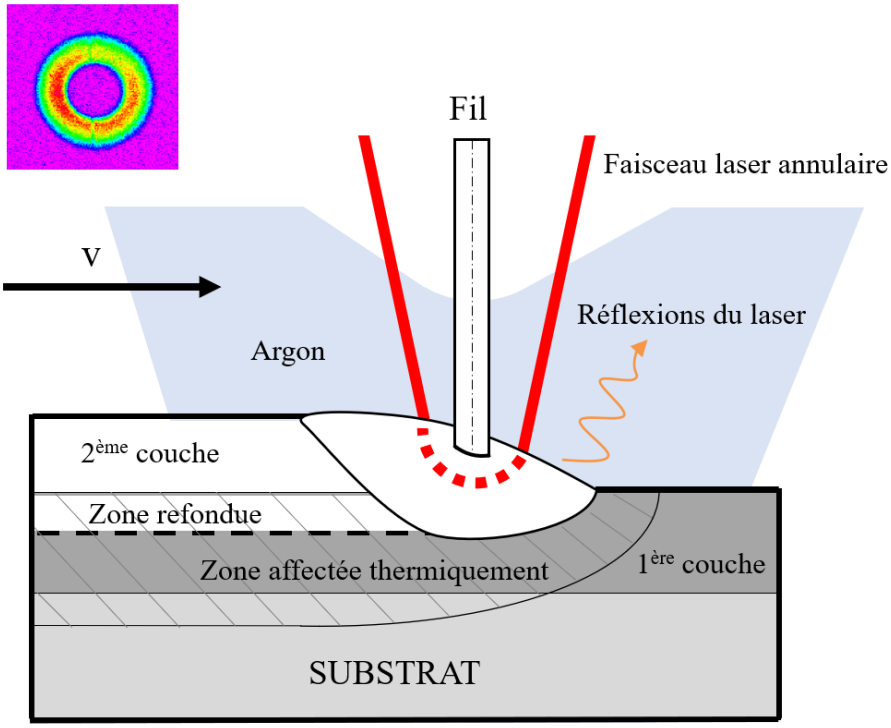

Figure 1: Représentation schématique du procédé laser-fil coaxial lors du dépôt à une vitesse d'avance pré-définie. La distribution d'énergie du faisceau laser annulaire est représentée en haut à gauche de la figure. Le fil est fondu par le faisceau laser annulaire sous atmosphère inerte.

Dans cette thèse, plusieurs mono-dépôts d'Inconel 718 ont permis d'établir une cartographie paramétrique du procédé, en identifiant les dépôts stables de ceux avec fils infondus et/ou des projections importantes. Le fil infondu est induit par une énergie insuffisante pour fondre correctement le fil et les projections par une énergie trop importante. Les fortes réflexions laser observées pour les énergies de dépôt les plus élevées ont conduit à limiter les hautes puissances et vitesse de fabrication. Un domaine de soudabilité opératoire a été établi avec une plage de variation de paramètre pour la puissance, la vitesse d'avance et la vitesse de dévidage du fil. Une étude de l'influence des paramètres sur la hauteur et la largeur de dépôt a conduit à une évaluation du taux de dépôt pour ce procédé qui varie de 1 à 2,75 kg/h, se situant ainsi entre les technologies de dépôt direct avec poudre (LMD-P) et l'arc-fil (WAAM).

Le domaine opératoire stable a permis la construction de murs avec différents paramètres sans aucune fissure interne trouvée dans la microstructure, sauf un cas isolé, localisé entre

des inclusions de carbures TiC. La présence de microporosités et d'inclusions TiC/NbC est régulièrement observée dans les dépôts. La taille des microporosités est inférieure à 5 µm et les inclusions se forment majoritairement lors de la solidification et peuvent également provenir du fil utilisé, avec une taille allant jusqu'à 10 µm pour celui-ci. L'espacement interdendritique primaire a été mesuré permettant une comparaison avec les données de la littérature ainsi que la détermination de l'influence de l'énergie déposée sur la finesse de la microstructure. La réduction de la densité d'énergie notamment du fait de l'augmentation de la vitesse d'avance permet d'augmenter la vitesse de refroidissement et donc de réduire l'espacement interdendritique.

La présence de données sur les vitesses de bain liquide étant très limitée dans la littérature, l'imagerie par caméra rapide s'est avérée nécessaire pour estimer la vitesse du liquide en surface du bain de fusion. Le suivi de la vitesse des oxydes en surface a mis en évidence des accélérations et décélérations du liquide ce qui suggère un régime turbulent, variant autour de 0,4 m/s pour un seul jeu de paramètres (une seule condition opératoire). Très peu d'études ont été trouvées dans la littérature sur les mesures thermiques du bain de fusion en utilisant le procédé laser-fil coaxial avec l'Inconel 718. L'imagerie thermique a par la suite permis d'accéder à la température en surface du bain de fusion pour estimer le gradient thermique en fond de bain en connaissant donc la température maximale atteinte en surface, pour deux conditions de dépôts différentes, c'est à dire deux densités d'énergies volumiques différentes. Cette température est présentée sur la Figure 2a pour une densitée d'énergie de 367 J mm^{-3} (courbe bleue) et 515 J mm^{-3} (courbe rouge). En considérant l'approximation géométrique présentée sur la Figure 2b, la longueur L entre la température maximale et le solidus peut être mesurée ainsi que la profondeur du bain de fusion d. Le gradient thermique peut être estimé à l'interface de solidification en considérant le plan (y-z). Nous avons calculé le gradient thermique pour différentes formes de fond de bain de fusion : évolution linéaire, en puissance et en ellipse. La vitesse du front de solidification R a pu être déterminée en fonction de la vitesse d'avance qui dépend de l'angle θ entre le vecteur de vitesse d'avance V et le vecteur de l'interface solide/liquide perpendiculaire à l'interface, comme schématisé sur la Figure 2b. Cet angle θ a pu être déterminé pour chaque forme de fond de bain considérée, dans le plan (y-z). A cette interface de solidification, le produit du gradient thermique G et de la vitesse d'interface R permet d'obtenir une estimation de la vitesse de refroidissement. Nous montrons que cette dernière est impactée par la forme du bain de fusion considérée, donc par la courbure de l'interface, mais reste du même ordre de grandeur (10^3 °C/s) pour les deux énergies de dépôts étudiées. Cependant nous avons négligé les phénomènes tels que la convection du liquide qui peut fortement augmenter le gradient thermique à l'interface de solidification. Afin de vérifier cette première estimation de vitesse de refroidissement, l'espacement interdendritique a été mesuré pour ces mêmes conditions opératoires. Par la suite, nous nous sommes basés sur le modèle de Trivedi afin de recalculer l'espacement interdendritique en utilisant la vitesse de refroidissement de 10^3 °C/s déterminée pour les deux conditions opératoires. Cet espacement calculé à partir du modèle fut bien supérieur à la mesure des espacements pour les deux conditions opératoires (367 J mm^{-3} et 515 J mm^{-3}). Nous avons donc recalculé la vitesse de refroidissement nécessaire afin d'obtenir l'espacement primaire mesuré, et il s'avère que la vitesse de refroidissement du procédé est plutôt de l'ordre de 10^4 °C/s. Ce résultat a été comparé avec les estimations des vitesses de refroidissement de la littérature pour les technologies de dépôt direct avec poudre et fil pour les alliages bases Nickel et confirment notre estimation basée sur l'espacement interdendritique.

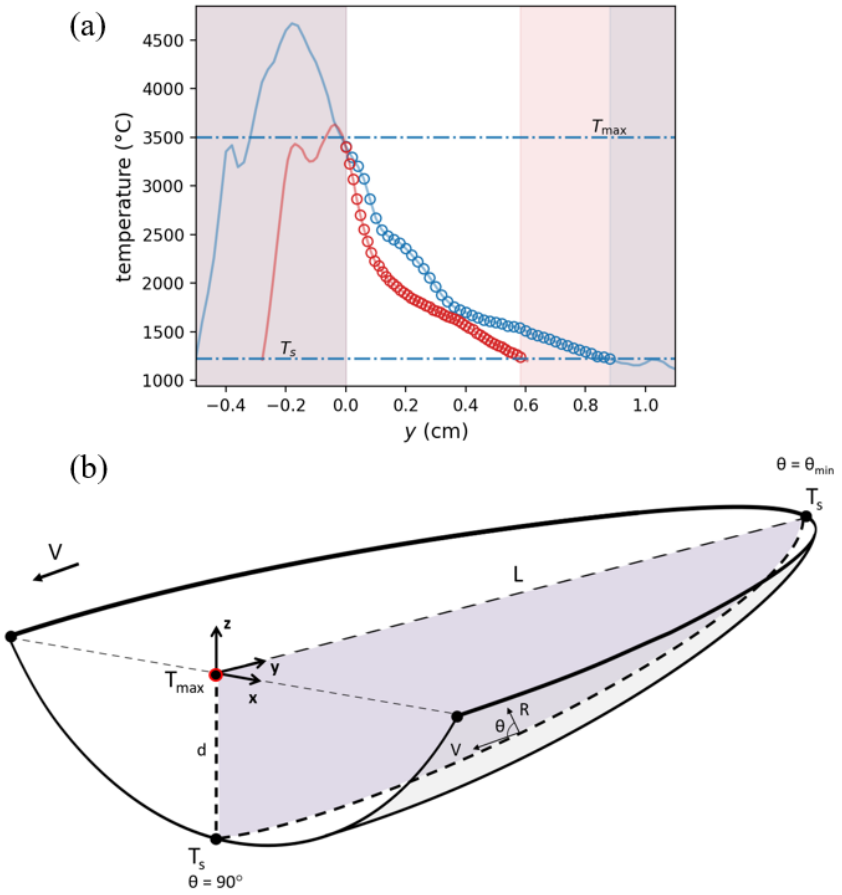

Figure 2: (a) Profil de température en surface du bain pour deux conditions opératoires : $E = 367\,\mathrm{J\,mm^{-3}}$ en bleu et $E = 515\,\mathrm{J\,mm^{-3}}$ en rouge. (b) Représentation schématique du bain de fusion lors du dépôt, où la température a été mesurée en surface de la température maximale T_{max} au solidus de l'alliage T_s. Le vecteur R correspondant à la vitesse d'interface S/L pour θ variant de θ_{min} à 90°.

L'exploration paramétrique ainsi que la caractérisation des dépôts a ouvert la possibilité de fabrication de murs multi-passes massifs pour le prélèvement d'éprouvettes et l'évaluation des propriétés mécaniques en traction, présentés en annexe B de ce manuscrit. Des zones équiaxes sont régulièrement rencontrées en fond de bain à chaque couche des murs fabriqués. Ces grains équiaxes sont présents pour une grande variation d'énergie linéaire et ont une grande influence sur la dureté, puisque cette dernière atteint des valeurs de 500 Hv par rapport aux zones colonnaires où des valeurs de l'ordre de 280 Hv sont atteintes. La présence de ces zones équiaxes semble persister de façon périodique lors de la fabrication des murs multipasses, et induit un changement de taille de grain très important, similaire au changement de taille de grain induit par de l'inoculation.

L'analyse EBSD ainsi que des figures de pôles de grains équiaxes multi-maclés a montré que des grains maclés partagent une symétrie d'ordre 5, comme exposé sur la Figure 3a-c. D'autres grains en relation d'orientation ont confirmé la présence d'une symétrie icosaédrique, comme schématisé sur la Figure 3d. La symétrie icosaédrique a été confirmée par superposition cohérente des directions ⟨110⟩ des grains identifiées et celles calculées à partir d'un icosaèdre théorique, détaillé dans le Chapitre 4 du présent manuscrit. Il en a été déduit que l'origine des grains équiaxes rencontrés dans les dépôts est induite par le phénomène appelé "Icosahedral Short Range Order (ISRO) mediated nucleation", identifié dans la littérature pour les alliages d'Al-Zn-Cr et d'Au-Cu-Ag [1, 2] uniquement avec addition de quelques ppm de Cr et Ir. C'est la première fois que ce mécanisme de germination de la phase Ni fcc est observé en fabrication additive pour l'Inconel 718, et pour tout procédé d'élaboration confondu. La mise en évidence de ce mécanisme fourni également une explication concernant la présence de zones à grains équiaxes auparavant observés dans la littérature pour le même alliage. Ce mécanisme de réduction importante de taille de grain est par ailleurs intéressant car les zones équiaxes se trouvent en fond de bain, là où le gradient thermique est le plus élevé et la vitesse de front de solidification la plus faible, ce qui va à l'encontre des modèles de transition colonnaires-équiaxes.

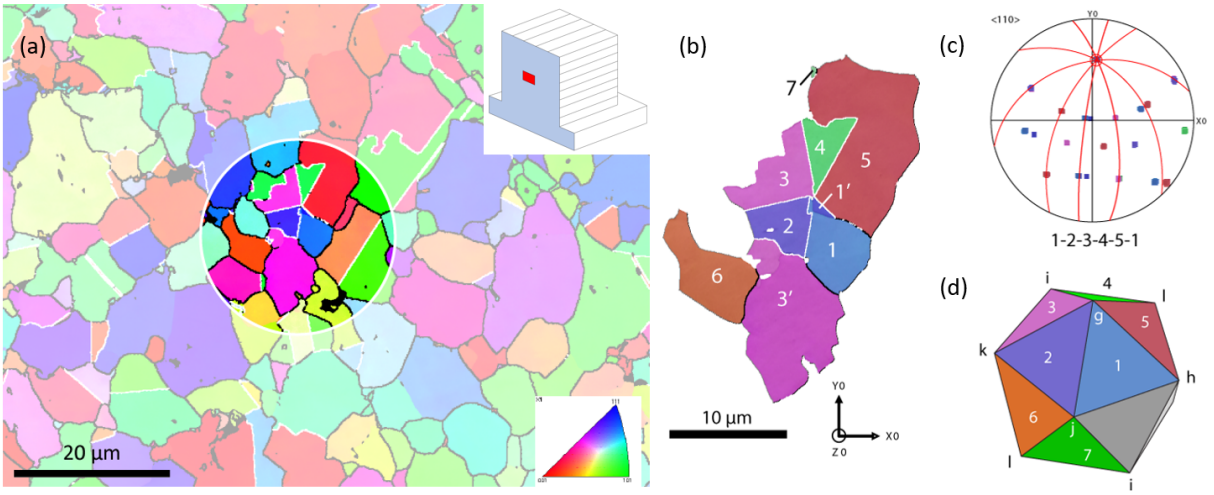

Figure 3: (a) Carte EBSD de la zone de grains équiaxes montrant la zone analysée (coloration IPF) (b) Grains proches voisins avec une relation d'orientation multi-maclée (c) figure de pôle ⟨110⟩ des grains 1-2-3-4-5 montrant un axe de symétrie 5 où les arcs de cercles rouges correspondent aux plans {111} en commun par paire de grains (d) Icosaèdre dont les facettes correspondent à la même couleur et au même nombre que les grains présentés précédemment (voir chapitre 4 pour plus de détail).

Dans ce travail de thèse, il est supposé que le mécanisme "ISRO mediated nucleation" est accentué par le procédé laser-fil lui-même puisqu'il combinerait d'importantes vitesses de refroidissement ainsi que des enrichissements locaux du liquide en fond de bain lors de la fonte des passes précédentes. La germination et croissance d'un grain en relation de macle afin de compléter le défaut de fermeture de 360° d'un axe de symétrie d'ordre 5 montre que les grains

fcc ont la capacité de germer par maclage afin de réduire l'énergie interfaciale plutôt que de germer avec une désorientation quelconque, lorsque les conditions thermiques le permettent. Ces résultats posent de nouvelles questions pour le système Ni fcc dans le mécanisme "ISRO mediated nucleation". Ce mécanisme a été appuyé par des observations complémentaires illustrant des grains voisins maclés sans relation d'orientation avec les autres grains aux alentours dans un volume en 3D caractérisé par EBSD et EDS. Cette caractérisation du volume de grains équiaxes a révélée la présence de joints de grains maclés autour d'inclusions de TiC dans le volume de la région équiaxe. Un axe de symétrie 5 a été identifié entre des grains fcc émergeant d'une inclusion de TiC comme montré sur la Figure 4a-b, sans relation d'orientation avec la particule TiC. Une caractérisation au MEB avec électrons secondaires de type II a révélé la présence de phases nanométriques sur la surface des carbures TiC dans la zone équiaxe pouvant jouer un rôle dans la germination hétérogène des grains fcc. Des précipités de tailles réduite à quelques centaines de nanomètres dans les zones eutectiques entre phase de Laves et grains fcc ont été également observés, ce qui a motivé l'utilisation d'une technique de caractérisation plus fine dans ces zones équiaxes et notamment autour des TiC.

La caractérisation au microscope électronique à transmission (MET) a permis de mettre en évidence la présence de carbures NbC sur la surface des TiC ainsi qu'une phase enrichie en Nb de structure fcc dans les zones à grains colonnaires. Des zones enrichies en Niobium ont été identifiées par EDS dans la zone à grains équiaxes autour des TiC, où le taux en Niobium atteint 32 %. La Figure 4c montre que la phase Nb_2Ni a été identifiée sur la surface d'un carbure TiC dans la zone équiaxe, ce qui révèle qu'une ségrégation locale en Nb est importante en fond de bain de fusion lors du dépôt et permet une solidification hors-équilibre de phases riches en Nb tel que Nb_2Ni. Cette phase n'a jamais été caractérisée auparavant pour l'Inconel 718 et a été récemment découverte dans le système binaire Ni-Nb [3]. La présence de cette phase métastable confirme le processus d'enrichissement local en éléments d'alliage, puisqu'une autre phase fcc $Mg_{0.32}Ti_{0.68}$ riche en Mg a également été identifiée en surface d'un TiC. La recherche d'autres phases métastables a été effectuée avec le logiciel ASTAR afin de réaliser une cartographie d'indexation automatique (ACOM) au MET permettant d'indexer la phase Ni_6Nb_7 dans une zone ségrégée en Nb dans la région à grains équiaxes. Certaines des zones ségrégées en Nb n'ont pas pu être indexés dû à leurs structures inconnues. La forte présence de phases avec des motifs icosaédriques dans leurs structures montre que leur origine peut être initiée par le mécanisme ISRO dans le liquide enrichi en Nb. Ces observations corroborent l'hypothèse que l'origine de "ISRO mediated nucleation" des grains Ni fcc dans ce cas précis est induite par des ordres icoasédriques locaux résultant de l'enrichissement en Nb. Cet enrichissement conduit localement à former un système Ni-Nb avec la présence de phases métastables qui ont été identifiées ainsi que des ordres icosaédriques d'ordre local et moyen (IMRO). Il est également possible que pour des vitesses de refroidissement importantes, des structures partiellement amorphisées se retrouvent dans les zones avec les plus fortes concentration en Nb.

Cependant, une seconde hypothèse est retenue suivant laquelle les phases métastables rencontrées enrichies en Nb peuvent également agir comme site de germination hétérogène pour la phase Ni fcc. Parmi les phases candidates potentielles à l'origine de la germination et croissance hétérogène de la phase Ni fcc, les icosaèdres dans les structures des différentes phases Ni_2Nb, Nb_2Ni et Ni_6Nb_7 ont été étudiés et comparés. Le décalage atomique entre les axes de symétrie 5

des icosaèdres et un tétraèdre fcc est donc respectivement déterminé et la phase Ni_6Nb_7 reste la phase qui possède une famille d'icosaèdre avec un décalage atomique le plus faible par rapport à la structure fcc du Ni. Cette phase Ni_6Nb_7 est donc celle qui pourrait servir de site de germination hétérogène mais cependant aucune relation d'orientation n'a été trouvée avec la matrice Ni fcc d'après la cartographie d'indexation automatique au MET.

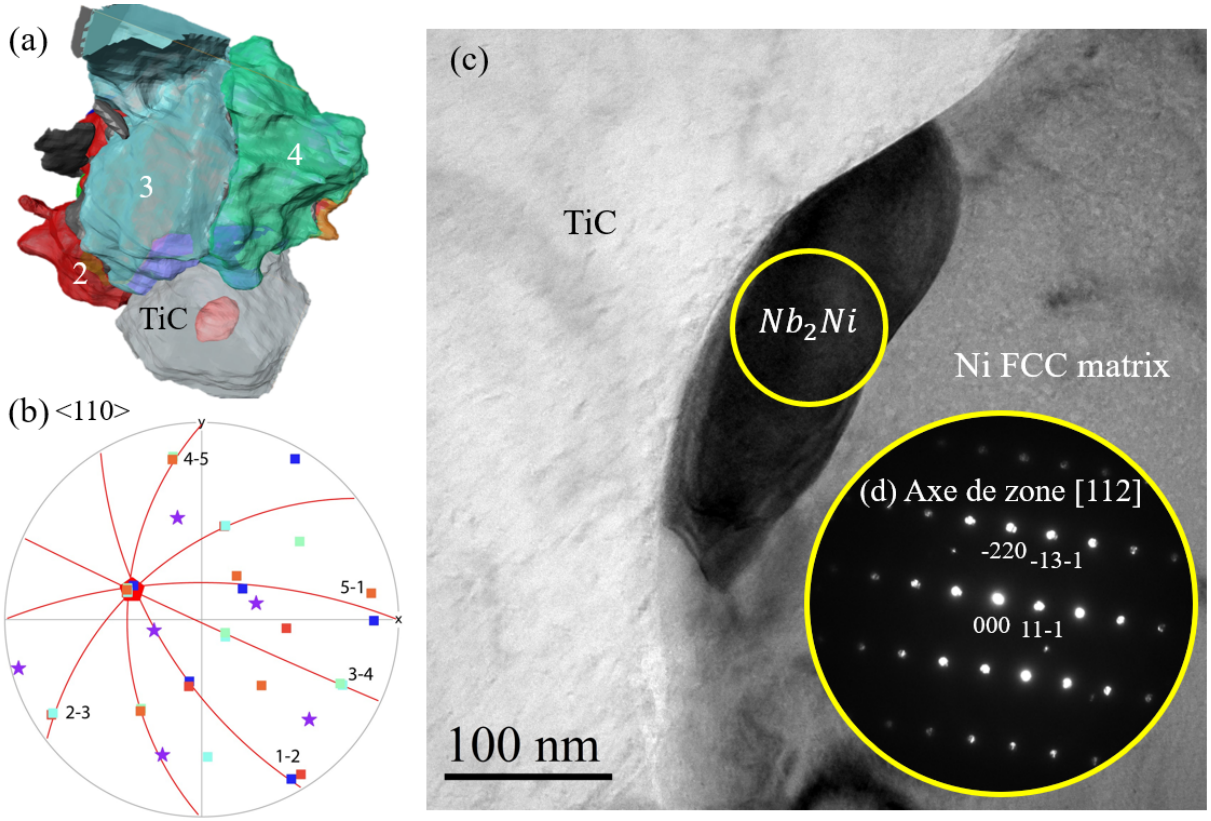

Figure 4: (a) Visualisation 3D des grains 1-2-3-4-5 partageant une symétrie d'ordre 5 connectés à une particule TiC. Les joints de macles sont représentés en gris foncé. (b) Figure de pôle ⟨110⟩ des grains 1-2-3-4-5 partageant une direction ⟨110⟩ commune correspondant à un axe de symétrie d'ordre 5, avec les plans {111} représentés par des arcs de cercles en rouge. Les étoiles en violet correspondent aux directions du TiC qui montre aucune relation d'orientation avec les grains précédents. (c) Image MET d'un précipité enrichie en Nb à la surface d'un TiC et (d) son cliché de diffraction correspondant à la phase Nb_2Ni, suivant l'axe de zone [112].

Les phases en présence entre les TiC des zones colonnaires et équiaxes suggèrent que la température atteinte en zone équiaxe et colonnaire est différente. Les TiC en fond de bain sont proches du solidus de l'alliage et donc potentiellement plus stables. L'importante microségrégation de Nb autour des TiC a montré que ces carbures ont tendance à attirer par affinité chimique certains éléments d'alliage tel que le Nb et le Mg. Les conditions thermiques locales autour des TiC ainsi que l'enrichissement en Nb peuvent expliquer la présence d'ISRO en fond de bain, couplé certainement à un brassage du bain liquide localement insuffisant lors de la refusion des passes précédentes.

La stabilité thermodynamique des différentes phases rencontrées dans la zone équiaxe autour des TiC a démontré qu'une forte concentration de motifs icosaédriques est possible entre le solidus et le liquidus de l'alliage. La stabilité des phases rencontrées ainsi que des zones amorphes est possible pour une concentration supérieure à 37 % de Nb. Les phases Ni_6Nb_7 et Nb_2Ni se forment respectivement autour de 42 % de Nb et entre 55 et 60 % de Nb. Il est fort probable que des ordres icosaédriques locaux dû au Nb se retrouvent donc dans le liquide en cohabitation avec le solide fcc en cours de solidification autour des carbures TiC. La Figure 5 schématise les phases rencontrées sur les TiC dans la zone équiaxe. L'enrichissement local en Nb en périphérie des TiC, de l'ordre du micromètre, accentué par les conditions thermiques du procédé en fond de bain permet localement l'ISRO. Cette présence d'ISRO voire "Icosahedral Medium Range Order" (IMRO) est probablement à l'origine des phases Nb_2Ni, Ni_6Nb_7 et des zones partiellement amorphes rencontrées, mais également à l'origine de la germination de la phase Ni fcc observée entre les grains de la zone équiaxe, comme résumé sur la Figure 5. Les carbures TiC jouent donc un rôle important dans la formation de l'ISRO et par conséquent dans l'affinement de grain en capturant les éléments minoritaires lors de la refusion des passes précédentes pendant l'opération de dépôt. Il est possible que d'autres éléments jouent un rôle dans la construction des icosaèdres et des potentiels quasi-cristaux dans le liquide.

Plusieurs annexes viennent compléter ce manuscrit. La première détaille l'optimisation du traitement thermique ainsi que l'évaluation des propriétés mécaniques en traction et en résilience. L'effet de l'énergie de dépôt ainsi que la présence des zones à grains équiaxes permettent une évaluation du procédé ainsi qu'une comparaison avec les résultats de la littérature pour l'Inconel 718. La deuxième annexe présente l'analyse EBSD grain à grain ainsi que la démonstration de la symétrie icosaédrique respectée par les grains fcc dans un cas précis. La dernière annexe expose la caractérisation fine de la phase de Laves (C14) Ni_2Nb et montre la possibilité de substitution des différents éléments dans la structure participant à la construction des motifs icosaédriques.

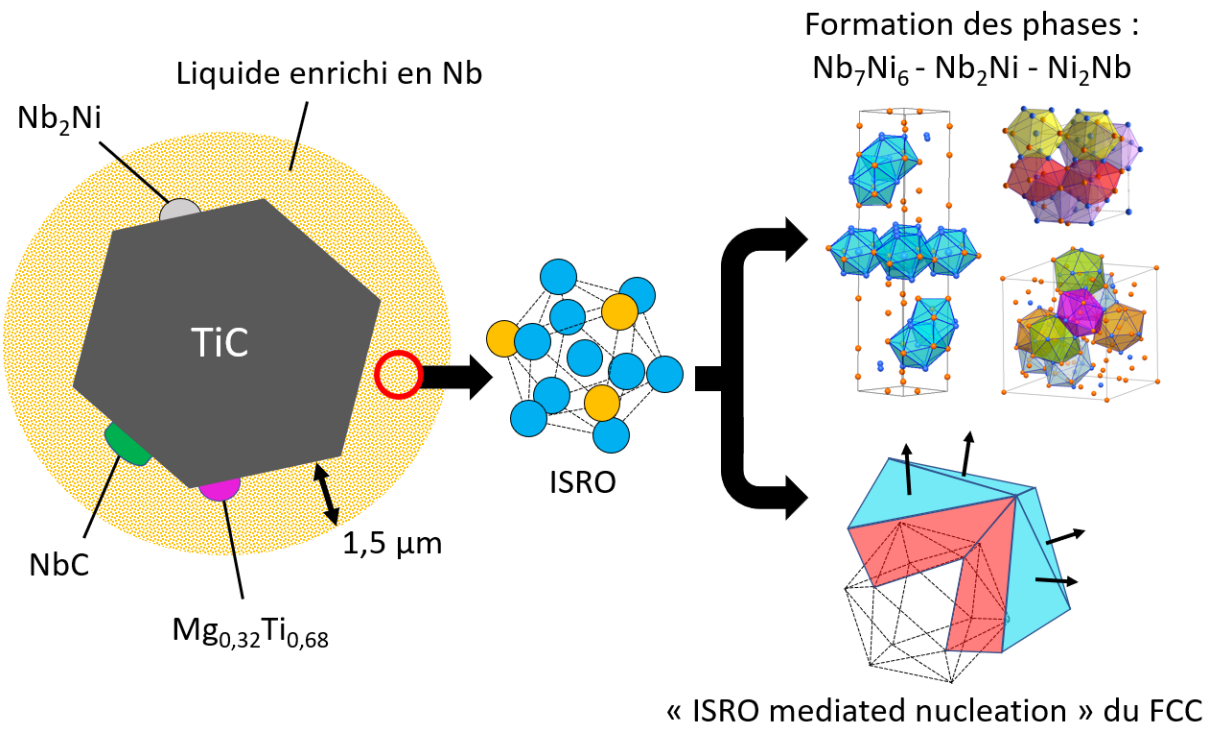

Figure 5: Représentation schématique du liquide enrichie en Niobium autour des inclusions TiC sur un rayon d'environ 1.5 µm. Ces enrichissements locaux permettent la formation d'ISRO qui peut induire la formation de phases métastables telles que Nb_2Ni et Ni_6Nb_7 mais aussi de l'ISRO mediated nucleation de la phase Ni fcc.

Sommaire

List of Figures

Nomenclature

Most of the acronyms are defined within the text. For clearance a nomenclature with all the acronyms is given below:

Symbols :	
AM	Additive manufacturing
LWAM	Laser and wire additive manufacturing
FCC	Face centered cubic
TEM	Transmission electronic microscopy
EB-PBF	Electron beam powder bed fusion
LB-PBF	Laser based powder bed fusion
LMD	Laser metal deposition
EBM	Electron beam melting
DED	Direct energy deposition
SLM	Selective laser melting
LMD-W	Laser metal deposition using wire
LMD-P	Laser metal deposition using powder
SEM	Scanning electronic imaging
SE	Secondary electrons
BSE	Back-scattered electrons
EBSD	Electron backscatter diffraction
IPF	Inverse pole figure
EDS	Energy dispersive X-ray spectroscopy
STEM	Scanning transmission electron microscopy
ADF	Annular dark field
BF	Bright field
HAADF	High angle annular dark field
SAED	Selected area electron diffraction
FIB	Focused ion beam
WAAM	Wire arc additive manufacturing
OM	Optical micrograph
CET	Columnar to equiaxed transition
ISRO	Icosahedral short range order
FCC	Face centered cubic
NT	Near twin
iQC	Icosahedral quasicrystal
FFT	Fast Fourier Transform
ACOM	Automated crystal orientation mapping
IMRO	Icosahedral Medium Range Order

Introduction

Over the recent years, global reduction of energy consumption in industry has driven the development of new technologies for manufacturing parts. The reduction of material wastes when producing parts while improving metallic alloys properties has become mandatory and a real technological challenge. For decades, both aeronautic and aerospace industries have been searching to reduce the weight of their components, increasing their lifetime and reliability. Additive manufacturing (AM) of Ni-based superalloys has been introduced first in these fields where manufacturing costs are significant, especially for small production series and complex alloys. Among AM technologies, with the recent laser developments, both powder and wire can be used as feedstock materials to build parts layer-by-layer, with low defect densities and macrosegregations compared to conventional processing techniques such as casting. Increasing demand for direct energy deposition technologies in industry has led to the development of coaxial laser and wire devices, with more flexible definition of trajectories and fast building cycles.

Inconel 718 nickel-based alloy is investigated in the present work. It is used in high temperature applications, keeping high tensile properties up to 650 °C. Controlling the microstructures, in particular those ensuing from solidification, is one of the main challenge for using routinely this alloy with AM. Indeed, AM implies rapid solidification conditions, beyond the ones usually prevailing in conventional processes. The resulting microstructures are most often composed of large elongated grains, often associated with defects, that are obviously detrimental to the mechanical properties. Hence, improving the process for this alloy requires a deeper understanding of the microstructure and defects formation. In particular, it has been reported recently that equiaxed grains can be obtained with Inconel 718 with different AM technologies. These observations have not been explained convincingly, although promoting these microstructures would largely improve the mechanical properties through grain size reduction and suppression of solidification texture and cracking susceptibility.

The main objectives of the present thesis are (i) the development of stable processing of Inconel 718 using a recent building process based on coaxial laser and wire; (ii) a deeper understanding of the microstructure formation, in particular during solidification.

To meet these objectives, the present manuscript is divided into five chapters.
The first one reviews briefly the literature on Inconel 718, with an emphasis on the different microstructures obtained in additive manufacturing, in particular with laser and wire processes.
The second chapter provides basic information about the experimental techniques used for this study, such as the laser and wire device and the different microstructure characterization techniques.
The development of the laser and wire for Inconel 718 is detailed in the third chapter. A careful parametric study is carried out to quantify the influence of the process parameters on the geometry of built material, metallurgical defects and grain morphologies. Moreover, we explain our analysis of the solidification conditions by combining thermal analysis as well as rapid imaging.
The fourth chapter deals with the formation of equiaxed crystals, based on a careful characterization of these microstructures, obtained in some conditions discussed in the previous chapter. The fifth chapter is devoted to the characterization of different phases and microstructures in relation with the mechanism at the origin of the equiaxed grains.

We conclude our manuscript with a short synthesis of the main achievements that open new perspectives of research.

The present work is part of the FAFil (Fabrication Additive Laser-Fil) project focused on the Additive Manufacturing technology of Laser and Wire for metallic alloys, supported by the european INTERREG programs and funded by the European Regional Development Fund (ERDF). This 4 years project is a partnership between 14 research and development centres: Institut de Soudure (lead partner), Materalia, SIRRIS, CRM, Cenaero, Luxinnovation, Pôle MecaTech, Skywin, University of Liège, University of Luxembourg, University of Saarland and Safran Aircraft Engines, Groulab, CRITT TJFU.
In this framework, Institut de Soudure has developed wire based additive manufacturing technologies for industrial scale applications and research purposes. Using wire arc AM (WAAM) technology on a daily basis, and more recently laser and wire AM, it has been the driving force for improving the quality of the parts build with the process investigated in the present thesis.

This thesis was funded by Institut de Soudure, INTERREG Program No. 050-4-08-126 and by ANRT FRANCE under CIFRE Ph.D. Fellowship 2018-1630.

Chapter 1
Literature review

The first chapter aims at providing a short literature review of the different fields investigated in the present work. First, we focus on the general features of Inconel 718. In particular, we introduce the different phases, their morphologies and their influence on the mechanical properties. Next, typical microstructures obtained by additive manufacturing are shortly reviewed, with a small emphasis on the formation of equiaxed grains. Finally, we give a small survey of recent works on processes using laser and wire, applied to Inconel 718.

1.1 Inconel 718

Inconel 718 is the most frequently used among the Nickel based superalloys. Its resistance to oxidation and its mechanical properties are excellent from cryogenic temperatures up to 650 °C [4]. Its resistance to severe environments is much higher than the resistance of common steels. This explains why Inconel 718 is widely used in aeronautic, petrochemical and energy industries. It is used in gas turbines, pumps and discs of aircraft engines for its good tensile strength, fatigue resistance and toughness [5].

Such properties are achieved by combining different hardening mechanisms such as solid solution, precipitation (carbides at grain boundaries and secondary phases) and grain refinement, thanks to optimized composition and treatments. Conventional Inconel 718 parts are either cast under vacuum and forged or rolled for producing plates, or wire drawing ; or produced by near-net shape casting. Still, conventional processes are often plagued with macrosegregations [6] that make difficult to obtain homogeneous microstructures and properties.

Besides these processes, additive manufacturing (AM) has been used these last years to build near-net shape Inconel 718 parts with more and more complex shapes, using either powder or wire as a feedstock material [7]. But due to the fast cyclic thermal history associated with the building process, they feature microstructures that usually differ from conventional ones. Among the different microstructural features that play a role on mechanical properties, grain size has a very large impact. Figure 1.1 illustrates that the smaller the grain size, the better these properties are. However, controlling grains morphology and size in AM processes is a real challenge. Hence, many studies have been devoted to decrease the solidification texture by promoting equiaxed grains through either thermal conditions [8, 9, 10], or alloying [11].

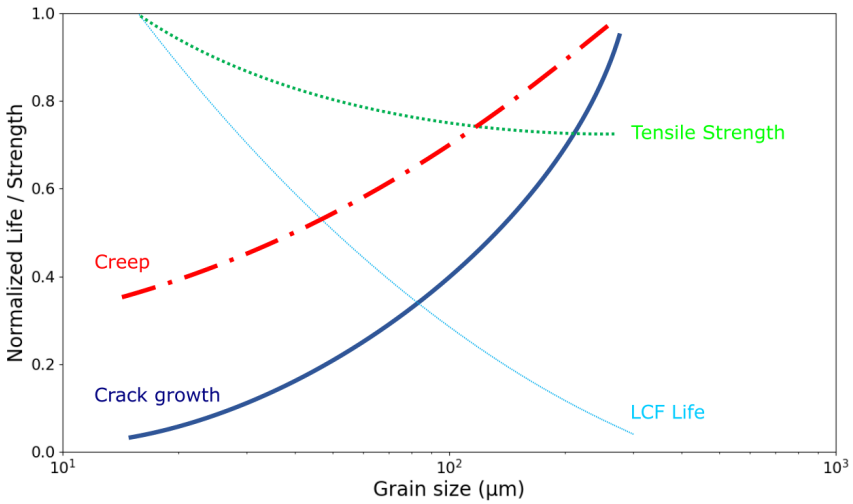

Figure 1.1: Effect of grain size on creep, low cycle fatigue life, fatigue crack growth rate and tensile strength [12].

Table 1.1: Chemical composition of Inconel 718.

Species	mass %
Ni	50-55
Cr	17-21
Fe	15-21
Nb	4.75-5.5
Mo	2.8-3.3
Ti	0.65-1.15
Al	0.2-0.8
Co	≤1.00
C	≤0.08
Mn	≤0.35
Si	≤0.35
Cu	≤0.3

1.2 Phases

Standard NF EN 3884 chemical composition of Inconel 718 is reported in Table 1.1. The most significant elements are Ni, Cr and Fe. These elements are the main constituents of the major phase, austenite γ, with faced cubic centered (fcc) structure (Fig. 1.3a). At room temperature, its lattice parameter is $a_\gamma = 0.3608\,\text{nm}$, and varies with temperature and composition [13]. γ is the first to solidify below liquidus temperature at 1340 °C (Fig. 1.2). During slow cooling, carbides NbC (or TiC) precipitate around 1280 °C and coexist with the liquid and γ [14]. Their structure is NaCl with lattice parameter $a = 0.444\,\text{nm}$ (Fig. 1.3b). It has also been observed that TiN can form in liquid before carbides, and occasionally act as nucleation sites.

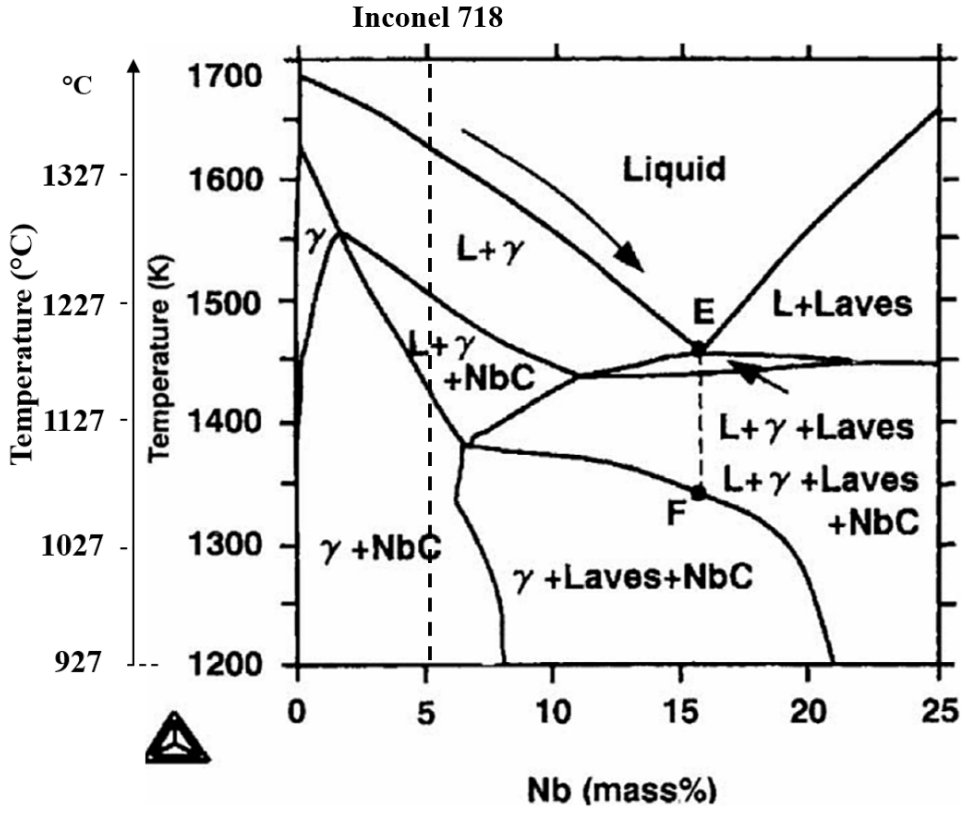

Figure 1.2: Isopleth section of the phase diagram containing the composition of Inconel 718 (dashed line) [15].

Due to the microsegregation resulting in the enrichment of interdendritic liquid in Nb and Mo, solidification ends with the formation of eutectic composed of γ and Laves phase C14 (Fig. 1.2). C14 solidifies at around 1175 °C (depending on the local composition). Its structure is hexagonal compact with formula $(Ni,Fe,Cr)_2(Nb,Mo,Ti)$ [13] and lattice parameters $a = 0.481$ nm and $c = 0.783$ nm (Fig. 1.3c). This phase does not provide any hardening and is considered as brittle.

The high tensile and fatigue properties of Inconel 718 are not given by γ nor any phases formed during solidification. These properties are achieved by the precipitation at the solid state of hardening secondary ordered phases such as γ' $Ni_3(Ti,Al)$ and γ" Ni_3Nb [13]. γ' is illustrated in Figure 1.3d and has an fcc structure with $a = 0.359$ nm and γ" in Figure 1.3e and has a tetragonal structure with $a = 0.362$ nm and $c = 0.741$ nm. As it can be observed, both γ' and γ" have a close lattice parameter a with γ, that shows the coherency between these phases and the matrix. γ' and γ" are formed with holding temperature between 600 and 900 °C. The conventional heat treatment in order to precipitate these phases is made of 2 stages: 720 °C for 8 h followed by 625 °C for 8 h [16], detailed in appendix A.

The last phase in Inconel 718 is δ: it is the stable structure of Ni_3Nb γ", and has an orthorhombic structure with lattice parameters of $a = 0.5141$ nm, $b = 0.4231$ nm and $c = 0.4534$ nm, as illustrated in Figure 1.3f. δ is incoherent with the other phases, provides no hardening to the matrix, and form between 700 and 1000 °C in microstructural areas enriched with Nb [17]. However, it can participate to limit grain growth and split Laves phases when precipitating [18]. Conventionnally, δ is forming during solution heat treatment at the grain boundaries to inhibit grain growth of the matrix during processing [19].

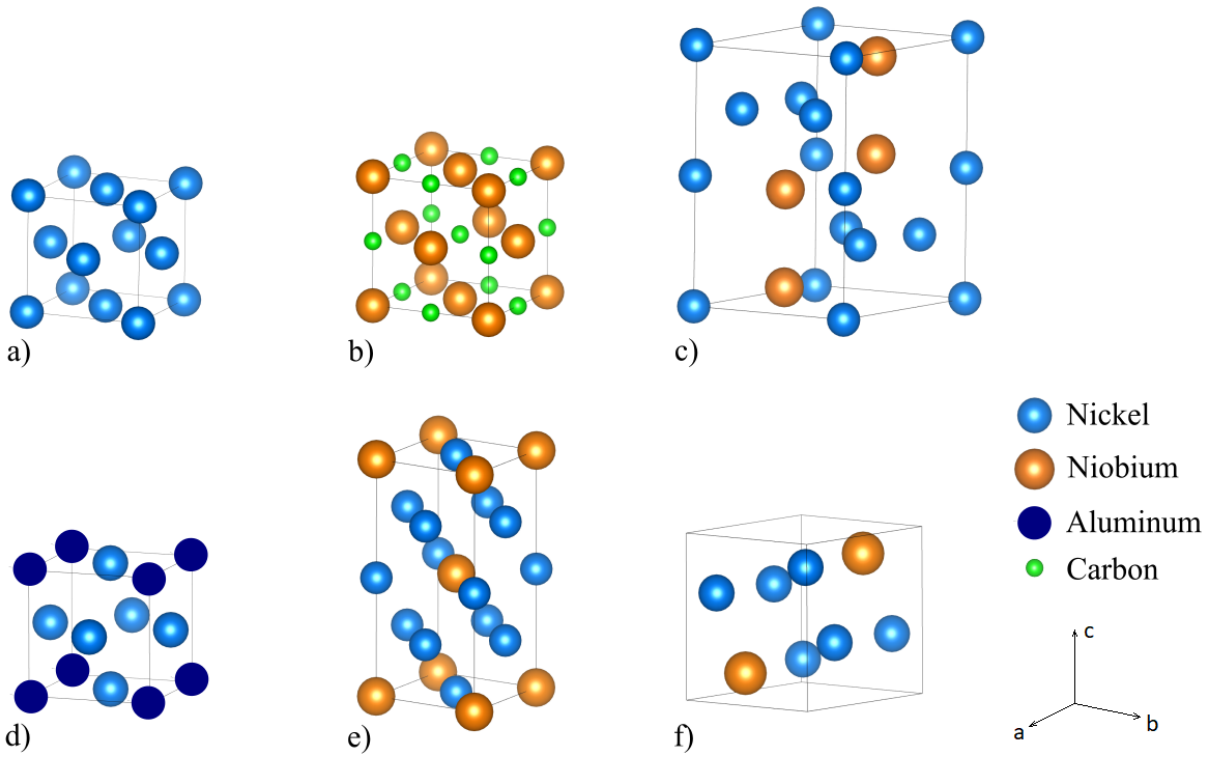

Figure 1.3: Atomic lattice structures of the phases of the alloy: (a) γ matrix fcc A1 (b) NbC carbide B1 phase (c) Laves phase Ni_2Nb C14 (d) γ' $Ni_3(Ti,Al)$ $L1_2$ phase (e) γ" Ni_3Nb $D0_{22}$ phase (f) primitive δ $D0_a$ phase. Note: Ni can be substituted by Cr and Fe; and Nb by Mo.

1.3 Microstructures obtained by additive manufacturing

1.3.1 As-built conditions

In Figure 1.4 [19] have compared the microstructures ensuing from either conventional casting or AM technologies. Except for casting, the grains are columnar dendritic/cellular for all processing conditions. The grain morphology is controlled by the ratio G/R (i.e. cooling rate), with G the thermal gradient and R the interface growth rate. The orientations of the columnar grains and the resulting texture are selected as in welding [20]. The grains with their $\langle 100 \rangle$ growth directions that are the closest to the thermal gradient are selected when the other are suppressed by the competing grains. The alignement of Laves phase precipitates along the interdendritic regions is illustrated in Figure 1.4. They are generally associated with NbC carbides. Laves phase is usually reported to increase liquation cracking in heat affected zones during AM [21][22]. Unfortunately, it is not possible to avoid their formation during solidification (Fig. 1.5), due to the microsegregation of Nb, Mo and Ti. Nonetheless, it has been reported that increasing the cooling rate can reduce their fraction and their morphology [19], and reduce the cracking risks and needs for homogenizing the microstructure.

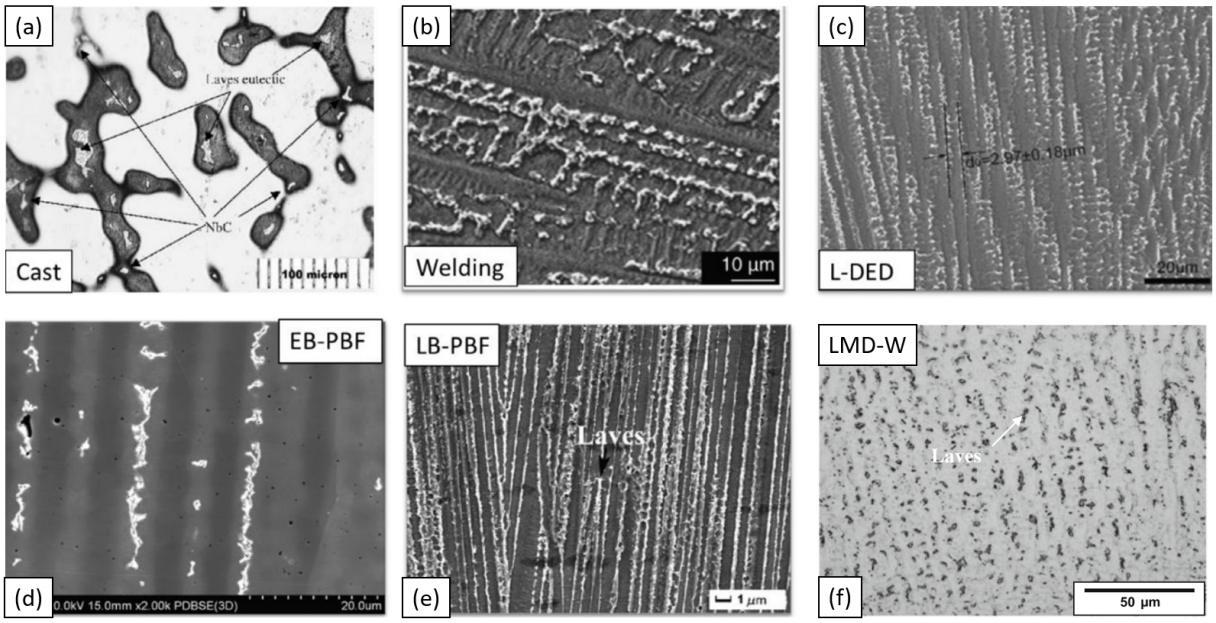

Figure 1.4: Microstructures obtained with different process: (a) casting, (b) welding, (c) LMD-P, (d) EB-PBF, (e) LB-PBF and (f) LMD-W. Adapted from [19][23]. Laves phase C14 and NbC carbides are in bright contrast in interdendritic regions except for LMD-W.

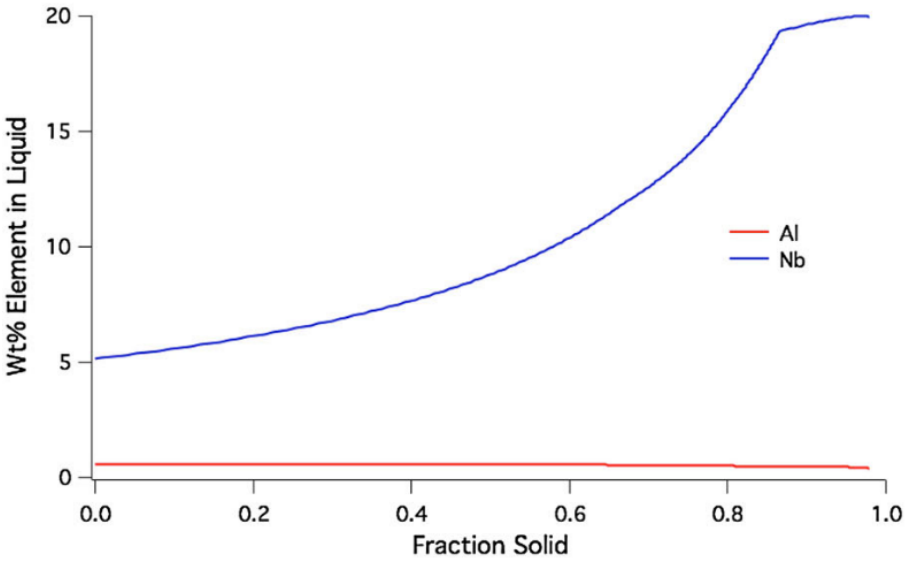

Figure 1.5: Microsegregation profiles in Al and Nb predicted by Scheil model in Inconel 718 [24].

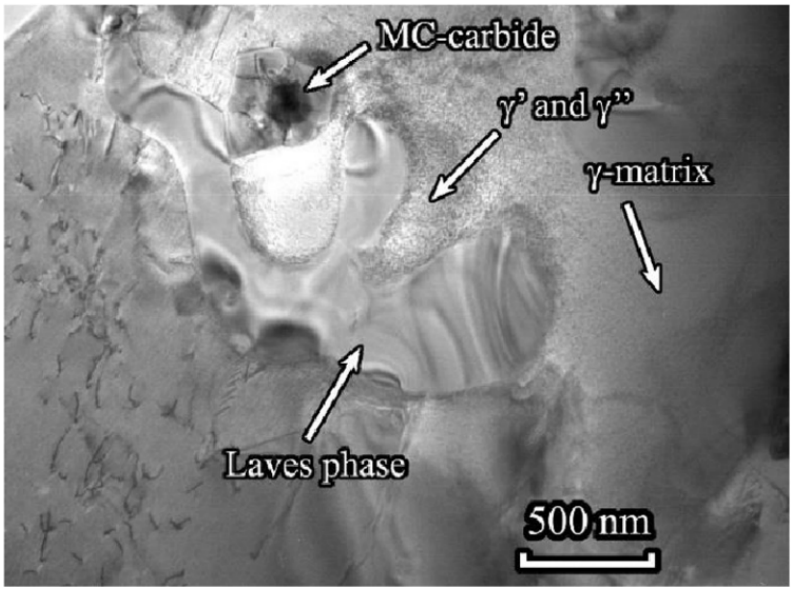

Figure 1.6: TEM micrograph of the interdendritic region in a specimen built by LMD-P showing γ matrix, Laves phase, MC carbide, and secondary γ' and γ" precipitates [25].

The enrichment in Nb around Laves phases promotes the precipitation of γ', γ" and δ in the interdendritic regions [19]: the higher the temperature, the faster the precipitation. For example, γ' and γ" have been observed around Laves phase in specimens built by LMD-P (Fig. 1.6). In specimens built using EB-PBF, δ needles were observed at grain boundaries [26], probably due to significant time spent at high temperatures associated with the high energy inputs of the process.

1.3.2 Towards equiaxed grain morphology

Different strategies have been proposed to control the grain structure ensuing from solidification. Unlike conventional casting, it is possible with AM to play with the process parameters, such as the input energy, scanning velocity and building strategy in order to establish thermal conditions promoting equiaxed grains, i.e. low temperature gradients G and fast interface velocity R.

To identify the relevant physical parameters affecting the columnar-to-equiaxed transition (CET), Hunt's model can be considered as a first step [27]. It compares two characteristic times: the time necessary for the columnar front to grow over the length of the undercooled liquid; and the time necessary for equiaxed grains to nucleate and grow in the undercooled liquid up to some critical volume fraction that blocks the columnar front. The transition from columnar to equiaxed is obtained when both times are equal. Considering that the critical volume fraction is about 50%, the condition for equiaxed growth can be expressed as:

$$G < 0.617\,(n^*)^{1/3}\left[1-\left(\frac{\Delta T_n}{\Delta T_c}\right)^3\right]\Delta T_c \tag{1.1}$$

where n^* is the density of nuclei, ΔT_n the nucleation undercooling.

In a multicomponent alloy, the constitutional undercooling ΔT_c reads:

$$\Delta T_c = \sum_i m_i \left(c_i^0 - c_i^{l*}\right) \tag{1.2}$$

where m_i are the slope of liquidus with respect to solute i, c_i^0 the nominal concentrations and c_i^{l*} the concentration at the dendrite tips in the liquid.
Considering a dendrite growth model to assess c_i^{l*}, Gäumann *et al.* [28] came up with the following expression for the constitutional undercooling:

$$\Delta T_c = (a\,R)^{1/n} \tag{1.3}$$

where R is the columnar growth rate, and a and n are materials specific constants.

From this model, three main parameters can be identified to promote equiaxed grains:

1. increasing the number of nuclei n^*. Gäumann *et al.* [28] have estimated this number for laser cladding of CSMX-4 alloy as $n^* = 2 \times 10^{15}\,\mathrm{m}^{-3}$. This number can also be assessed using the average grain size D after solidification as $n^* \approx 1/D^3$.
2. Decreasing the thermal gradient G.
3. Increasing the growth rate R (and the constitutional undercooling ΔT_c).

Using this model as a guidance, the most successful solution to obtain equiaxed grains to date has relied upon preheating the substrate or previous built layers. This has been performed mainly with electron beam melting (EBM) technology [29, 30]. It has been suggested that this strategy would be efficient also with other technologies such as direct energy deposition (DED) and selective laser melting (SLM) [30]. This solution is often associated with high energy inputs contributing to establish low temperature gradients in the top layers [31].
It seems more difficult to identify general trends for the scanning speed because its relation with the velocity of the solidification front R is not straightforward [31, 32, 33]. For example, Dehoff *et al.* [10] changed the electron beam current and velocity in order to affect the thermal gradient G and the solidification front velocity R to form equiaxed grains. A pre-heating at 977 °C was applied and a large advance speed of 48 m/min. Despite these conditions compliant with the guidelines listed above, only a mixed columnar-equiaxed morphology has been achieved. Other studies have investigated different conditions in terms of pre-heating temperatures and beam parameters, and were able to obtain equiaxed grains ranging from 80 to 400 µm [8, 9]
Figure 1.7 shows an example of microstructures obtained with EBM and two different spot beam currents [9]: for the smallest current, a mixed columnar-equiaxed microstructure has been obtained, whereas fully equiaxed grains have been achieved for the largest current. This effect has been attributed to the decrease of G, although the relation between the beam current and the temperature gradient is not obvious.

The influence of the process conditions has also been investigated for SLM. In [34], they have considered low heat input and high processing speed to achieve low G/R condition. They have obtained mixed columnar-equiaxed grains with size ranging from 5 to 125 µm (zones 1 and 3 in Fig. 1.8). As expected, the associated tensile properties (elongation, yield and ultimate strengths) are much improved in the equiaxed zone compared to the anisotropic columnar microstructure.

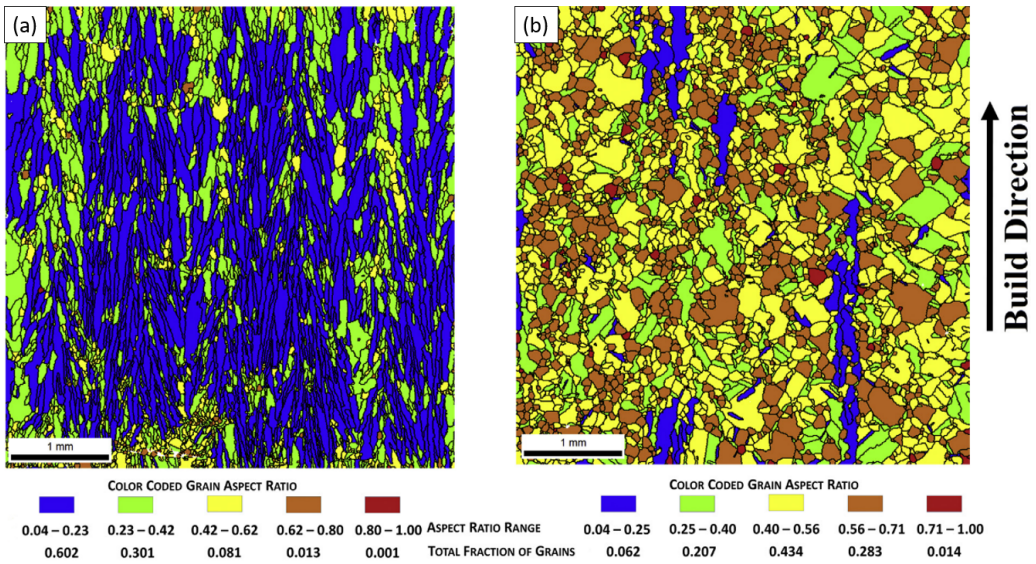

Figure 1.7: Grain aspect ratios in samples built using EBM with 1 ms beam ON time, and beam spot currents of (a) 10 mA and (b) 20 mA [9].

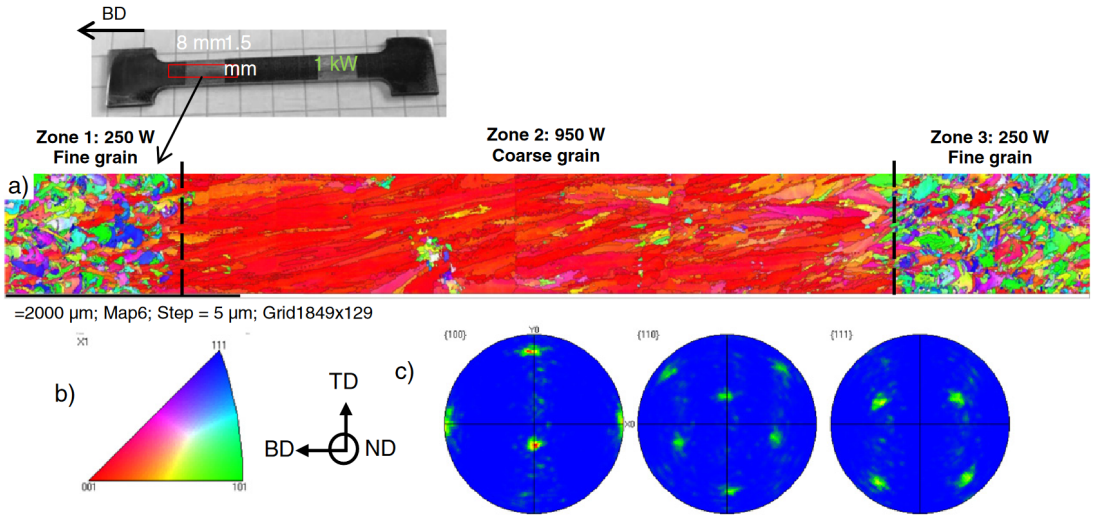

Figure 1.8: EBSD analysis of a graded Inconel 718 sample featuring a central columnar zone surrounded by regions with fine equiaxed grains. (a) Inverse Pole Figure of the longitudinal cross section. (c) Pole figures of columnar zone 2 [34]. Building direction is indicated as BD.

A number of attempts to control the grain structure have been proposed based on designing building strategies, although the link is not obvious between the strategy and the physical parameters G and R controlling the CET. Nonetheless, it is worth mentioning a successful work on Al alloy using direct laser sintering [35].
Rather than playing with G and R, enhancing the nucleation of new grains (i.e. increasing n^* in Eq. (1.1)) is another promising route for controlling the grain structure. Hence, solutions similar to usual practices in conventional casting or welding have been proposed, such as addition of grain refiners in Ti64 [36], dendrite fragmentation in high entropy alloys [37] and endogenous nucleants generated by the remelting

of intermetallic in Al alloys with Sc [38]. In some studies using DED process, it has been suggested that partially melted powder can act as heterogeneous nucleation sites and promotes equiaxed grains [39, 40]. Modifying the compositions is another promising approach to increase the fraction of equiaxed grains, as shown by Kong *et al.* [11]. Indeed, these authors have changed the Nb content of Inconel 718 and demonstrated that increasing the Nb content from 1 to 6% refines the grains from 450 to 100 µm and changes the morphology from columnar to equiaxed. As a side effect, the fraction of Laves phase increases with the Nb content. Although no mechanism has been proposed for explaining this trend, it can be assumed that the alloying content modifies the number of nuclei and may favor equiaxed grains according to Hunt's model, Eq. (1.1). Still, this remains to be proved.

Finally, it is worth mentioning that fine equiaxed grains (typically $\leq 10\,\mu m$) have been observed for low to medium linear energy densities ranging from 0.11 J/mm (SLM) to 117 J/mm (DED) in Inconel 718. Similar observations have been made for SLM [41, 42], DED using powder (or LMD-P) [43, 44], electron-beam wire (EBM-W) [45] and coaxial laser-wire (LMD-W or LWAM) [46] processes. When the information is provided, the equiaxed grains are systematically located at the bottom of the layers in all the AM processes mentioned above and for a wide range of advance speeds (from 3 to 1000 mm/s). Different explanations have been proposed so far. Hence, Bambach *et al.* have attributed the formation of equiaxed grains to some local recrystallisation [46]. On the contrary, Mostafa *et al.* and Choi *et al.* have both advocated that high concentrations of impurities in remelted areas could act as heterogeneous nucleation sites for equiaxed grains [41, 42]. As discussed earlier, other authors have pointed out the effect of the thermal gradient G and solidification velocity R, through the ratio G/R [45, 44, 9, 34]. In addition, Parimi *et al.* have underlined the possible local fluctuations of G due to Marangoni effect and of nucleation sites due to powder injection [43]. They have also shown that increasing power prevents the equiaxed grains to appear. Finally, they have demonstrated that the building strategy does not seem to play any role in the appearance of equiaxed grains, whereas increasing power leads to fully columnar grains. On the contrary, Helmer *et al.* [47] have found for EBM that some building strategies can promote the appearance of equiaxed grains coexisting with columnar grains in mixed regions, attributed to the change of growth direction at each layer. The same kind of observations has been done by [43] for LMD-P. They even achieved to obtain fully equiaxed zones at the bottom of layers, with 20 µm equiaxed grains.

1.3.3 Laser and wire processing

The use of wire instead of powder for producing Inconel 718 parts has been introduced recently in laser processing, for the following advantages:

- higher materials efficiency;
- larger dimensions;
- lower fractions of internal porosities;
- cleaner processing environment;
- and easier storage since oxidation is not an issue for wires whereas it is for the stability of powders [48, 49, 50].

When using front wire feeding, the microstructure is composed of NbC carbides and δ spread in the γ matrix, as in conventional laser and wire cladding [23]. The grain structure is columnar dendrites oriented parallel to the building direction. Liquation hot cracking was reported in interdendritic regions of previous layers, due to re-heating in the heat affected zone when adding new layers. Bergs *et al.* [51] also observed oxides, Fig. 1.9. These oxides are rich in Titanium and Oxygen, and their formation has been attributed to due to the combination of unoptimized gas shielding and heat accumulation. Using in-

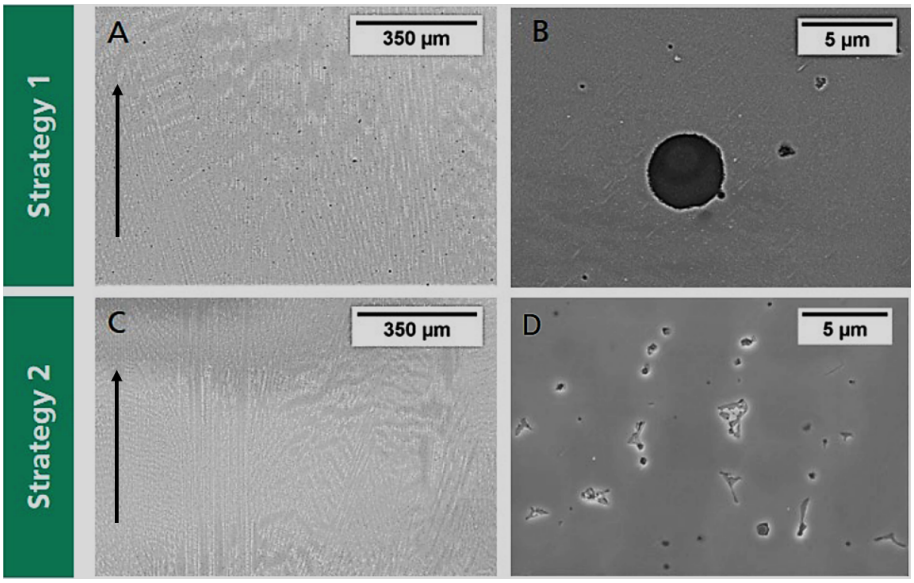

Figure 1.9: SEM micrographs of microstructures of Inconel 718 thin-walls processed with two different strategies [51]: (A,B) no interlayer cooling; (C,D) with interlayer cooling. (A,C) columnar dendritic structrure; (B,D) oxides.

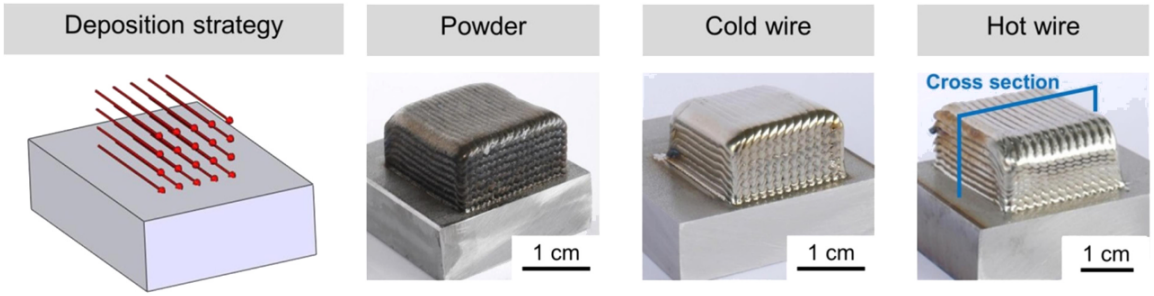

Figure 1.10: Deposition strategy and multitrack built walls by coaxial laser with: powder, cold and hot wire [46].

terlayer cooling reduces the oxide size (Fig. 1.9) and prevent hot cracking. Moreover, interlayer cooling improves processing stability.

Bambach *et al.* [46] compared the use of powder, cold wire and hot wire during coaxial laser processing (Fig. 1.10), in the case of a unique wall. Lack of fusions have been observed for hot wire samples. The microstructures for the three different feedings are reported in Figure 1.11. Typical columnar grains are observed with powder, as in other AM processes (Figs. 1.11a-d). When using wire, equiaxed grains are reported, and their fraction increases with hot wire (Figs. 1.11b,c,e,f). Based on a qualitative estimation of the dislocation density with the Kernel average misorientation of EBSD measurements (Figs 1.11g-i), the authors have explained the occurrence of equiaxed grains by some local recrystallisation. However, they did not emphasized the presence of equiaxed grains with cold wire. It is worth mentioning that such large equiaxed zones with drastic grain size reduction (6.4 µm in average) were not observed previously in AM processing of Inconel 718, and could be beneficial to prevent hot cracking and for mechanical properties.

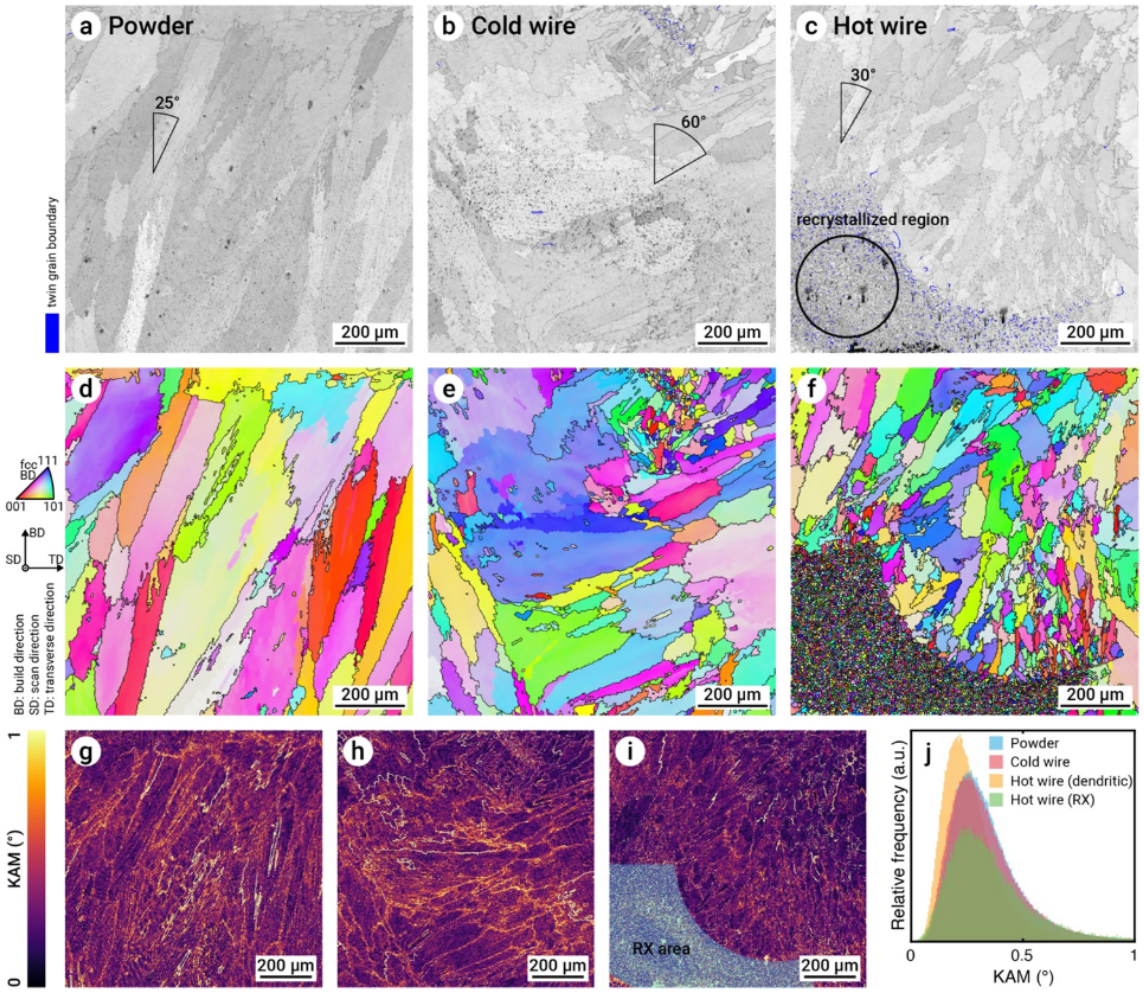

Figure 1.11: Microstructures of samples [46] built with (a) powder (b) cold wire, (c) and hot wire processing. (d-f) Orientation IPF. (g-i) Corresponding kernel average misorientations.

1.4 Conclusion

This short literature review has demonstrated first, the importance of the processing conditions on the grain morphology, in AM of Inconel 718. It has been shown that interdendritic segregations are associated with the precipitation of intermetallic phases that may be detrimental in terms of hot cracking and porosity. Finding a way to get rid of these defects by using a new technology such as coaxial laser and wire is one of the motivation of the present study.
Second, it has been shown that it would be possible to control the grain structure. Hence, building parts with equiaxed grains would improve the resistance to hot cracking, as well as the overall mechanical properties. Two routes have been proposed so far to refine the grain structure: either by modifying the composition or by imposing specific thermal conditions. Nonetheless, the rationalization of the observations of equiaxed grains in the different technologies for Inconel 718 (and similar alloys) has not really been achieved because it is difficult to access to the local compositions and thermal conditions. Moreover, the recent findings of wide zones of fine equiaxed grains using coaxial laser and wire is another motivation for investigating more deeply the microstructure formation using this technology.

Chapter 2
Experimental techniques

In this chapter, we briefly describe, on one hand the laser and wire additive manufacturing process that has been developed in this work, and on the other hand the techniques that we have used to characterize the microstructures in the subsequent chapters.

2.1 Laser and wire process

2.1.1 Installation

In this study, manufacturing was conducted using a Precitec CoaxPrinter laser head (Fig. 2.1). The laser head is carried by an ABB IRB 6640-185 polyarticulated robot. The laser source is an IPG 10 kW Yb^{3+} doped fibre solid state laser providing a laser beam with wavelength of 1070 nm, brought by an optical fibre, 600 µm core diameter. The wire feeding system is a push-pull ABICOR BINZEL, where the output is aligned axially to the laser head. An Argon atmosphere is provided by two copper gas nozzles in front and at the back of the wire tip.

Stainless steel 304L plates of $20 \times 200 \times 100\,mm^3$ have been fixed on the working table as substrates when building samples. Commercially available Inconel 718 welding wire, 1.2 mm in diameter, was used in this study with the chemical composition given in table 2.1.

Figure 2.2 illustrates the process during the building of two layers (the energy density of the annular laser beam is plotted at the top left insert). The molten pool is created by the incident photons, as in laser welding ; the photons melt the wire feed into the liquid metal, and create a weld bead when moving on the work surface.
The ability of the alloy to be processed depends on its laser absorption coefficient, its reflectivity and wettability. The laser absorption depends on the material and its surface roughness, the higher the roughness the greater the absorption coefficient [52]. During the impact of the laser with the metal surface, a part of the laser intensity is lost by reflection. This depends on the reflectivity of the metal surface. The wettability of the alloy depends on the alloy, but also on the heat input and the metal surface.

The scheme of the focal lens focusing the annular laser beam used in this study is shown in Fig. 2.3. Considering an annular laser beam crossing a focal lens, the beam is focused at a fixed spatial reference, the focal point O, depending on the diameter of the focal lens d and on the diameter of the annular laser beam. At this focal point, it can be defocused either positively or negatively (resp. defocus+ and defocus- in Fig. 2.3). If we consider now the coaxial laser and wire system, the wire will be fed before crossing the focal point, at position w on the working surface. We call working distance (or stand-off position) the fixed spacing between the laser head reference and the wire position, melted by a ring created by the annular beam at the position w in the positive defocus. The annular laser spot ring at position w has a radius that may change if the working distance change. This can lead to a variation of the input energy on the wire. In this study, the resulting focal point diameter is 0.5 mm, the working distance 105 mm and the radius of the annular ring at the position $w = 2.5$ mm.

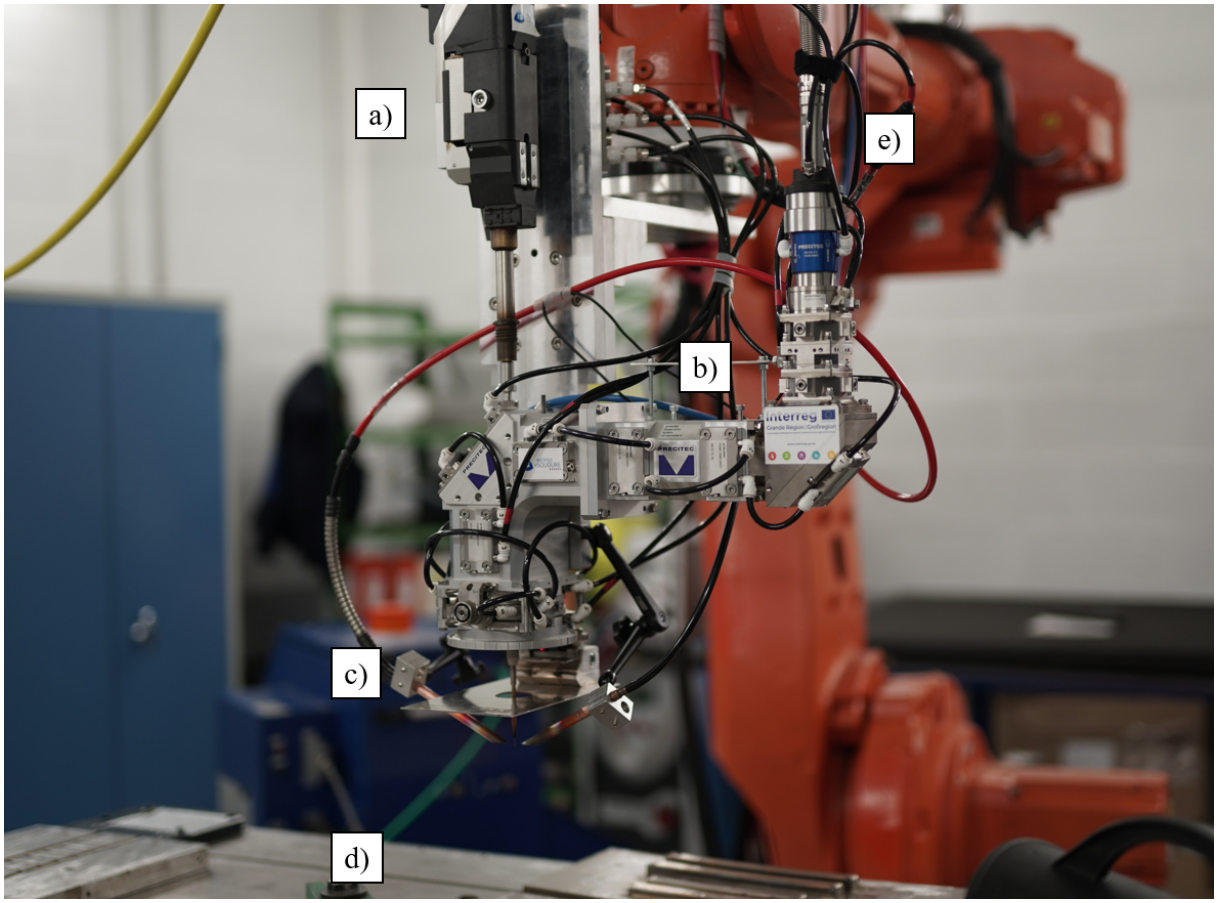

Figure 2.1: Laser and wire robotic setup at the Institut de Soudure with the (a) wire feeding delivery system, (b) laser head CoaxPrinter, (c) gas and wire nozzle, (d) working table, and (e) optical fibre connected to the CoaxPrinter.

Table 2.1: Chemical composition of Inconel 718 wire used in this study.

Species	Ni	Cr	Fe	Nb	Mo	Ti	Al	Co	C	Mn	Si	Cu	Ta
mass %	52.6	18.4	18.8	5.13	3.06	0.93	0.66	0.30	0.05	0.24	0.08	0.05	0.01

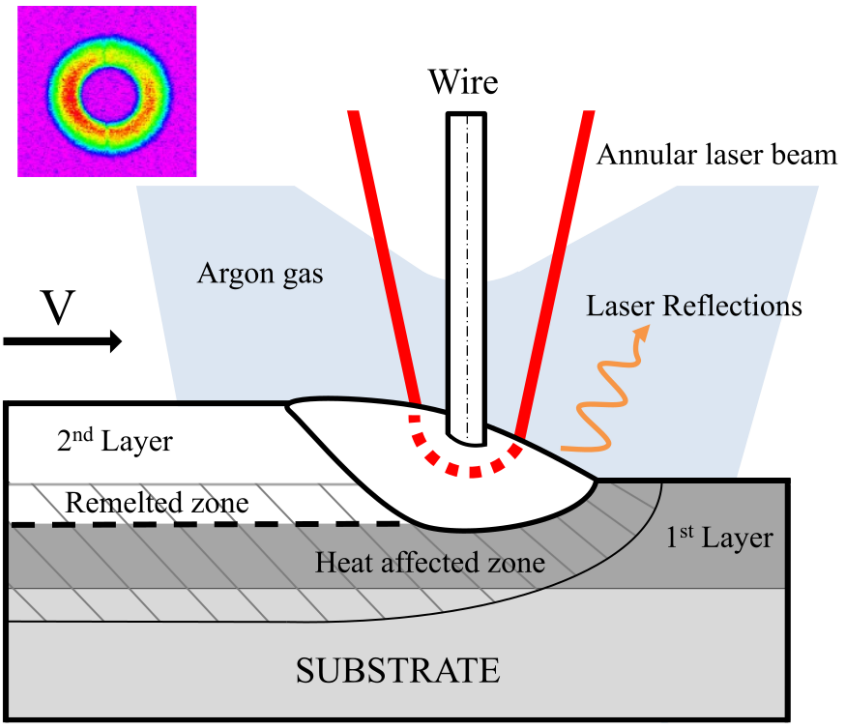

Figure 2.2: Scheme of the coaxial LMD-W process with advance speed V (top left insert: energy distribution in the annular beam).

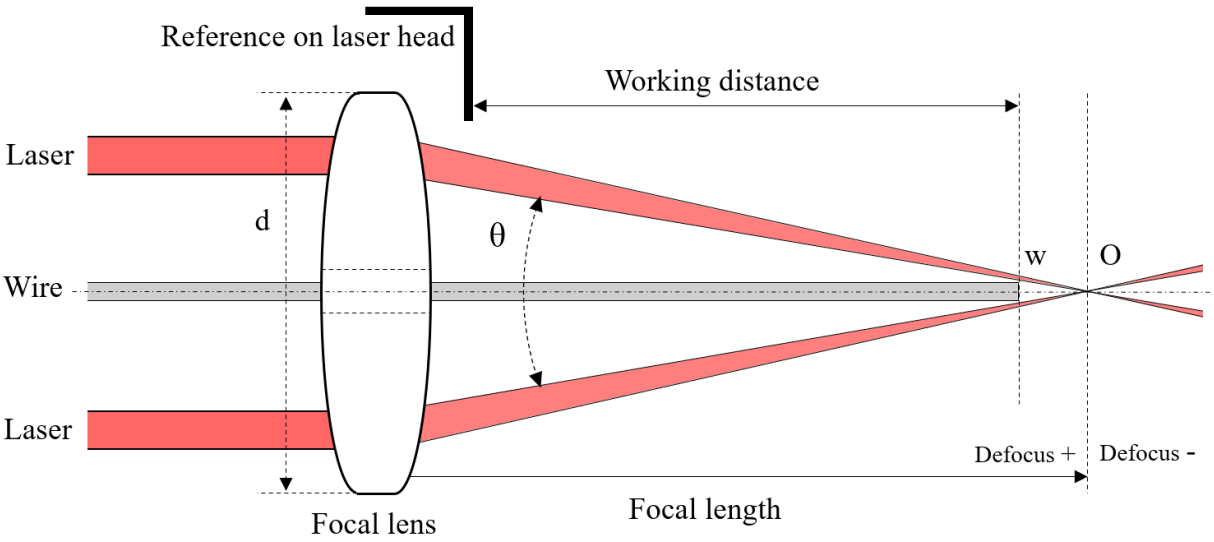

Figure 2.3: 2D section of the focal lens focusing the annular laser beam.

2.1.2 Scanning strategies

Manufacturing samples was carried out along different types of scanning strategies as illustrated in Figure 2.4, to investigate the process. Unidirectional processed beads are defined as single track beads (Fig. 2.4a). The single track wall (Fig. 2.4b) is built by stacking single tracks with an height increment iZ, resulting in an additive manufacturing strategy along the z axis. Multi-track wall is also incremented in height, but with a bidirectional scanning strategy consisting in alternating the direction of deposition in the $x-y$ plane, as explained in Fig. 2.4c. The hatch spacing H between beads controls the overlapping of neighboring beads in the $x-z$ plane to prevent any lacks of fusion. Figure 2.5 shows an example of a manufactured multitrack wall.
An example of cross section of a single track bead is shown in Fig. 2.6, where the bead height Ht, the width W and penetration depth Pl are defined. The hatch spacing H between beads is defined as $H = W/2 + r$ with r is the wire radius.

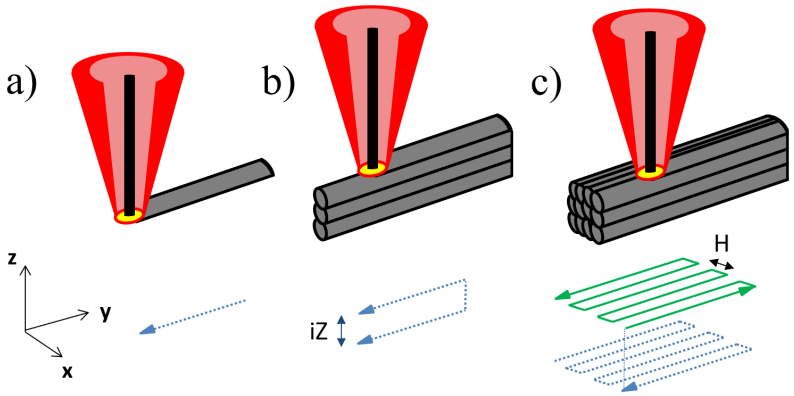

Figure 2.4: Strategies of deposition: (a) single bead track along the y axis; (b) single track wall in the $y-z$ plane; (c) multi-track wall alternating the building directions at each layer along the x axis.

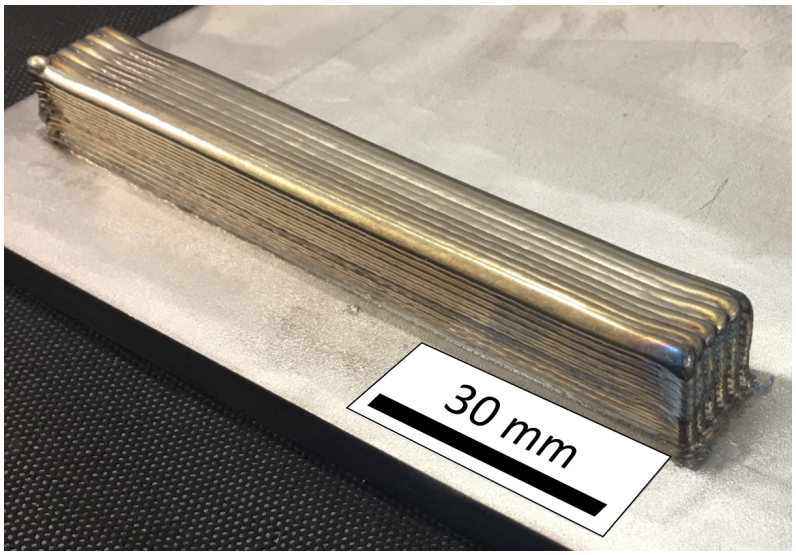

Figure 2.5: Example of a manufactured multi-track wall sample.

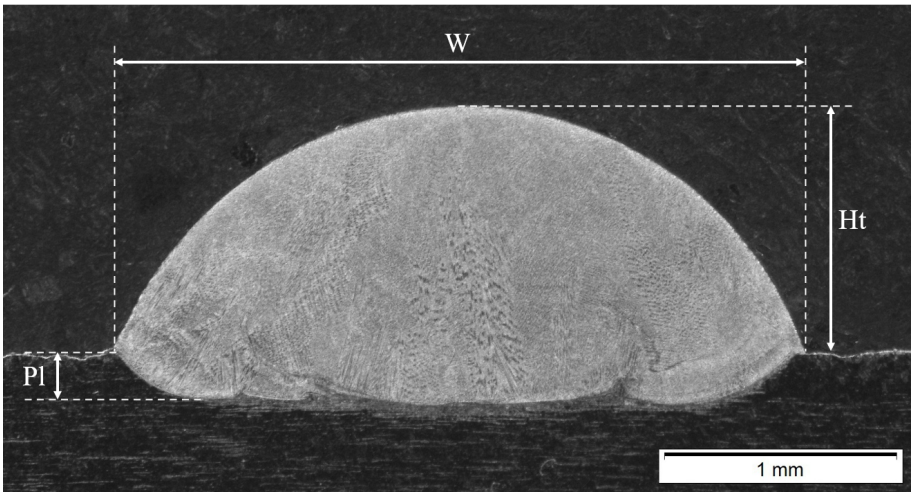

Figure 2.6: Cross section in $x-z$ plane of a single track bead: width W, height Ht and penetration depth Pl.

2.1.3 Thermal and rapid imaging

A FLIR X6540sc camera has been used for thermal imaging of the molten pool. A distance of 0.37 m of the molten pool was set and a constant emissivity of 0.11 was considered for the liquid. An integration time of 10 µs from 300 to 1500 °C was selected during the experiments. The acquisition of temperature start to saturate above 3500 °C. The molten pool is identified with the pixels where temperature is above solidus temperature.

Rapid imaging has been performed using a Phantom SA1 (mini exposition 282 ns) with a resolution of 1024×1024 pixels. In full frame, the acquisition speed is 7000 pictures/s and in reduced frame a maximum speed of 10^6 pictures/s.

2.2 Microstructural charaterization techniques

The characterization has been undertaken from the macroscale to the scale of the microstructures, in the following order:

- cross section dimensions,
- grain morphologies, grain boundaries, interdendritic spacing,
- hardness,
- defects such as micro-porosities/inclusions,
- grains orientations,
- phases.

2.2.1 Sample preparation

Samples were cut using a Struers cutting machine. Samples were polished with 80 to 4000 grid papers (FEPA standard), and then with 3 to 1 µm diamond solutions. For SEM observations, a final OPS (colloidal silica STRUERS of 0.25 µm) polishing was performed. Additional 10 min of OPS polishing were performed for Electron Backscatter Diffraction (EBSD) analyses along with Ion polishing using a GATAN PECS II at 4 keV.

2.2.2 Optical microscopy and hardness measurements

For the detection of grain boundaries and segregations, the etching was performed with a solution of 95% HCl and 5% H_2O_2, during 1 to 5 s. Optical observations have been carried out using an Olympus binocular microscope from ×10 to ×1000 magnification, in order to identify macro defects. Hardness measurements and mapping have been performed using a Presi HZ50-4 machine with a charge of 500 g (HV0.5).

2.2.3 Orientations and pole figures

The orientations of the grains, as provided by EBSD (§2.2.4), are given by the Euler angles of the rotation bringing the cartesian frame attached to the sample (O, x, y, z) to the one attached to a single crystal (K, x_3, y_3, z_3) (Fig. 2.7a). In the case of cubic lattices, (x_3, y_3, z_3) is simply the conventional basis of the crystal structure, i.e. ⟨100⟩ directions. The three Euler angles are usually defined following the Bunge convention, as follows [53].

- First, (x, y, z) are rotated ϕ_1 about z (Fig. 2.7b);
- Second, the new vectors (x_1, y_1, z_1) are rotated Φ about x_1 (Fig. 2.7c);
- Finally, vectors (x_2, y_2, z_2) are rotated ϕ_2 about z_2 to give vectors (x_3, y_3, z_3) (Fig. 2.7d).

To analyze the orientations, we have resorted to the usual pole figures. Considering the single cubic crystal in Fig. 2.8a misoriented with respect to the sample, its ⟨100⟩ directions intersect the northern hemisphere at three points. The stereographic projection of these points on the equatorial plane is illustrated in Fig. 2.8b and results in the pole figure, shown in Fig. 2.8c.

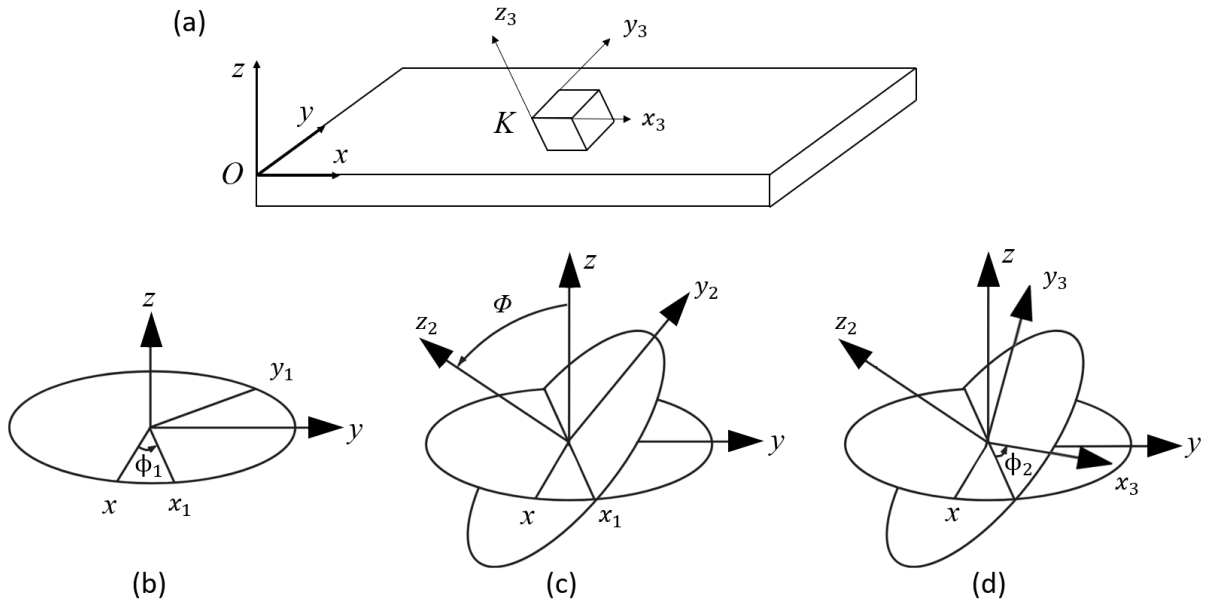

Figure 2.7: (a) Relation between the specimen and crystal cartesian frames. (b) Definition of Euler angles defining the crystal orientation.

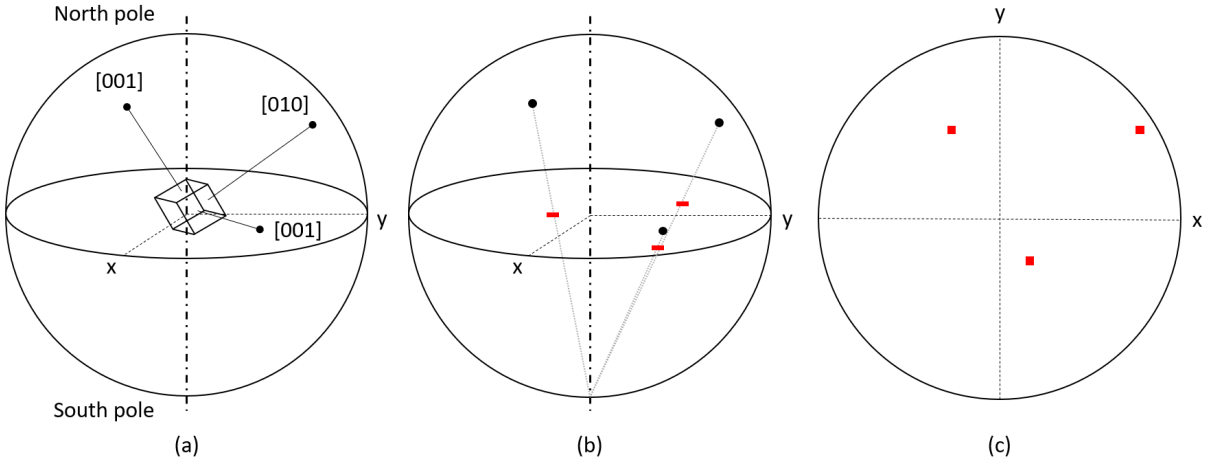

Figure 2.8: Pole figure construction: (a) cubic lattice and intersections of its ⟨100⟩ on the northern hemisphere; (b) stereographic projection in the equatorial plane using the south pole; (c) resulting pole figure of ⟨100⟩ directions.

2.2.4 Scanning electron microscopy

Scanning electronic microscopy has been performed using two different microscopes: Quanta 650 FEG, and Zeiss Gemini SEM500 with an InLens detector. Both are equipped with secondary electrons imaging (SE) and back-scattered electrons (BSE) imaging. SE imaging has been used for topographic surface investigations, when BSE imaging has been used to distinguish dendrites, phases or inclusions by chemical contrast. SE and BSE images were taken at 10 mm working distance, spot size of 4 to 5 and with 10 to 15 kV voltages. Imaging using InLens detector was performed using 0.5 to 2 kV with 4 mm distance between the sample surface to the detector.

Electron Backscatter Diffraction (EBSD)

Grain orientation maps were obtained using Electron Backscatter Diffraction (EBSD). This technique is based on the acquisition and analysis of Kikuchi diffraction patterns, resulting from the interaction between the electron beam and the electrons scattered by atomic planes under Bragg conditions. The identification and orientation of the crystals are obtained by their indexation.
Rather than plotting the orientations of all crystals in the same reference as in pole figures, the results of EBSD are usually plotted using the Inverse Pole Figure (IPF) convention. In this representation, the direction in each grain that is collinear to some specific direction of the sample is projected on the standard orientation triangle, as shown in Figure 2.9a for a cubic system. Figure 2.9b gives one example of such an IPF map for equiaxed grains with random orientations: grains having their ⟨100⟩ directions close to the Y direction in the plane of the sample are colored in red.

Energy Dispersive Spectroscopy (EDS)

Qualitative and semi-quantitative chemical analyses have been performed using Energy Dispersive Spectroscopy (EDS). EDS is based on the characteristic X-rays photons produced by the interaction between the electron beam and the sample. The incident beam excites matter and results in various emissions, such as secondary and backscattered electrons used in electron imaging, or characteristic X-

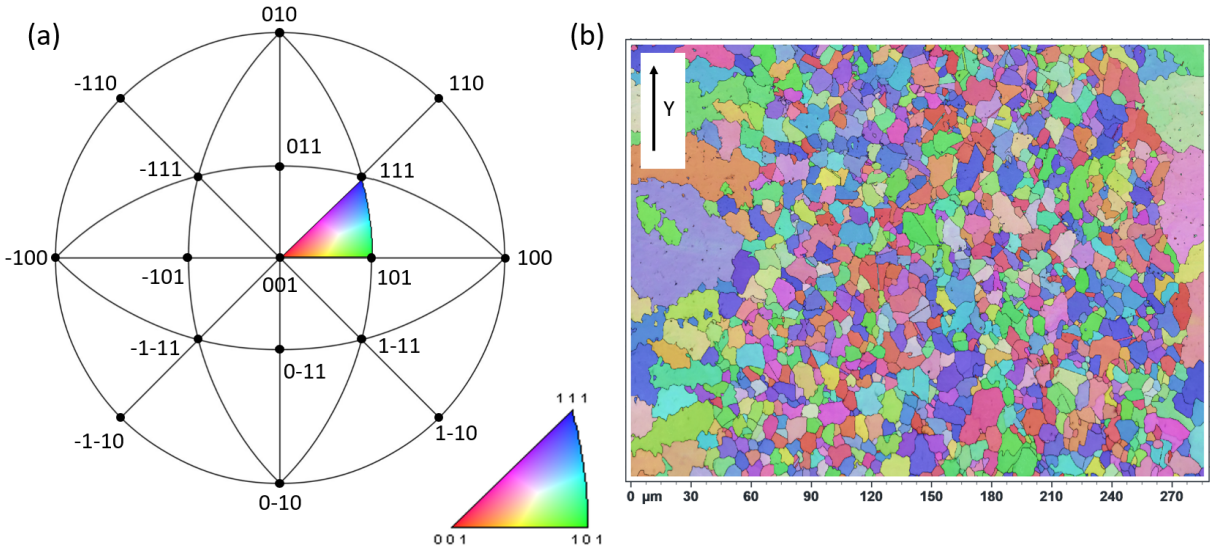

Figure 2.9: (a) Stereographic projection of the cubic system: directions/normals to planes are indicated by dots; traces of {110} planes with lines (except horizontal and vertical ones). (b) IPF map of equiaxed grains, with the standard orientation triangle code colouring along the direction Y of the sample.

rays. Each of these characteristic photons has energy and wavelength that correspond to a single element. With this technique, the chemical composition in a volume of interaction about 1 μm^3 can be determined.

3D EDS and EBSD

A Thermo Fisher Helios Xe-PFIB microscope equipped with an EDAX Velocity EBSD camera and EDAX Octane EDS system has been used. Using FIB technique, volumes of $60 \times 60 \times 60\,\mu m^3$ have been sliced every 100 nm. For each slice, both SE and BSE images have been taken. Every two slices, EDS and EBSD 2D mapping have been realized at 20 kV, as illustrated in Fig. 2.10. A total of 300 EDS and EBSD images have been used for the reconstruction of 3D microstructures.

2.2.5 Transmission electron microscopy

Transmission electron microscopy (TEM) technique has been used to characterize details features of the microstructures, e.g. inclusions, nanometric precipitates, interfaces.
An electronic microscope Helios Nanolab 600i equipped with a Focused Ion Beam (FIB) has been used to collect the $12 \times 10\,\mu m$ thin foils by abrasion using a Gallium ions gun. On the area where the foil is extracted, a layer of Platinum is coated for protection against polishing. The foils is then thinned with low energy beam varying from 3 to 1 keV in order to achieve thickness between 70 and 100 nm.
Observations have been performed using a Jeol ARM200F FEG corrected in source and image, with a resolution in Scanning TEM (STEM) of 0.083 nm and 0.12 nm in TEM with a voltage of 200 kV. The microscope is equipped with an EDS detector. The STEM mode scans the sample with high resolution and projects the atomic columns along the crystallographic direction parallel to the electron beam. The STEM mode is equipped with three different electron detectors: Bright Field (BF), Annular Dark Field (ADF) and High Angle Annular Dark Field (HAADF). Micro-diffraction of selected areas (SAED) has been used for the phases identification. Automated crystal orientation mapping (ACOM) has been done

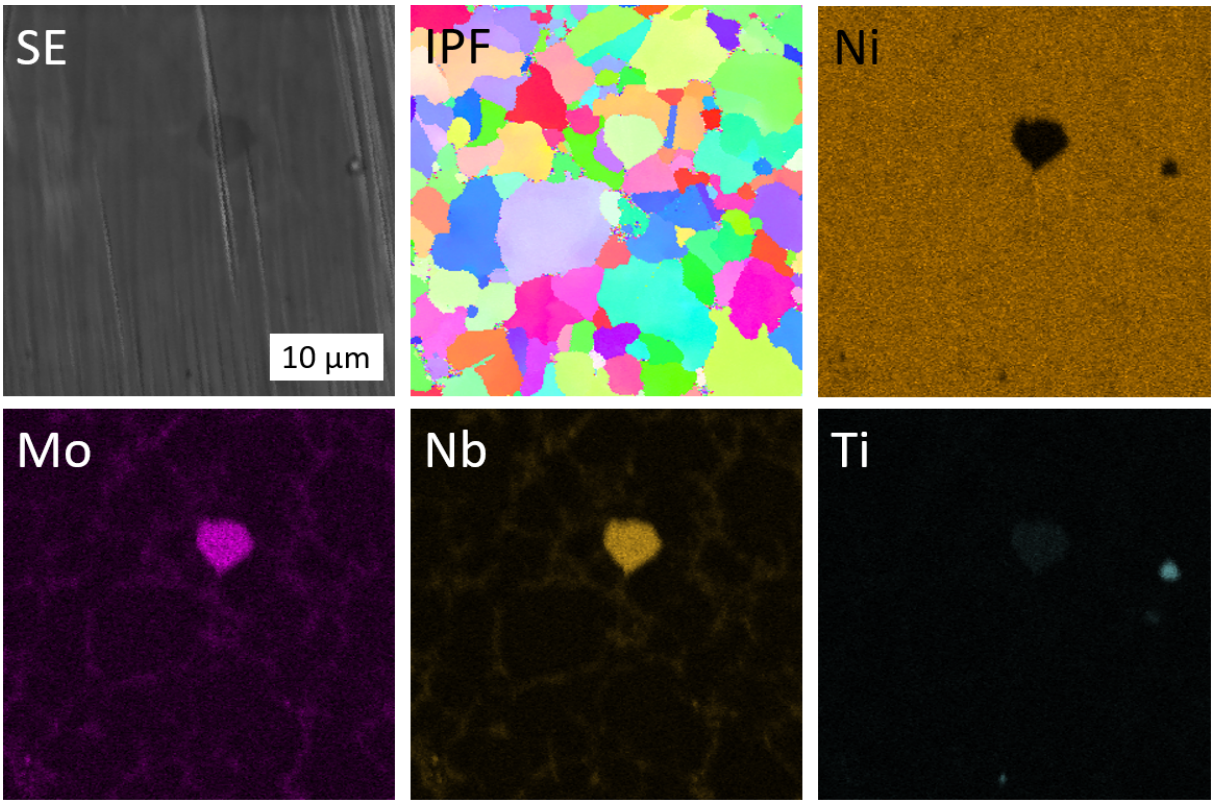

Figure 2.10: Full characterization by SE, EBSD and EDS of one 2D slice used for the 3D reconstruction of the microstructure, exhibiting inclusions of Nb-Mo and Ti in some equiaxed zone.

using ASTAR software on the TEM microscope. This software relies on the comparison between computed diffraction patterns of suspected phases and the experimental pattern. For that purpose, normalized cross correlations are computed using only subsets of the patterns where they are non-zero (i.e. at diffraction spots). Then, the resulting correlation indices of the two best candidates i_1 and i_2 are compared in a reliability coefficient $R = 100(1 - i_1/i_2)$. The identification is considered as successful when $R \geq 15$, as described in [54].

Chapter 3

Coaxial laser wire process development of Inconel 718

In this chapter, the coaxial laser and wire additive manufacturing process applied to Inconel 718 is discussed. First, we report on a parametric study to determine the best processing conditions, i.e. avoiding the different geometrical and internal defects. Then, we focus on the estimation of the physical quantities that govern the solidification process and the microstructure formation.

3.1 Parametric study

3.1.1 Process stability

The use of coaxial laser and wire is more appealing than the classic side wire feeding because it is flexible in terms of built volumes, and because pre-heating of the wire is possible during manufacturing [55, 56]. In this process, the main input parameters are the wire feeding rate, laser power, advance speed and focal position. The influence of these parameters have already been studied on bead geometry for different alloys such as Aluminium [57], Inconel 625 [58], Ti-based [59] and stainless steel AISI 308 [60]. The importance of keeping constant the wire tip position for smooth adherence during processing was demonstrated [61] and is a major monitoring development for LMD-W.

Improvements of the process window stability, with a better monitoring accuracy for building parts smoothly, without internal defects, have been regularly proposed, mainly for building stainless steel parts. These improvements rely on determining the link between the input parameters and the geometry of tracks. Stability has been achieved within a process window for lateral wire feeding by Abioye *et al.* [58] in the case of Inconel 625. Indeed, they have found the conditions to avoid irregular transfers such as stubbing and dripping, observed respectively by unmelted wire and irregular drop formation at the wire tip. The wire dripping and stubbing are attributed to respectively low and high wire volume deposition per unit of length, that is highly dependent on wire feeding and advance speed ratio. For lateral wire feeding and micro LMD-W applications (0.5 mm wire), Demir [62] has established a process window depending on the energy input, pulse energy and advance speed, in the case of stainless steel AISI 301. He has determined stable processing conditions by building beads geometry maps using regression models for height, width, dilution and efficiency.

Several coaxial laser head technologies have been studied in the literature, either with annular laser beam or with diverse laser beams focused on the work piece where the wire is fed. For example, Ocylok *et al.* [55] have developed a three focused laser-beams head (CoaxWire), also used by Elmer *et al.* [63] for successfully producing stainless steel parts. They have shown that this technology (and all other

Table 3.1: Processing parameters applied for single track deposits.

Parameters	Range	Unit
Laser Power P	1000 – 3500	W
Wire feeding rate Wf	1 – 3.5	m/min
Advance speed V	0.6 – 3	m/min
Working distance	10.5	cm
Focused beam diameter	2.5	mm
Argon gas flow rate	15	min^{-1}

LMD-W processes) features much smaller molten bath, and higher deposition velocity and cooling rate, compared to Wire-Arc AM (WAAM) and Electron Beam AM (EBAM). For a similar three focused laser beam technology, Ji *et al.* [64] have determined the process map by linking the focusing distance and other parameters to the tracks geometry, in the case of 304 stainless steel.
Beside these annular laser beam technologies, different laser heads have been engineered. For example, Shi *et al.* [65] have developed their coaxial system, and studied the influence of the main input parameters on the geometry of 304 stainless steel tracks, using a regression model for predicting the bead geometry. Similarly, Kotar *et al.* [66] have designed their own in-house laser head system and established a process window linking the focusing distance and energy input to the deposition stability, again in the case of 316 stainless steel. Very recently, Precitec has commercialized the CoaxPrinter laser head. Using this device, Motta *et al.* [60] and Becker *et al.* [67] have pointed out the need for monitoring the track height to keep the working distance constant. They also emphasized the importance of establishing the processing window for stable processing, as another recent study [68].
Regarding Inconel 718, the deposition stability has been investigated either for laser and powder based technologies [69, 70] or for Wire-Arc AM (WAAM) [71], but no process window for laser-wire technologies has been proposed so far.

The ranges of processing parameters, i.e. laser power P, wire feeding rate Wf and advance speed V (all defined in the steady building regime), used in our campaign on single tracks are reported in table 3.1. A total of 80 single track beads were built using these parameters. Three categories of processability were considered:

(i) stable deposition,
(ii) wire stubbing,
(iii) high reflections and spatters.

The resulting process map is plotted in Figure 3.1. The stable deposition test runs are shown with green dots. They are quite independent of the advance speed V, but a strong correlation is clearly observed between the wire feeding rate Wf and the laser power P. Runs with wire stubbing leading to unstable deposition are indicated with red triangles, which are observed for low values of the laser power, insufficient to melt the wire, independently of the advance speed. On the contrary, for high values of P, runs exhibit high reflections and spatters during deposition (blue squares). We have fitted the set of green dots with the following polynomial:

$$P = 30 + 909\,Wf + 45.3\,V^2 - 4.3\,Wf\,V^2 \tag{3.1}$$

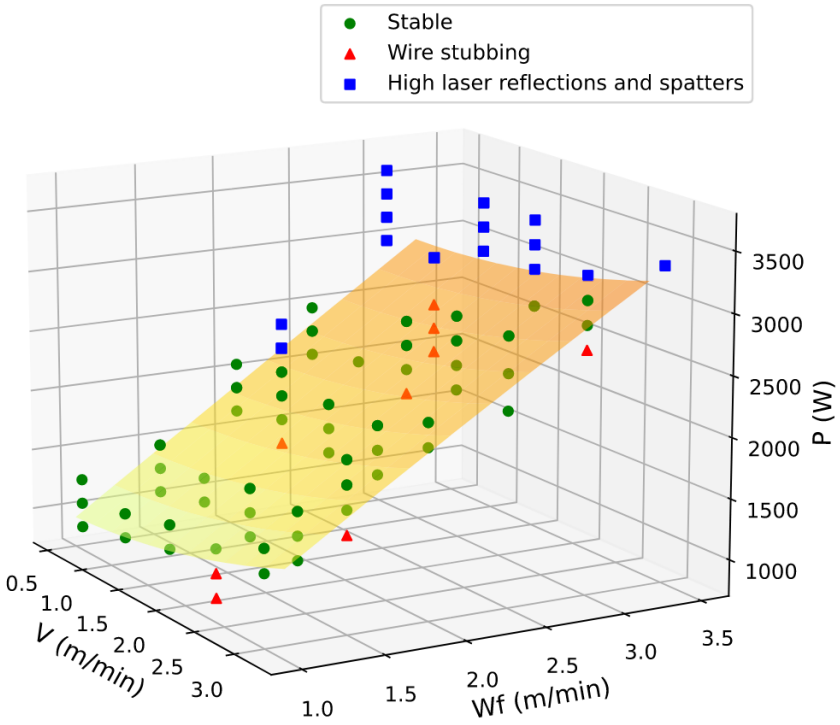

Figure 3.1: Process map for single tracks, where V is the advance speed, Wf the wire feeding rate and P the laser power.

where the parameters have been determined by least-square regression, and where P is expressed in W and the rates in m/min.
The resulting surface in the 3D parameter space is plotted in yellow in Fig. 3.1. It can be used to find process parameters to build simple and multitrack walls, as well as to perform parametric studies.

3.1.2 Track dimensions

Using the established process map, we have analyzed how the dimensions of the tracks is influenced by the process parameters. It must be stressed that our analysis is different from the usual ones where each process parameter is varied independently. Indeed, using the process map (or with Eq. (3.1)) implies that power P and wire feeding rate Wf have to be changed concomitantly. On the contrary, it is possible to modify the advance speed V at almost constant P and Wf.
First, it is shown in Fig. 3.2 that the dimensions of the tracks decrease when V increases, as expected from simple geometric arguments proposed in the literature [61]: the faster the deposition, the lesser matter is deposited at a given position of the track. The slight irregularities of the evolution of W is likely to be associated with more complex phenomena driving the bead spreading. It is difficult to conclude on the effect of P or Wf separately because both parameters are varied at the same time. Based on the literature, it is likely that the increase in Ht is mainly due to the increase in wire feeding rate Wf which would overcome the opposed influence of P. In Fig. 3.3, the height Ht and width W of a single track (Fig. 2.6) increase with Wf/V. The collapse of all experiments on a single master curve for Ht indicates that the ratio of the feeding rate to the advance velocity is better than Wf alone to rationalize our results. Still, the trends are consistent with what has been reported in the literature for stainless steel [61], Ti64

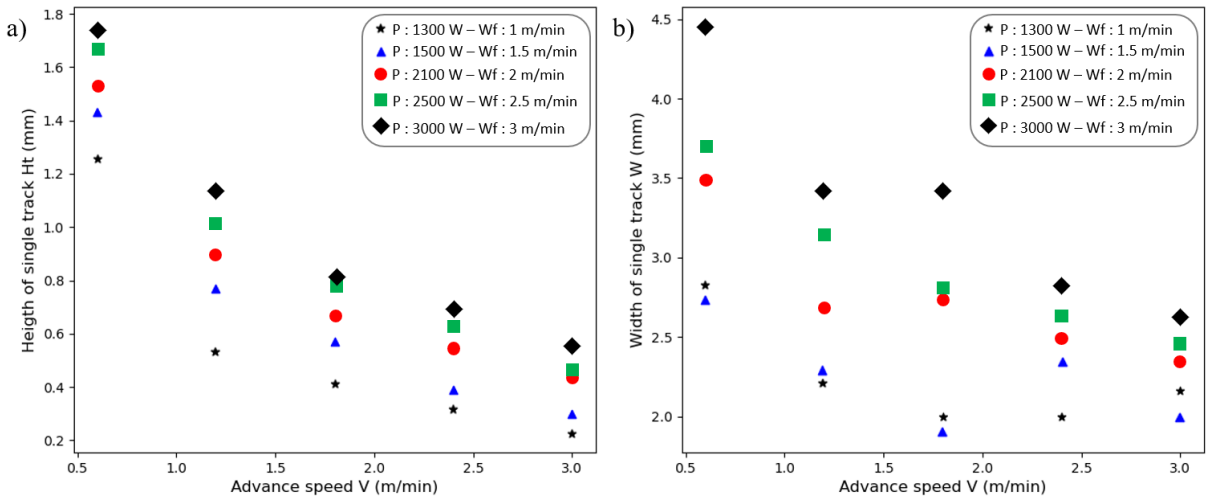

Figure 3.2: (a) Height and (b) width of a single track versus advance speed V.

[72] and Al alloys [68]: the larger Wf, the higher and wider the tracks.

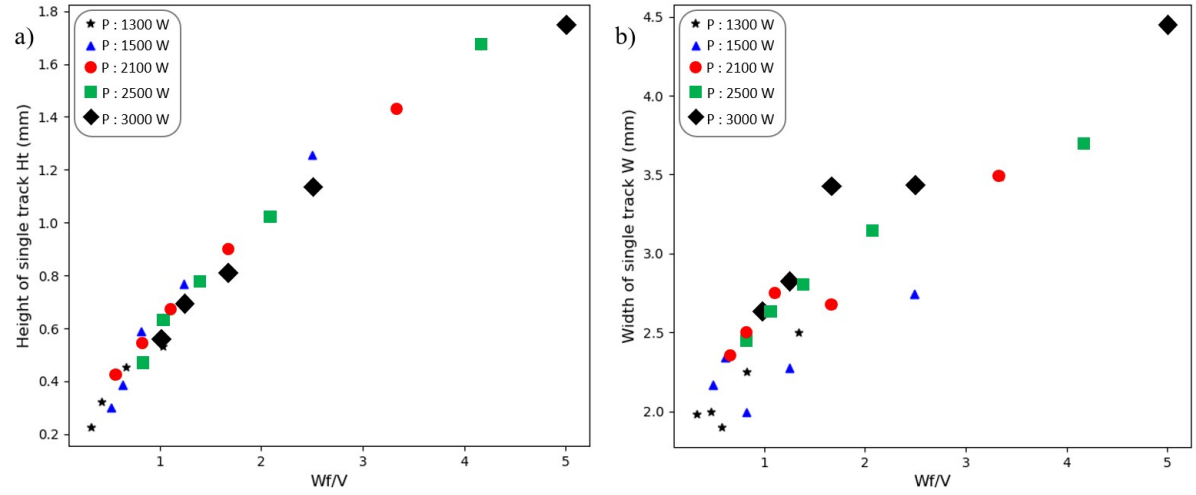

Figure 3.3: (a) Height and (b) width of a single track versus wire feeding rate Wf.

Using Ht and W, it is straightforward to quantify the deposition rate D_r as:

$$D_r = \rho V A \tag{3.2}$$

where the density of the alloy is $\rho = 8250\,\mathrm{kg/m^3}$, V the advance speed V and $A = \pi/4\,WHt$ the area of bead cross section.
In figure 3.4, the resulting deposition rate is plotted with respect to the wire feeding rate Wf and advance speed V. It can be seen that increasing both parameters enhances the deposition rate, although the dominant parameter is clearly Wf. The positive effect of V on D_r is not in contradiction with the reduction of the dimensions W and Ht with V (Fig. 3.2). Indeed, the cross section $A \propto 1/V^n$, with $n < 1$ such that D_r scales as V^{1-n}.

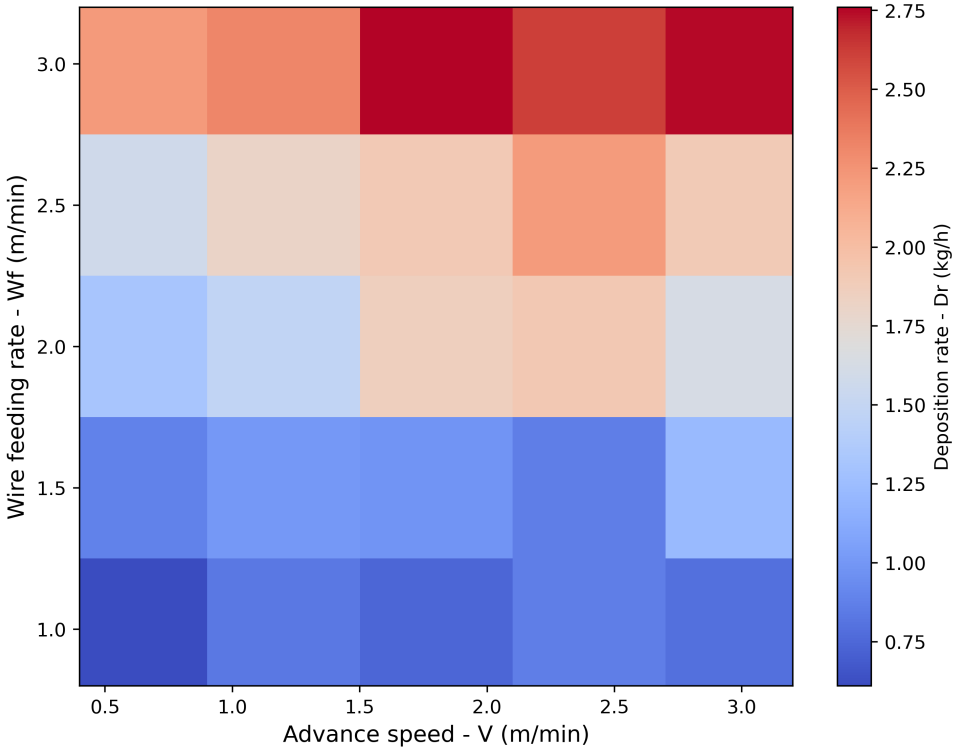

Figure 3.4: Deposition rate vs. the wire feeding rate and advance speed V.

The deposition rates achieved with coaxial LMD-W are higher than those reported for laser powder bed fusion technologies (SLM). Hence, it seems more relevant to compare our values with those obtained with other DED technologies. Although LMD-powder technologies achieve mean deposition rates of the order of 0.5 kg/h, recent developments have reached high deposition rates (HDR-LMD) of 2 kg/h [73]. The rates of other wire based processes, such as WAAM and EBAM, are in the range 1 to 5 kg/h [74, 75], even up to 10 kg/h [76]. Thus, with rates up to 2.75 kg/h LMD-W is a serious competitor of HDR-LMD. With higher wire diameters and wire feeding rates, it would even compete with WAAM and EBAM. Moreover, compared to these last processes, LMD-W would exhibit faster cooling rates and lesser internal defects [77].

3.1.3 Substrate

Using a substrate made of a different alloy (in our case stainless steel) can be an issue, usually called dilution. Indeed, when building the first layers, the substrate is partially melt and is mixed with the deposited materials. Hence, the Ni content has been measured across the substrate and the first built layers, for different cases such as single track deposits, single track walls and multitrack walls. It has been observed that increasing the laser power increases the dilution in the first layer. But in all cases, concentration in Ni is 50 % in the second layers, and reaches ~ 53 % in the third ones. This means that dilution is negligible as early as the third layer, whatever the process parameters in the investigated ranges. Consequently, LMD-W induces lower dilution than arc-based AM technologies and can be preferred when the substrate and the material to built have different chemical compositions.

3.1.4 Defects

Among Ni-based alloys, Inconel 718 is well known for its good weldability [78]. Nonetheless, in AM conditions, several studies have reported liquation cracking in the heat affected zones. Such defects have also been observed in Inconel 718 in other technologies such as WAAM and LMD-P [79, 22]. To prevent liquation, it is usually agreed that input energy must be minimal. In the case of laser and wire with side feeding, Zhang *et al.* [23] have observed liquation cracking in a few columnar regions in multitrack walls.
Besides cracking, two other defects have been found. Bergs *et al.* have observed Ti oxides in the microstructure of single track walls [51]. They have reduced their size with increasing interlayer cooling. For both powder and wire technologies, interdendritic shrinkage pores and lacks of fusion have been regularly reported [26].

In this work, several types of defects have been encountered. First, Ti-rich inclusions have been observed as shown in Figure 3.5 either alone (a) or in small groups (d). They can come from existing TiC particles found in the wire cross section as shown in Figure 3.6a; or they can form during solidification, associated with oxides and nitrides regularly observed within the TiC particles.

Macro-defects such as lacks of fusion have also been observed when laser power is insufficient, as shown in the first layer in Figure 3.5b. Their size can vary from a few to hundreds of µm, and they can be detrimental to the final mechanical properties. They can be suppressed by increasing P. The lacks of fusion can also ensue from too large hatch spacings between tracks.

Spherical micro-porosities have been observed with a mean size of 5 µm (from a few to 10 µm) as shown in Figure 3.5c. Large porosities have been suppressed thanks to a sufficient Ar gas flow on the liquid during processing, as proposed in other studies [58, 23]. Improving the inert gas atmosphere is likely to totally suppress these porosities. Unexpectedly, we have not found any hot cracking or liquation cracking in the interdendritic regions. This may be due to the good combination of the wire chemical composition, temperature field and history (with high cooling rates involved), low internal stress induced by the process and the good weldability of the alloy. Nevertheless, one cracking region has been observed in a Ti particles cluster as shown in Figure 3.6b. It can be seen that the matrix is cracked in between the inclusions. Such an observation is rare and could be explained by impurities in-between the columnar dendrites.

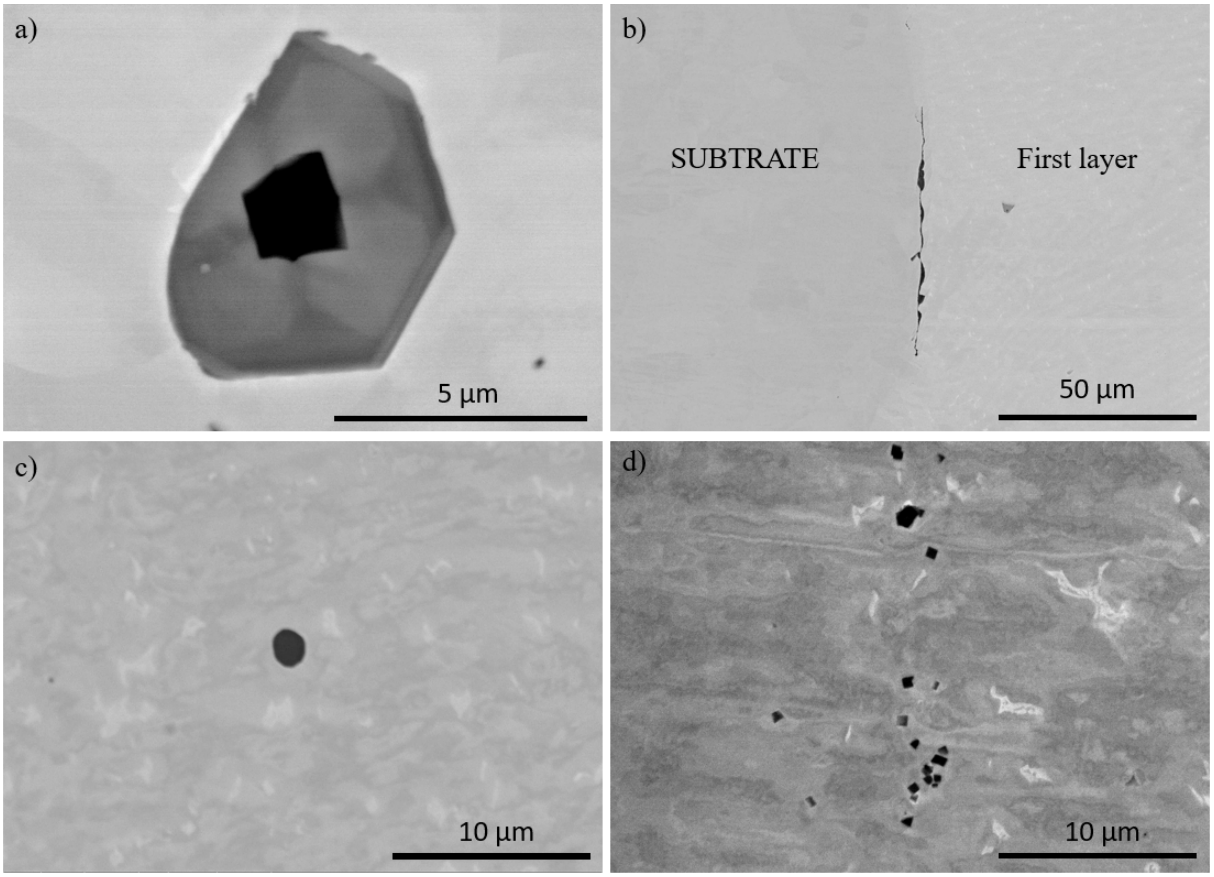

Figure 3.5: SEM micrographs (BSE) of several defects: (a) single Ti-rich inclusion around an oxide; (b) Lack of fusion between the substrate and the first layer; (c) microporosity; (d) Ti-rich inclusions.

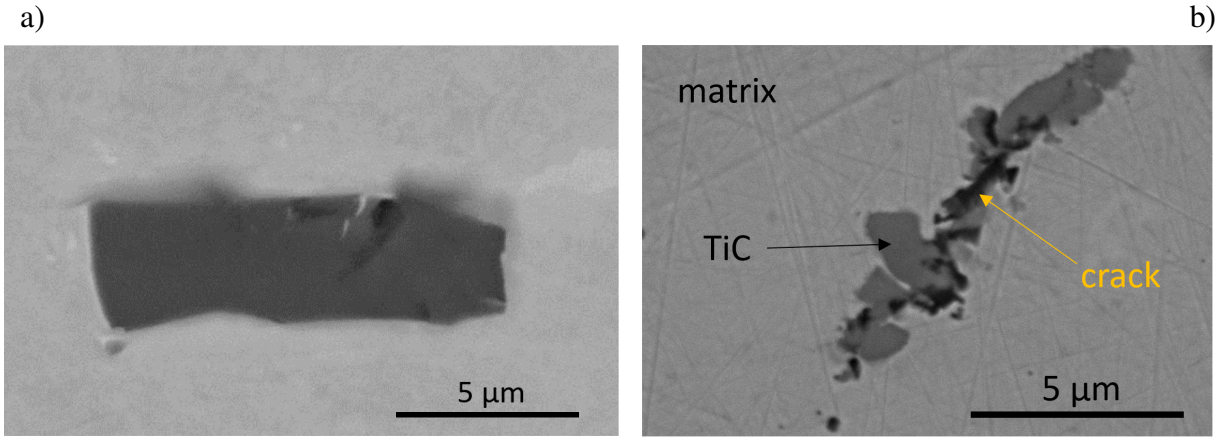

Figure 3.6: SEM micrographs (BSE) of TiC particles: (a) in the wire; (b) with a crack in-between.

3.2 Molten pool

3.2.1 Liquid motion

We have used rapid imaging to obtain information on (i) the interaction between the laser and molten pool, and (ii) the liquid flows. Figure 3.7a shows the molten bath during one single track processing, where the interaction between the laser and liquid metal is imaged by the annular bright reflection. Plasma is observed above the molten pool corresponding to high temperatures at the surface of the molten pool. It could be composed of ionized Ar from the inert atmosphere and of impurities in the wire. High reflections are surrounding the molten pool, and the solidification front is visible at its tail. It is worth mentionning that the wire is melted by the molten pool and not directly by the laser beam that only heats the wire below its melting temperature.

Figure 3.7a illustrates the melting of the wire and the formation of the molten pool, at the beginning of a single track processing. This step is mandatory to melt the wire and to proceeds smoothly. Oxides particles are visible at the liquid surface and their position in the image can be followed with time as shown in Figure 3.7b-c.

The projection of the trajectories of two oxides have been determined using two different camera orientations, in the same processing conditions (Fig. 3.8a-b). Unfortunately, the durations where the particles remained visible are short. We have estimated the velocities from these 2D trajectories, that are lower bounds for the real velocities (Fig. 3.8c). The mean values are around 0.3 and 0.4 m/s. These values are in good agreement with the computations of Gan *et al.* [80] providing fluid velocities between 0.2 and 0.3 m/s in DED of stainless steel using powder. The present indirect assessment suggest that the liquid velocity can reach higher values (≥ 0.7 m/s) and that the flow is likely to be turbulent. Obviously, more work is needed to obtain quantitative measurements and computations for the LMD-W.

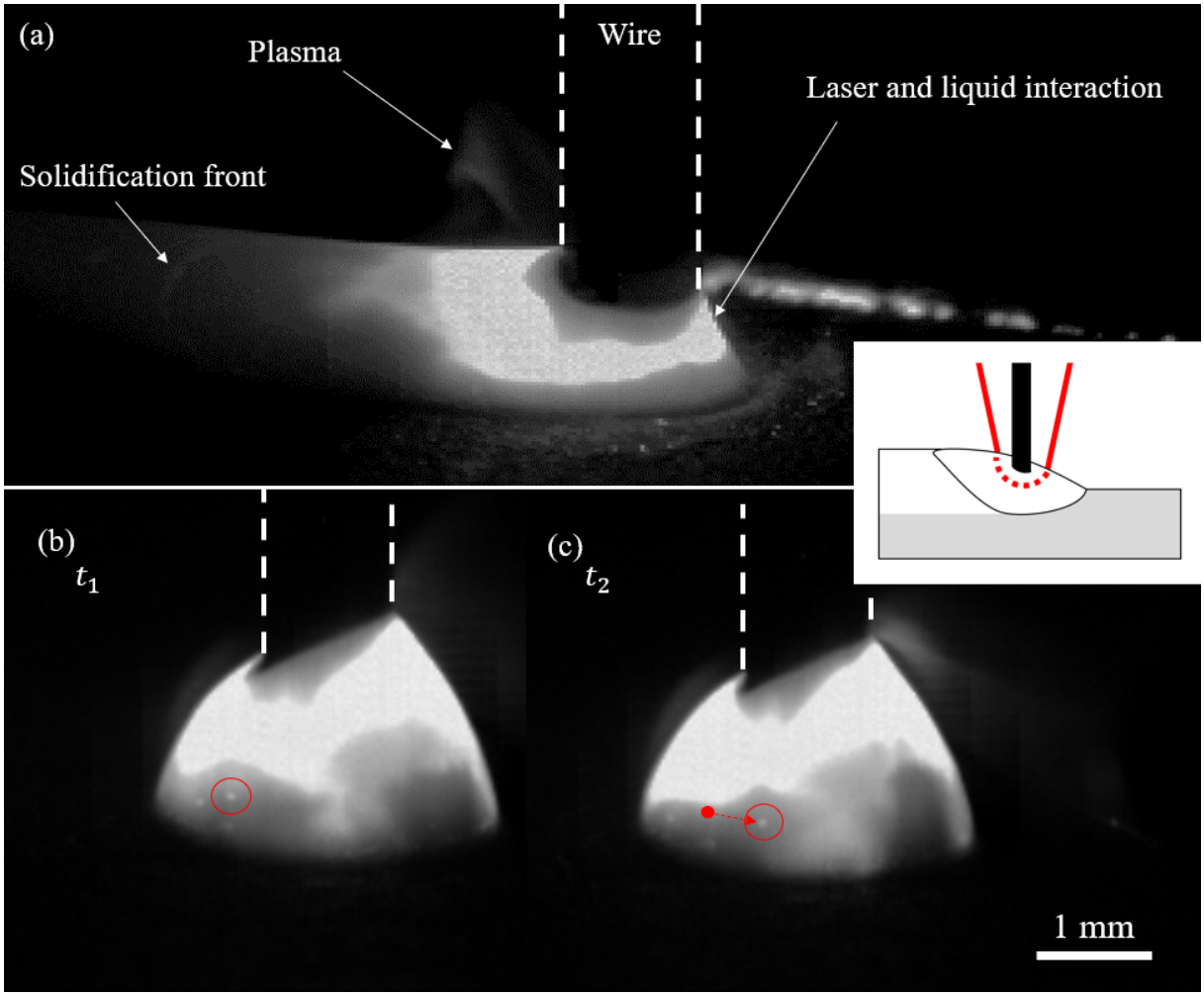

Figure 3.7: Rapid imaging of the molten bath (the wire is indicated by white dotted lines) during (a) single track processing. (b-c) Snapshots showing the movement of an oxide particle. Processing conditions: $P = 2200$ W, $V = 1.2$ m/min and $Wf = 1.8$ m/min.

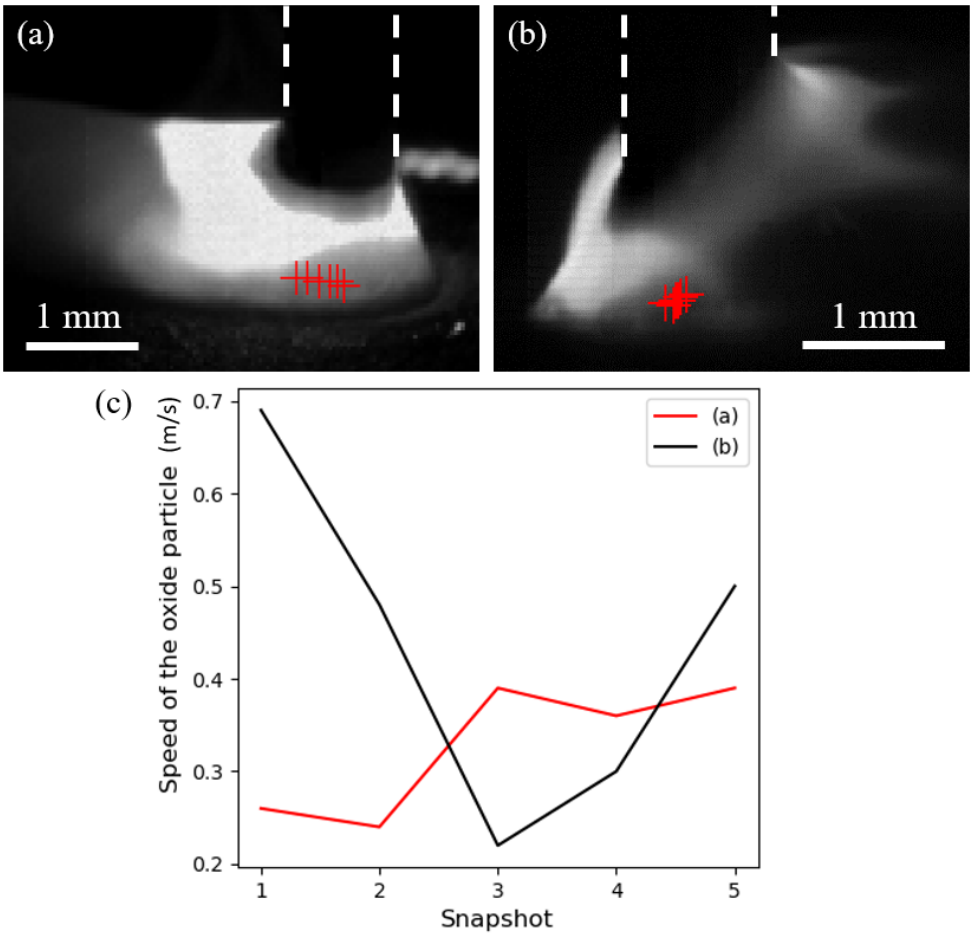

Figure 3.8: Snaphots of the molten bath with successive positions of oxides (red crosses) every: (a) 0.333 ms; (b) 0.1 ms. (c) Oxides apparent velocities. Processing condition: $P = 1600\,\mathrm{W}$, $V = 0.6\,\mathrm{m/min}$ and $Wf = 1.5\,\mathrm{m/min}$.

3.2.2 Thermal field

In the case of multi-track walls, two sets of processing parameters have been considered to estimate the cooling rates from thermal imaging: (i) $P = 2200\,\mathrm{W}$ and $V = 1.2\,\mathrm{m/min}$, or (ii) $P = 1700\,\mathrm{W}$ and $V = 0.6\,\mathrm{m/min}$, both with $Wf = 1.8\,\mathrm{m/min}$. To differentiate both conditions, P and V can be combined to define the energy density E as:

$$E = \frac{P}{VH\Delta} \tag{3.3}$$

where H is the hatch spacing taken as 2 mm and 2.2 mm for conditions (i) and (ii) respectively, and $\Delta = 2.5\,\mathrm{mm}$ the focused laser beam diameter.
Hence, conditions (i) and (ii) correspond respectively to $E = 367\,\mathrm{J/mm^3}$ and $E = 515\,\mathrm{J/mm^3}$.

An example of thermal imaging is shown in Figure 3.9. Temperature profiles at the liquid surface have been taken along the white line. The schematic representation of the molten pool, used to estimate the temperature gradient G and the local cooling rate $\dot{T}$, is drawn in Figure 3.10. The maximal depth d of the molten pool can be measured from cross sections of the walls. The maximal temperature $T_{\max}$ is assumed to be located where the laser source interacts with the liquid surface. Because of the large uncertainty of the camera above 3500 °C, we have considered $T_{\max} = 3500\,°\mathrm{C}$. Solidus temperature T_s defining the bottom of the molten pool is assumed to be the alloy solidus, i.e. $T_s = 1198\,°\mathrm{C}$. The distance L between $T_{\max}$ and T_s at the surface of the molten pool is determined using thermal imaging.
Assuming crudely that the temperature field along the axis y of the molten pool is linear along z (neglecting off-vertical components and any effect of fluid flow), we have estimated G as:

$$G(x=0,y) \approx \frac{T(x=0,y) - T_s}{|\delta(y)|} \tag{3.4}$$

where $\delta(y)$ is the local depth of the molten pool along the y axis. Because the real shape is unknown, we have considered different variations of $\delta(y)$.
The interface growth rate R is perpendicular to the solidification front. Assuming that this front is parallel to the solidus isotherm T_s, defining the bottom of the molten bath, we can write:

$$R = V\cos\theta \tag{3.5}$$

where V is the advance speed and θ the angle between the normal to the bottom of the molten bath and the y axis, in the purple plane (Fig. 3.10). This angle can be related to the shape of the molten pool $\delta(y)$ as $\theta = \arctan\left(-(d\delta/dy)^{-1}\right)$. Realistic pool shapes must feature $\theta = 90°$ at $(x=0, y=0, z=-d)$ below the maximal temperature at the surface. θ must be minimal at $(x=0, y=L)$.
Finally, the cooling rate is simply defined as $\dot{T} = G\,R$.

The temperature profiles measured at the surface of the molten pool are shown in Figure 3.11, for both conditions ($E = 367\,\mathrm{J/mm^3}$ and $E = 515\,\mathrm{J/mm^3}$). The lower the input energy density (i.e. in this case increase of advance speed), the longer the molten pool. Both temperature profiles exhibit similar shapes with two peaks, generated by the annular interaction betweeen the laser and the liquid surface. Both maximal temperatures are above 3500 °C, i.e. beyond the saturation of the camera detectors. They are consistent with what has been reported in the literature. Indeed, maximal temperatures ranging from 3500 °C to 3900 °C have been computed for Ti64 [81, 82], IN625 [83] and stainless steel [64], from process simulations of LMD-W. For LMD using Inconel 718 powder, Lee *et al.* [84] have predicted that temperature can reach 4500 °C.

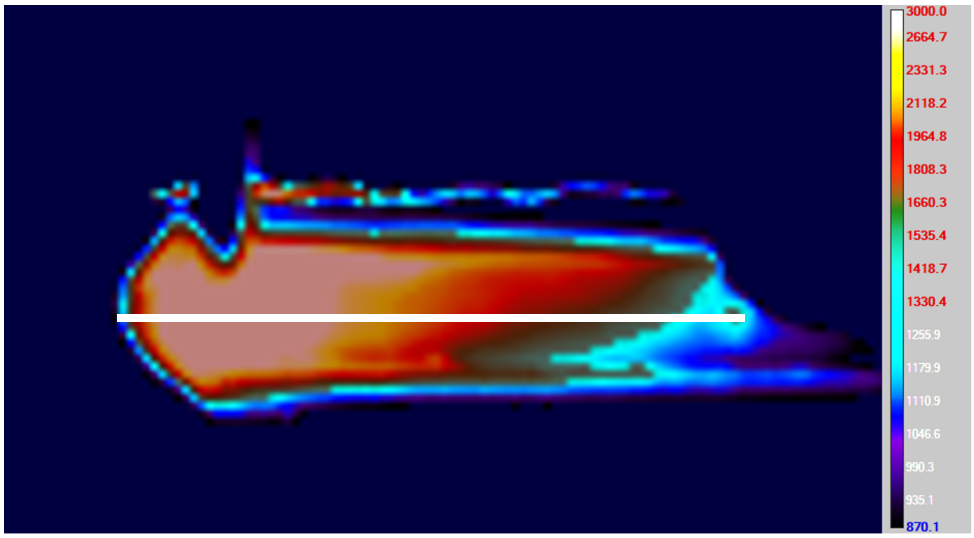

Figure 3.9: Thermal imaging of the molten pool when building a multi-track wall with the following processing conditions: $P = 2200\,\mathrm{W}$, $V = 1.2\,\mathrm{m/min}$ and $Wf = 2\,\mathrm{m/min}$. Temperature profiles are extracted along the white line.

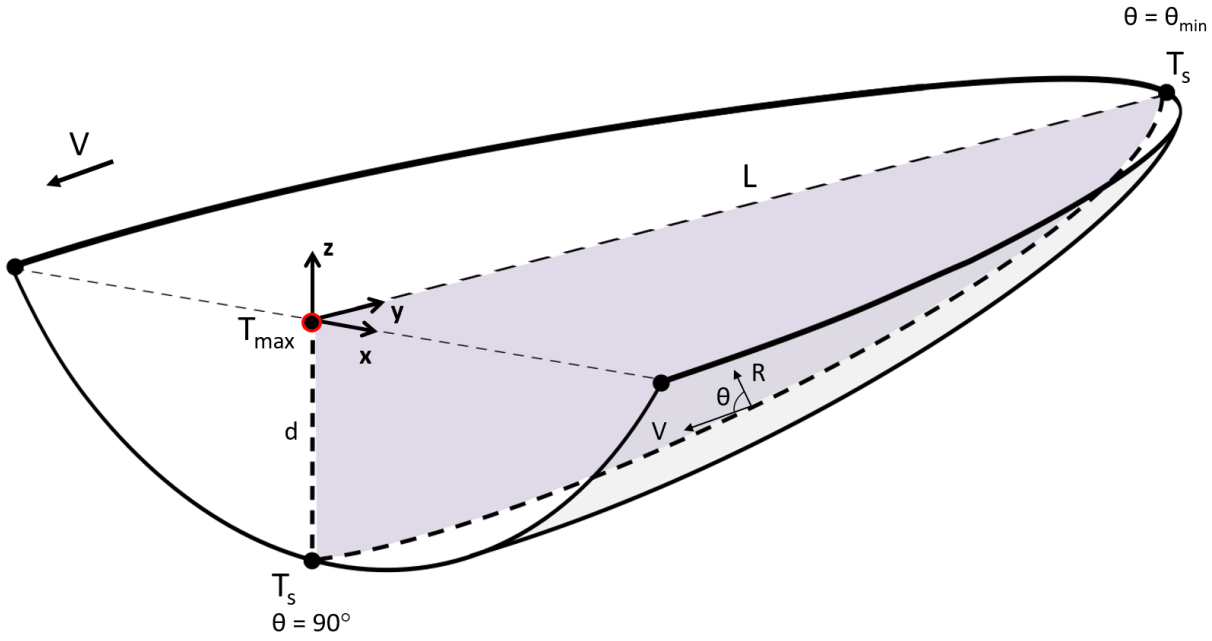

Figure 3.10: Schematic representation of the molten pool.

Considering different pool shapes and using the thermal measurements thresholded at 3500 °C (dots in Fig. 3.11), the thermal gradients along the pool have been computed with Eq. (3.4), for different shapes of the molten pool (Figs. 3.12b and 3.13b): linear (orange), power laws (red and green) and elliptical (purple). The results are plotted in Figs. 3.12d and 3.13d for $367\,\mathrm{J/mm^3}$ and $515\,\mathrm{J/mm^3}$ respectively. The gradients are minimal at the rear of the molten pool ($y = L$) and increase toward the heat source,

following the temperature profiles in the considered domains (dots in the temperature profiles). The sharper the pool shape at $y = L$, the more amplified the gradients at the rear positions. The maximal values are of the order 10^6 °C/m in agreement with the value of 1.8×10^6 °C/m predicted in [85] in similar deposition conditions.
The solidification front velocities R have been computed considering the geometric relation Eq. (3.5) with the advance speed, accounting for the pool shape (θ in Figs 3.12c and 3.13c). They are plotted in Figures 3.12e and 3.13e. For monotonous increasing pool shapes, R is maximal at the rear of the molten pool, and equal to some fraction of the pooling velocity depending on the angle of the front. The linear pool is a degenerate case where the orientation of the solidification front (θ) is constant such that R is constant all along the pool. When the bottom of the pool is flat at the position of the laser source ($x = 0, y = 0, z = -d$), $R(y = 0) = 0$. By construction, the front velocity is higher for higher advance speed at a given pool shape. It is worth mentioning that similar tendencies for G and R have been obtained for SLM [86] and for LMD-P [87].
Using G and R, the cooling rates $\dot{T}$ are determined with respect to the position along the molten pools (Figs. 3.12f and 3.13f). The larger the input energy density (corresponding to the lower advance speed) the lower the cooling rate at constant pool shape, although the differences are not large. Considering the pool shapes described by power laws (red and green intermediate cases) the cooling rate increases only slightly from $T_{\max}$ to T_s and $\dot{T}$ are of the order of 10^3 °C/s. These values are in between those reported in the literature for WAAM (10^2 to 10^3 °C/s) [36] and LMD-powder (10^3 °C/s to 10^4 °C/s) [88, 89]. Moreover, it can be noted that they are much lower than the values reported for powder bed processes such as SLM, in the range [10^5; 10^7 °C/s] [90]. Still, our values are likely to be lower bounds of the real cooling rates, since many phenomena like fluid flow can increase G at the solidification front.

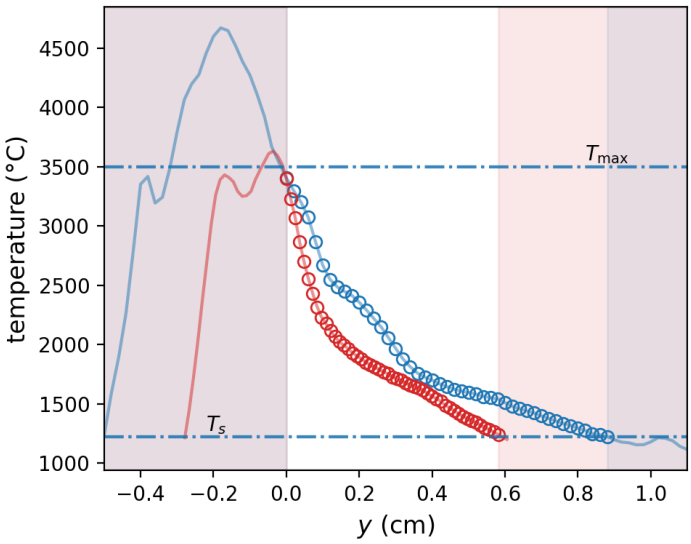

Figure 3.11: Temperature profiles at the surface of the molten bath inferred from thermal imaging when building the second layer during some multi-track processing for: $E = 367\,\mathrm{J/mm^3}$ ($P = 2200\,\mathrm{W}$, $V = 1.2\,\mathrm{m/min}$) in blue, and $E = 515\,\mathrm{J/mm^3}$ ($P = 1700\,\mathrm{W}$, $V = 0.6\,\mathrm{m/min}$) in red. Only dots are considered for the analysis.

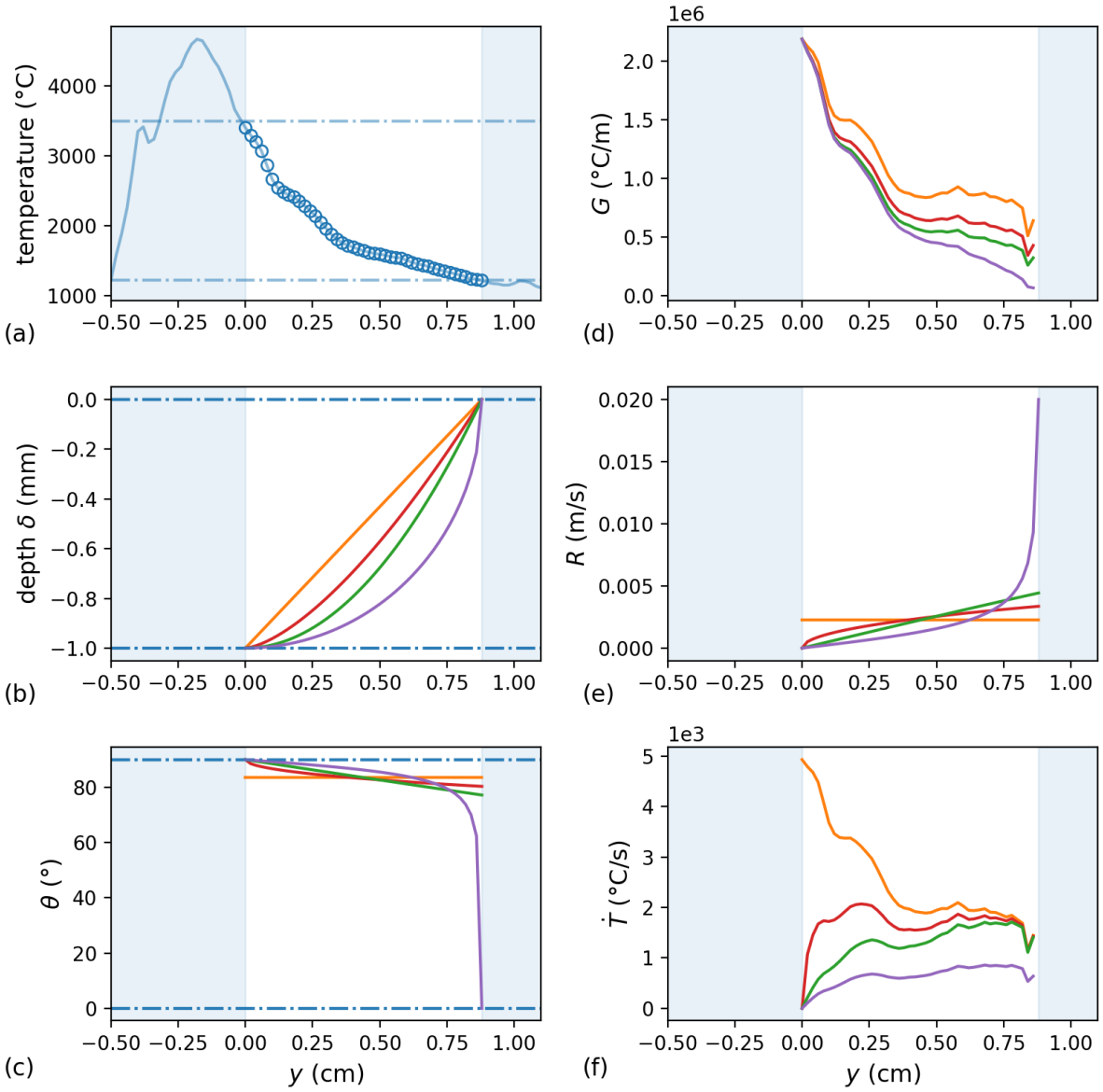

Figure 3.12: Case (i) with $E = 367\,\mathrm{J/mm^3}$ ($P = 2200\,\mathrm{W}$, $V = 1.2\,\mathrm{m/min}$). Profiles along y of (a) temperature at the surface of the molten bath inferred from thermal imaging; (b) pool depth δ (shape): linear (orange), $\propto y^{3/2}$ (red), quadratic (green) and elliptical (purple); (c) orientations θ of the solidification fronts; (d) thermal gradients G; (e) solidification front velocities R; (f) cooling rates $\dot{T}$.

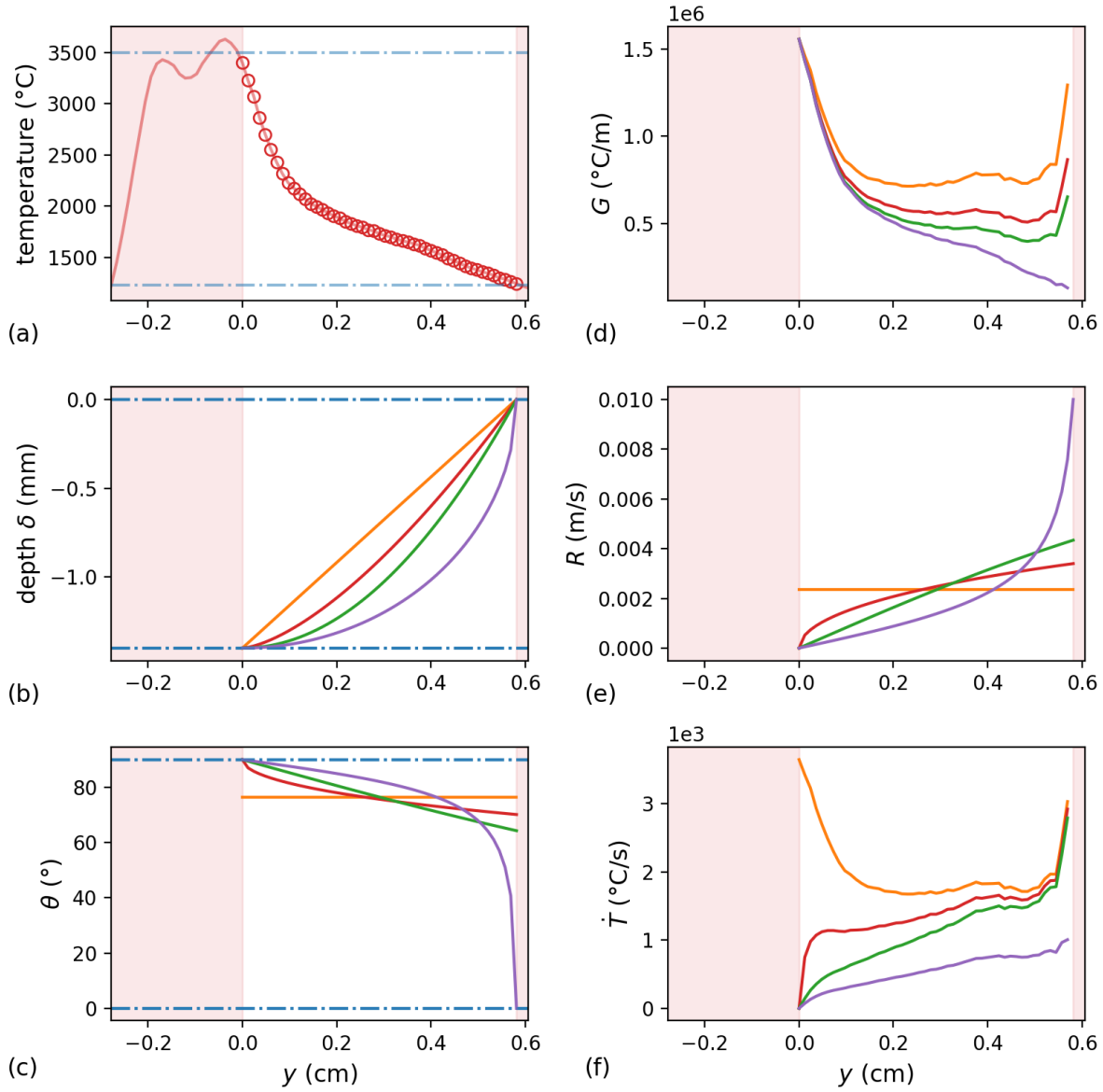

Figure 3.13: Case (ii) $E = 515\,\mathrm{J/mm^3}$ ($P = 1700\,\mathrm{W}$, $V = 0.6\,\mathrm{m/min}$). Profiles along y of (a) temperature at the surface of the molten bath inferred from thermal imaging; (b) pool depth δ (shape): linear (orange), $\propto y^{3/2}$ (red), quadratic (green) and elliptical (purple); (c) orientations θ of the solidification fronts; (d) thermal gradients G; (e) solidification front velocities R; (f) cooling rates $\dot{T}$.

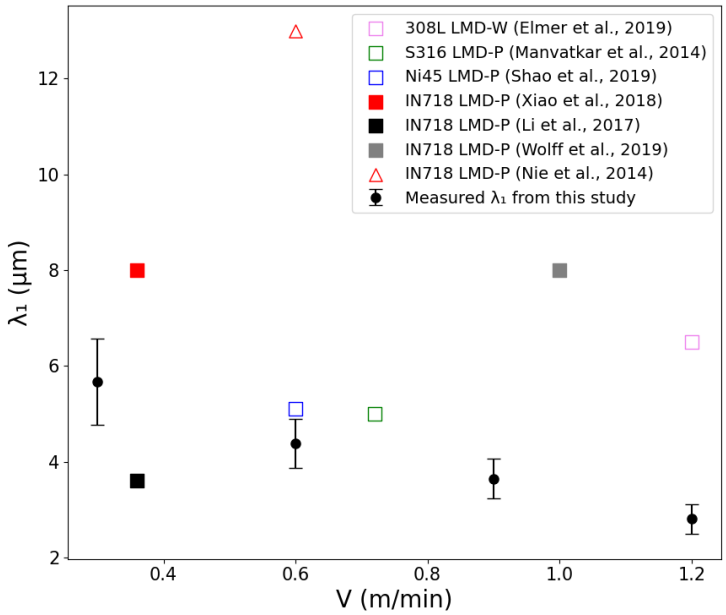

Figure 3.14: Primary dendrite arm spacing λ_1 vs. advance speed V. Black circles: measured in single track walls. Other symbols: data from the literature for LMD processes, both experimental (squares) and computed (triangles).

In a second step, we have measured the primary dendrite arm spacing λ_1 in single track walls built with different advance speed V, because this quantity can be used to assess indirectly the cooling rate. Our measurements are shown in Fig. 3.14 as dots with error bars related to the standard deviations: λ_1 decreases from 6 µm to 3 µm when V increases from 0.15 m/min to 1.2 m/min. This trend can be attributed to the increase of cooling rate $\dot{T}$ with V. Our measurements are in line with some λ_1 reported in the literature for LMD processes of stainless steel and Ni-based alloys [91, 92, 93]. Nonetheless, a few studies give larger values determined either experimentaly [63, 87, 94] or by simulation [21].
To relate λ_1 to the cooling rate, one can resort first to the simple models proposed by Trivedi [95], specialized for Inconel 718 by Raghavan *et al.* [96]. In this model, λ_1 reads:

$$\lambda_1 = \frac{A}{G^{1/2}\,R^{1/4}} \tag{3.6}$$

where $A = 2145.952$ (in $\mu m(K/m)^{1/2}(m/s)^{1/4}$). Another version of scaling (3.6) with a larger constant A has been proposed by Kurz and Fisher [97].

Using the curves in Figs. 3.12 and 3.13, we have computed λ_1 along the molten pool using Eq. (3.6), as shown in Fig. 3.15d for case (ii) ($E = 515\,J/mm^3$, $V = 0.6$ m/min). In average, we obtain $\lambda_1 = 12.4\,\mu m$ for $V = 0.6$ m/min and $\lambda_1 = 11.2\,\mu m$ for $V = 1.2$ m/min, more than the double of the measurements in Fig. 3.14. Obviously, G and/or R computed from our temperature measurements are too small, if Trivedi model is reliable. Among the different assumptions on which our estimations of G and R are based, we have identified the one with the largest impact on the predictions. As expected from Eq. (3.6), our estimation of G is the most critical. In particular, Eq. (3.4) is very likely to underestimate the temperature gradient at the solidification front, assuming a simple linear temperature profile along the depth of the molten pool. Indeed, we have seen that fluid flows at high velocity ($O(0.2m/s)$) so that it can strongly homogenize the temperature of the molten pool, confining the gradient in a boundary layer close to the solidification front. Consequently, we have performed new calculations of G using a fraction of δ as the

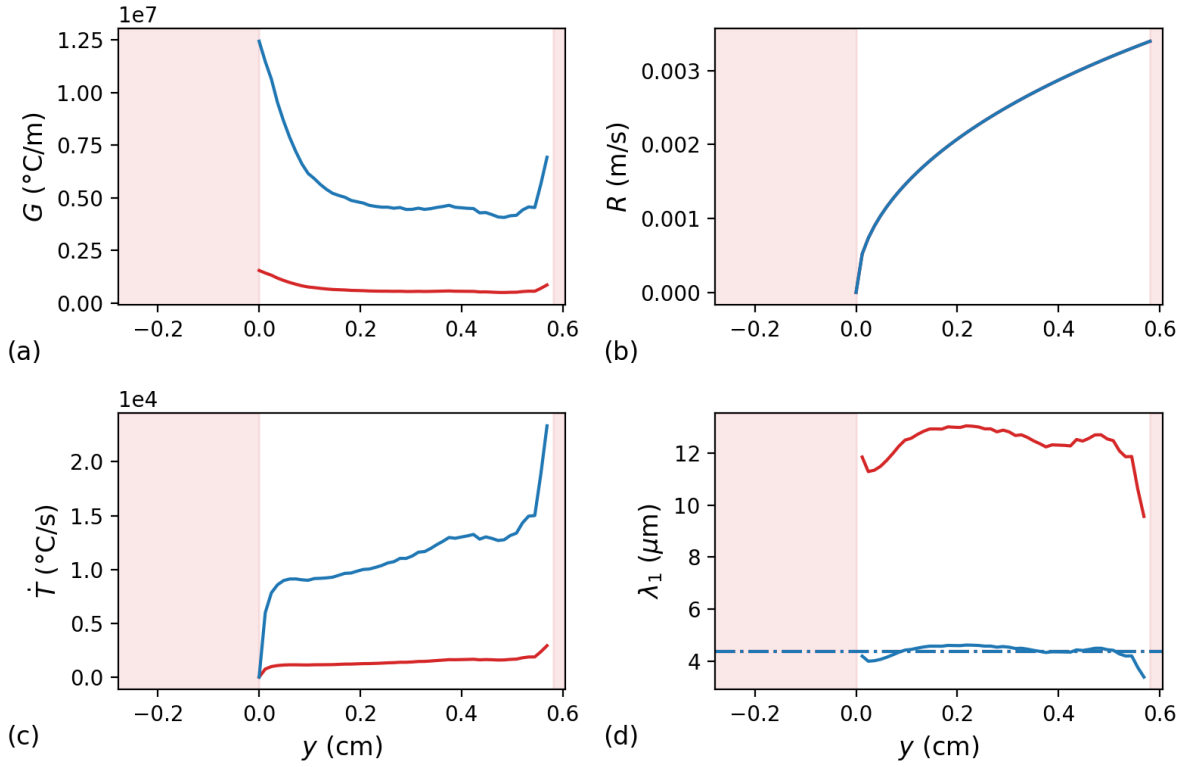

Figure 3.15: Case (ii) $E = 515\,\mathrm{J/mm^3}$ ($P = 1700\,\mathrm{W}$, $V = 0.6\,\mathrm{m/min}$). For the pool shape $\delta \propto y^{3/2}$, profiles along y of (a) thermal gradients G; (b) solidification front velocities R; (c) cooling rates $\dot{T}$; (d) primary dendrite arm spacing λ_1. The measured λ_1 is indicated by the dashed horizontal line.

characteritic length in Eq. (3.4). In Fig. (3.15), we have compared the predictions with δ (red) and $\delta/8$ (blue), assuming that the pool shape is $\propto y^{3/2}$. As expected, the values of G are 8 times larger for $\delta/8$. On the contrary, the profile of R is not modified because it depends only on the advance speed and on the pool shape. Hence, the cooling rates $\dot{T} = GR$ are also 8 times larger, reaching values of the order of 10^4 °C/s, more compliant with what is usually reported in the literature for LMD technologies. As a consequence, the primary dendrite arm spacing decreases from 12.4 down to 4.4 µm, very close to the measurement (horizontal dashed line, see also Fig. 3.14). We have carried out the same analysis for case (i) ($E = 367\,\mathrm{J/mm^3}$, $V = 1.2\,\mathrm{m/min}$) and found that the best agreement with the measured λ_1 is obtained with $\delta/15$.

Finally, we have compared in Figure 3.16 how our best estimations of the cooling rates $\dot{T}$ (with respect to λ_1) compare to the values reported in the literature, concerning Ni base alloys. Two different sets can be clearly distinguished: values related to SLM [90][98][99][100] on one hand; values related to LMD on the other hand. Both feature a decrease of $\dot{T}$ with increasing input energy density E, but they differ quantitatively. It is worth noticing that the dispersions of the collected values are quite significant, and may be attributed to differences in Ni content and specificity of the different processes (e.g. atmosphere). SLM exhibits larger cooling rates than LMD, reaching values as large as 10^7 °C/s [90]. LMD reaches at most a few 10^4 °C/s [101, 92], of the order of what we have obtained.

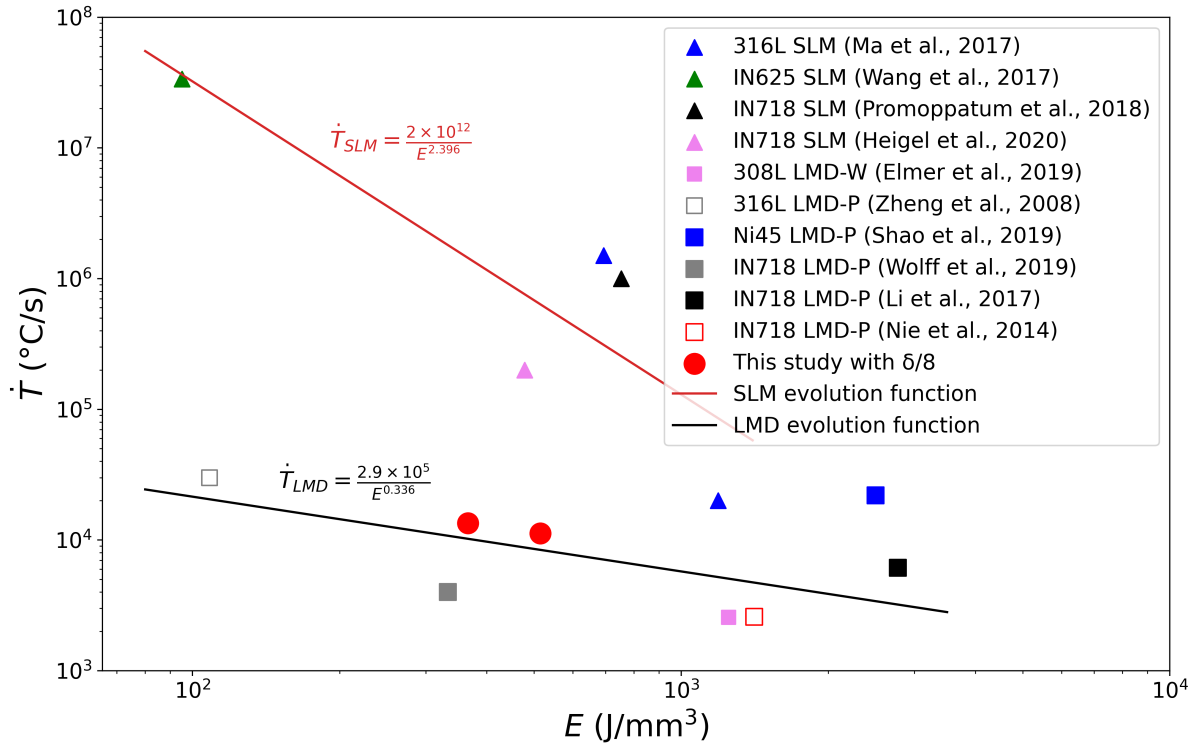

Figure 3.16: Cooling rate $\dot{T}$ of the molten pool vs. energy density E, obtained in the present study (red circles) and according to the literature for different technologies and Ni base alloys. triangles: SLM; squares: LMD; filled symbols: experiments; empty symbols: simulations.

If our analysis can be considered as satisfactory with respect to other estimations in the literature, it has required a number of simplifications and adjustements such that it cannot be considered as fully quantitative. In particular, besides the crude assumptions already discussed, our estimations could change if we had performed measurements for a larger number of built layers than two. Indeed, Bennett *et al.* [102] have shown that the cooling rate decreases when increasing the distance to the substrate. This would be definitevely interesting to carry out the same kind of analysis as a function of the number of built layers. To conclude on this section, it is clear that there is a strong need for further instrumental and simulation developments for LMD technologies and particularly coaxial LMD-W.

3.2.3 Microstructures

In the samples cross-sections, two grain morphologies have been observed: columnar and equiaxed. Columnar grains are expected due to the thermal conditions, in agreement with what is classically observed (§1.3.1). In Figure 3.17, typical long dendritic grains oriented with one of their ⟨001⟩ directions along the building direction, i.e. along the thermal gradient. The interdendritic regions, segregated in Nb, exhibit Laves phase and NbC carbides, delineating the primary dendrites. They feature different shapes and sizes. For most processing conditions, secondary arms are not visible enough so as to measure their spacing.

Equiaxed grains have not been observed in single track beads, whatever the investigated input energy and wire feeding rate. On the contrary, they have been observed systematically in single and multitrack walls close to the interface with the previous layer, as shown in Figure 3.18. On top of these equiaxed zones, solidification has proceeded further in the remaining layer by columnar growth. Hence, the equiaxed grain zones are likely to be located where the previous layer has been remelted. Bambach *et al.* have reported similar equiaxed grain zones for LMD-W of Inconel 718 [46].

These equiaxed grains have been found for different processing conditions (labelled in Table 3.2). They are present for both low and high input energy (1350 – 4000 J/m), even with large thermal gradients and low advance speeds. An example of equiaxed grain zone in the first layer of a built wall with condition *b* is given in Fig. 3.19. At the bottom of the molten bath, grains have grown from the substrate as a small layer of columnar dendrites, before the columnar to equiaxed transition has occurred. Then equiaxed grains have nucleated and grown in a region spanning over 200 µm. Finally, columnar dendrites have been grown over the equiaxed grains.

Such equiaxed grain zones have also been observed in built walls, as illustrated in Figure 3.20, where a macroscopic "zigzag" grain structure is the signature of the bidirectional deposition strategy of multitrack walls [43]. The fractions of equiaxed zones per layer is approximately constant. Nonetheless, they are not observed at the edges of the cross section of the manufactured parts (Fig. 3.20).

Table 3.2: Example of manufacturing conditions with equiaxed grain zones.

Condition	P (W)	V (m/min)	Wf (m/min)	Linear Energy (J/m)
a	2400	0.6	2	4000
b	2200	1.2	2	1833
c	1600	0.9	1.6	1777
d	2000	1.2	2	1666
e	2700	2	3	1350

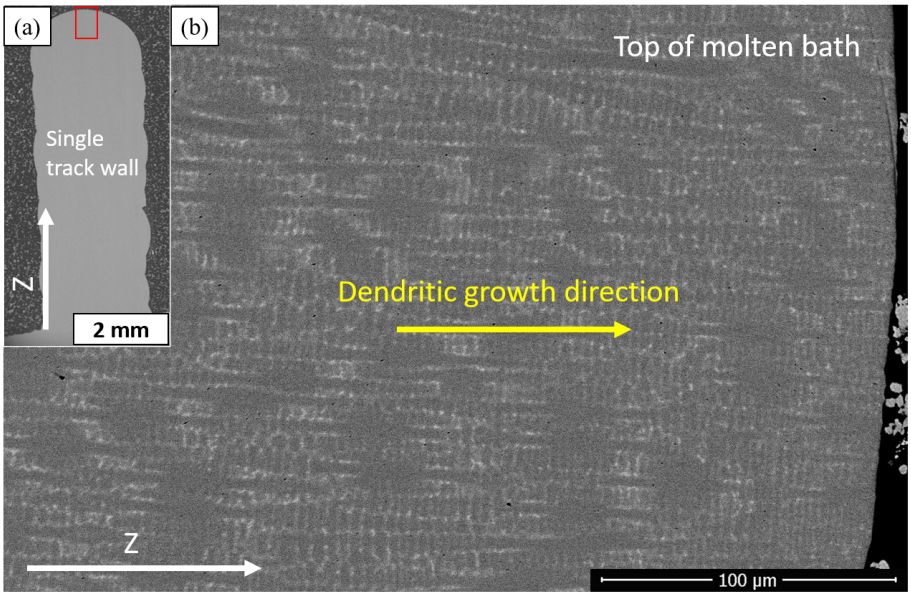

Figure 3.17: (a) Cross section of a single track wall. (b) SEM-BSE micrograph of the square on top of the wall. Laves phase and NbC are in light grey contrast and Ni matrix in darker grey.

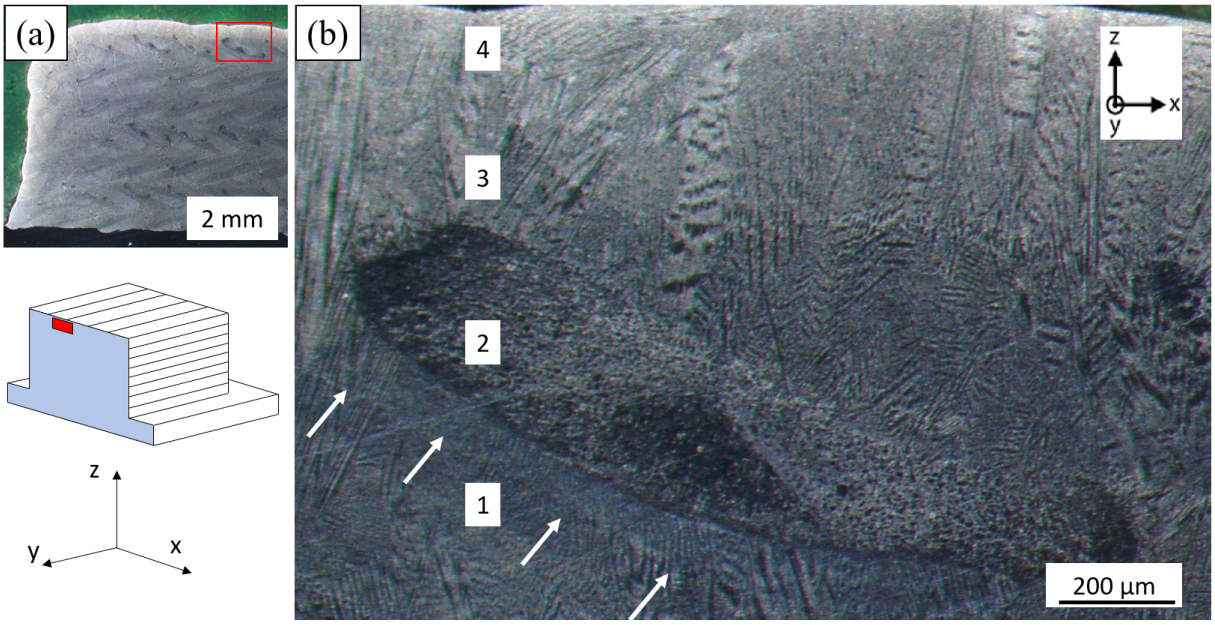

Figure 3.18: Optical micrographs of (a) the last two layers with equiaxed zones; (b) zoom of the square in (a). White arrows: melting front between the last layer and the top one; 2: equiaxed zone; 3: columnar zone; 4: top of the part.

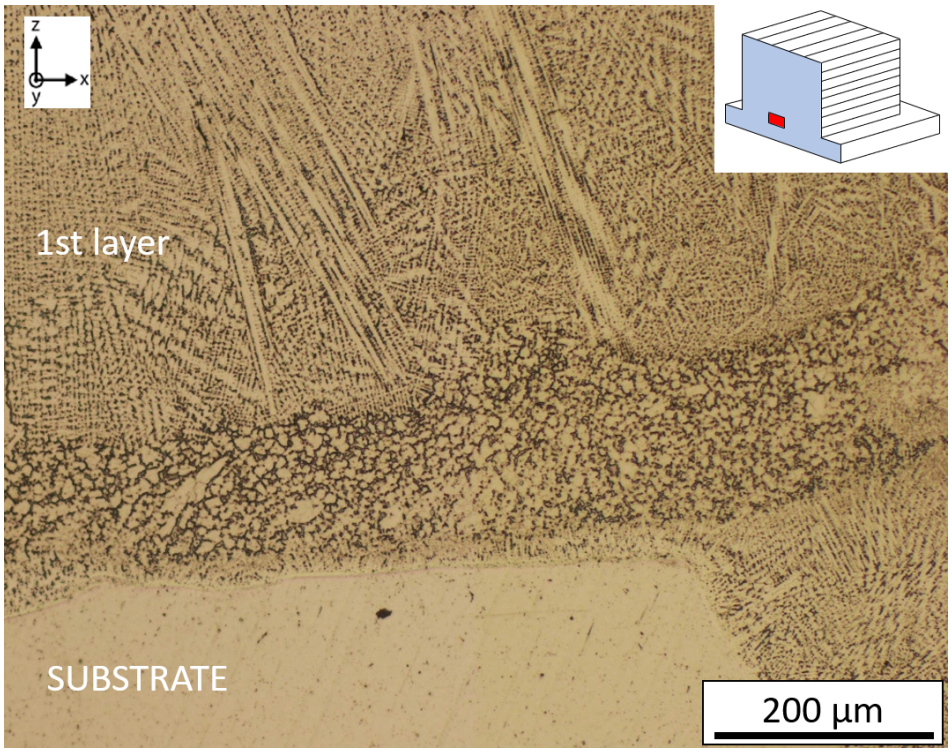

Figure 3.19: Optical micrograph of the first built layer with condition *b* (Tab. 3.2) with equiaxed grains at bottom of the first layer.

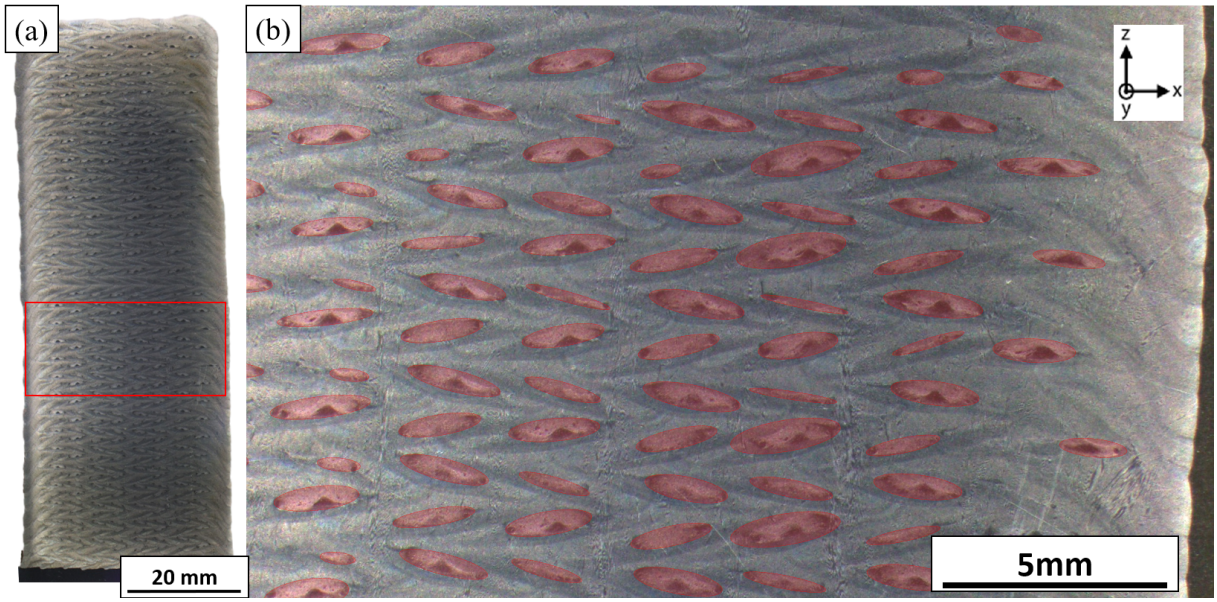

Figure 3.20: (a) Optical image of the cross section of a $30 \times 100 \times 50$ mm multitrack wall. (b) Optical micrograph zooming on the rectangle in (a) with equiaxed regions indicated with red ellipses. Processing conditions *cf* (Tab. 3.2).

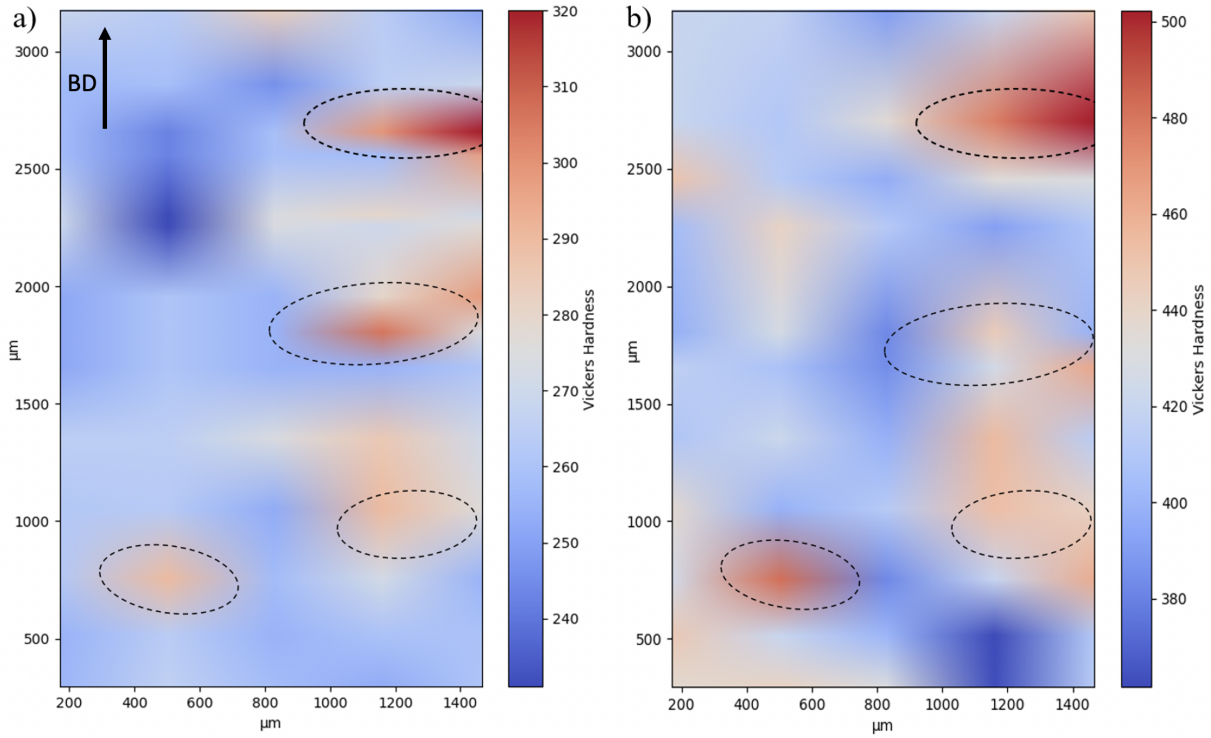

Figure 3.21: Hardness maps (HV0.5) of some cross section of (a) as-built multi-track wall; (b) after direct aging. Equiaxed grain zones are indicated by dotted lines.

In Figure 3.21a a hardness map is plotted with both columnar and equiaxed grains in as-built condition. It can be noted that hardness increases in the equiaxed zones up to 320 Hv while the columnar grain zones feature hardnesses below 280 Hv, with a mean value of 275 Hv similar to as-built LMD-P parts [25]. Hardness in as-built condition would be equal to non heat treated wrought condition [103]. Figure 3.21b shows the hardness map of the same cross section after direct aging at 720 °C for 8 h and 620 °C for 8 h. Equiaxed zones are still harder with 500 Hv, when columnar zones feature at most 450 Hv. Aging of equiaxed zones gives the same mean hardness as with SLM that provides the highest hardness among other AM and conventional processing techniques. Variations of hardness among the different equiaxed zones after ageing can be noticed and may be attributed to measurement uncertainties or Laves phase.

3.3 Conclusion

Stable processability of Inconel 718 using coaxial laser-wire has been achieved from single to multi-track building strategy. The influence of the process parameters on the height and width of the tracks has been found to be similar to what is reported in the literature. Moreover, we have been able to determine the deposition rate for a wide range of input parameters. LMD-W features a higher deposition rate than most of the powder based additive manufacturing technologies but remains inferior to other wire based AM processes such as WAAM or EBAM.

The investigation of the molten pool has demonstrated the intense interaction between laser and liquid, with important laser reflections and high temperatures. Movements of oxides measured in the liquid indicate that significant convection takes place and suggest that fluid flows may be turbulent. From temperature measurements at the surface of the molten pool during multi-track processing, we have estimated crudely thermal gradients, solidification front velocities, and ultimately lower bounds for the cooling rates. Crossing this analysis with measurements of primary dendrite arm spacing, we have been found an order of magnitude of 10^4 °C/s for the cooling rates, in agreement with estimations proposed in the literature for LMD processing in similar conditions.

With the process parameters defining stable processing conditions, only few defects have been found in the as-built materials: Ti enriched particles, probably coming from the wire, and microporosities of a few μm. It is worth stressing that our building conditions did not give rise to any hot cracking or liquation cracking. The as-built solidification microstructure is composed of columnar dendritic grains as well as zones with small equiaxed grains. These zones are observed at the bottom of each layer, except for single track beads. They have a direct effect on the hardness of the alloy, and their formation needs to be understood.

Chapter 4
Equiaxed grains in LMD-W Inconel 718

In this chapter, a thorough characterization of equiaxed grains is carried out that combines different techniques. Based on the different elements, we discuss the possible mechanisms that would explain the formation of equiaxed grains, as published in [104]. Moreover, we provide extra support with respect to [104] based on 3D EBSD and EDS mapping performed at the University of Saarland.

4.1 Mechanism for equiaxed grain formation

4.1.1 EBSD Analyses

EBSD maps were taken in the longitudinal cross-section (y-z plane) in the scanning direction, an example is shown in the IPF map along Z axis in Figure 4.1 where the equiaxed grains are forming continuously along the layer. The change of grain size is drastic and surprisingly in an important volume of 100-400 µm width to the length of the built sample (several millimeter). It is interesting how sharp the columnar to equiaxed transition (CET) is, while some isolated grains are forming before the transition.

The effect of presence of such equiaxed regions layer by layer affects the texture of the microstructure as shown in pole figures in Fig. 4.2. There is clearly a change of orientation and partition of the columnar grains orientation before and after the equiaxed region, which indicates a grain selection operates during the growth of columnar grains once they grow by epitaxy from the equiaxed ones. As it can be seen in Figure 4.1, the columnar grains meeting the equiaxed grain zones before and after present low [001] texture, that is usually the preferred growth direction in AM conditions.

More rarely, smaller equiaxed grain zones were observed in single track walls in the first layers as shown in Fig.4.3c, but not for all samples, as both maps of single track walls in Fig. 4.3 were processed with same parameters and strategy. Equiaxed zones are therefore less repetitively present in single track wall processing. However, it can be seen that for both conditions at same height (15th layer) in Figure 4.3b-d. The absence of equiaxed grains leads to higher texture along [001] direction, which is due to less columnar grain growth competition and thus more favoured aligned grains with the thermal gradient, as shown in 4.3d more columnar grains are highlighted in red. The same observation can be made with the ⟨100⟩ pole figures shown in Figure 4.4, where it can be seen that the columnar grains after growing from equiaxed regions show less ⟨100⟩ texture (a) than without equiaxed grains (b).

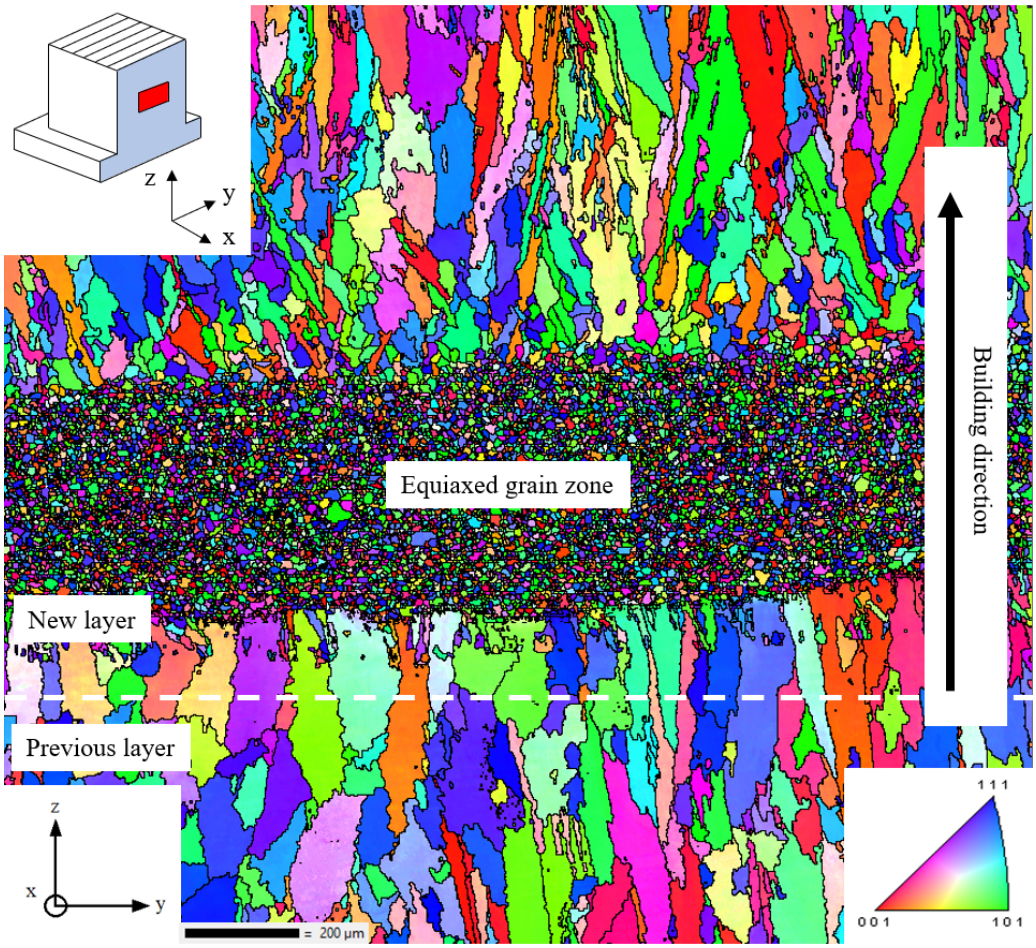

Figure 4.1: Macro EBSD IPF colouring image of equiaxed grain zone inbetween columnar microstructure in the longitudinal cross-section of a multi-track wall.

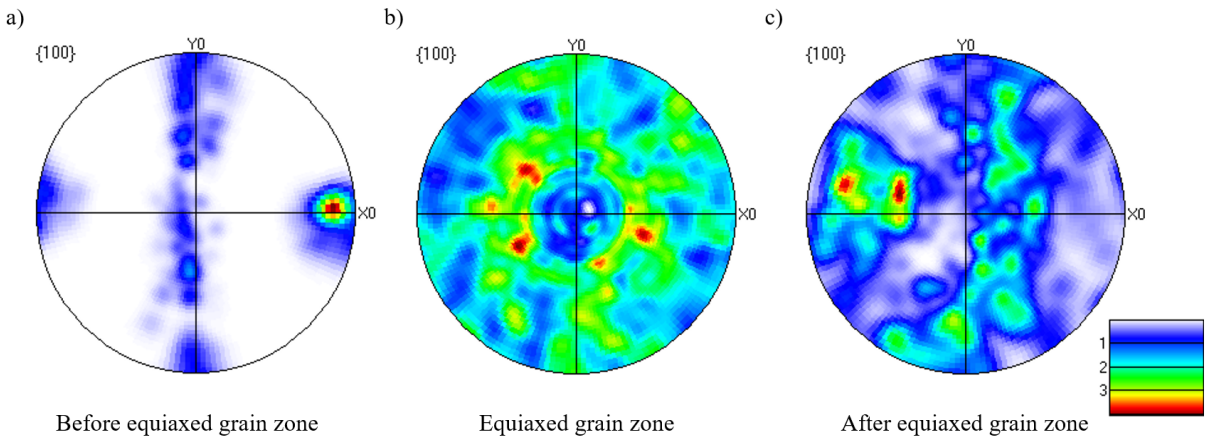

Figure 4.2: Pole figures ⟨100⟩ of (a) columnar grains before the equiaxed grain zone (b) equiaxed region (c) columnar zone after the equiaxed grain region.

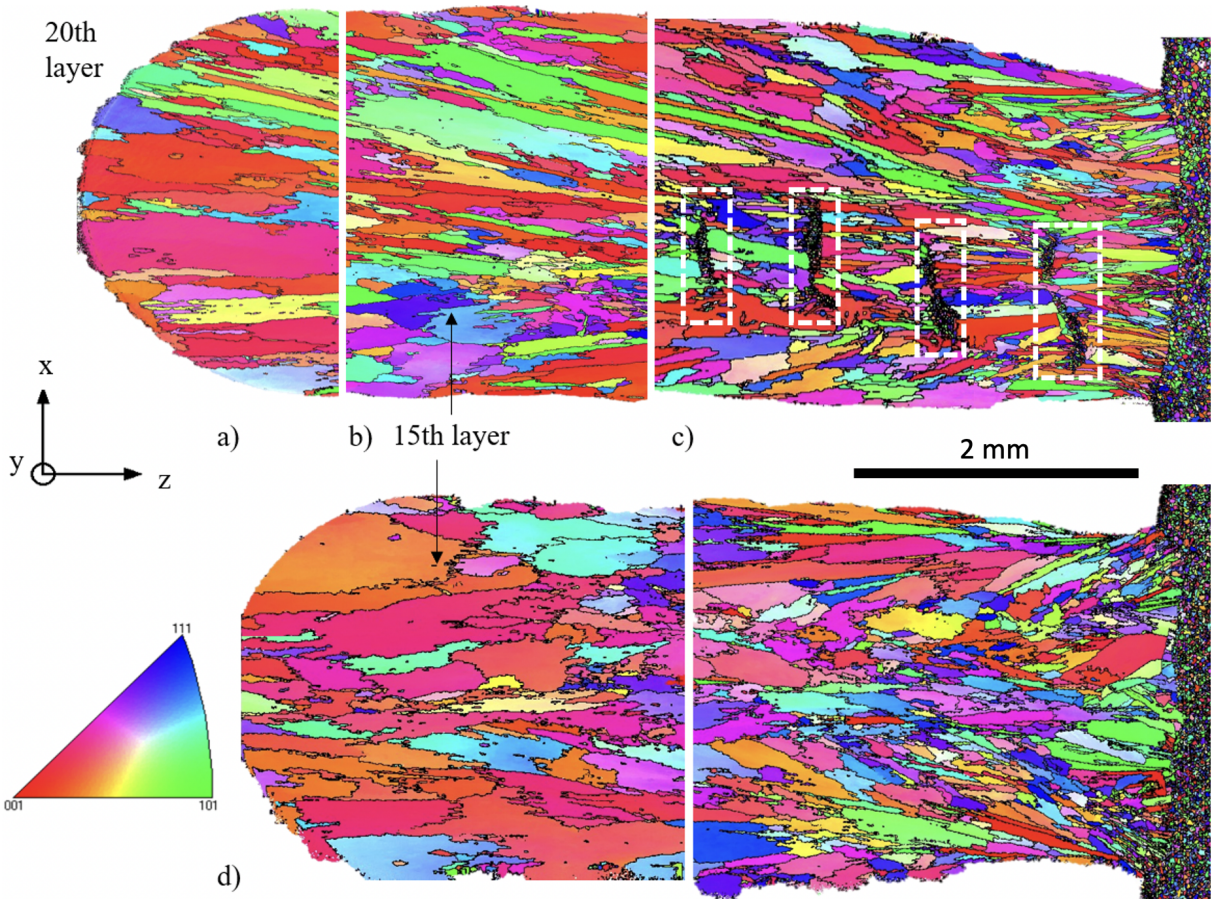

Figure 4.3: Macro EBSD IPF colouring image (Z axis) of (a) 20th layer (b) 15th layer (d) dashed rectangles represents the equiaxed grain zone in-between columnar microstructure at change of each layer, in the first 5 layers in the cross section of a single track wall. (d) Single track wall without equiaxed grains for same building conditions, built up to 15 layers. Substrate equiaxed microstructure is at the right.

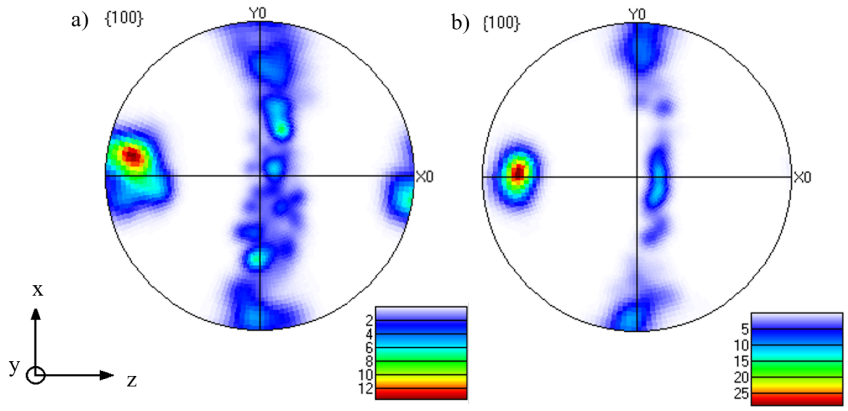

Figure 4.4: Pole figures ⟨100⟩ of (a) columnar grains after equiaxed zone (b) full columnar grains, from 15th layer of macro EBSD map in Figure 4.3.

Figure 4.5a shows an optical micrograph (OM) in the x-z plane cross section. Some areas, indicated by white arrows in Figure 4.5a, appears in darker contrast and correspond to the fine equiaxed microstructure areas. One of the equiaxed zones is shown in more details in Figure 4.5b on a SEM-BSE image. The area corresponds to the white dashed rectangle in Fig. 4.5a. Four distinct zones can be observed: (i) the $n-1$ layer in which growth direction is indicated by an arrow; (ii) columnar growth in the n^{th} layer by epitaxy from layer $n-1$ where the change of growth direction is indicated with a white arrow; (iii) columnar-to-equiaxed transition leading to a fine equiaxed microstructure; (iv) equiaxed-to-columnar transition in which oriented growth leads to a columnar microstructure. Figure 4.5c is the false-colour EBSD map corresponding to Figure 4.5b where the different transitions are clearly visible, similarly to Bambach *et al.* observations [46]. In this Figure, identified twin grain boundaries are outlined with white lines whereas random grain boundaries (GB) with a misorientation > 10 degree are shown with black lines.

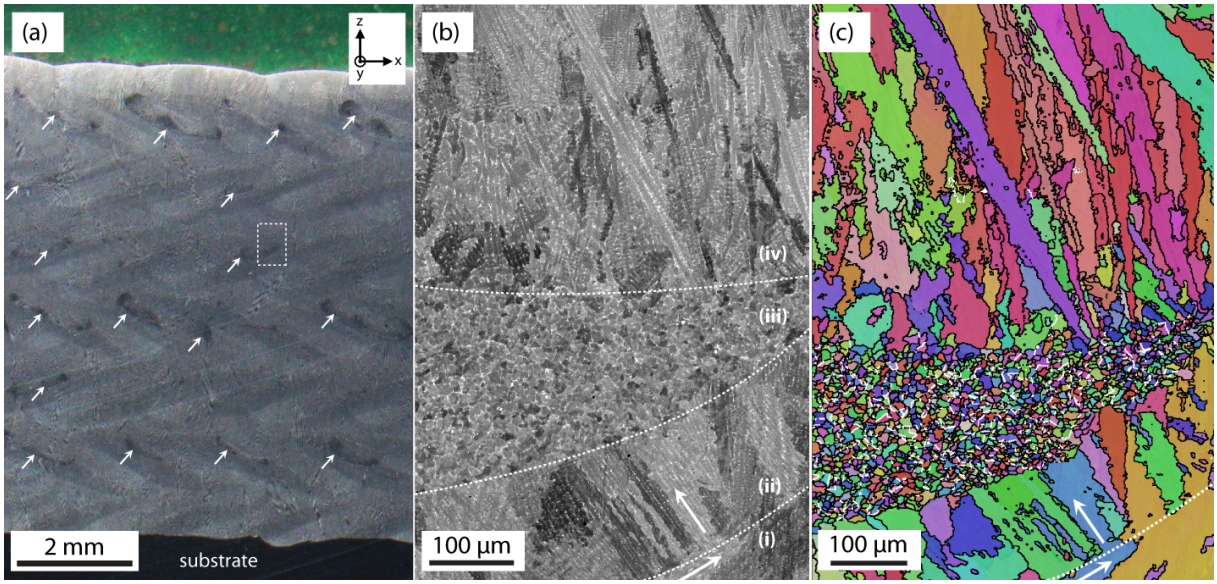

Figure 4.5: (a) OM in the x-z plane of the built Inconel 718, (b) SEM-BSE image corresponding to the dashed rectangle in (a), (c) EBSD false-color map of (b). The white arrows in (a) correspond to the equiaxed zone areas. (i-iv): see text for details.

The distributions of the grain size and orientation have been obtained from the EBSD data. Table 4.1 shows the average grain size deduced from EBSD measurements and the relative twin frequency. For columnar grains, the minimum Feret diameter was chosen to evaluate the grain size since their length can vary significantly depending on the observation plane. The columnar grains are $\approx 37\,\mu m$ in width and their length can reach hundreds of micrometers, or even millimeters. The equiaxed zone shows a significant grain refinement with a size $< 5\,\mu m$. Moreover, the twin frequency is about 1.3% in the columnar zone, close to the value in a MacKenzie distribution [105] as it can be seen in Fig.4.6a. On the contrary, as it is also shown in Fig. 4.6b it is about 13% in the equiaxed zone, close to the value reported by Kutuldu *et al.* when 200 ppm Ir is added to Au–Cu–Al alloys in which an icosahedral short range order (ISRO) mediated nucleation mechanism has been demonstrated [1].

Table 4.1: Grain sizes and twin frequencies for the columnar and equiaxed regions. For columnar grains, the grain size corresponds to the width of the grain corresponding to the minimum Feret diameter.

	Columnar region	Equiaxed region
Twin frequency (%)	1.3	12.8
Grain size (μm)	37.76 ±7.14	4.54 ±3.62

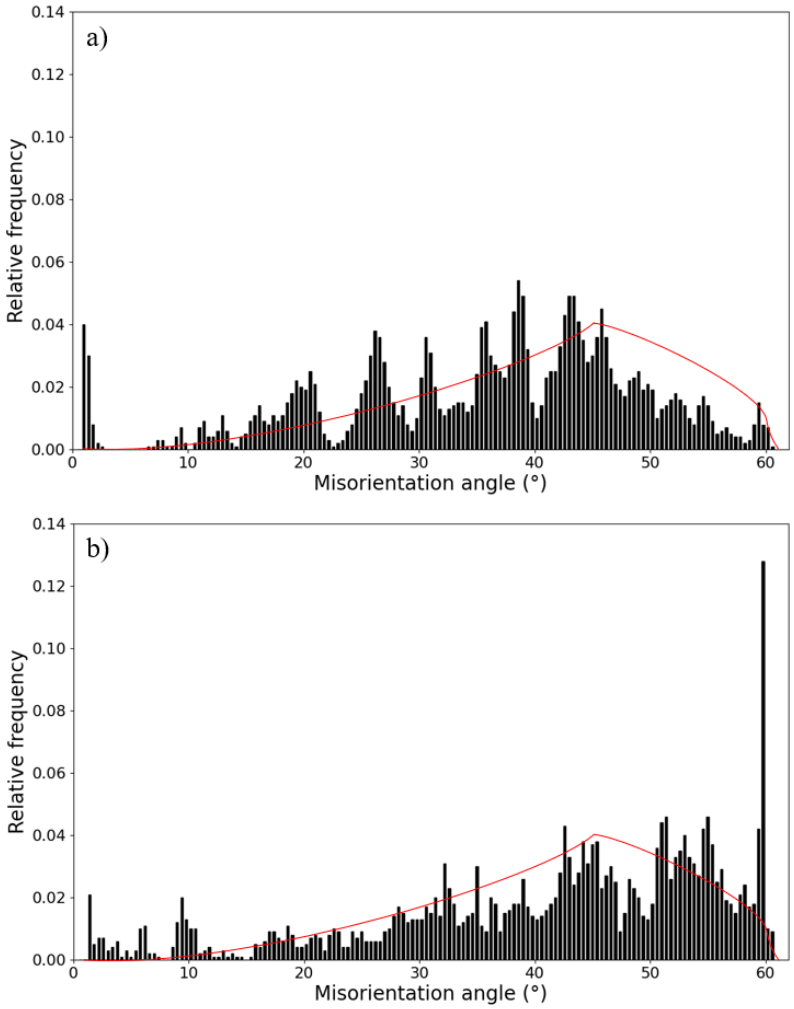

Figure 4.6: Grain boundary misorientation distributions of the (a) columnar zone (b) equiaxed zone; compared with the theoretical Mackenzie distribution of randomly nucleated grains (dark curve). A peak appears at 60 degree in the equiaxed grain zone for a twin frequency of 12.8 % while the twin frequency is 1.3 % in the columnar zone.

Figure 4.7 shows an EBSD orientation map of the equiaxed grain zone where several nearest-neighbour grains are in multiple-twin relationships, and a grain-to-grain analysis can be performed to find any symmetry. Moreover, smaller-scale grains with a size of just a few μm are visible in the microstructure. In order to prove that this nucleation mechanism is similar to that identified in Al–Zn–Cr

alloys [2] and Au–Cu–Ag–Ir alloys [1, 106], multiple-twin orientation relationships between several fcc grains sharing an icosahedral symmetry must be identified.

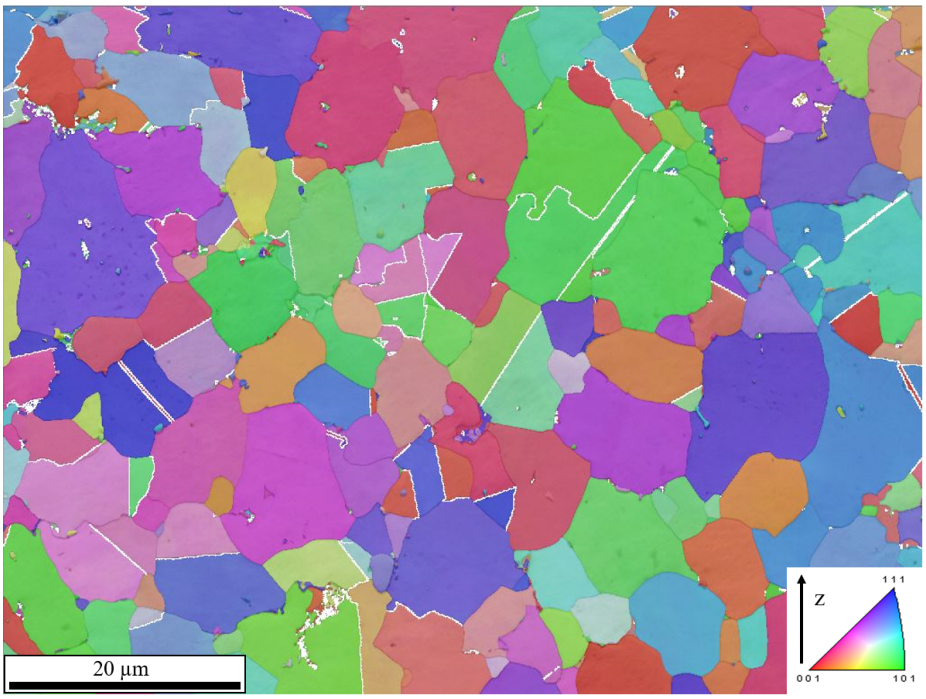

Figure 4.7: EBSD orientation map in IPF colouring along Z axis of the zoomed equiaxed grain zone. Twin grain boundaries are in white and regular grain boundaries in thin black lines.

4.1.2 Icosahedral Short Range Order (ISRO) mediated nucleation

Several aggregates of nearest-neighbour grains having multiple-twin orientation relationships (OR) have been found in the equiaxed zone. Figure 4.8a shows an assembly of grains in twinning orientation relationships, obtained from a high-resolution EBSD map, and labeled from 1 to 7. The ⟨110⟩ pole figures showing their mutual twin orientations are given in Fig. 4.8b-d where the red arc of a circle is the trace of their common {111} plane. Between each pair of grains in Figure 4.8b, the common {111} plane is rotated by 70.5 degree. around a common ⟨110⟩ direction, which is indicated by the red circle where all the pole figures in (b) are superimposed. The pairs of grains 1-2, 2-3, 3-4, 4-5 show perfect twin orientation relationships (OR). The orientation relationship between grains 5 and 1 correspond to what Kurtuldu *et al.* define as near-twin OR [2]: a twin OR and a rotation of about 7 to 8 degree around a common ⟨110⟩ direction. This assembly of 5 grains is compatible with the symmetry of a decahedron with grains 1 and 5 that accommodate the default aperture angle of 7.5 degree. This rotation corresponds to the cumulated angle difference between 5 tetrahedra of the icosahedron (360 degree) and 5 regular {111} tetrahedra of the fcc structure (352.5 degree) [107]. Interestingly, the default gap angle of 7.5 degree between 1-5 is filled with an extra grain 1' as shown in Figure 4.8a. The grains 1-1' have close orientations, with a shift of 7.5 degree that corresponds to the default aperture angle of 7.5 degree described previously.

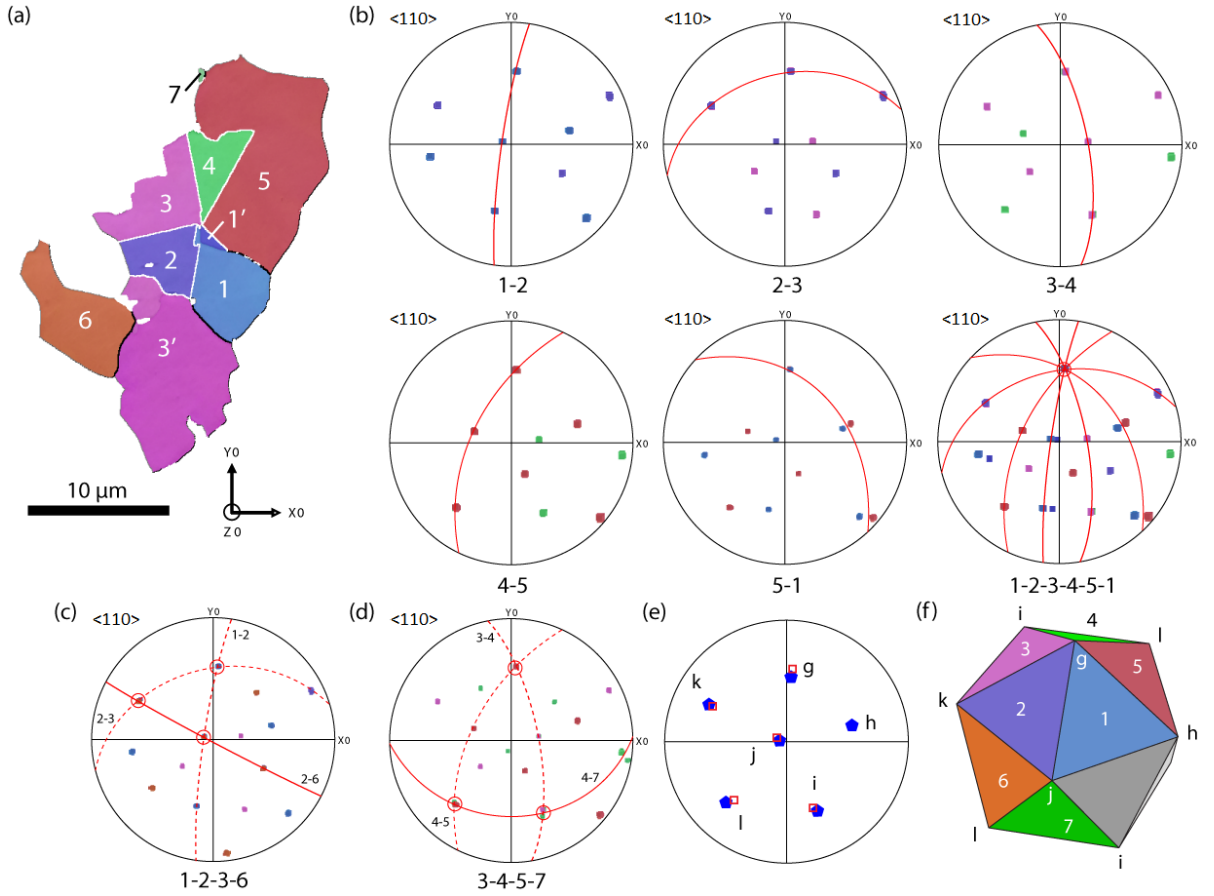

Figure 4.8: (a) EBSD map of seven nearest-neighbour grains with multiple-twin orientation relationships taken from the equiaxed zone. The ⟨110⟩ pole figures in (b) shows the orientation relationships between pairs of grains, and the red arcs of a circle correspond to the trace of the common {111} plane (they are all drawn in the last pole figure). (c-d) ⟨110⟩ pole figures of grains 1-2-3-6 and 3-4-5-7. At the crossing of common {111} twin planes, there are 3 common ⟨110⟩ directions for grains 1-2-3, 1-2-6, 2-3-6 and 3-4-5, 3-4-7, 4-5-7, respectively. (e) Stereographic projections of the 5 common ⟨110⟩ directions of the fcc grains found (red squares), together with the calculated stereographic projection of the fivefold symmetry axes of the icosahedron (blue pentagons). (f) A perfect icosahedron with facets from which the fcc phase formed have the same colour and number as the grains in (a) and 5-fold axis have the same letter as in (e). Detailed procedure is given in Appendix B.

Two other grains were found to have a twinning OR with one of the 5 grains presented in Figure 4.8, and four additional ⟨110⟩ directions, common to at least 3 grains, were found, as shown in Figure 4.8c-d. The grain labelled 6 displays a twin OR with grain 2 and share a common ⟨110⟩ axis with grain 1 and 3; the grain labelled 7 displays a twin OR with grain 4 and share a common ⟨110⟩ axis with grain 3 and 5. Grains 6 and 7 have a near-twin OR (not represented in the Figure). The ⟨110⟩ pole figure in Fig.4.8e shows the 5 common ⟨110⟩ directions of the fcc grains, together with the calculated stereographic projection of the fivefold symmetry axes of the icosahedron. A perfect icosahedron is also shown in Fig. 4.8f with facets that have given rise to the fcc grains with the same color and number in Fig. 4.8a. This confirms as in Al-based and Au-based alloys that ISRO-mediated nucleation mechanism can apply for fcc Ni in Inconel 718 alloy.

In Al-Zn and Au-Cu-Ag alloys, the occurence of ISRO in the liquid is induced by minute additions of Cr and Ir, respectively. Approximant phases exhibiting icosahedral building blocks have been found in the Al-Cr system [108] as well as a few Au-rich Tsai-type icosahedral quasicrystals (i-QC) [106], but there is no known Ni-rich i-QC. Also, no specific element has been added and the microstructures have been obtained in this work with a commercial Inconel 718 wire. As shown by Zollinger *et al.* [106], rapid processing of ISRO-containing alloys can lead to a spinodal-like decomposition of the liquid phase, leading to local heterogeneities in the liquid phase. The effect of ISRO on heterogeneous local ordering has also been evidence by ab-initio molecular dynamics simulations in Al-Zn-Cr [109]. In the present work, the local heterogeneity leading to icosahedral clusters in the liquid may not be intrinsic, i.e. induced by a specific chemical element (such as Cr additions in Al-Zn alloys leading to Cr-centered icosahedra [109]), but induced by the rapid melting and solidification conditions inherent to AM processes.

4.2 3D characterization of the equiaxed grain zone

The 3D volume reconstruction of the EBSD IPF images from equiaxed grains analysed volume (60*60*60 µm) is represented in Figure 4.9, where equiaxed grains seem to have random orientations. The measured volume fraction of TiC is about 1 pct and the twin fraction is about 12 pct. In this volume, a research from grain-to-grain analysis is performed in order to find any multi-twinning relationships between grains, sharing icosahedral symmetries.

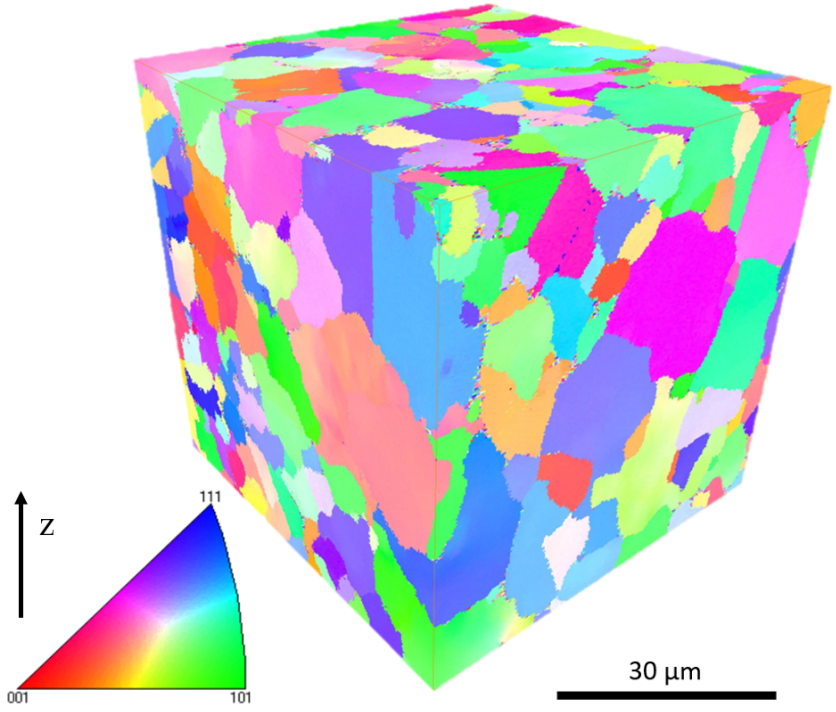

Figure 4.9: 3D EBSD reconstruction of the analysed volume in the equiaxed grain zone with IPF colouring. EBSD reconstruction is performed using Dream3D software and visualization is done with Avizo software.

From the grain-to-grain analysis in the 3D volume, no full icosahedral symmetry were identified but a 3D visualisation of identified grains labelled 1-2-3-4-5 is shown in Figure 4.10a showing a multi-twinning relationship that is similar to a 5-fold symmetry axis. The twin grain boundaries are represented in dark grey planes and each grain is represented by a respective orientation color. Figure 4.10b shows that the multi-twinning relationship and the grains seem to emerge from the surface of the TiC particle. An Al oxide is present at the center of the TiC particle, acting as a nucleation site for the TiC phase.

The grains sharing a multi-twinning relationship and the identified TiC are presented in a 2D slice EBSD image in Figure 4.11a in IPF colouring. The corresponding ⟨110⟩ pole figure of the grains 1-2-3-4-5 is shown in Figure 4.11b, that shows the common direction ⟨110⟩ of all 5 grains (circle in red), where the red arcs represent the common {111} planes between each pair of grains. The common {111} plane of each pair of grain is rotated by 70.5 degree, which is compatible with a 5-fold symmetry axis. The grains 1-5 presents a rotation around the common direction ⟨110⟩ of 7 to 8 degree, which was already reported as a near-twin previously. No other symmetry axis was identified with the grains 1 to 5 than the 5-fold symmetry axis which is a decahedron symmetry and not an icosahedron. It could be possible that the fcc phase nucleated on the faces of only one 5-fold symmetry axis of an icosahedron.

The relationship between the TiC and twin grain boundaries is unclear. The twin partition in the volume and the present TiC particles can be seen in Fig.4.12. From this volume, a search for twin surrounding the TiC particles can be performed in order to see if there is any connection between twin grain boundaries and TiC particles.

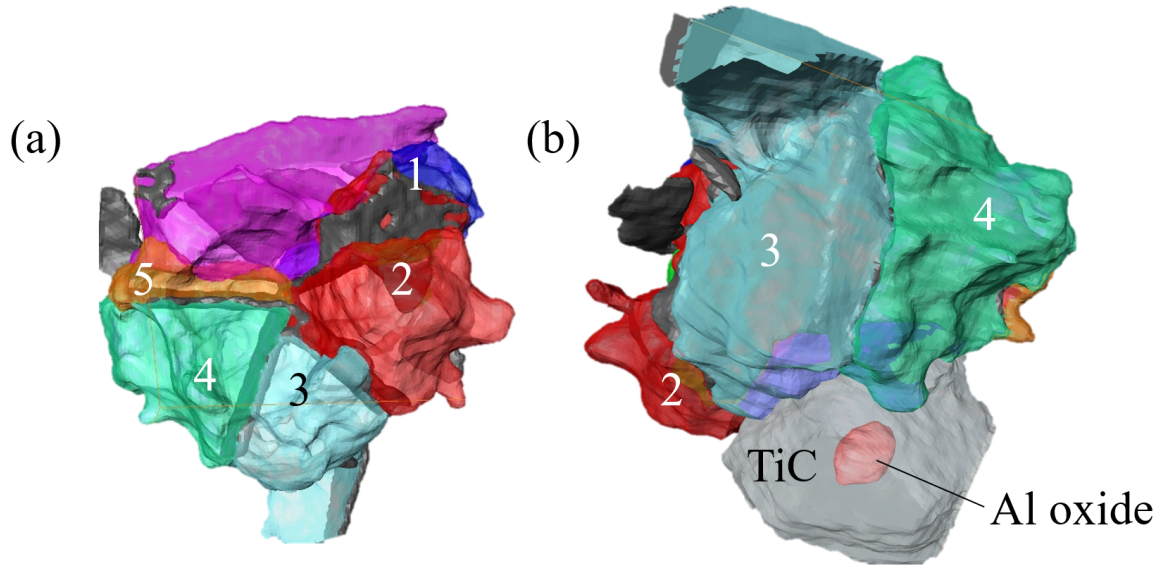

Figure 4.10: 3D representation of the (a) grains 1-2-3-4-5 sharing a multi-twinning OR with their corresponding colours and twins in between in dark grey. An external grain in pink is completing the void in-between the grains 1-5 with no relationship with the other grains. (b) 3D visualisation of the grains 1-2-3-4-5 and twin grain boundaries connected to the TiC particle. An Aluminium oxide is identified at the center of the TiC particle.

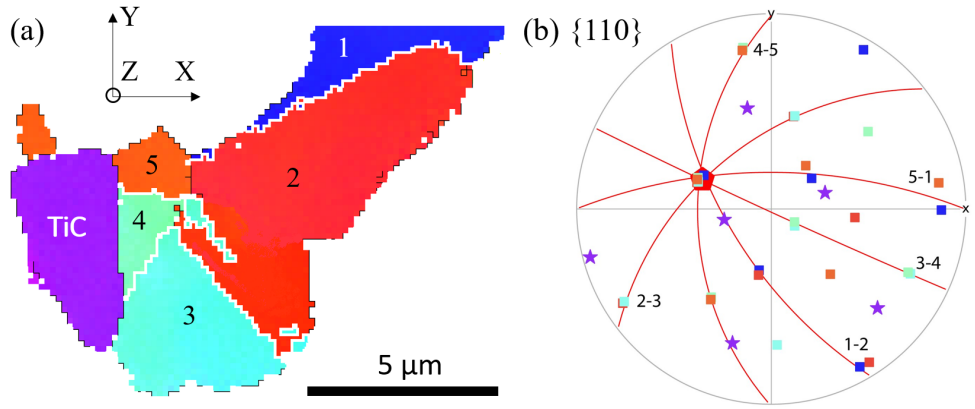

Figure 4.11: (a) 2D EBSD IPF map (Z) of 5 nearest-neighbour grains (1-2-3-4-5) with multiple-twin orientation relationships and the attached TiC particle in purple, taken from one EBSD slice in the 3D equiaxed zone. Twin grain boundaries are indicated in white and regular grain boundaries in black. (b) Respective colouring pole figure ⟨110⟩ of grains from 1 to 5 sharing a common ⟨110⟩ direction, highlighted in a red pentagon shape. The ⟨110⟩ directions of the TiC particle are represented by purple stars sharing no common orientation relationship with the fcc grains.

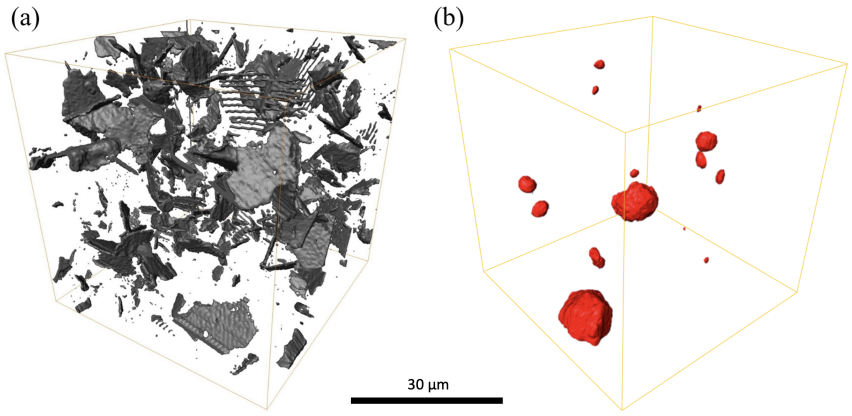

Figure 4.12: 3D representation of (a) the twin grain boundaries in the volume and (b) the TiC particles.

Figure 4.13 shows from (a) to (f) different population size of TiC particles encountered in the 3D analysed volume, other than the previous discussed. It seems there is a link between the presence of twin grain boundaries in the fcc phase and TiC inclusions, for a TiC fraction in the volume that is only 0.77 pct. It also can be observed that the size of the TiC particles also has an influence on the presence of twin grain boundaries, as shown in Fig.4.13f. The TiC can act as a nucleation site for various alloys [110]. It was reported in literature that the addition of NbC and TiC particles during processing of Inconel 718 with SLM promoted equiaxed grain morphology and reduce the grain size [111]. Yet its relationship with the 5-fold symmetry axis of the Ni fcc grains is not possible, due to its NaCl structure type. An intermediary phase on the surface of the TiC that helps the fcc grains to nucleate and grow respecting the 5-fold symmetry is a more realistic hypothesis.

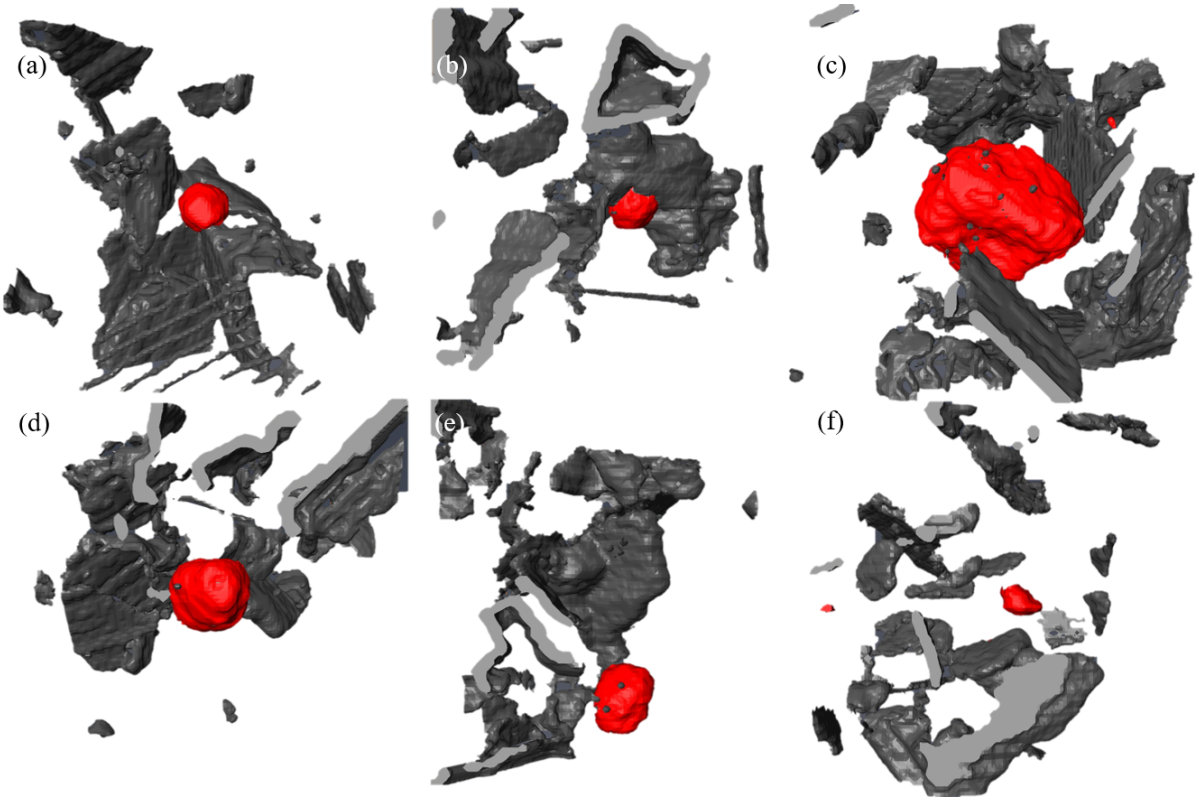

Figure 4.13: 3D representation of the TiC particles (red) with the respective twin grain boundaries in the fcc matrix around (with 8 deg of tolerance).

4.3 Discussion

4.3.1 Process conditions

Figure 4.14 shows the view of a molten pool remelting the adjacent layer where the equiaxed grain zone is typically observed. With heating rate in the general range of 1 to 8.10^4 K/s [98] and as demonstrated in the previous chapter, cooling rate in this study is in order of 1.10^4 K/s, the $n-1$ layer and adjacent bead (as shown in Figure 4.14) that partially remelt has little time for the ordered fcc phase to disordered liquid transition that could lead to partially ordered liquid or even metastable short-range order configurations including a certain fraction of ISRO. It is possible when remelting previous layer and adjacent bead, local enriched zones of a specific element such as Nb could play a role.

This hypothesis can be corroborated by an analysis based on the columnar-to-equiaxed transition (CET). According to Hunts steady state model [27], the CET mainly depends on three factors: the thermal gradient G, the solid/liquid interface velocity V and the number of potent nucleants ahead of the columnar front. Such analysis has been performed for AM Inconel 718 by Raghavan *et al.* for electron-beam melting process [9] using powder. Based on a heat-transfer model and considering a constant nucleation density of 2.10^{15} nucleus.m^{-3}, the authors showed that CET is more likely to occur at the end of the solidification of the layer, i.e. close to the free surface. Contrariwise, the high G and low V at the interlayer boundary in this case is not favorable to a CET. Yet this is the position where the CET

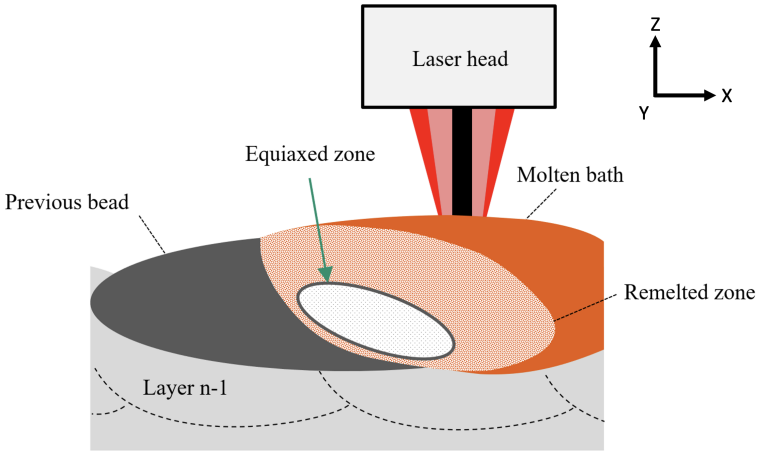

Figure 4.14: Schematic representation of remelting the previous bead and layer during processing. The equiaxed grain zone is represented where typically observed.

has been observed in this work, about 100 µm from the interlayer boundary. Assuming the G-V path determined by Raghavan *et al.* is valid, this means that the number of potent nucleus varies in the layer thickness, and is much more significant close to the interlayer boundary where the liquid phase comes from remelting of the $n-1$ layer. From the twin frequency measured in this work, and following the analysis of Kurtuldu and Rappaz [112], $\approx 13\%$ of twin GBs relates to fraction of icosahedral nucleants over the total number of nucleants of 10%, each icosahedral cluster giving birth to potentially 20 fcc grains. The ISRO-mediated nucleation mechanism induced by the fast melting can explain why a CET occurs in high G and low V regions, by increasing strongly the local number of nucleation sites close to the interlayer boundary. This statement can be supported through the estimation of nuclei from the grain size, that is accordingly $1.10^{16} m^{-3}$, that is one order higher than the value from Gäumann *et al.* [28] for SX alloys processed with LMD-P in different conditions. In addition, presence of equiaxed grains have been reported in this study in first layer of built wall on stainless steel substrate. This observation complicates the previously discussed hypothesis, since the substrate is not enriched in specific elements that could promote iQC formation. This could mean that adjacent bead play an important role in the equiaxed grain formation and poses further investigation. The recent findings of ISRO mediated nucleation being present in pure Ni processed by SLM shows the ability of fcc phase to reproduce this mechanism at much higher cooling rate involved than coaxial laser and wire [113]. It is not known yet if presence of residual elements in the powder have an influence on ISRO since it was shown that only a few ppm of Cr and Ir could induce this mechanism for Al-Zn and Au-Cu-Ag alloys. The more important grain size with the use of SLM suggest a different source involved for inducing ISRO mediated nucleation.

This shows that to understand the formation of microstructures in additive manufacturing, even for very well-known alloys, it is not sufficient to apprehend the solidification and rapid solidification phenomena, and that the melting stage also has an important role. More in depth characterization of the equiaxed grain zone is needed in order to undertand what induce ISRO mediated nucleation in the case of Inconel 718.

4.3.2 The role of Titanium carbides

During rapid melting and re-melting conditions of the previous layer, TiC are originating from the wire and can also form in the new layer during solidification of the alloy. The use of laser and wire pro-

cess induces high temperature gradients and high cooling rates but could induce chemical heterogeneities in the molten bath, and especially in the remelting conditions at bottom of molten pools. Alloying elements combined with Ti could therefore form metastable short-range order configurations as explained in the previous section, but also form metastable phases in chemically enriched clusters of other elements.

As shown in Figure 4.15a, the TiC is nucleating on oxides during alloy processing, but also on TiN as shown in Figure 4.15b. In Figure 4.15a, the TiC is divided in few parts which indicates it can fragment in the liquid, while some phases are nucleating and growing on its surface as indicated. Nano sized precipitates were also observed being spread out randomly in the matrix, with undetermined chemical composition. Such population of phases were not observed in BSE or SE electronic imaging modes, nor observed in literature, due to the spot size and high voltage using BSE or SE classic detectors. InLens detector also revealed precipitates in the Laves phase C14 area as shown in Fig. 4.15b. The size of such precipitates can vary from a few hundreds of nm to µm, which indicates different population of phases.

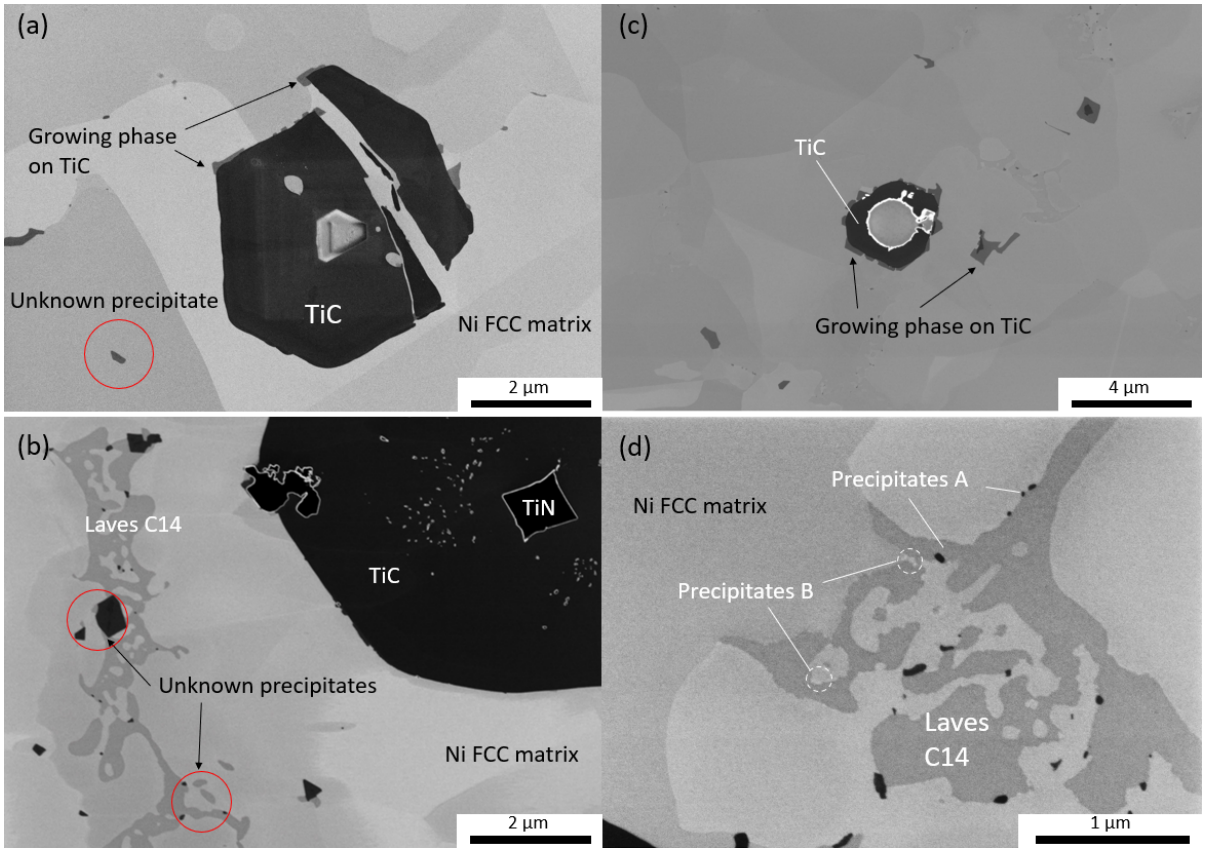

Figure 4.15: InLens SE image of (a) a TiC in the equiaxed grain region. Various unknown phases are growing on the surface of the TiC particle that is cracked. Some undetermined nano sized precipitates are present randomly in the matrix (b) another TiC particle in an equiaxed grain zone, that has a TiN at the center and possibly at the surface as well. Presence of Laves phase C14 with unknown precipitates within are indicated in the matrix. (c) Oxides at the center and at the surface of the TiC (d) eutectic region C14-Ni fcc matrix, where different contrast types of precipitates were observed A (dark contrast) and B (smaller size and lighter).

Observation of unknown phases surrounding the TiC particles indicates that the hypothesis of an intermediary phase on the surface of the TiC acting as a nucleation site for fcc grains to grow and respect the 5-fold symmetry is possible. This observation could also mean that AM conditions creates metastable configurations in the liquid and these phases remain during solidification, since locally it would not be the alloy Inconel 718 anymore due to segregations. The contrast of InLens collecting secondary electrons of type II provide both a chemical and crystallographic contrast. Two types of nanosized precipitates were observed in the Laves phase region eutectic with the Ni matrix, as shown in Figure 4.15d. The dark precipitates A that were observed in Fig. 4.15 are $\sim$ 100 nm of size while the precipitates B are in lighter contrast. To investigate at a lower scale for understanding what phases are present and their connection to ISRO, transmission microscopy (TEM) is a more precise characterization tool and is needed.

4.3.3 Secondary nucleation by twinning mechanism

It has been established previously that the grains in Fig. 4.8 respected the symmetry of an icosahedron, and more specifically the grains 1-2-3-4-5 completed a full 5-fold symmetry axis. The same grains are shown in Fig. 4.16a with the highlighted grains 1-1'-2-5 and the $\langle 110 \rangle$ pole figures between grains 1-2, 5-1, 5-1' and 1-1'. It can be seen that the grains 1-2 are in twinning OR indicated by the white grain boundary, also schematically represented in Figure 4.16a. As observed previously in this chapter, the default aperture angle gap of 7.5 degree from the assembly of the grains 1-2-3-4-5 is filled with the extra grain 1' and is shown in Figure 4.16. The pole figure $\langle 110 \rangle$ of grains 1-1' shows a 7.5 degree tilt around their common $\langle 110 \rangle$ direction. It is unexpected that the grain 1' could fill the gap of 7.5 degree and at the same time being in twinning OR with the grain 5, since a near twin (NT) is already present between the grains 5-1 and could have fulfilled the default aperture by growth. This observation could be explained by the interfacial energy between grains, as Kurtuldu pointed out [114], the multiple grains in OR during growth try to minimize their interfacial energy by favouring twin grain boundaries. Figure 4.18 provides the grain boundary energies for symmetric tilt angles of the [110] direction for several fcc elements. Two deep cusps are present for the $\{113\}$ and $\{111\}$ planes, respectively with the angles 50.5 and 109.5 degree [115, 116]. All presented fcc elements seem to follow the same grain boundary energy distribution, but the Ni have the higher gap for the 109.5 degree of tilt angle, that is the $\{111\}$ twin grain boundary. This could mean that the fcc system could have the ability of nucleation by twinning mechanism if possible, in order to reduce the interfacial energy. It should be considered now that this mechanism most probably cost less interfacial energy than a regular heterogeneous nucleation, since a twin grain boundary $\{111\}$ cost almost null energy.

The twin OR and the near twin OR between respectively grains 5-1' and 5-1 are indicated in Figure 4.18 with their corresponding tilt angles. The grains 1-1' have an interfacial energy higher than a NT or a twin grain boundary since they have a tilt angle of 7.5 degree. A near twin (NT) between 5-1 can vary 5 to 7 degree around the twin tilt angle and therefore as has a higher interfacial energy as shown in Fig. 4.18 compared to the twin (T) grain boundary 5-1'. This could explain the presence of the grain 1'. Indeed, the nucleation and growth of a new grain 1' on the grain 5 in twinning OR cost less energy than a regular grain boundary to close the default aperture of 7.5 degree, which proves the ability of the fcc system to nucleate and grow by twinning mechanism.

This seem not to be an isolated case, the grains 1-2-3 taken from Fig. 4.11 are represented in Fig. 4.17a. Unexpectedly, the grain 2 is divided into two sub-grains 2-2', with a misorientation of 5 degree. The respective $\langle 110 \rangle$ pole figures of grains 1-2'-3, 1-2-3 and 2-2' are shown in Figure 4.17b. The de-

viation of 5 degree between 2-2' has a near equal interfacial energy to a NT OR (Figure 4.18) that is higher than a T boundary. As shown in pole figures of grains 1-2'-3 and 1-2-3, the sub-grain 2' is perfectly twinned with the grain 3 and possess a near-twin OR with the grain 1. Inversely, the grain 2 is not twinned with the grain 3, but has a twin OR with the grain 1. This observation shows that the grains 2-2' are divided accordingly to favourite a perfect twin OR with its first neighbour grains in order to reduce the interfacial energy and seem to be originating in the very first moments of nucleation and growth steps.

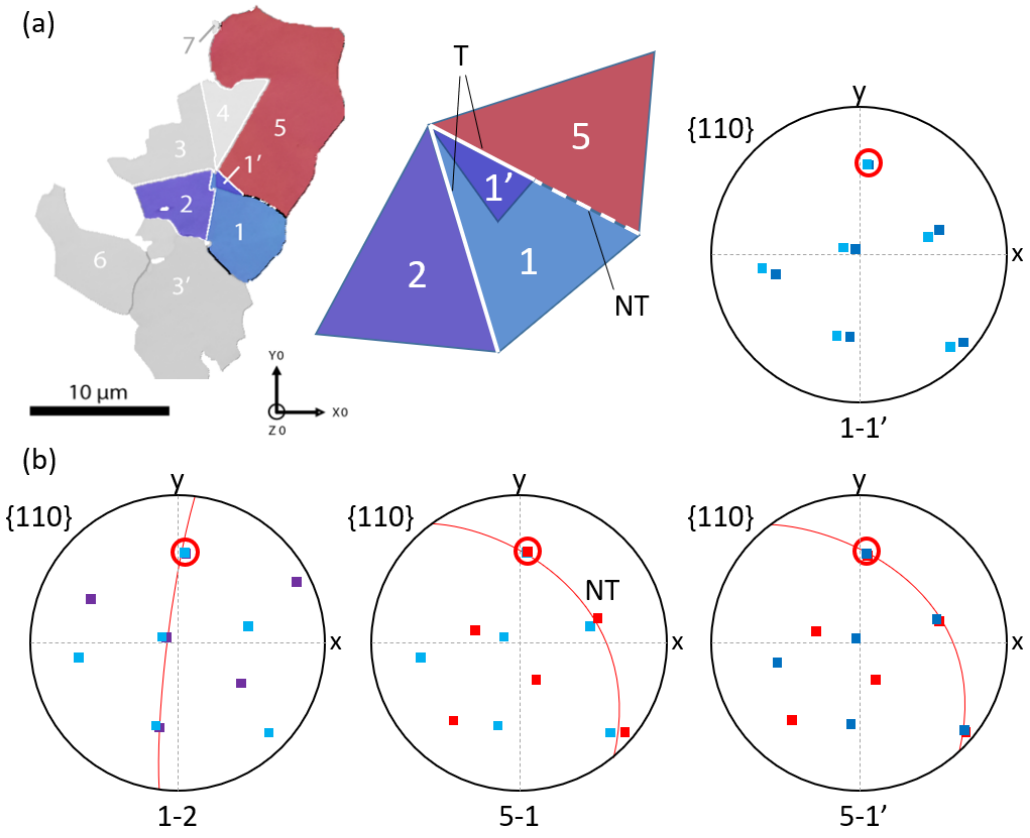

Figure 4.16: (a) Isolated grains 1-1'-2-5 from Figure 4.8. Schematic representation of twin and near twin (NT) grain boundaries between grains. (b) ⟨110⟩ pole figures of each pair of grains 1-1', 1-2, 5-1, 5-1'. Near twin (NT) relationship between the grains 5-1 is indicated. Red circle indicates common ⟨110⟩ direction to isolated grains 1-1'-2-5. A misorientation of 7.5 degree is inbetween grains 1-1' and 5-1.

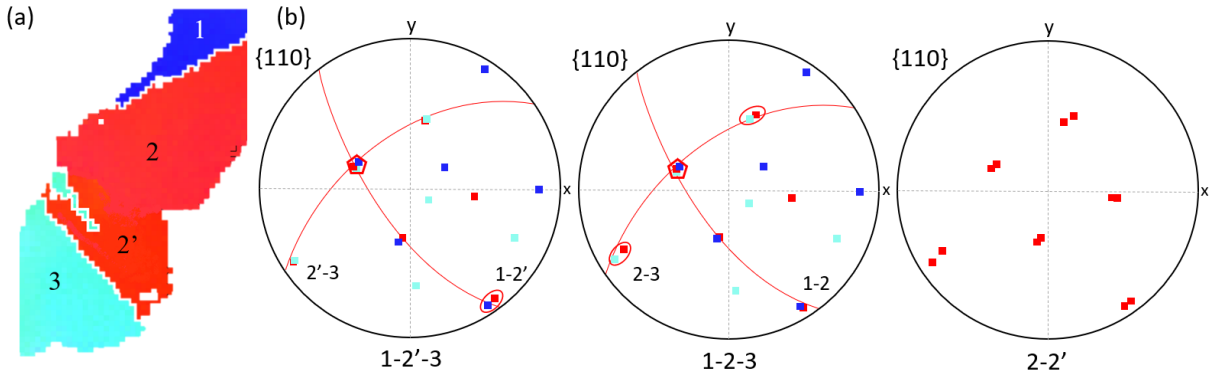

Figure 4.17: (a) Isolated grains 1-2-2'-3 from Figure 4.11, twin grain boundaries are indicated in white. (b) ⟨110⟩ pole figures between the same respective grains, twin OR between 2'-3 and 1-2. Misorientation of 5 degree between grains 2-2'.

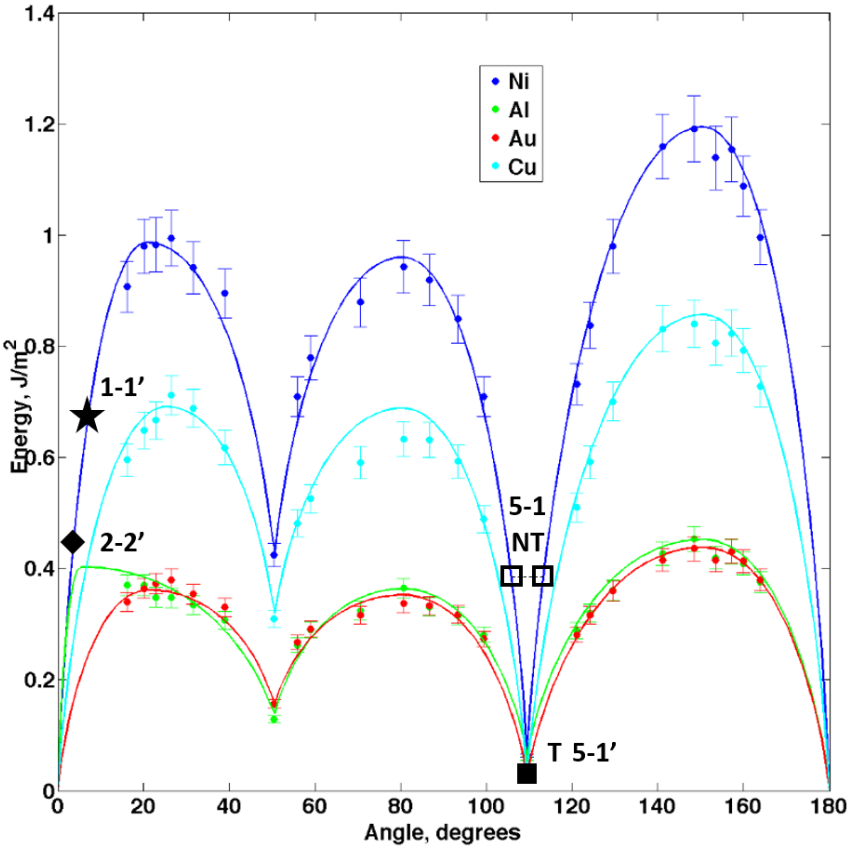

Figure 4.18: Energy grain boundary of [110] symmetric tilt. Minimum energy at the orientation of the coherent twin {111} with an angle of 109.5 deg. Grain boundary energies between pairs of grains depending on their misorientation angle from Figures 4.16 and 4.17 are indicated by: a dark square for the grains 5-1', empty square for near twin (NT) 5-1, a star for the grains 1-1' and a rhombus for grains 2-2'. Taken and modified from [115].

Another example is presented in Figure 4.19a-b where isolated twinned fcc grains are surrounding a TiC particle. From the pole figure in Figure 4.19b, it can be seen that the grains 1-2 have a twin OR. What is interesting is that two more grains seem to have nucleated from grains 1-2, since the grains 2-3 are in twinning OR as well as 1-4 but not between 3-4. It is probable that the grain 3 nucleated and grew on the grain 2 and on the other side the grain 4 on grain 1. All these grains are sharing a common ⟨110⟩ direction (circled in red) but does not have any OR with the TiC particle. The grains 1-2 seem to have nucleated on the surface of the TiC particle. This observation also shows the possibility of nucleation by twinning mechanism, since the grains 3 and 4 have respectively nucleated on the surface of the growing grains 2 and 1. Such observation is supported by the 3D representation of these grains in Figure 4.20, where it can be seen that the grains 3 and 4 are not connected. This could be a similar mechanism to the previously observed sub-grains divided for twin OR with their respective neighbours (Figure 4.17). This shows as well the ability of the fcc system to nucleate by twinning mechanism by growing on existing neighbour grains. The capability of the fcc Ni system to reproduce multi-twin OR during nucleation and growth widens the mechanisms involved in the equiaxed grain formation. It is unclear if this mechanism is linked to ISRO mediated nucleation, but it shows that the fcc Ni system is sensitive to nucleation by twinning mechanism and it can have a major impact in the first steps of nucleation and growth.

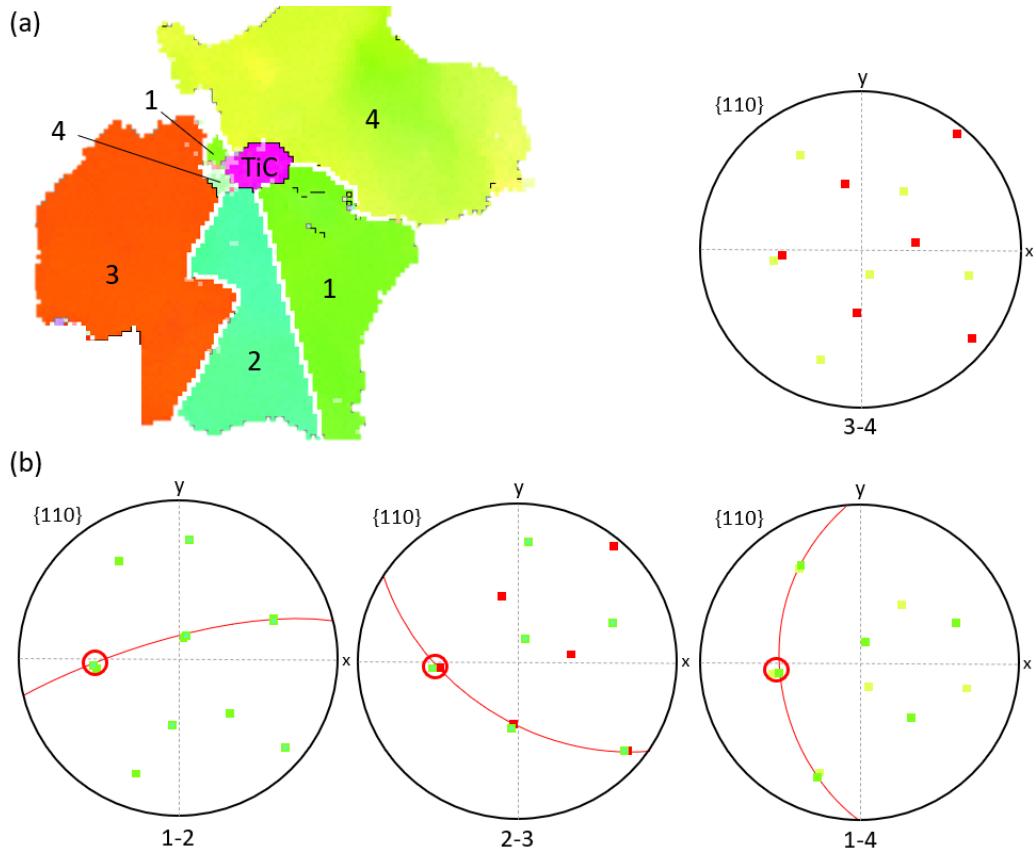

Figure 4.19: (a) Isolated grains 1-2-3-4 around a TiC, with their respective pole figure (b) ⟨110⟩ showing the twinning OR between pairs of grains 1-2, 2-3 and 1-4. The grains 3-4 shares no twin grain boundary and no OR was found with the TiC particle. Twin grain boundaries are indicated in white.

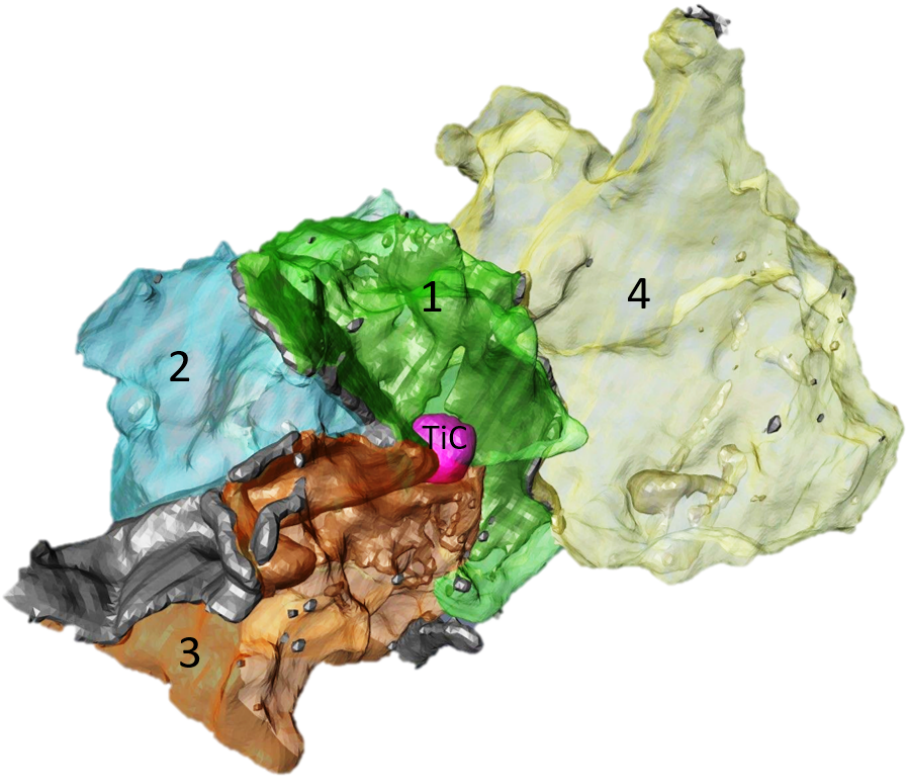

Figure 4.20: Isolated grains 1-2-3-4 from Figure 4.19, with the TiC at the center, in 3D representation. The grains are in their respective IPF colour and the twin grain boundaries are in dark grey. No other grains in the volume were found to share OR with the grains 1-2-3-4.

4.4 Conclusion

To conclude, the characterization of the microstructures showed that the equiaxed grain zones were not present repetitively in the single track walls, on the contrary to multi-track samples where equiaxed grain regions were periodically observed. The presence of equiaxed grain has an impact on the texture, since a new grain selection operates in the columnar dendrites after crossing each equiaxed region, which reduces the preferred grain growth [001] direction. The grain refinement induces drastic change of grain size and increase of twin grain boundary density and are positioned at the bottom of molten bath at each built layer.

Based on detailed EBSD analysis, it has been shown that the equiaxed grains forms from an ISRO-mediated nucleation mechanism, previously observed in Al-based and Au-based fcc alloys only. The icosahedral symmetry is respected between multi-twinned fcc grains and is compared to calculated stereographic projection of all 5-fold symmetry axes in a specific region. The 3D EBSD combined with 3D EDS mapping revealed presence of high twinning OR around TiC particles. A 5-fold symmetry axis was identified between fcc grains and was observed to emerge from a TiC particle. The relationship between this symmetry axis and the TiC is unclear due to the cubic fcc structure of the TiC, but it shows that potential phase (or iQC) formation in-between the TiC and the fcc grains could act as nucleation site.

Secondary electronic imaging using InLens detector revealed presence of various phases surrounding and growing on the TiC particles surface in the equiaxed grain regions. It is worth mentioning that fine precipitates were also reported in the Laves phase C14 and in the matrix. It is expected that ISRO mediated nucleation could originate from the fast remelting of the previous layer, providing metastable configurations in the liquid favorable to the nucleation of the fcc phase, and the presence of TiC in chemical enriched zones could play a role. The twin orientation relationships found in the 3D volume of equiaxed grains suggests that the fcc system is capable of nucleating and growing by twinning mechanism in order to reduce interfacial energy. Further characterization using TEM is needed to understand which phase is present and what is their relationship with ISRO mediated nucleation and what causes this mechanism.

Chapter 5

Origin of Icosahedral Short Range Order mediated nucleation: TEM investigation

In this chapter, the role of TiC particles is investigated for Inconel 718 processed by LMD-W. The microstructure around TiC particles is characterized using TEM in both columnar and equiaxed grain zones. Several hypotheses are given and discussed on the origin of the ISRO mediated nucleation mechanism.

5.1 Characterization of TiC particles environment

The microstructure characterized in this chapter is taken from as-built condition from a multi-track wall. Laser power of 2000 W, scanning speed of 1.2 m/min and wire feeding rate of 2 m/min were used for building the samples. The characterization is focused on the TiC particles present in both columnar and equiaxed grain regions.

5.1.1 Columnar grain zone

Figure 5.1 shows an EDS map of a thin foil where a TiC particle is surrounded by the matrix in the columnar dendritic zone. Smaller particles enriched in Ni-Fe-Cr-Al are present at the center of the TiC, while Nb is also present within the TiC. As columnar zones are mainly located in the top region of the layer, corresponding to the hottest part of the melt pool, this observation shows that the TiC possibly experienced melting. The presence of Nb and C at the surface of the TiC suggests presence of NbC carbides but some Nb-enriched particles shows no carbon enrichment.

A zoom on the outer surface of the TiC is shown in Figure 5.2, where a layer enriched in Nb and C is covering the surface of the TiC that could be the NbC carbide which is isostructural with TiC. The chemical analysis using EDS of each phase is presented in table 5.1. Interestingly, small Al rich particles with a size of 50 nm are also present on the surface of the TiC, as if they were nucleating before the NbC layer. The Al and Ti content from table 5.1 suggest this small precipitate is the Ti_3Al phase. Another observation can be made on the presence of a different layer present on the supposed NbC. Such phase is enriched in Ni-Cr-Fe-Nb but seem depleted in Carbon. Same phase seem also present with a elongated plate like shape in the matrix, as indicated by an arrow on the Nb map.

The interface between the TiC and NbC is presented in the TEM image in Figure 5.3 with the diffraction pattern of the zone axis [110] of both phases. The epitaxy relationship can be seen in the diffraction pattern with the shared directions, however a slight space between diffracted spot is visible. This is due to the different lattice parameter between TiC and NbC, that is measured as $a = 0.43$ nm and $a = 0.44$ nm, respectively.

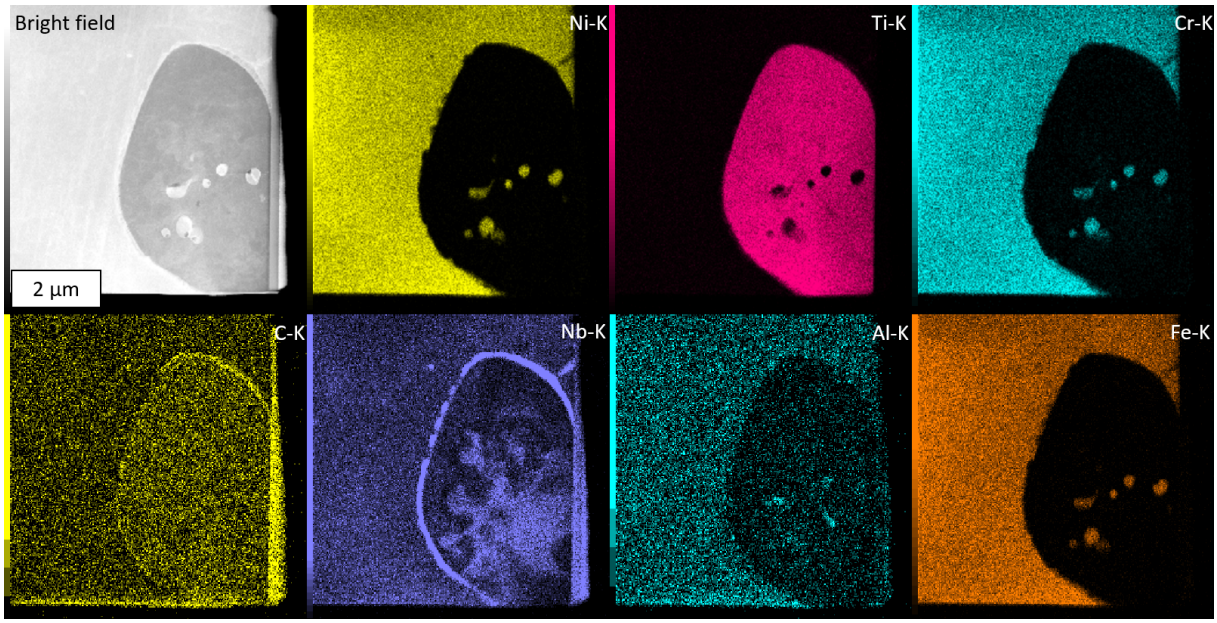

Figure 5.1: TEM bright field micrograph and EDS maps of a TiC particle in the columnar dendritic zone. Note: Enriched in C vertical zone at the right of the image correspond to the Platinum coating.

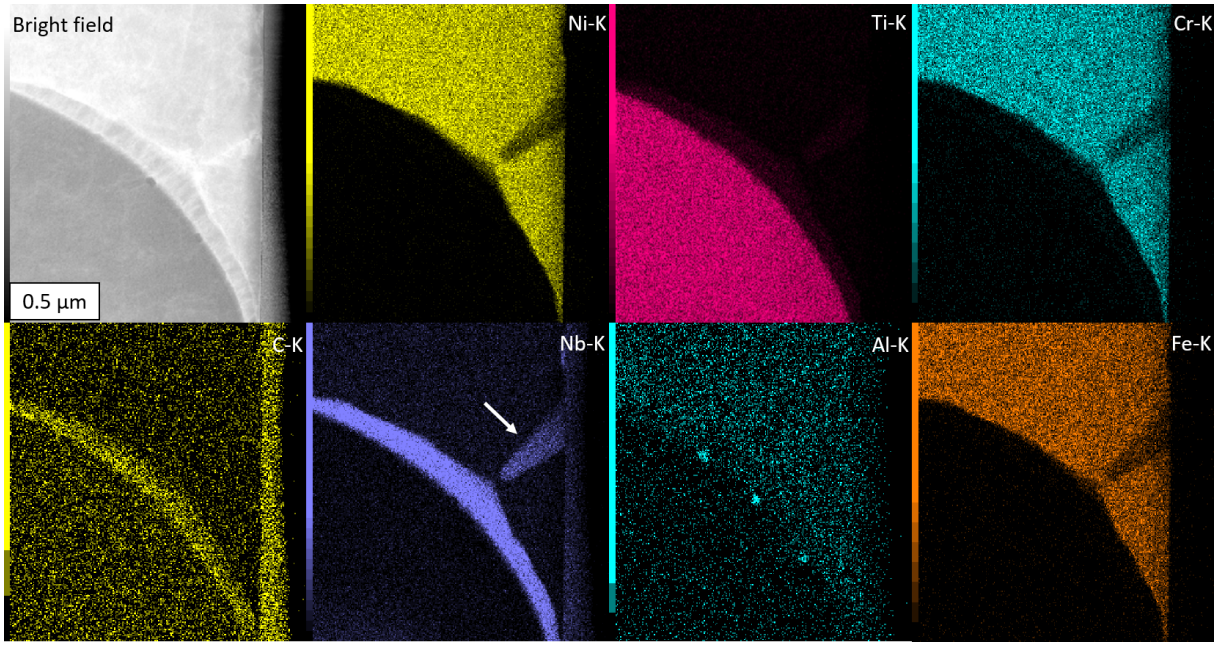

Figure 5.2: TEM bright field micrograph and EDS maps of the zoomed area from Figure 5.1 at the surface of the TiC particle in the columnar dendritic zone. Enriched zone in Nb and depleted of C is indicated by an arrow.

Figure 5.4a-b shows a TEM micrograph of a phase enriched in Nb but not containing carbon, that seem to nucleate and grow on the NbC. The diffraction pattern of this Nb rich phase is presented in Fig.

5.4c with the same orientation and zone axis as the NbC and TiC, indicating an epitaxial relationship. This can be verified with the fast-fourier-transform (FFT) (from the HRTM) of the different phases in Figure 5.4d, that shows the common diffracted spots (circled). The matrix surrounding is enriched in Al and Ti while slightly depleted in Nb content. Also, the Nb-rich phase has a lower content in Nb than the NbC. But it is possible that this metastable fcc NiNb structure is inherited from the lattice structure of the NbC. The different phase identified seem to indicate chemically heterogeneous zones in the liquid promoting new phase nucleation and growth.

Table 5.1: EDS identification of the different phases (at.%). C is not identified.

	Al	Ti	Cr	Fe	Ni	Nb
Matrix FCC	1.73	2.09	21.38	18.09	53.18	3.52
TiC	0.22	93.41	0.33	0.08	0.15	5.81
NbC	0.21	12.01	1.32	0.82	1.31	84.33
Nb-rich phase	0.83	6.3	11.61	9.36	28.49	43.41
Ti_3Al	20.18	69.75	0.67	0.07	0.13	9.2

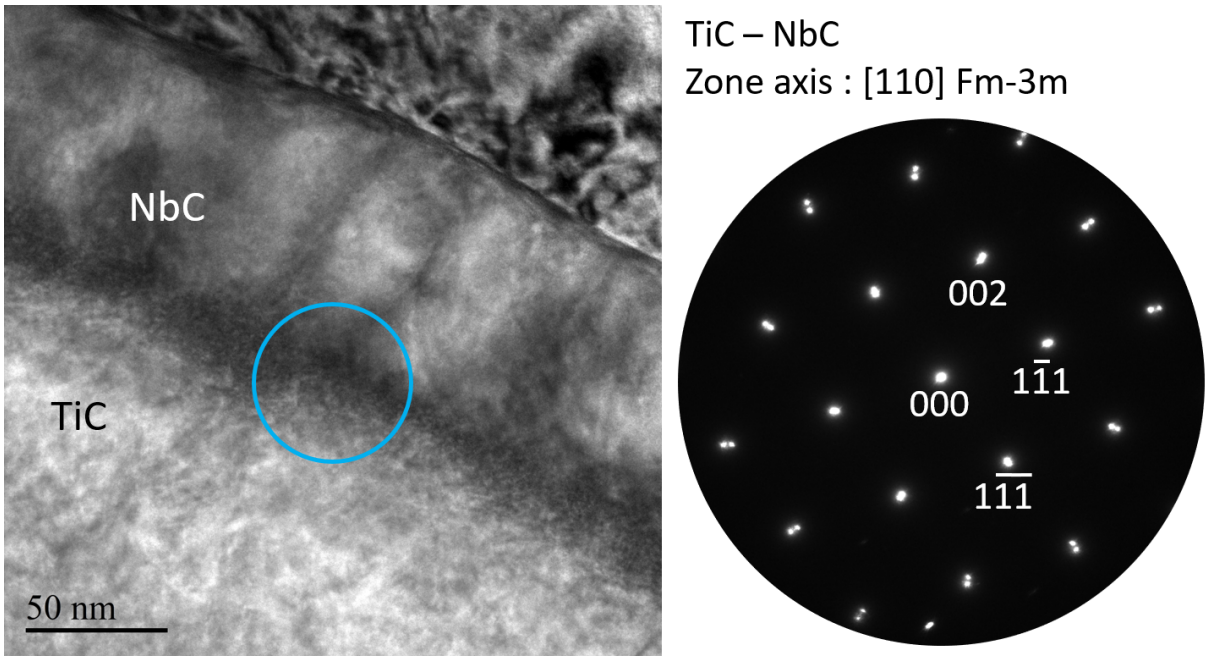

Figure 5.3: TEM image of the TiC and NbC interface with corresponding diffraction pattern of the zone axis [110] of both phases, where the epitaxy relationship can be seen.

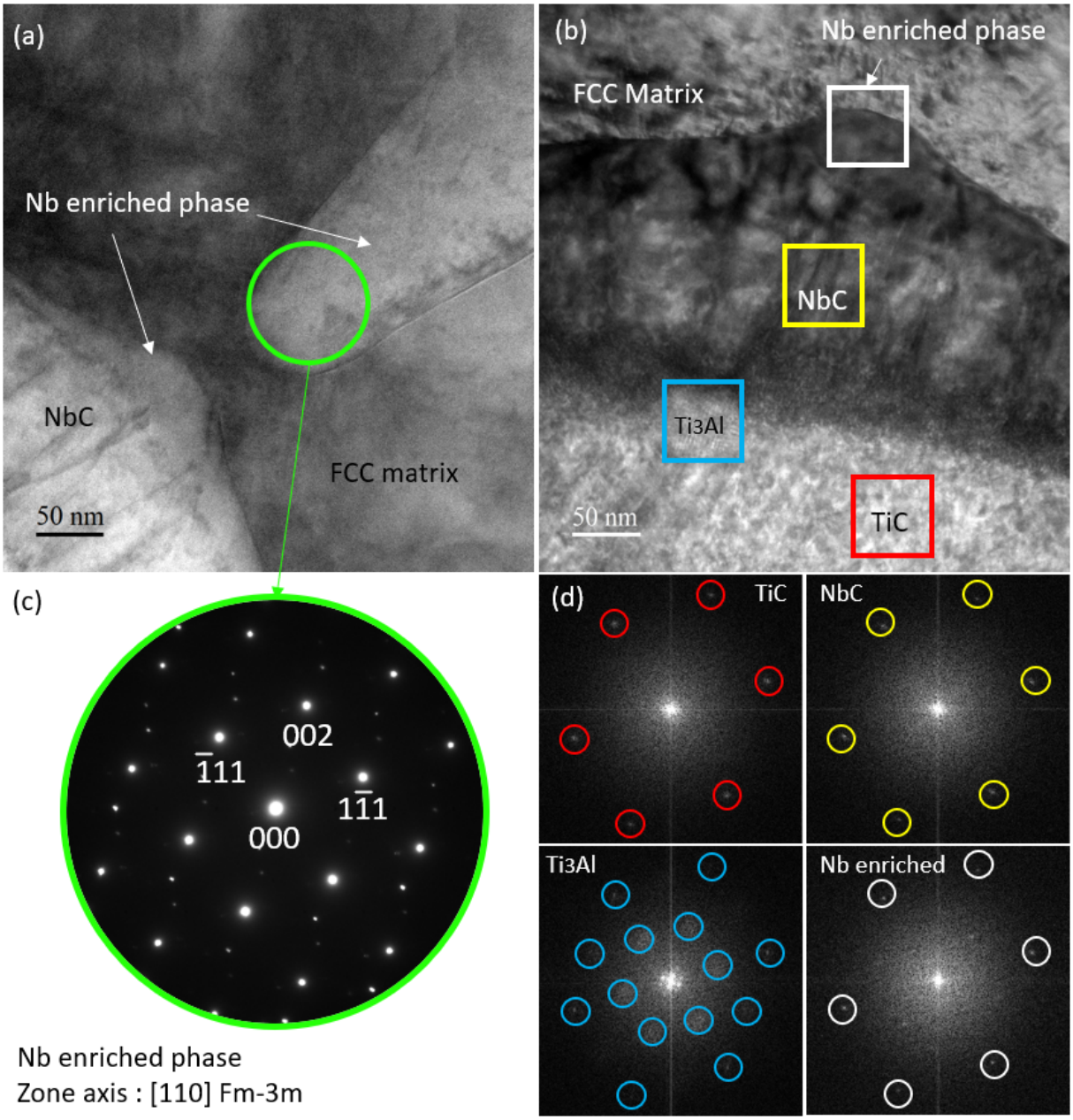

Figure 5.4: TEM micrograph of (a) the NbC with a layer of the Nb enriched phase with also a particle in the matrix (b-d) epitaxy relationship between the encountered phases growing on the TiC surface, FFT image along the axis zone [110] for each phase (c) diffraction pattern of the enriched Nb phase showing the cubic structure with an axis zone [110].

5.1.2 Equiaxed grain zone

Similarly to the columnar zone, a thin foil was sampled from a TiC in the equiaxed zone. Besides carbides, the C14 Laves phase can be found within the matrix surrounding the TiC in equiaxed region, as shown in the TEM micrograph in Fig. 5.5 with lighter contrast. The chemical identification analysis of the EDS spots from A to D (table 5.2) indicates the small grain in B is the same chemical composition as the matrix while the spots C and D indicates a chemical composition closely that of C14 Laves phase. Variations in chemical values can be due to the overlapping of the different phases in the thin foil thickness.

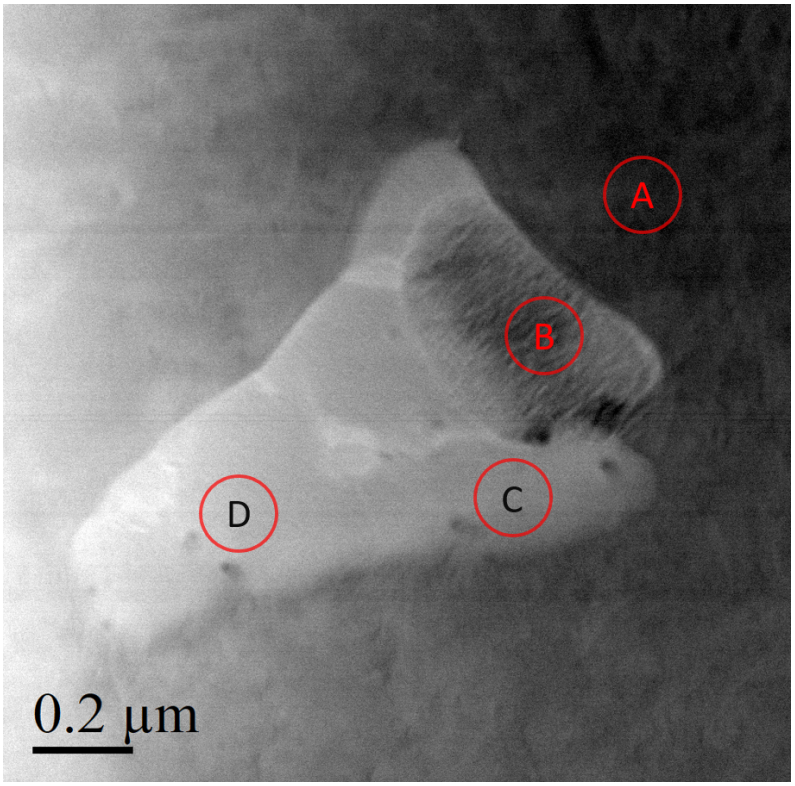

Figure 5.5: TEM micrograph of a Laves phase C14 within the matrix. EDS chemical analysis spots are indicated from A to D and the identification results are listed in table 5.2.

Table 5.2: EDS identification of the spots from Fig. 5.5 (at.%).

	Ti	Cr	Fe	Ni	Nb
A	2.24	21.62	17.57	53.70	4.87
B	2.38	19.48	15.62	50.49	12.03
C	2.6	17.96	14.11	44.52	20.81
D	2.36	17.85	12.19	53.94	15.93

Figure 5.6 shows the diffraction patterns of the different phases presented earlier in Figure 5.5 for zones A, B and D. In zone A, the zone axis is [110] and the lattice parameter was measured as $a = 0.35$ nm. The cubic structure is also visible in zone B, with a [100] zone axis and same lattice parameter as in A, which indicates the grain in B is also an fcc grain. Finally, the zone D shows a [0001] zone axis of the C14 structure with a measured lattice parameter of $a = 0.47$ nm. Such observation of an isolated fcc grain in the matrix and stuck to the Laves phase could be due to nucleation and growth of fcc on C14 (HCP structure), along one orientation relationship between both phases such as for example $(0001)_{HCP}//(001)_{FCC}$ and $\langle 11\bar{2}0\rangle_{HCP}//\langle 110\rangle_{FCC}$, during the eutectic reaction Liquid → fcc + C14 at the end of solidification. Smaller precipitates seem to be present within the Laves phase but their presence did not add diffracted spots in the diffraction patterns.

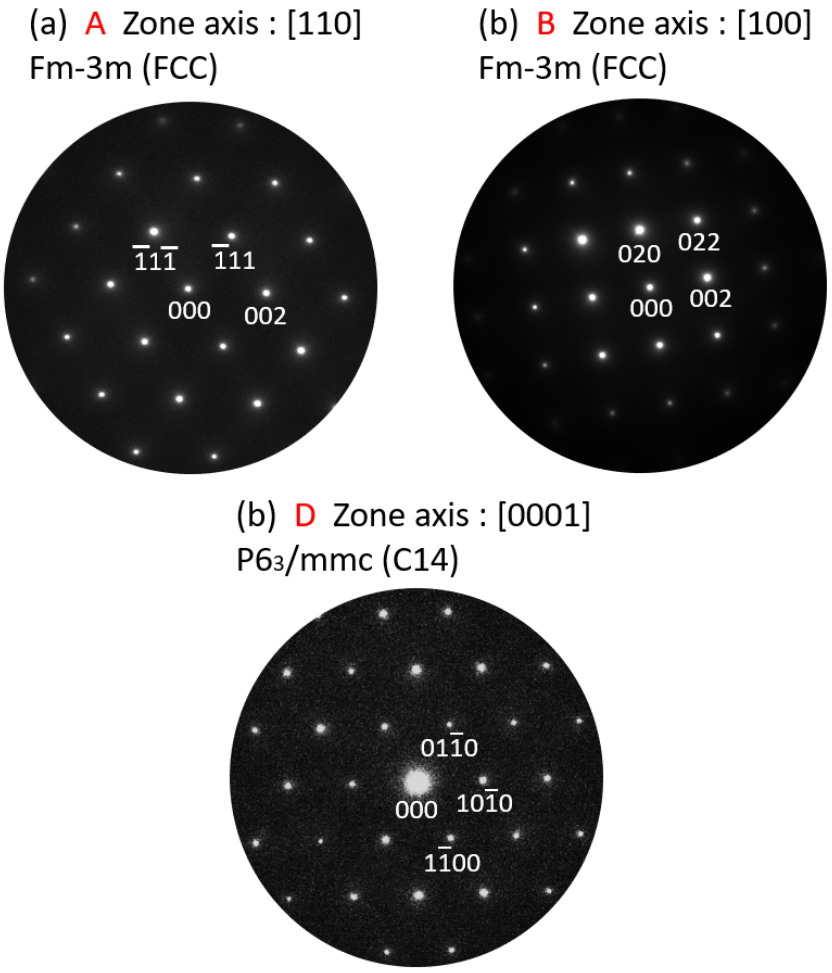

Figure 5.6: Diffraction pattern of different zones from Figure 5.5 of (a) fcc matrix in zone A along [110] zone axis (b) fcc grain in zone B along [100] zone axis (c) Laves phase C14 in zone D along [0001] zone axis.

Figure 5.7 present an EDS map of the environment of a TiC particle in the equiaxed region, with what seems to be a MgAl oxide at the center. Enriched zones in Nb and C suggest also presence of NbC at the surface of the TiC but also an isolated NbC grain (right lower side of the map) in the matrix. However, less C is present at the TiC outer surface while Nb and Mg is identified. It is worth noticing that a

Nb enriched zone in the matrix is visible within a grain in the matrix (right of the EDS map), where it is depleted in other elements. The Nb content in this zone achieves in average 32 %. The irregular shape of the TiC in the equiaxed region is much different from TiC in the columnar zone shown previoulsy, where no Mg nor Mg-rich oxyde was identified.

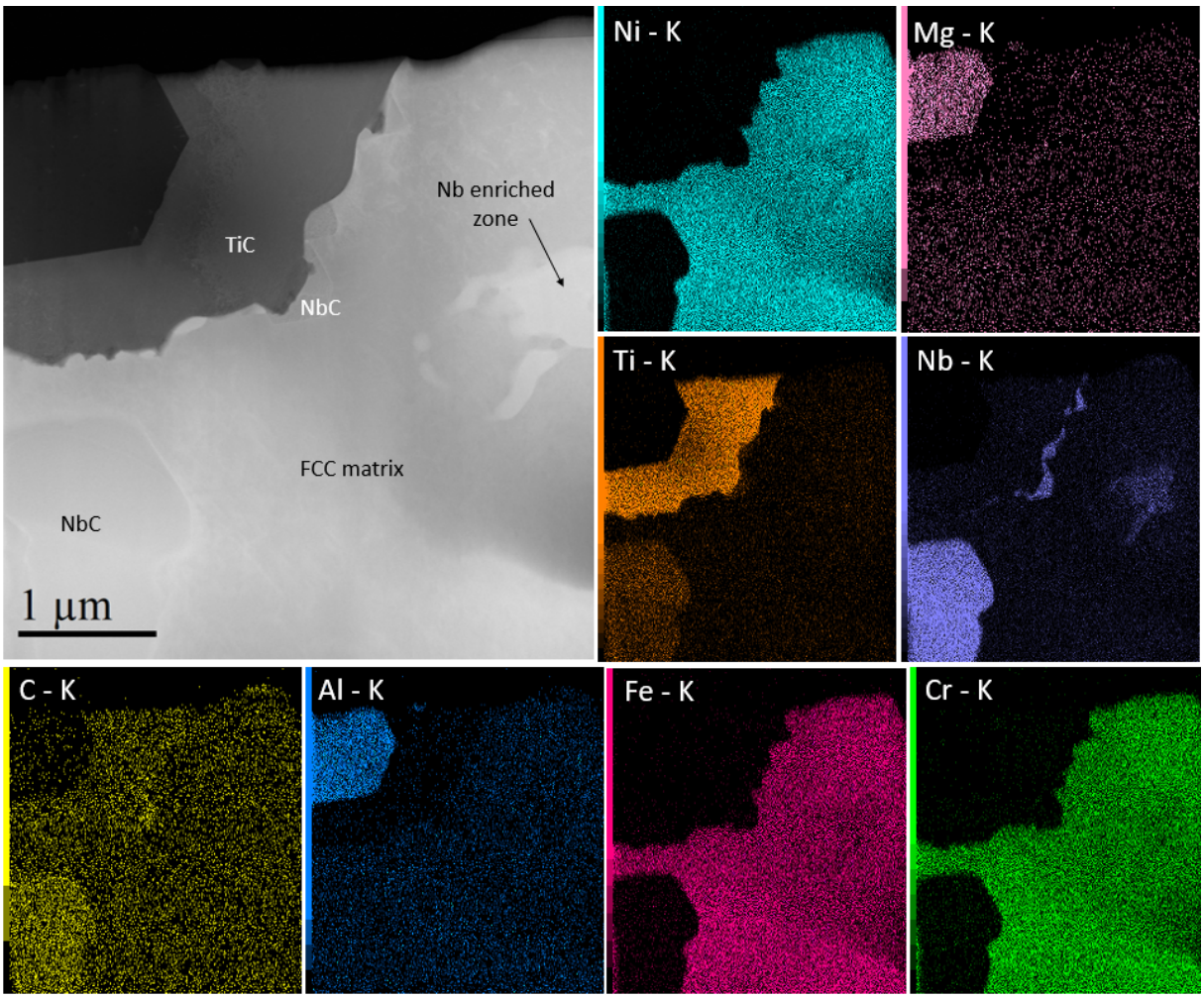

Figure 5.7: STEM micrograph of a TiC taken from the equiaxed grain zone with an EDS map of element distribution. Nb map indicates enriched Nb zone in the matrix as well as at the surface of the TiC.

Figure 5.8 shows a STEM micrograph of an oxide at the center of a TiC particle, taken from the equiaxed grain zone. Interestingly, the identified Al_2MgO_4 oxide and the TiC shares common diffracted directions. It seem the TiC particle has grew epitaxially along [-11-1], [-111] and [002] directions that are parallel to those from the oxide. As can be seen in Figure 5.8, various contrasts are visible at the outer surface of the TiC, at the interface with the matrix, indicating structural and/or chemical modifications. At this interface, the areas enriched in Nb and Mg are also depleted in C.

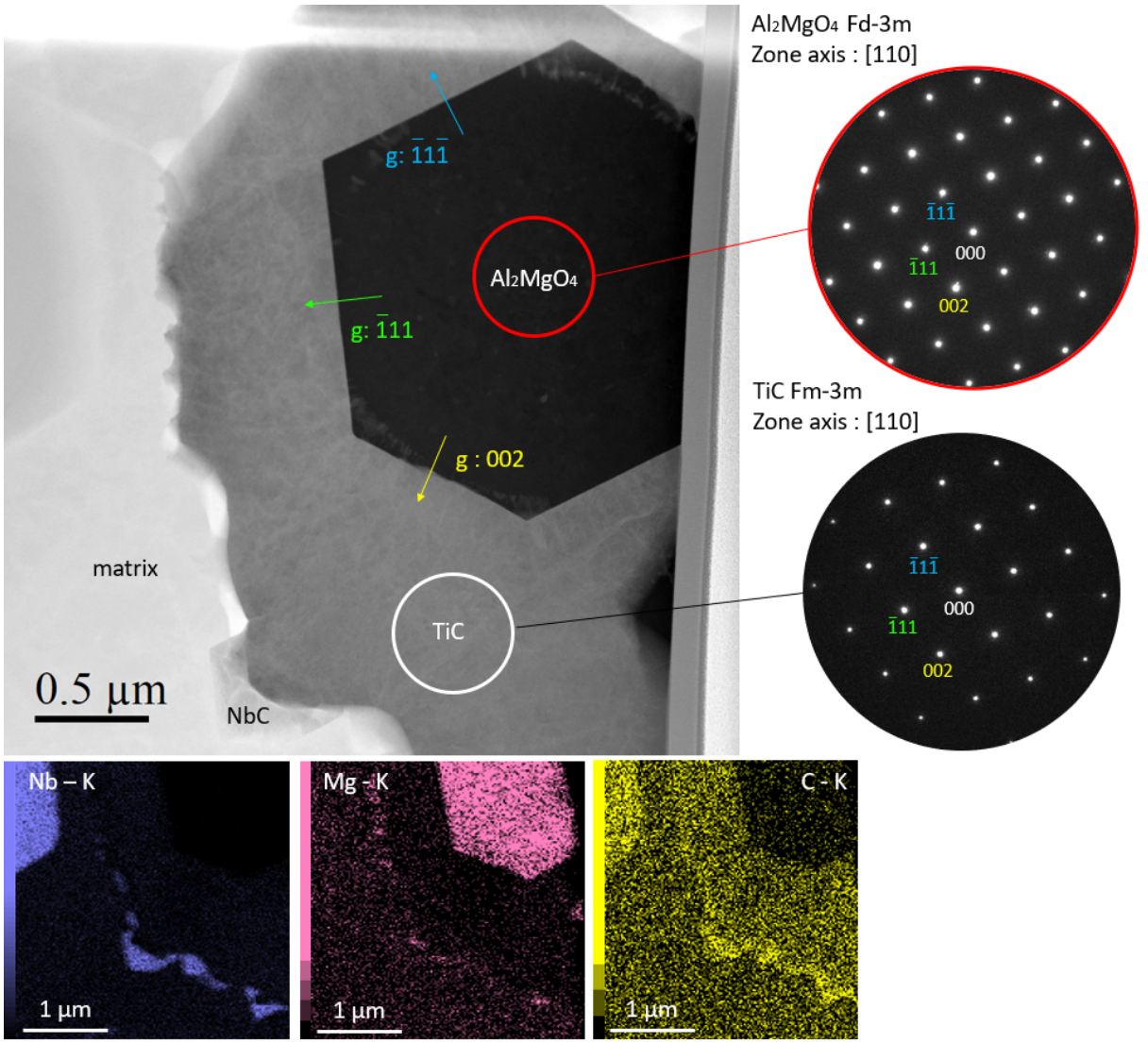

Figure 5.8: STEM HAADF micrograph of Al_2MgO_4 and TiC epitaxy growth relationship. NbC is growing on the TiC surface. EDS map of Nb-Mg-C indicating the enriched Mg surface of the TiC as well as Nb without C on the left of the TiC surface.

5.1.3 Discussion

Large differences are observed between the TiC particles in columnar and equiaxed regions. In the columnar regions, TiC are close to ellipses with smooth surfaces and they are covered with layers of NbC. A metastable fcc phase with Ni and Nb was also identified surrounding in epitaxy the NbC layer. On the contrary, in the equiaxed regions, TiC are irregular, with only few NbC at their surfaces. The surrounding fcc matrix is rich in Nb, with small particles rich in Mg. In both regions, the observations indicate that the liquid around TiC was enriched in Nb. However, the difference of phases at the surface of the TiC particles suggests that they have undegone different temperature histories with different trajectories in the melting pool.

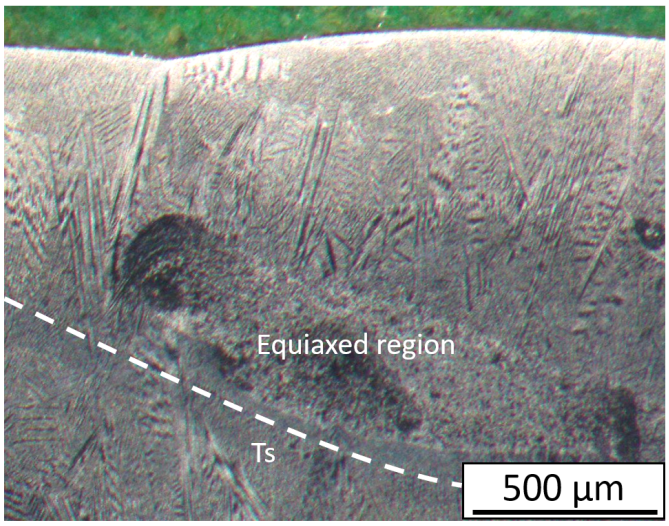

Figure 5.9: OM cross-section of the last built layer with an equiaxed region.

As shown in Fig. 5.9, the equiaxed regions are systematically close to the bottom of the layers. Hence, the TiC particles in these regions have nucleated and grown early and at low temperatures (i.e. closer to T_s than to T_{max}). The formation of layers of NbC would be promoted by the relatively low temperature and smooth temperature history. The Mg particles surrounding TiC would come from the remelting of the previous layer and adjacent bead as well as the oxides. On the contrary, the TiC particles in the columnar regions may have travelled in the melting pool, conveyed by the significant convection observed at the liquide surface in §3.2.1. Their temperature history would be more complex, involving successive precipitation and melting, therefore less metastable phases observed.

5.2 Evidence of concentrated ISRO around TiC particles

5.2.1 Nucleation burst of metastable phases

Nano-sized precipitates are regularly observed in equiaxed regions as shown in Figure 5.10 in-between an eutectic region and a TiC particle. Interestingly, the precipitates are located in both the eutectic formed between Laves phase C14 and the fcc near carbides, as it was observed in SEM in the previous chapter. No diffraction pattern could be obtained due to their size and chemical analysis did not give variation of chemical composition, nor could be seen in EDS mapping. A notable enriched zone was noticed in the matrix close to the NbC surrounding the TiC particle as indicated in Figure 5.10. Such zones in the matrix have a Nb content varying from 12 to 33 %, and curiously the diffraction pattern of the zone labelled (1) in Figure 5.10 shows a diffracted ring within the matrix spots. Such ring could indicate presence of slightly amorphous structure. Amorphous structure could be due to the Ion polishing of the surface, but such diffracted ring was not observed in other regions of the microstructure which shows possible amorphization induced by Nb enrichment. No carbon is present in these Nb enriched regions and nothing but the matrix is visible in diffraction patterns. This shows that the matrix could locally be highly enriched in Nb around the TiC particles.

A zoomed EDS map in the equiaxed zone on the interface between the TiC and the matrix is shown in Figure 5.11a where Mg segregation is present within the NbC and a precipitate is enriched in Nb at the TiC surface. The measured Nb content is about 20 at.% which is similar to the C14 Laves phase Nb

content. This isolated precipitate is shown in the TEM image in Figure 5.11b and is identified as Nb_2Ni, which structure belongs to the Laves phase family (C15 type) [117], with $a = 1.183$ nm measured from the diffraction pattern with a [112] zone axis in Fig. 5.11c. This phase was recently discovered by Zhao *et al.* [3] in Nb-Ni binary alloy, with a similar measured lattice parameter of $a = 1.188$ nm. It is unexpected that this phase is present in Inconel 718, moreover without addition of Nb and also in additive manufacturing conditions. This means that the enrichment in Nb allows metastable phase formation such as Nb_2Ni in the liquid. However, it is unclear why the measured Nb content is that low (20 % at.) for the phase Nb_2Ni. Such low content could be due to the overlapping with the matrix in the volume of the thin foil during the chemical measurement. An other reason is that the phase might be enriched in Mo, which could not be measured due to overlapping peaks in the EDS spectrum. The Mo follows the same segregation tendency as Nb and participates in the Laves phase C14 formation. The additional Mo in this zone is therefore possible and could promote Nb_2Ni formation when substituting with Nb in the structure as the element substitution is possible in topologically close packed (TCP) phases, detailed in Appendix C with the C14 Laves phase. The Ni is substituted with Cr and Fe, as the EDS map in Figure 5.11(a) shows. Contrary to the binary system Nb-Ni, the Nb_2Ni formation could be favoured by all the other elements in Inconel 718 and stabilize this phase. The precipitate Nb_2Ni does not share orientation relationship with the TiC and the matrix, but its presence on the surface of the TiC shows that such inclusions can act as nucleation sites for many phases in AM conditions.

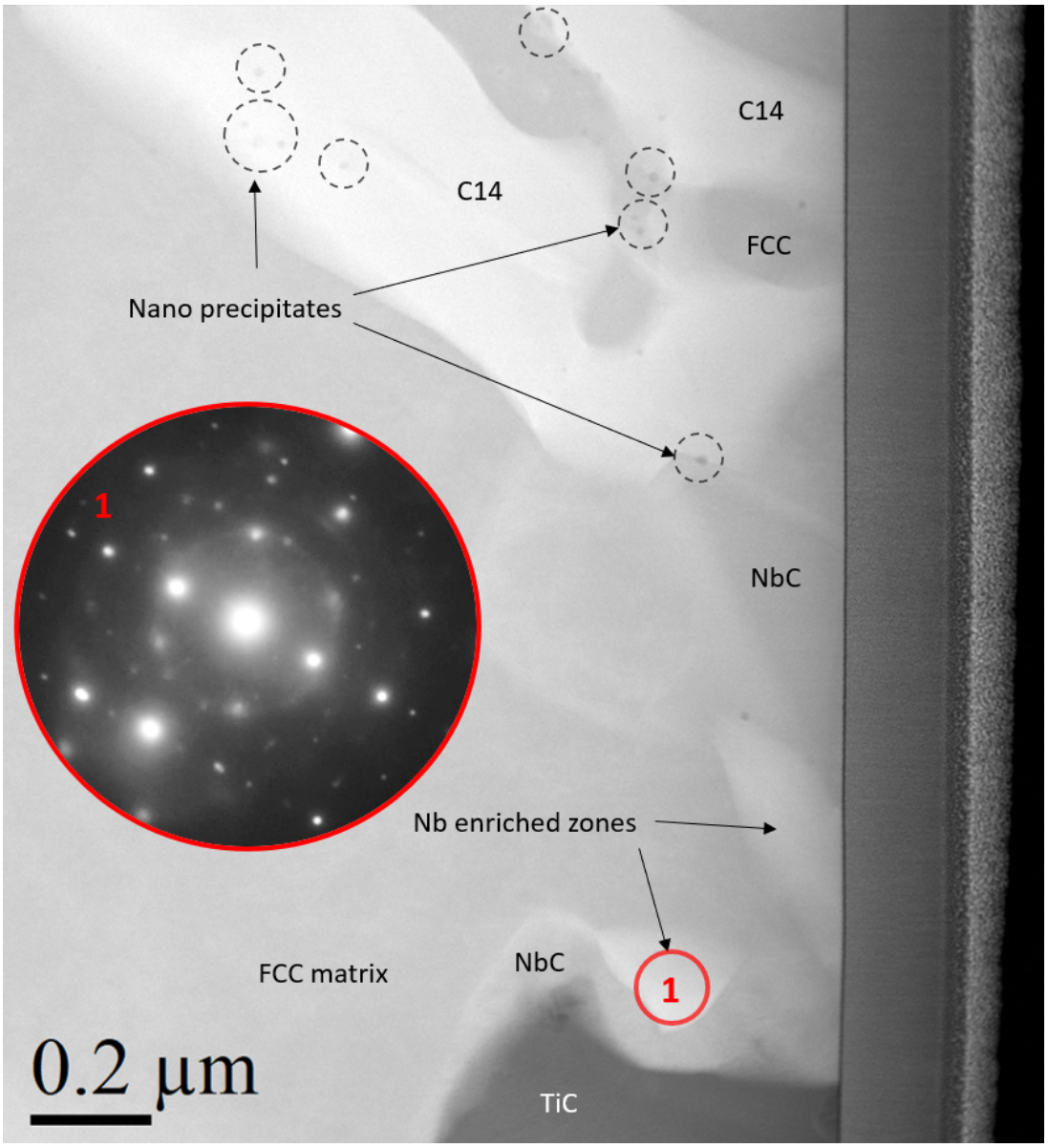

Figure 5.10: STEM micrograph of the region in-between a TiC particle and eutectic fcc-C14 in the equiaxed grain zone. Presence of Nb enriched zones around the NbC surrounding the TiC particle. Nano precipitates are visible in the eutectic region between the matrix fcc and the Laves phase C14. (1) Micro-diffraction pattern of non oriented matrix in the enriched zone indicates presence of slightly amorphous structure.

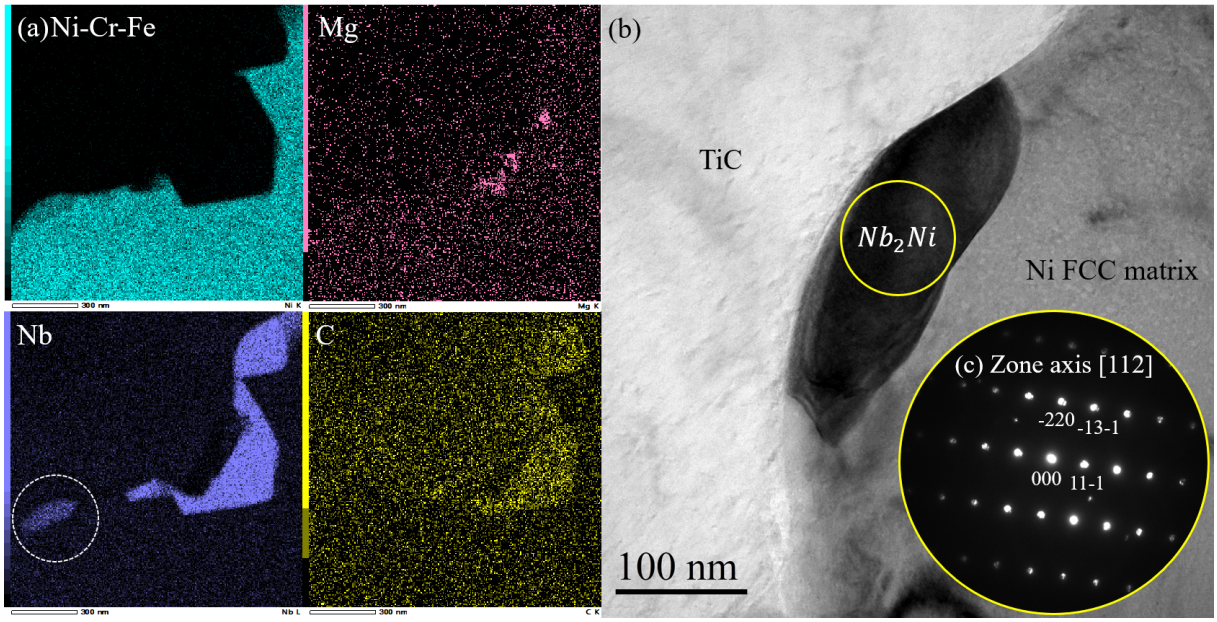

Figure 5.11: (a) EDS map of the interface between the TiC and the fcc matrix in the equiaxed grain zone, with Mg segregation within the NbC phase. A circled precipitate enriched in Nb is analysed in TEM (b) TEM micrograph of the precipitate enriched in Nb identified to be the Laves phase Nb_2Ni (C15) with diffraction pattern (c) along identified zone axis [112].

The Mg enriched area within the NbC from previous Fig. 5.11 is presented in Fig. 5.12. The measured Mg and Ti content is respectively 15.2 and 33.5 % for this precipitate, while the rest is mostly Nb due to the close position of NbC. The local Mg enrichment led to the formation of the $Mg_{0.32}Ti_{0.68}$ phase (Fm-3m), indexed as an MgTi fcc structure sharing an epitaxial relationship with both the TiC and NbC, as shown with the FFT of both NbC and $Mg_{0.32}Ti_{0.68}$ phases. Such phase is not expected to be forming in the alloy, since the content of the alloy in Mg is very low (few hundred ppms). Its formation can be attributed to local enrichment of residual Mg at the surface of the TiC. The absence of carbon in the $Mg_{0.32}Ti_{0.68}$ precipitate shows no overlapping with the NbC. This observation shows the NbC nucleated and grew on the $Mg_{0.32}Ti_{0.68}$ phase in the liquid. The formation of $Mg_{0.32}Ti_{0.68}$ is therefore either induced by the presence of the Al_2MgO_4 oxide at the center of the TiC or residual Mg in the alloy. Nevertheless, the unexpected phase $Mg_{0.32}Ti_{0.68}$ shows that highly unfavourable and metastable phase could form from the liquid, and that the TiC particles act a major role in local segregation, since several chemical elements seem to aggregate around these carbides.

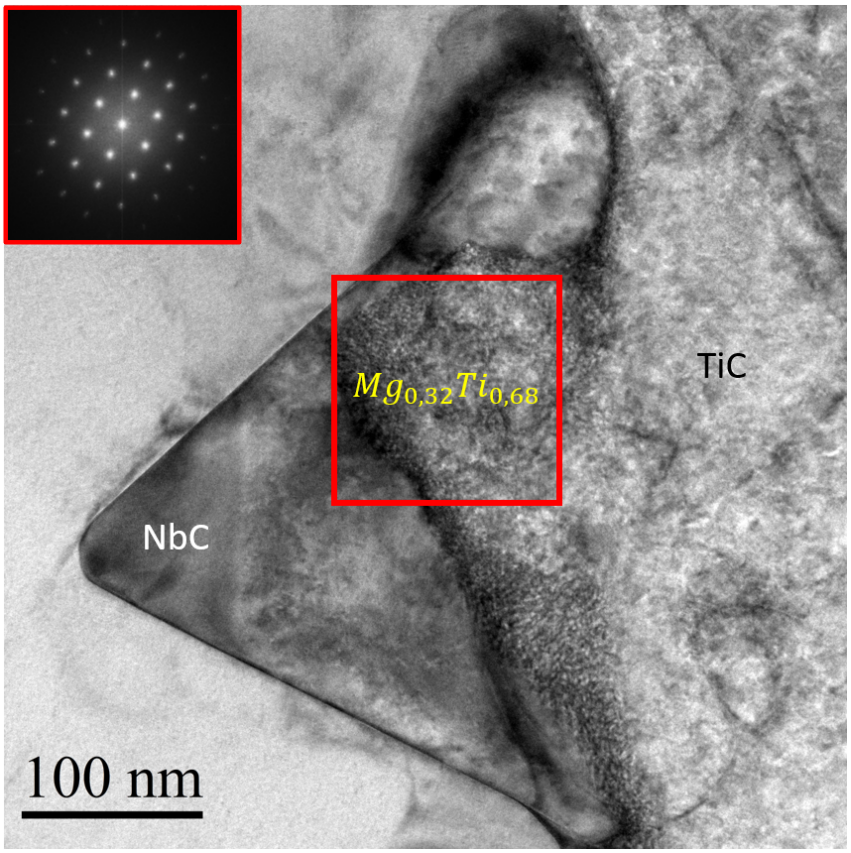

Figure 5.12: Identified $Mg_{0.32}Ti_{0.68}$ precipitate at the interface between NbC and TiC with corresponding FFT.

Figure 5.13a shows a STEM image of the same zone analysed previously in Fig. 5.7 and Fig. 5.11. The matrix, the TiC particle and the Nb enriched zone can be seen in Figure 5.13a with different zones of interests labelled from 1 to 3. The diffraction pattern obtained in zone 1 allowed to identify a NbC, and shown along its [110] zone axis in Figure 5.13b. The High Resolution TEM (HRTEM) image of the zone 2 enriched in Nb is shown in Figure 5.13c, which shows presence of slight amorphous structure in one grain, while the fcc matrix is clearly visible for the FFT matrix oriented along the [100] zone axis. Some spots are shared between the Nb enriched grain and the matrix, that indicates these two grains could have an orientation relationship. The zone 3 shown in Figure 5.13d seems not composed of a single grain as it can be seen on the FFT. The first FFT shows a structure that is curiously similar to a theoretical two-fold symmetry axis of a iQC [118]. The overlap of the FFT image and the two-fold symmetry axis is shown in Figure 5.14. An interesting similarity can be seen in both patterns since some spots shares the same positions and indicates possible presence of iQC in the Nb enriched zone 3. However, due to the size of region (containing few hundreds of atoms), it has not be possible to characterize further the symmetry. The second FFT in Figure 5.13d shows presence of a diffracted ring that indicates slight amorphous structure as well as an undetermined structure. The zone axes could not be identified in both grains.

No iQC was evidenced when diffracting the zones of interests, but the resemblance shown in Figure 5.14 between the FFT and the theoretical 2-fold axis shows the need for further characterization and perhaps identification of new phases for Inconel 718. The unknown structures observed in enriched Nb zone 3 needs to be determined and if the phases in such areas have iQC structure or contain icosahedral polyhedra in their lattice structure.

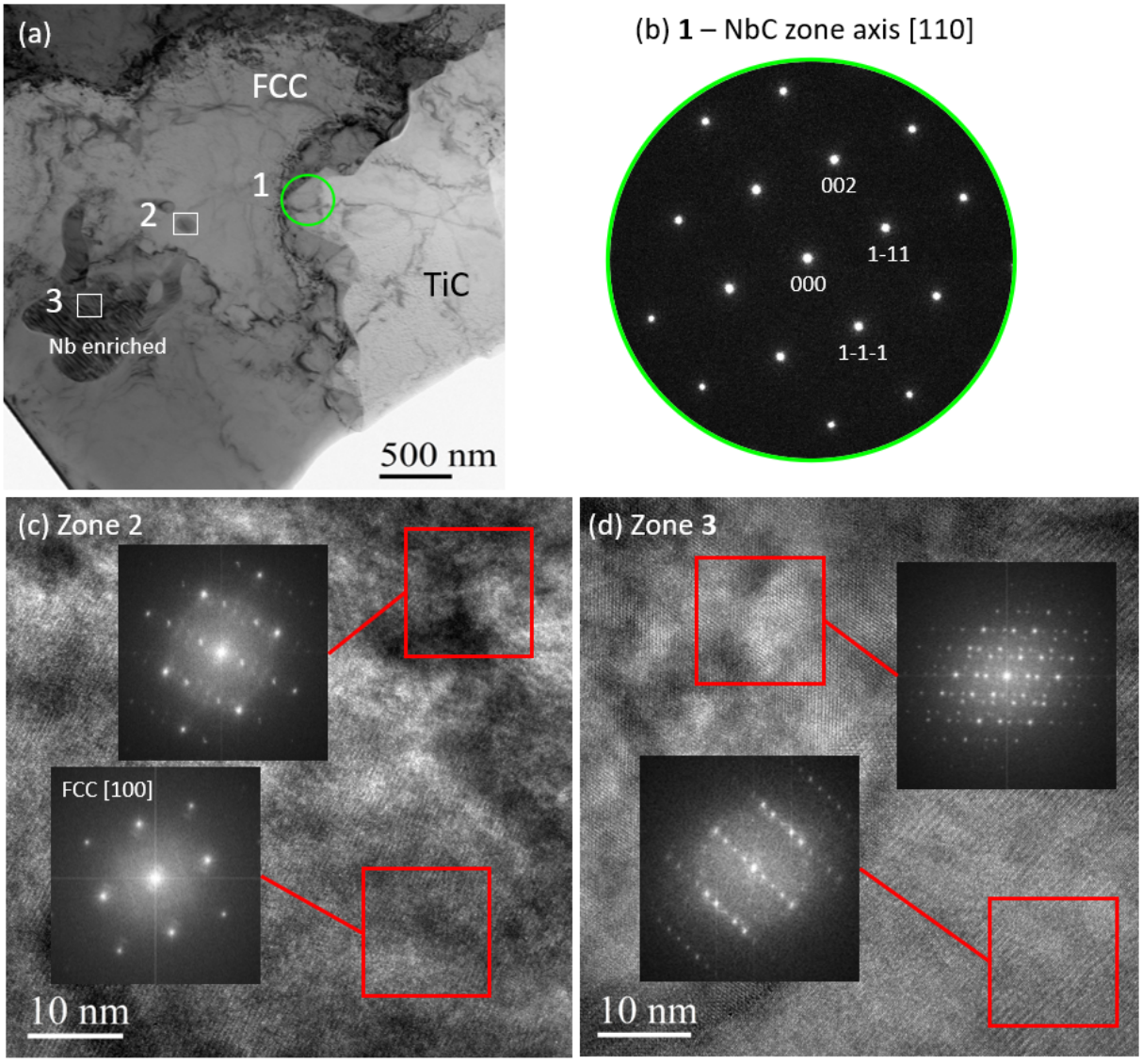

Figure 5.13: (a) STEM micrograph of the TiC particle, the matrix fcc and the Nb enriched zone, with analysed squared zones labelled from 1 to 3. (b) Diffraction pattern of zone axis [110] of the NbC in zone labelled 1. (c) High Resolution (HRTEM) micrograph of the zone 2 with Fast Fourier Transform (FFT) of two different grains with one identified as the matrix fcc (d) HRTEM micrograph and FFT images of two grains with unknown structures in zone 3.

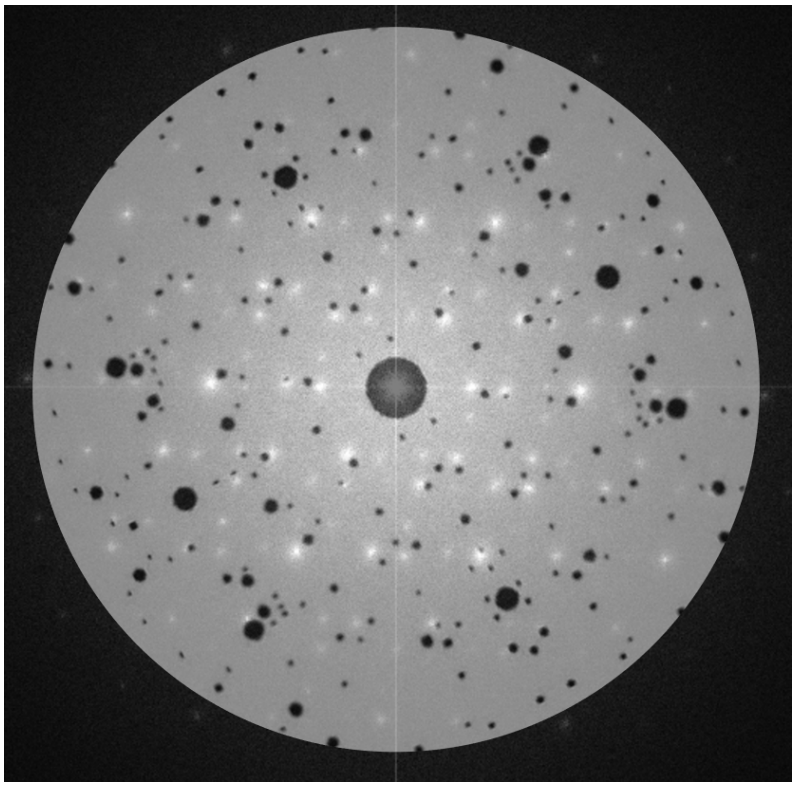

Figure 5.14: Overlap of FFT image from a grain in Nb enriched zone from Figure 5.13(d) and theoretical diffraction pattern of a 2-fold symmetry axis of a iQC with an icosahedral symmetry (dark spots) taken from [118].

In the Nb-Ni system, several intermetallics and TCP phases can be found in the literature such as Laves phase C14 Ni_2Nb, commonly observed. It is worth stressing that icosahedral symmetry has been reported in the crystal structure of Laves phase Ni_2Nb [119]. Phase Nb_2Ni has been found recently [3] to form concomitantly with phases Nb_7Ni_6 and Nb_5Ni: they all feature icosahedral polyhedra in their lattice structures, contrary to Ni_3Nb. An automated crystal orientation mapping (ACOM) can be performed to identify the phases among different possible candidates.

Figure 5.15a-b shows the ACOM correlation index map (equivalent to band contrast image in EBSD) of the Nb enriched zone 3 in Fig. 5.13, together with the corresponding indexed phases. The correlation index map exhibits a large dark zone where indexation was impossible. We have plotted in Fig. 5.15c-g the diffraction patterns of the different expected phases, both experimental and simulated. The fcc matrix is perfectly indexed as shown in Fig. 5.15c, with an excellent reliability parameter $R = 45$. The diffraction patterns corresponding to NbC and TiC, in Fig. 5.15d and g, exhibit rings and non-indexed spots. Still their indexations are very good with $R > 25$. This is not the case for Ni_6Nb_7 with $R = 18$, slightly above the threshold at which indexation can be considered as reliable (Fig. 5.15f). This can be attributed to some overlapping with other phases and/or the contribution of amorphous structures. Finally, we have not been able to index the large precipitate denoted C14*. Although its 30% of Nb and its morphology would suggest that it is C14 Ni_2Nb, R has never reached a sufficient value to identify this precipitate.

Figure 5.15h provides the IPF orientation map of the zone of interest, with the dashed white square corresponding to Fig. 5.15b. The TiC particle and the NbC carbides at its surface are clearly in epitaxy.

The structure in zone 2 in Fig. 5.13, indicated by a white dashed circle in Fig. 5.15b, has not been detected: (i) the phase is unknown in the indexation software, and (ii) it may share common diffraction spots with the matrix, i.e. both features orientation relationships. It should be noted that ACOM failed to index Nb_2Ni, probably due to overlapping problems already mentioned.

We can conclude from these observations and identifications that Nb segregations can promote the nucleation of Nb-rich phases around TiC, different from the usual C14. Moreover, some of these phases such as Ni_6Nb_7 and Nb_2Ni feature high fractions of icosahedron clusters in their lattice structure. We believe that this occurrence is not incidental but is related to ISRO in Inconel 718 built by LMD-W.

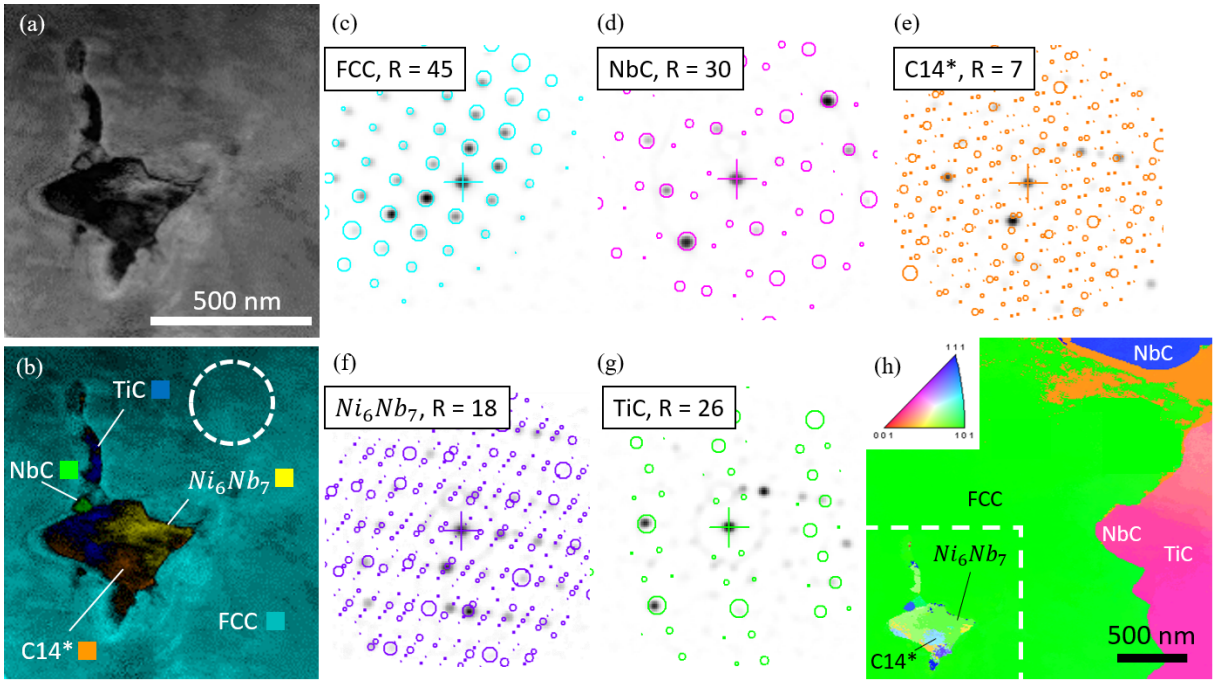

Figure 5.15: (a) ACOM correlation index map; (b) phase + correlation index map; (c-g) experimental and simulated (colored circles) diffraction patterns; (h) IPF map of the region of interest.

From these results, we propose two hypotheses for explaining the ISRO mediated nucleation of equiaxed grains.

- Fcc grains nucleate on some iQC or from ISRO in Nb-rich liquid around TiC particles, with other elements participating in the local ordering.
- Fcc grains nucleate from some phase in Nb-rich liquid, that features icosahedral clusters.

The first hypothesis is that ISRO is promoted by the enrichment of liquid surrounding TiC at the bottom of the molten pool. Enrichment in Nb is known to promote glass formation in binary Ni-Nb alloys [120], with the frequent occurrence of distorted icosahedra in liquid near the melting temperature, as shown by Ab Initio molecular dynamics simulations [121] (Fig. 5.16). It is not known if other elements such as Mg, Al or Mo could play a role in the formation of such icosahedral clusters. In this scenario, ISRO would promote the nucleation of fcc grains but also the nucleation of Ni_6Nb_7 and Nb_2Ni phases, both featuring icosahedral clusters.

The second hypothesis would be supported by orientation relationships between the phases featuring icosahedral clusters, such as Ni_6Nb_7, Nb_2Ni and Ni_2Nb, and fcc grains. In that case, distances between atoms in the icosahedral clusters should be as close as possible to the distance in fcc {111} planes. Indeed, this argument has been successfully used by Kurtuldu *et al.* for explaining ISRO mediated nucleation in Al-Zn-Cr alloys [2].

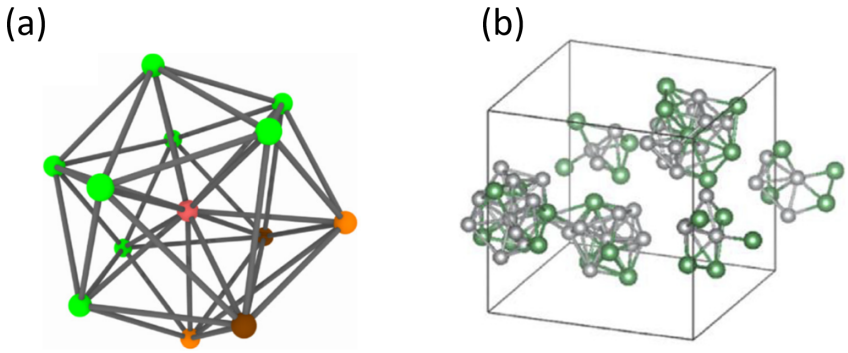

Figure 5.16: (a) Distorted icosahedron in $Ni_{62}Nb_{38}$ glass forming alloy (colours related to the deviations from perfect icosahedron); (b) snapshot of $Ni_{75}Nb_{25}$ liquid with icosahedral clusters [121].

5.2.2 Icosahedral clusters analyse and possible orientation relationship with fcc phase

Several potential candidates such as Ni_6Nb_7, Nb_2Ni and Ni_2Nb acting as nucleation sites for the fcc phase from the Ni-Nb system are provided in Fig. 5.17. The Ni atoms are represented in blue, the Nb atoms in orange and the icosahedra in the different structures are indicated by different colours corresponding to their respective orientation. The phase Ni_6Nb_7 in Fig. 5.17a present 2 types of icosahedra that differs in volume, orientation and directions, labelled A and B. The phase Nb_2Ni present 4 different icosahedra orientations as shown in Fig. 5.17b that are actually the same icosahedron, labelled C. The C14 Laves phase Ni_2Nb possess 2 types of icosahedra, labelled D and E, one type that is connected through edges and the other through center (E). The icosahedra connected through edges have 2 different orientations as shown in Figure 5.17(c). The variety of icosahedral symmetries as well as the high fraction of icosahedra in these structures support so far both hypothesis evoked in the previous section.

In order to give new insights on the possible mechanisms, an evaluation of the lattice mismatch between the icosahedra in these phases and the fcc structure can be done. The outcome could therefore select which of these candidates has a better match for Ni fcc nucleation and promote equiaxed grain growth. The Bramfitt lattice mismatch criterion [122] can be used for comparing the structures with the Ni fcc system. The mismatch can be evaluated when respecting parallel planes $(hkl)_{substrate}//(hkl)_{particle}$ and parallel directions $[uvw]_{substrate}//[uvw]_{particle}$, with θ the angle between directions $[uvw]_s$ and $[uvw]_p$:

$$\delta = 100 \sum_{i=1}^{2} \frac{|d_{[uvw]_p^i} cos(\theta) - d_{[uvw]_s^i}|}{2d_{[uvw]_s^i}} \tag{5.1}$$

Figure 5.18a illustrates an icosahedron with a potential nucleation facet for an fcc tetrahedron along a (111) plane. The highlighted facets are in common for both systems, along a 3-fold symmetry axis of the icosahedron. The angles within the tetrahedron are constantly equal to 60 degree while the angles in the icosahedron of different structures are variable, as the edges a, b and c. Each 5-fold symmetry axis possess 5 facets but the ⟨hkl⟩ index of the family direction of the 5-fold axes can vary. During nucleation and growth, the 5 grains in multi-twinning relationship per 5-fold axis are growing along one of the ⟨hkl⟩ direction that is parallel to ⟨110⟩ in the fcc system. In Figure 5.18b, the atomic mismatch between the facets of the icosahedra and the fcc tetrahedra is shown. The mismatch between the two facets lies in the edges length (interatomic distance) difference and the angular deviation θ.

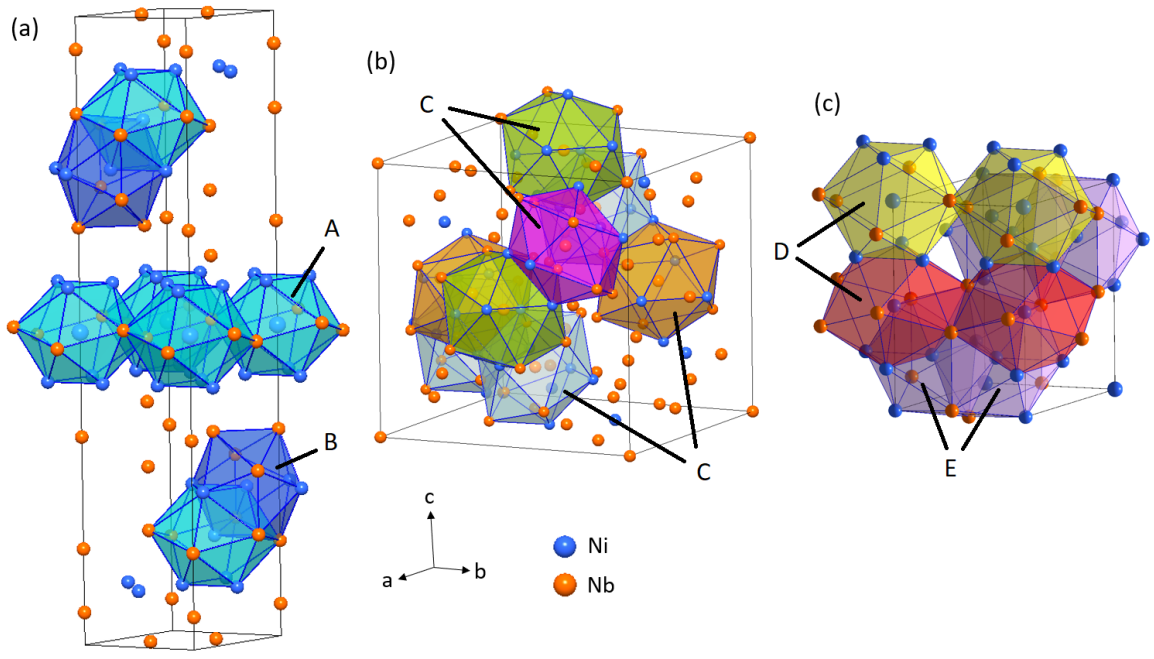

Figure 5.17: Crystal lattice structure of (a) Ni_6Nb_7 (b) Nb_2Ni (c) C14 Ni_2Nb, where Ni atoms are illustrated in blue and Nb atoms in orange. Distorted icosahedra in the structures are identified by type: A and B for Ni_6Nb_7, C for Nb_2Ni, D and E for Ni_2Nb. Distorted icosahedra are represented by colour corresponding to their orientation in the structure.

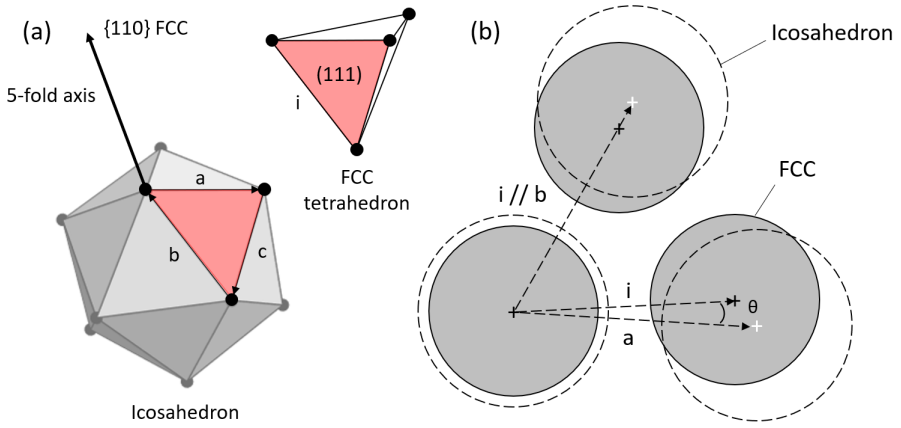

Figure 5.18: (a) Icosahedron with an example of highlighted facet corresponding to a potential nucleation site for the fcc phase, where a regular fcc tetrahedron can share a common plane (111) with constant edge value of $i = 0.2543$ nm for Inconel 718. The regular tetrahedron is composed of $\langle 110 \rangle$ directions and the fcc grains shares a common $\langle 110 \rangle$ direction when growing from the icosahedron. The facets of the fcc tetrahedron have a constant angle of 60 deg. (b) Atomic mismatch between icosahedron and tetrahedron facets along a 3-fold symmetry axis of the icosahedron, where the fcc atoms composing the (111) plane are in grey and the icosahedron atoms are in dashed circles. The edges of the icosahedron facet are variables here a and b while the angular difference between the two facets is characterized by the variable angle θ.

Table 5.3 shows the listed phases Ni_6Nb_7, Nb_2Ni and Ni_2Nb with their respective icosahedron types labelled from A to E from Fig. 5.17. For each icosahedron type, several families of direction corresponding to the 5-fold symmetry axes are listed. The icosahedron C of Nb_2Ni phase is composed of only 2 families of directions for 4 different orientations of icosahedra in the lattice structure. The other icosahedra for Ni_6Nb_7 and Ni_2Nb present much more direction families. The lattice mismatch variation (min and max values) per facets of the icosahedra are therefore calculated for each 5-fold symmetry axis, depending on the measured edges and angles of the various facets of the icosahedra, and the results are presented in table 5.3. Bramfitt demonstrated that the heterogeneous nucleation and growth is effective under 6 % of mismatch, moderately effective for 6 to 12 % and least effective when above 12 %. The Ni_6Nb_7 phase present icosahedra with the lowest mismatch variation for a high number of directions compared to the other phases, that is up to 56.7 % and 89.02 % for Nb_2Ni and Ni_2Nb respectively. The icosahedra in the Ni_6Nb_7 phase have a maximum mismatch of 29.92 % and the icosahedron type A in its structure possess facets with a mismatch of only 0.01 to 24.59 % per 5-fold symmetry axis. This makes Ni_6Nb_7 the most suitable candidate phase for nucleation and growth of the Ni fcc on icosahedral facets. The efficiency of nucleation and growth in the criterion of Bramfitt can be argued in this specific case since the elements are in common, unlike Bramfitt study that is based on the use of various nitrides and carbides as nucleation agents for Iron. The interfacial energy can therefore be considered lower when the same elements are involved. Moreover, the ISRO present in the liquid have lower interfacial energy with the liquid than the fcc phase [123]. It could be possible that such icosahedral clusters in the liquid and with the fcc phase could present a lower nucleation barrier due to the combination of both low lattice mismatch and low interfacial energy. The heteroepitaxy of the fcc grains on icosahedral facets respecting the 5-fold symmetry axis is possible due to the nucleation by twinning mechanism sensitivity of the fcc system in order to reduce interfacial energy. Such hypothesis cannot be proved alone by this demonstration and requires to revisit further aspects.

Table 5.3: Lattice mismatch variation per icosahedron of the different phases with the fcc system.

Phase	Icosahedron type	⟨hkl⟩ of 5-fold symmetry axes	mis.% (min-max) - fcc
Ni_6Nb_7	A	⟨4,0,3⟩	
		⟨4,4,3⟩	0.01 - 24.59
		⟨1,0,9⟩	
		⟨1,1,9⟩	
	B	⟨2,2,9⟩	
		⟨7,7,53⟩	
		⟨3,3,32⟩	
		⟨1,2,0⟩	10.38 - 29.92
		⟨17,17,181⟩	
		⟨1,1,9⟩	
		⟨51,51,539⟩	
Nb_2Ni	C	⟨4,4,23⟩	12.13 - 56.70
		⟨41,61,41⟩	
Ni_2Nb (C14)	D	⟨0,5,13⟩	
		⟨5,5,13⟩	
		⟨95,0,32⟩	3.53 - 89.02
		⟨0,4,1⟩	
		⟨95,95,32⟩	
		⟨181,0,61⟩	
		⟨181,181,61⟩	
	E	⟨1,2,0⟩	
		⟨2,2,4⟩	
		⟨5,5,13⟩	16.55 - 51.69
		⟨0,5,13⟩	
		⟨18,18,61⟩	

5.2.3 Role of TiC in local Nb enrichment

It has been shown previously that the equiaxed grains are located where the previous layer and adjacent bead are remelted, for heating and cooling rates involved up to 10^4 °C/s. It was demonstrated that the segregations of Nb in the areas surrounding the TiC in equiaxed zones provides metastable configurations that form phases such as Nb_2Ni and Ni_6Nb_7. These phases are located near the solidus temperature of the alloy, which indicates that the local conditions are favourable for them to stabilize in the regions surrounding the TiC. This suggest that the lower temperatures in the bottom of the molten pool allows ISRO to exist in an enriched Nb liquid.

To support this assumption, Figure 5.19 shows an isopleth section of Inconel 718 with variable Nb content in the temperatures that are involved near the solidification interface, i.e. between the liquidus and solidus temperatures for the nominal composition range of the alloy (about 5 % mass. Nb). The different curves in Figure 5.19 shows the value below which a thermodynamic driving force exist for the different phases. As expected, the C14 Laves phase Ni_2Nb can form when the Nb content achieve 16 - 21 %, that is naturally observed in the interdendritic regions due to microsegregation. It is worth noting that

the Nb_2Ni phase is able to form when the Nb content achieve 55-60 % below the liquidus temperature, which proves the important Nb enrichment in the periphery of the TiC. The Ni_6Nb_7 phase is stable at lower Nb content, for approximatively about 42 %, also below the liquidus of the alloy. In Fig. 5.19, we also indicate the composition for which presence of amorphous structure is possible, from 37.5 %, as Lu *et al.* [120] demonstrated presence of amorphous structure for $Ni_{62.5}Nb_{37.5}$ among glass forming Ni-Nb alloys. They also highlight presence of ISRO from 1226.5 °C to lower temperatures for high cooling rates involved. ISRO is present in amorphous structures for a wide range of Nb composition and temperatures [121], and it is regularly reported that Icosahedral Medium Range Order (IMRO) is present; and we believe could play a role in mediated nucleation of the fcc phase as well as for the formation of Nb rich phases. ISRO and IMRO could be at the origin of the amorphous regions observed in Nb enriched areas in equiaxed zones obtained by LMD-W. All these arguments provides the evidence that the origin of ISRO mediated nucleation of the Ni fcc phase is caused by local Nb enrichment around the TiC particles, but is triggered by the favourable temperature conditions induced by the process.

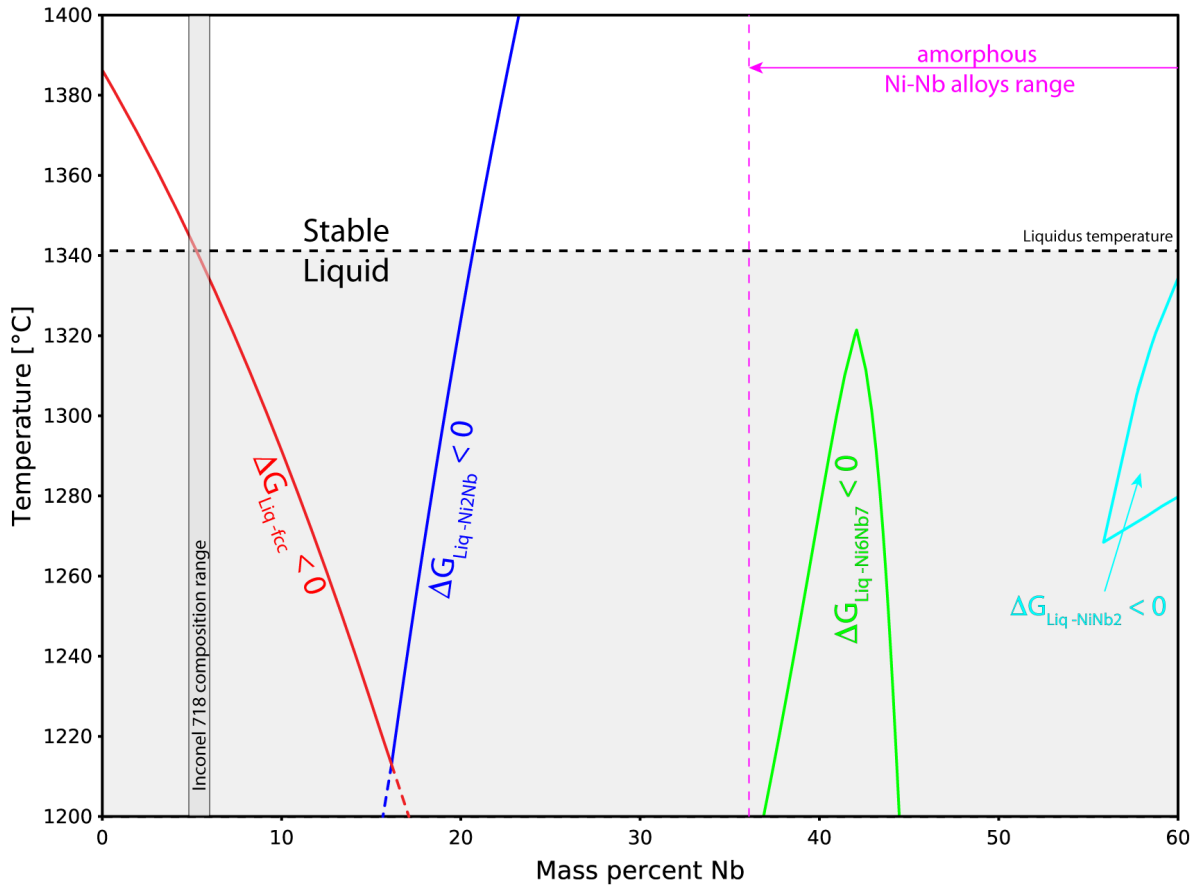

Figure 5.19: Isopleth section of Inconel 718 - Nb system in the solidification temperature range. The Inconel 718 nominal composition range is indicated for 5 mass % Nb. The limits between the driving forces ΔG of the solid phases formation and the liquid are represented for each phases respectively by different colors. The field under which the fcc phase form is highlighted by the curve in red. The formation of the Laves phase C14 Ni_2Nb is highlighted in blue. The phase Ni_6Nb_7 forms from 37 to 44% Nb and is indicated in green, while the Nb_2Ni phase forms for higher Nb content (55-60 %). The different limits were calculated using Thermocalc software (version 2021b) and with the database TTNI8.

The question that remains without answer would be: why the Nb tends to segregate in the environment around the TiC ? It has been shown in columnar zone that the Nb tends to form an fcc phase with the Ni to inherit the structure of the NbC by epitaxy. This observation shows that the Nb tends to aggregate around the TiC in both columnar and equiaxed zones in the molten pool. It is possible that the thermal conditions in the columnar zone due to higher temperatures are not favourable for ISRO, as they are not favourable for Nb rich phases. The liquid flow being important at higher temperatures could impact the conditions for ISRO and it is why equiaxed grains are not found at top of molten pool. Moreover it has been shown in the previous chapter the clear cut limit between the columnar and equiaxed zones, which indicates a temperature limit between possible equiaxed formation and only columnar grain growth. The role of TiC in capturing Nb in this case could be similar to TiB_2 nucleation effect in Al alloys [124]. When (even limited) excess Ti is present in the liquid, it forms a few atomic layers of Al_3Ti at the surface of the TiB_2 particles on which the solid fcc Al forms epitaxially and grows. The TiB_2 seem to attract the present Ti to form a thin layer stabilized by favourable chemical interaction between the planes $\{112\}_{Al_3Ti}$ and $\{0001\}_{TiB_2}$, even out of the stability domain of Al_3Ti. In the case of Inconel 718, the TiC could also have favourable chemical interactions with various elements since it was found formation of various metastable phases with increased Al, Mg and Nb content. The high content of Nb in the enriched zones near the TiC suggests that the favourable chemical interaction is not alone involved in the heavy segregation, but accentuated by the process conditions itself, i.e. overlapping with remelted previous layer.

To summarize the observed phases on the TiC in equiaxed regions in this work as well as the origin and role of ISRO, a schematic representation is shown in Figure 5.20. The Nb-rich liquid is responsible of the formation of several Nb-rich phases. Local ISRO and IMRO of Nb-Ni atoms could therefore promote the formation of the observed phases and be responsible for mediated nucleation for the Ni fcc phase, as schematically represented in Fig. 5.20. It is also possible that ISRO is involved in the C14 Laves phase formation in the eutectic regions where the Nb local composition would increase, and form locally other precipitates. ISRO around TiC could explain why a 5-fold symmetry axis was characterized between fcc grains that emerged from the surface of a TiC in the previous chapter. The role of Nb_2Ni and Ni_6Nb_7 phases as heterogeneous nucleation sites for the fcc phase would be complex to prove since no OR was found between the identified precipitates with the fcc matrix, but such possibility should not be excluded since Ni_6Nb_7 possess great number of similarly aligned icosahedra in its lattice with low mismatch with the fcc phase, and they coexist simultaneously in the solidification range temperatures of the alloy.

The role of TiC particles in capturing elements should also be investigated further in order to understand how the presence of Nb_2Ni is possible for an alloy that only contains 5 % of nominal Nb composition. The absence of such great grain refinement in other AM technologies than LMD-W for Inconel 718 [46] shows the effect of TiC on CET. The recent finding of ISRO mediated nucleation in SLM [113] for pure Ni shows that heavy microsegregation is not required for local ordering in the liquid. This can therefore support the role of TiC acting as an ISRO trigger, by accelerating kinetics of local ISRO with segregation of alloying elements.

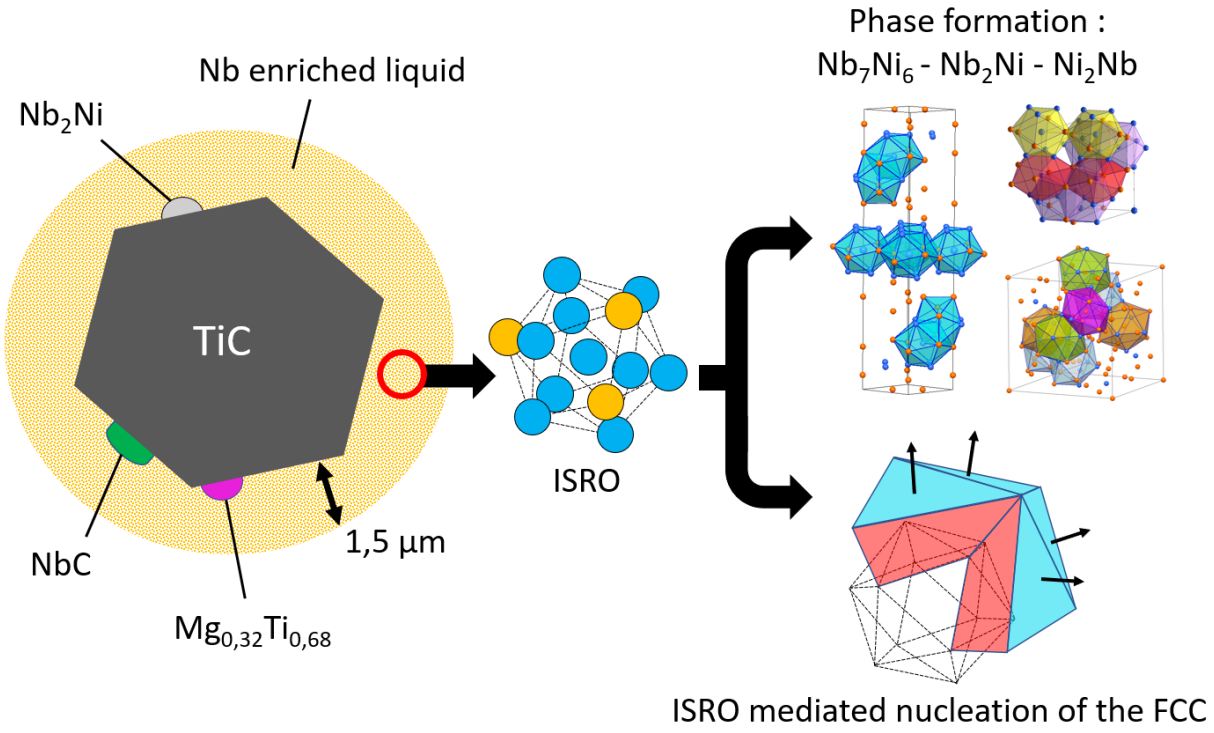

Figure 5.20: Schematic representation of enriched Nb liquid surrounding the TiC particles promoting various phase formations. ISRO is promoted by Nb enrichment that can induce the characterized phases Ni_6Nb_7 and Nb_2Ni as well as ISRO mediated nucleation of the fcc phase.

5.3 Conclusion

The TEM characterization revealed microstructure differences between the columnar and equiaxed grain zones at the nanometric scale. The shape of TiC particles and identified phases was very different in these two zones. In the columnar grain zone, the TiC are covered with NbC carbides and possess a smooth surface. A layer enriched in Ni-Cr-Nb on the NbC was found to be depleted in carbon and yet keep the NbC fcc structure by epitaxy. In the equiaxed grain zone, the TiC particles have a more irregular shape with NbC that are also present locally at the outer surface of the particles. Surprisingly, the phase Nb_2Ni was characterized on the surface of a TiC, which was never observed before for Inconel 718. Presence of precipitates with unknown structure is visible in the Nb-rich zones but could not be indexed, while fine precipitates requires further characterization in the eutectic regions. Such precipitates in the equiaxed grain region shows the segregations inherited from previous layer that can be involved during the remelting stage. We found the possible presence of Ni_6Nb_7 phase in the Nb enriched zone, using ACOM technique. The high presence of icosahedral clusters in the phases identified by TEM shows the implication of ISRO mechanism in the Nb enriched liquid that participate in those phases formation. The potential role of these phases as nucleation sites for Ni fcc phase was discussed regarding the mismatch of the 5-fold symmetry axes with the fcc phase. It was found out that the Ni_6Nb_7 phase have icosahedra with the smaller mismatch compared to Nb_2Ni (C15) and Ni_2Nb (C14) phases. These observations makes Nb the principal element that contribute to ISRO in the liquid.

The role of Ni_6Nb_7 as a potential nucleation site for the fcc phase should be moderated since we do not provide a high population of characterized equiaxed grain zones. It is now needed to know what phases are exactly present in the non-indexed areas as well as if more phases could be present with icosahedral polyhedra. Similarity between a FFT and a theoretical 2-fold symmetry axis of an icosahedral QC shows the possible presence of i-QC in enriched Nb zones and that could be participating in ISRO mediated nucleation of the fcc phase. Nevertheless, such diversity of non reported phases so far for this alloy shows the strong out of equilibrium conditions during processing with LMD-W. The thermodynamic stability of the different phases in the solidification temperature range of the alloy shows that enumerated Nb rich phases requires high Nb content around the TiC particles in the equiaxed grains. For instance, the Nb_2Ni phase is stable for at least 55 % Nb and was observed, which clearly shows the important microsegregation of Nb around the TiC at bottom of molten pool. The reason why the TiC particles attract Nb and other alloying elements is probably due to favourable chemical interaction, but requires further study. Such mechanisms depends on the conditions of the process i.e. the local temperatures involved as well as liquid flow during remelting of previous layers. Finally, we believe that ab initio and molecular dynamics could help to understand ISRO mediated nucleation of the Ni fcc phase, the role of Nb and the conditions of the metastable phases formation.

General conclusion and prospects

During this study, I developed an AM coaxial laser and wire process (LMD-W), in the framework of a CIFRE agreement with the Institut de Soudure. In particular, I investigated Inconel 718 using the LMD-W process. The objectives of this work were to characterise the process in terms of processability and to characterise the microstructure obtained for various processing conditions.

Firstly, a process window was established that led to deposition rate evaluation and to stable building conditions from single to multi-track walls. Lacks of fusion were removed by applying higher input energies, while no defects such as liquation cracking or macro porosities in the microstructures were found. Fine equiaxed grains zones were found periodically in the microstructure for various input energies. Such equiaxed grain zone were found to significantly increase the hardness of the alloy in as built conditions. The input energy directly impacts the primary dendritic arm spacing, grain size, potential defects and therefore the future tensile properties. Using fast camera and thermal imaging allowed to characterize further the LMD-W process. The liquid flow velocity was estimated using oxide tracking at the surface of molten pools for one parametric set. The results showed turbulent liquid flow varying from 0.2 to 0.7 m/s at the liquid surface, which could be verified with further simulation tools. Some first attempt of cooling rate evaluation for LMD-W of Inconel 718 was done with the thermal gradient evaluation from thermal measurements. We show the importance of considering the profile of the solidification interface as well as liquid flow that greatly affects the thermal gradient, therefore the calculated cooling rates. It has been found that the cooling rates involved during processing is an order of magnitude of 10^4 °C/s, that is in accordance with literature findings for LMD processing in similar conditions. These results demonstrate the strong liquid flow combined with significant cooling rates involved in LMD-W processing.

The equiaxed grain microstructure encountered in selected processing conditions was deeply investigated. The increase of the fraction of twin grain boundaries and drastic grain size reduction in equiaxed grain zones suggested similar mechanism involved for grain refinement already observed for Al-Zn-Cr and Au-Cu-Ag alloys [1, 2]. The analysis of the multi-twinned grains confirmed presence of Icosahedral Short Range Order (ISRO) mediated nucleation mechanism, that is at the origin of the equiaxed morphology, with fcc grains having orientation relationships respecting the icosahedral symmetry. This mechanism has been identified for the first time in this work for additive manufacturing conditions and also for an fcc Ni-based alloy. This evidence explains the presence of equiaxed microstructures for various processes in wide range of input energies in literature, with or without control of input process conditions for grain morphology control. The 3D characterization using EBSD and EDS techniques highlighted presence of twin grain boundaries surrounding TiC particles in the equiaxed region. This led to the identification of a 5-fold symmetry axis between fcc multi-twinned grains connected to a TiC particle in the analysed volume, which created new interest in the TiC environment. The grain-to-grain analyse of the equiaxed region demonstrated nucleation and growth by twinning mechanism of the Ni fcc phase. Indeed, the nucleation and growth of a grain on existing neighbour grain while respecting the twinning orientation relationship cost less interfacial energy than a regular grain boundary. The presence of ISRO and aptitude of Ni fcc system to nucleate and grow by twinning mechanism explains the equiaxed grains encountered for a wide range of processes and input energy in literature.

The TEM characterization revealed different characteristics on the TiC particles in columnar and equiaxed regions. EDS mapping revealed that TiC were capped by NbC in the columnar region while Nb enriched areas were identified around TiC particles in equiaxed grain zone. In the equiaxed regions, many phases were identified, and even region exhibiting a slight amorphous structure. Residual Mg segregations were identified as well on the TiC particles, that allowed the formation of an fcc $Mg_{0.32}Ti_{0.68}$ phase. Unexpected Nb-rich metastable topologically closed pack (TCP) phases Nb_2Ni and Ni_6Nb_7 were identified in the TiC environment, exhibiting icosahedral clusters in their crystal structure. Their origin is attributed to important segregation of Nb in the liquid at bottom of molten pool and especially in the TiC particles environment. Regarding the maximum temperature reached by the melt during processing, the equiaxed grain zone is forming approximatively right after the solidus temperature. It is believed that an important ISRO density around TiC is originating the TCP phase formation. Implication of such Nb rich phases in heterogeneous nucleation was discussed with their respective lattice mismatch when considering their 5-fold symmetry axes of present icosahedra with the Ni fcc phase. The phase Ni_6Nb_7 present the least lattice mismatch with the fcc system, that makes this phase a potential candidate for heterogeneous nucleation of the Ni fcc phase. However, no experimental evidence such as an OR between Ni_6Nb_7 and the fcc matrix has been found in this work but this possibility should not be excluded. ISRO mediated nucleation is accelerated by local Nb enrichment during rapid processing and remelting of previous layers and is believed to be increased by the presence of TiC particles attracting Nb. The study of the different stabilities of the phases with the fcc phase in the solidification temperature range has shown the important Nb content achieved around the TiC particles at the bottom of molten pool providing metastable conditions for nucleation and growth of Nb_2Ni and Ni_6Nb_7 phases.

Several perspectives can be drawn from the presented work. Simulation tools could bring additional information concerning the temperatures and flow rate at the bottom of molten pool in front of the solidification interface. The simulation of the different flows of the liquid could also bring additional results to explain the absence of equiaxed grains at the top of molten pool. The importance of overlapping should be considered as well as it can be extended to other AM processes and seem to have an important effect on local segregation levels when remelting previous layers.

Further characterization is needed to identify the fine precipitates in Nb enriched zones, as well as their potential relationship to ISRO mediated nucleation and if there is presence of iQC in the segregated areas. The curious similarity between an acquired FFT image in an enriched Nb zone and a theoretical diffraction pattern of a 2-fold symmetry axis of an iQC needs to be investigated further to understand if iQC formation is possible in the solidification temperature range or above. Nb seem to play a major role in the formation of such rich in icosahedral clusters phases, but the role of other alloying elements should also be investigated such as Al and Mo. The understanding of the role of TiC in capturing minor alloying elements should be investigated and especially their movement in the molten pool to validate the hypothesis given in this work. All this variety of phases and local ISRO cohabiting in the liquid in the same temperature range opens new perspectives for grain size control of Ni based alloys in AM. A study on a simpler binary system, such as Ni-Nb with TiC additions could help deepen the current understanding and could possibly be supported by AIMD simulation. The control of equiaxed grains in AM materials could be an interesting route for further improving in-service mechanical properties.

The effect of input energy and beneficial presence of equiaxed grain zone on the tensile and toughness properties are presented in Appendix A with a comparison with literature results. The evolution of the microstructure during processing, such as the residual stress and secondary phases precipitation is not presented in this work.

Bibliography

[1] Güven Kurtuldu, Alberto Sicco, and Michel Rappaz. Icosahedral quasicrystal-enhanced nucleation of the fcc phase in liquid gold alloys. *Acta Mater.*, 70:240–248, 2014.

[2] Güven Kurtuldu, Philippe Jarry, and Michel Rappaz. Influence of cr on the nucleation of primary al and formation of twinned dendrites in al–zn–cr alloys: Can icosahedral solid clusters play a role? *Acta Mater.*, 61(19):7098–7108, 2013.

[3] JF Zhao, HP Wang, and B Wei. A new thermodynamically stable nb2ni intermetallic compound phase revealed by peritectoid transition within binary nb-ni alloy system. *Journal of Materials Science & Technology*, 100:246–253, 2022.

[4] Blaine Geddes, Hugo Leon, and Xiao Huang. *Superalloys: alloying and performance*. Asm International, 2010.

[5] M. A. Moiz. The influence of grain size on mechanical properties of inconel 718. 2013.

[6] Y Murata, M Morinaga, N Yukawa, H Ogawa, and M Kato. Solidification structures of inconel 718 with microalloying elements. *Superalloys*, 718:81–88, 1994.

[7] Bernd Baufeld. Mechanical properties of inconel 718 parts manufactured by shaped metal deposition (smd). *Journal of materials engineering and performance*, 21(7):1416–1421, 2012.

[8] Michael M Kirka, Duncan A Greeley, C Hawkins, and Ryan R Dehoff. Effect of anisotropy and texture on the low cycle fatigue behavior of inconel 718 processed via electron beam melting. *International Journal of Fatigue*, 105:235–243, 2017.

[9] Narendran Raghavan, Ryan Dehoff, Sreekanth Pannala, Srdjan Simunovic, Michael Kirka, John Turner, Neil Carlson, and Sudarsanam S Babu. Numerical modeling of heat-transfer and the influence of process parameters on tailoring the grain morphology of in718 in electron beam additive manufacturing. *Acta Mater.*, 112:303–314, 2016.

[10] Ryan R Dehoff, MM Kirka, WJ Sames, H Bilheux, AS Tremsin, LE Lowe, and SS Babu. Site specific control of crystallographic grain orientation through electron beam additive manufacturing. *Materials Science and Technology*, 31(8):931–938, 2015.

[11] Decheng Kong, Chaofang Dong, Xiaoqing Ni, Liang Zhang, Cheng Man, Jizheng Yao, Yucheng Ji, Yupeng Ying, Kui Xiao, Xuequn Cheng, et al. High-throughput fabrication of nickel-based alloys with different nb contents via a dual-feed additive manufacturing system: Effect of nb content on microstructural and mechanical properties. *Journal of Alloys and Compounds*, 785:826–837, 2019.

[12] James C Williams and Edgar A Starke Jr. Progress in structural materials for aerospace systems. *Acta materialia*, 51(19):5775–5799, 2003.

[13] Alexis Pautrat. *Étude expérimentale quantitative de la solidification de l'inconel 718 en fonderie*. PhD thesis, Paris, ENMP, 2013.

[14] T Antonsson and Hasse Fredriksson. The effect of cooling rate on the solidification of inconel 718. *Metallurgical and Materials Transactions B*, 36(1):85–96, 2005.

[15] Hongjie Wang, Kenji Ikeuchi, Makoto Takahashi, and Akio Ikeda. Microstructures of inconel 718 alloy subjected to rapid thermal and stress cycle–joint performance and its controlling factors in friction welding of inconel 718 alloy. *Welding International*, 23(9):662–669, 2009.

[16] Cui E Seow, Harry E Coules, Guiyi Wu, Raja HU Khan, Xiangfang Xu, and Stewart Williams. Wire+ arc additively manufactured inconel 718: Effect of post-deposition heat treatments on microstructure and tensile properties. *Materials & Design*, 183:108157, 2019.

[17] Andreas Segerstark. *Laser Metal Deposition using Alloy 718 Powder: Influence of Process Parameters on Material Characteristics*. PhD thesis, University West, 2017.

[18] Fencheng Liu, Feiyue Lyu, Fenggang Liu, Xin Lin, and Chunping Huang. Laves phase control of inconel 718 superalloy fabricated by laser direct energy deposition via δ aging and solution treatment. *Journal of Materials Research and Technology*, 9(5):9753–9765, 2020.

[19] Chamara Kumara, Arun Ramanathan Balachandramurthi, Sneha Goel, Fabian Hanning, and Johan Moverare. Toward a better understanding of phase transformations in additive manufacturing of alloy 718. *Materialia*, 13:100862, 2020.

[20] Thomas Billotte. *Caractérisation et modélisation des structures de solidification en soudage TIG d'alliages austénitiques*. PhD thesis, Université de Lorraine, 2017.

[21] Pulin Nie, OA Ojo, and Zhuguo Li. Numerical modeling of microstructure evolution during laser additive manufacturing of a nickel-based superalloy. *Acta Materialia*, 77:85–95, 2014.

[22] Yuan Chen, Ke Zhang, Jian Huang, Seyed Reza Elmi Hosseini, and Zhuguo Li. Characterization of heat affected zone liquation cracking in laser additive manufacturing of inconel 718. *Materials & Design*, 90:586–594, 2016.

[23] YN Zhang, X Cao, and P Wanjara. Microstructure and hardness of fiber laser deposited inconel 718 using filler wire. *The International Journal of Advanced Manufacturing Technology*, 69(9-12):2569–2581, 2013.

[24] Yuan Tian, Donald McAllister, Hendrik Colijn, Michael Mills, Dave Farson, Mark Nordin, and Sudarsanam Babu. Rationalization of microstructure heterogeneity in inconel 718 builds made by the direct laser additive manufacturing process. *Metallurgical and Materials Transactions A*, 45(10):4470–4483, 2014.

[25] Andreas Segerstark, Joel Andersson, Lars-Erik Svensson, and Olanrewaju Ojo. Microstructural characterization of laser metal powder deposited alloy 718. *Materials Characterization*, 142:550–559, 2018.

[26] Esmaeil Sadeghi, Paria Karimi, Niklas Israelsson, James Shipley, Tomas Månsson, and Thomas Hansson. Inclusion-induced fatigue crack initiation in powder bed fusion of alloy 718. *Additive Manufacturing*, 36:101670, 2020.

[27] James D Hunt. Steady state columnar and equiaxed growth of dendrites and eutectic. *Mater. Sci. Eng.*, 65(1):75–83, 1984.

[28] M Gäumann, C Bezencon, P Canalis, and W Kurz. Single-crystal laser deposition of superalloys: processing–microstructure maps. *Acta materialia*, 49(6):1051–1062, 2001.

[29] Carolin Körner, Harald Helmer, Andreas Bauereiß, and Robert F Singer. Tailoring the grain structure of in718 during selective electron beam melting. In *MATEC Web of Conferences*, volume 14, page 08001. EDP Sciences, 2014.

[30] Pengwei Liu, Zhuo Wang, Yaohong Xiao, Mark F Horstemeyer, Xiangyang Cui, and Lei Chen. Insight into the mechanisms of columnar to equiaxed grain transition during metallic additive manufacturing. *Additive Manufacturing*, 26:22–29, 2019.

[31] Michael M Kirka, Yousub Lee, Duncan A Greeley, Alfred Okello, Michael J Goin, Michael T Pearce, and Ryan R Dehoff. Strategy for texture management in metals additive manufacturing. *Jom*, 69(3):523–531, 2017.

[32] Gerry L Knapp, Narendran Raghavan, Alex Plotkowski, and Tarasankar Debroy. Experiments and simulations on solidification microstructure for inconel 718 in powder bed fusion electron beam additive manufacturing. *Additive Manufacturing*, 25:511–521, 2019.

[33] Mengyao Zheng, Chuanwei Li, Xinyu Zhang, Zhenhua Ye, Xudong Yang, and Jianfeng Gu. The influence of columnar to equiaxed transition on deformation behavior of fecocrnimn high entropy alloy fabricated by laser-based directed energy deposition. *Additive Manufacturing*, 37:101660, 2021.

[34] VA Popovich, EV Borisov, AA Popovich, V Sh Sufiiarov, DV Masaylo, and Laurie Alzina. Functionally graded inconel 718 processed by additive manufacturing: Crystallographic texture, anisotropy of microstructure and mechanical properties. *Materials & Design*, 114:441–449, 2017.

[35] Amir Hadadzadeh, Babak Shalchi Amirkhiz, Jian Li, and Mohsen Mohammadi. Columnar to equiaxed transition during direct metal laser sintering of alsi10mg alloy: effect of building direction. *Additive Manufacturing*, 23:121–131, 2018.

[36] MJ Bermingham, DH StJohn, J Krynen, S Tedman-Jones, and MS Dargusch. Promoting the columnar to equiaxed transition and grain refinement of titanium alloys during additive manufacturing. *Acta Materialia*, 168:261–274, 2019.

[37] Shuai Guan, Klas Solberg, Di Wan, Filippo Berto, Torgeir Welo, TM Yue, and KC Chan. Formation of fully equiaxed grain microstructure in additively manufactured alcocrfeniti0. 5 high entropy alloy. *Materials & Design*, 184:108202, 2019.

[38] Kun V Yang, Yunjia Shi, Frank Palm, Xinhua Wu, and Paul Rometsch. Columnar to equiaxed transition in al-mg (-sc)-zr alloys produced by selective laser melting. *Scripta Materialia*, 145:113–117, 2018.

[39] Sudarsanam Suresh Babu, Narendran Raghavan, Jacob Raplee, Sarah J Foster, Curtis Frederick, Michael Haines, R Dinwiddie, MK Kirka, A Plotkowski, Yousub Lee, et al. Additive manufacturing of nickel superalloys: opportunities for innovation and challenges related to qualification. *Metallurgical and Materials Transactions A*, 49(9):3764–3780, 2018.

[40] B Attard, S Cruchley, Ch Beetz, M Megahed, YL Chiu, and MM Attallah. Microstructural control during laser powder fusion to create graded microstructure ni-superalloy components. *Additive Manufacturing*, 36:101432, 2020.

[41] Ahmad Mostafa, Ignacio Picazo Rubio, Vladimir Brailovski, Mohammad Jahazi, and Mamoun Medraj. Structure, texture and phases in 3d printed in718 alloy subjected to homogenization and hip treatments. *Metals*, 7(6):196, 2017.

[42] Joon-Phil Choi, Gi-Hun Shin, Sangsun Yang, Dong-Yeol Yang, Jai-Sung Lee, Mathieu Brochu, and Ji-Hun Yu. Densification and microstructural investigation of inconel 718 parts fabricated by selective laser melting. *Powder Technol.*, 310:60–66, 2017.

[43] Lakshmi L Parimi, GA Ravi, Daniel Clark, and Moataz M Attallah. Microstructural and texture development in direct laser fabricated in718. *Mater. Charact.*, 89:102–111, 2014.

[44] Mario Renderos, Amaia Torregaray, M[a] Esther Gutierrez-Orrantia, Aitzol Lamikiz, Nicolas Saintier, and Franck Girot. Microstructure characterization of recycled in718 powder and resulting laser clad material. *Mater. Charact.*, 134:103–113, 2017.

[45] Raymond C Benn and Randy P Salva. Additively manufactured inconel alloy 718. In *Proceedings of the 7th International Symposium on Superalloy 718 and Derivatives*, pages 455–469. TMS, 2010.

[46] Markus Bambach, Irina Sizova, Fabian Kies, and Christian Haase. Directed energy deposition of inconel 718 powder, cold and hot wire using a six-beam direct diode laser set-up. *Additive Manufacturing*, 47:102269, 2021.

[47] H Helmer, A Bauereiß, RF Singer, and C Körner. Grain structure evolution in inconel 718 during selective electron beam melting. *Materials Science and Engineering: A*, 668:180–187, 2016.

[48] Almir Heralić, Anna-Karin Christiansson, Mattias Ottosson, and Bengt Lennartson. Increased stability in laser metal wire deposition through feedback from optical measurements. *Optics and Lasers in Engineering*, 48(4):478–485, 2010.

[49] Erhard Brandl, Vesselin Michailov, Bernd Viehweger, and Christoph Leyens. Deposition of ti–6al–4v using laser and wire, part i: Microstructural properties of single beads. *Surface and Coatings Technology*, 206(6):1120–1129, 2011.

[50] Amir Baghdadchi, Vahid A Hosseini, Maria Asuncion Valiente Bermejo, Björn Axelsson, Ebrahim Harati, Mats Högström, and Leif Karlsson. Wire laser metal deposition additive manufacturing of duplex stainless steel components—development of a systematic methodology. *Materials*, 14(23):7170, 2021.

[51] Thomas Bergs, Sebastian Kammann, Gabriel Fraga, Jan Riepe, and Kristian Arntz. Experimental investigations on the influence of temperature for laser metal deposition with lateral inconel 718 wire feeding. *Procedia CIRP*, 94:29–34, 2020.

[52] LK Ang, YY Lau, RM Gilgenbach, and HL Spindler. Analysis of laser absorption on a rough metal surface. *Applied physics letters*, 70(6):696–698, 1997.

[53] T.B. Britton, J. Jiang, Y. Guo, A. Vilalta-Clemente, D. Wallis, L.N. Hansen, A. Winkelmann, and A.J. Wilkinson. Tutorial: Crystal orientations and EBSD – Or which way is up? *Materials Characterization*, 117:113–126, 2016.

[54] EF Rauch and MJMC Véron. Automated crystal orientation and phase mapping in tem. *Materials Characterization*, 98:1–9, 2014.

[55] S Ocylok, M Leichnitz, S Thieme, and S Nowotny. Investigations on laser metal deposition of stainless steel 316l with coaxial wire feeding. In *9th International Conference on Photonic Technologies (LANE 2016)*, 2016.

[56] Petter Hagqvist, Almir Heralić, Anna-Karin Christiansson, and Bengt Lennartson. Resistance based iterative learning control of additive manufacturing with wire. *Mechatronics*, 31:116–123, 2015.

[57] Wenhao Huang, Shujun Chen, Jun Xiao, Xiaoqing Jiang, and Yazhou Jia. Laser wire-feed metal additive manufacturing of the al alloy. *Optics & Laser Technology*, 134:106627, 2021.

[58] TE Abioye, J Folkes, and AT Clare. A parametric study of inconel 625 wire laser deposition. *Journal of Materials Processing Technology*, 213(12):2145–2151, 2013.

[59] A Ayed, G Bras, H Bernard, P Michaud, Y Balcaen, and J Alexis. Study of arc-wire and laser-wire processes for the realization of ti-6al-4v alloy parts. In *MATEC Web of Conferences*, volume 321, page 03002. EDP Sciences, 2020.

[60] Maurizio Motta, Ali Gökhan Demir, and Barbara Previtali. High-speed imaging and process characterization of coaxial laser metal wire deposition. *Additive Manufacturing*, 22:497–507, 2018.

[61] TE Abioye, A Medrano-Tellez, PK Farayibi, and PK Oke. Laser metal deposition of multi-track walls of 308lsi stainless steel. *Materials and Manufacturing Processes*, 32(14):1660–1666, 2017.

[62] Ali Gökhan Demir. Micro laser metal wire deposition for additive manufacturing of thin-walled structures. *Optics and Lasers in Engineering*, 100:9–17, 2018.

[63] John W Elmer, Jay Vaja, John S Carpenter, Daniel R Coughlin, Matthew J Dvornak, Pat Hochanadel, Parogya Gurung, Andy Johnson, and Gordon Gibbs. Wire-based additive manufacturing of stainless steel components. *Welding Journal*, 99(LLNL-JRNL-771645; LA-UR-19-23147), 2020.

[64] Shaoshan Ji, Fan Liu, Tuo Shi, Geyan Fu, and Shihong Shi. Effects of defocus distance on three-beam laser internal coaxial wire cladding. *Chinese Journal of Mechanical Engineering*, 34(1):1–22, 2021.

[65] Jianjun Shi, Ping Zhu, Geyan Fu, and Shihong Shi. Geometry characteristics modeling and process optimization in coaxial laser inside wire cladding. *Optics & Laser Technology*, 101:341–348, 2018.

[66] Matjaž Kotar, Makoto Fujishima, Gideon Levy, and Edvard Govekar. Initial transient phase and stability of annular laser beam direct wire deposition. *CIRP annals*, 68(1):233–236, 2019.

[67] Dina Becker, Steffen Boley, Rocco Eisseler, Thomas Stehle, Hans-Christian Möhring, Volkher Onuseit, Max Hoßfeld, and Thomas Graf. Influence of a closed-loop controlled laser metal wire deposition process of s al 5356 on the quality of manufactured parts before and after subsequent machining. *Production Engineering*, 15(3):489–507, 2021.

[68] Avelino Zapata, Christian Bernauer, Christian Stadter, Cara G Kolb, and Michael F Zaeh. Investigation on the cause-effect relationships between the process parameters and the resulting geometric properties for wire-based coaxial laser metal deposition. *Metals*, 12(3):455, 2022.

[69] Benjamin Bax, Rohan Rajput, Richard Kellet, and Martin Reisacher. Systematic evaluation of process parameter maps for laser cladding and directed energy deposition. *Additive Manufacturing*, 21:487–494, 2018.

[70] L Jyothish Kumar and CG Krishnadas Nair. Laser metal deposition repair applications for inconel 718 alloy. *Materials Today: Proceedings*, 4(10):11068–11077, 2017.

[71] Xin Lu, Mengnie Victor Li, and Hongbin Yang. Comparison of wire-arc and powder-laser additive manufacturing for in718 superalloy: unified consideration for selecting process parameters based on volumetric energy density. *The International Journal of Advanced Manufacturing Technology*, 114(5):1517–1531, 2021.

[72] Sui Him Mok, Guijun Bi, Janet Folkes, and Ian Pashby. Deposition of ti–6al–4v using a high power diode laser and wire, part i: Investigation on the process characteristics. *Surface and Coatings Technology*, 202(16):3933–3939, 2008.

[73] Shang Sui, Chongliang Zhong, Jing Chen, Andres Gasser, Weidong Huang, and Johannes Henrich Schleifenbaum. Influence of solution heat treatment on microstructure and tensile properties of inconel 718 formed by high-deposition-rate laser metal deposition. *Journal of Alloys and Compounds*, 740:389–399, 2018.

[74] Amagoia Paskual, Pedro Álvarez, Alfredo Suárez, et al. Study on arc welding processes for high deposition rate additive manufacturing. *Procedia Cirp*, 68:358–362, 2018.

[75] B Baufeld, R Widdison, and T Dutilleu. Electron beam additive manufacturing: Deposition strategies and properties. In *Proceeding of 4th IEBW International Electron Beam Conference Aachen*, pages 114–117, 2017.

[76] Filomeno Martina, Jialuo Ding, Stewart Williams, Armando Caballero, Gonçalo Pardal, and Luisa Quintino. Tandem metal inert gas process for high productivity wire arc additive manufacturing in stainless steel. *Additive Manufacturing*, 25:545–550, 2019.

[77] Agnieszka Kisielewicz, Karthikeyan Thalavai Pandian, Daniel Sthen, Petter Hagqvist, Maria Asuncion Valiente Bermejo, Fredrik Sikström, and Antonio Ancona. Hot-wire laser-directed energy deposition: Process characteristics and benefits of resistive pre-heating of the feedstock wire. *Metals*, 11(4):634, 2021.

[78] DJ Tillack. Nickel alloys and stainless steels for elevated temperature service: weldability considerations. *Materials Solutions*, 1997.

[79] Xin Ye, Xueming Hua, Min Wang, and Songnian Lou. Controlling hot cracking in ni-based inconel-718 superalloy cast sheets during tungsten inert gas welding. *Journal of Materials Processing Technology*, 222:381–390, 2015.

[80] Zhengtao Gan, Gang Yu, Xiuli He, and Shaoxia Li. Surface-active element transport and its effect on liquid metal flow in laser-assisted additive manufacturing. *International Communications in Heat and Mass Transfer*, 86:206–214, 2017.

[81] Xiang Wang, Lin-Jie Zhang, Jie Ning, Sen Li, and Suck-Joo Na. Effect of addition of micron-sized lanthanum oxide particles on morphologies, microstructures and properties of the wire laser additively manufactured ti–6al–4v alloy. *Materials Science and Engineering: A*, 803:140475, 2021.

[82] Nejib Chekir. *Laser Wire Deposition Additive Manufacturing of Ti-6Al-4V for the Aerospace Industry*. McGill University (Canada), 2019.

[83] Roya Darabi, André Ferreira, Erfan Azinpour, Jose Cesar de Sa, and Ana Reis. Thermal study of a cladding layer of inconel 625 in directed energy deposition (ded) process using a phase-field model. 2021.

[84] Yousub Lee, Mark Nordin, Sudarsanam Suresh Babu, and Dave F Farson. Effect of fluid convection on dendrite arm spacing in laser deposition. *Metallurgical and Materials Transactions B*, 45(4):1520–1529, 2014.

[85] YL Hu, X Lin, XF Lu, SY Zhang, HO Yang, L Wei, and WD Huang. Evolution of solidification microstructure and dynamic recrystallisation of inconel 625 during laser solid forming process. *Journal of Materials Science*, 53(22):15650–15666, 2018.

[86] Kubra Karayagiz, Luke Johnson, Raiyan Seede, Vahid Attari, Bing Zhang, Xueqin Huang, Supriyo Ghosh, Thien Duong, Ibrahim Karaman, Alaa Elwany, et al. Finite interface dissipation phase field modeling of ni–nb under additive manufacturing conditions. *Acta Materialia*, 185:320–339, 2020.

[87] Wenjia Xiao, Simeng Li, Cunshan Wang, Yan Shi, Jyotirmoy Mazumder, Hui Xing, and Lijun Song. Multi-scale simulation of dendrite growth for direct energy deposition of nickel-based superalloys. *Materials & Design*, 164:107553, 2019.

[88] T Debroy, HL Wei, JS Zuback, T Mukherjee, JW Elmer, JO Milewski, AM Beese, A de Wilson-Heid, A De, and W Zhang. Progress in materials science additive manufacturing of metallic components–process, structure and properties. *Prog. Mater. Sci*, 92:112–224, 2018.

[89] Garrett J Marshall, W Joseph Young, Scott M Thompson, Nima Shamsaei, Steve R Daniewicz, and Shuai Shao. Understanding the microstructure formation of ti-6al-4v during direct laser deposition via in-situ thermal monitoring. *Jom*, 68(3):778–790, 2016.

[90] Xiaoqing Wang and Kevin Chou. Effects of thermal cycles on the microstructure evolution of inconel 718 during selective laser melting process. *Additive Manufacturing*, 18:1–14, 2017.

[91] Simeng Li, Hui Xiao, Keyang Liu, Wenjia Xiao, Yanqin Li, Xu Han, Jyoti Mazumder, and Lijun Song. Melt-pool motion, temperature variation and dendritic morphology of inconel 718 during pulsed-and continuous-wave laser additive manufacturing: A comparative study. *Materials & design*, 119:351–360, 2017.

[92] Jiayun Shao, Gang Yu, Xiuli He, Shaoxia Li, Ru Chen, and Yao Zhao. Grain size evolution under different cooling rate in laser additive manufacturing of superalloy. *Optics & Laser Technology*, 119:105662, 2019.

[93] V Manvatkar, A De, and Tarasankar DebRoy. Heat transfer and material flow during laser assisted multi-layer additive manufacturing. *Journal of Applied Physics*, 116(12):124905, 2014.

[94] Sarah J Wolff, Zhengtao Gan, Stephen Lin, Jennifer L Bennett, Wentao Yan, Gregory Hyatt, Kornel F Ehmann, Gregory J Wagner, Wing Kam Liu, and Jian Cao. Experimentally validated predictions of thermal history and microhardness in laser-deposited inconel 718 on carbon steel. *Additive Manufacturing*, 27:540–551, 2019.

[95] R. Trivedi. Interdendritic spacing: Part II. A comparison of theory and experiment. *Metallurgical Transactions A*, 15:977–982, 1984.

[96] Narendran Raghavan, Srdjan Simunovic, Ryan Dehoff, Alex Plotkowski, John Turner, Michael Kirka, and Suresh Babu. Localized melt-scan strategy for site specific control of grain size and primary dendrite arm spacing in electron beam additive manufacturing. *Acta Materialia*, 140:375–387, 2017.

[97] W. Kurz and D.J. Fisher. Dendrite growth at the limit of stability: tip radius and spacing. *Acta Metallurgica*, 29:11–20, 1981.

[98] Mingming Ma, Zemin Wang, and Xiaoyan Zeng. A comparison on metallurgical behaviors of 316l stainless steel by selective laser melting and laser cladding deposition. *Mater. Sci. Eng. A*, 685:265–273, 2017.

[99] Patcharapit Promoppatum, Shi-Chune Yao, P Chris Pistorius, Anthony D Rollett, Peter J Coutts, Frederick Lia, and Richard Martukanitz. Numerical modeling and experimental validation of thermal history and microstructure for additive manufacturing of an inconel 718 product. *Progress in Additive Manufacturing*, 3(1):15–32, 2018.

[100] Jarred C Heigel, Brandon M Lane, and Lyle E Levine. In situ measurements of melt-pool length and cooling rate during 3d builds of the metal am-bench artifacts. *Integrating Materials and Manufacturing Innovation*, 9(1):31–53, 2020.

[101] B Zheng, Y Zhou, JE Smugeresky, JM Schoenung, and EJ Lavernia. Thermal behavior and microstructure evolution during laser deposition with laser-engineered net shaping: part ii. experimental investigation and discussion. *Metallurgical and materials transactions A*, 39(9):2237–2245, 2008.

[102] Jennifer L Bennett, Sarah J Wolff, Gregory Hyatt, Kornel Ehmann, and Jian Cao. Thermal effect on clad dimension for laser deposited inconel 718. *Journal of Manufacturing Processes*, 28:550–557, 2017.

[103] E Hosseini and VA Popovich. A review of mechanical properties of additively manufactured inconel 718. *Additive Manufacturing*, 30:100877, 2019.

[104] Ivan Cazic, Julien Zollinger, S Mathieu, Maxime El Kandaoui, Peter Plapper, and Benoit Appolaire. New insights into the origin of fine equiaxed microstructures in additively manufactured inconel 718. *Scripta Materialia*, 195:113740, 2021.

[105] JK Mackenzie. Second paper on statistics associated with the random disorientation of cubes. *Biometrika*, 45(1-2):229–240, 1958.

[106] Julien Zollinger, B Rouat, J Guyon, SK Pillai, and M Rappaz. Influence of ir additions and icosahedral short range order (isro) on nucleation and growth kinetics in au-20.5 wt pct cu-4.5 wt pctag alloy. *Metall. Mater. Trans. A*, 50(5):2279–2288, 2019.

[107] Michel Rappaz, Philippe Jarry, Güven Kurtuldu, and Julien Zollinger. Solidification of metallic alloys: Does the structure of the liquid matter. *Metall. Mater. Trans. A*, 2020.

[108] M Audier, M Durand-Charre, E Laclau, and H Klein. Phase equilibria in the Al–Cr system. *J. Alloys Compd.*, 220(1-2):225–230, 1995.

[109] A Pasturel and N Jakse. Influence of cr on local order and dynamic properties of liquid and undercooled al–zn alloys. *J. Chem. Phys.*, 146(18):184502, 2017.

[110] Ming-Yue Shen, Xiang-Jun Tian, Dong Liu, Hai-Bo Tang, and Xu Cheng. Microstructure and fracture behavior of tic particles reinforced inconel 625 composites prepared by laser additive manufacturing. *Journal of Alloys and Compounds*, 734:188–195, 2018.

[111] Tzu-Hou Hsu, Kai-Chun Chang, Yao-Jen Chang, I Ho, Sammy Tin, Chen-Wei Li, Koji Kakehi, Chih-Peng Chen, Kuo-Kuang Jen, Ho-Yen Hsieh, et al. Effect of carbide inoculants additions in in718 fabricated by selective laser melting process. In *Superalloys 2020*, pages 982–989. Springer, 2020.

[112] Güven Kurtuldu and Michel Rappaz. Probability of twin boundary formation associated with the nucleation of equiaxed grains on icosahedral quasicrystal templates. In *IOP Conf. Ser. Mater. Sci. Eng.*, volume 84, page 12012, 2015.

[113] C Galera-Rueda, X Jin, J LLorca, and MT Pérez-Prado. Icosahedral quasicrystal enhanced nucleation in commercially pure ni processed by selective laser melting. *Scripta Materialia*, 211:114512, 2022.

[114] Güven Kurtuldu. *Influence of trace elements on the nucleation and solidification morphologies of fcc alloys and relationship with icosahedral quasicrystal formation*. PhD thesis, 2014.

[115] Vasily V Bulatov, Bryan W Reed, and Mukul Kumar. Grain boundary energy function for fcc metals. *Acta Materialia*, 65:161–175, 2014.

[116] JD Rittner and David N Seidman. < 110> symmetric tilt grain-boundary structures in fcc metals with low stacking-fault energies. *Physical Review B*, 54(10):6999, 1996.

[117] Alexander Kerkau. *Disorder in Laves Phases*. PhD thesis, Technische Universität Dresden, 2013.

[118] F Fang, J Kovacs, G Sadler, and K Irwin. An icosahedral quasicrystal as a packing of regular tetrahedra. *arXiv preprint arXiv:1311.3994*, 2013.

[119] Ping Liu, A Hultin Stigenberg, and J-O Nilsson. Quasicrystalline and crystalline precipitation during isothermal tempering in a 12cr-9ni-4mo maraging stainless steel. *Acta metallurgica et materialia*, 43(7):2881–2890, 1995.

[120] Wenfei Lu, Jo-Chi Tseng, Aihan Feng, and Jun Shen. Structural origin of the enhancement in glass-forming ability of binary ni-nb metallic glasses. *Journal of Non-Crystalline Solids*, 564:120834, 2021.

[121] TQ Wen, Y Zhang, Cai-Zhuang Wang, N Wang, Kai-Ming Ho, and Matthew J Kramer. Local structure orders and glass forming ability of ni-nb liquids. *Intermetallics*, 98:131–138, 2018.

[122] Bruce L Bramfitt. The effect of carbide and nitride additions on the heterogeneous nucleation behavior of liquid iron. *Metallurgical Transactions*, 1(7):1987–1995, 1970.

[123] Michel Rappaz and Güven Kurtuldu. Thermodynamic aspects of homogeneous nucleation enhanced by icosahedral short range order in liquid fcc-type alloys. *Jom*, 67(8):1812–1820, 2015.

[124] P Schumacher, AL Greer, J Worth, PV Evans, MA Kearns, P Fisher, and AH Green. New studies of nucleation mechanisms in aluminium alloys: implications for grain refinement practice. *Materials science and technology*, 14(5):394–404, 1998.

[125] Ahmad Mostafa, Ignacio Picazo Rubio, Vladimir Brailovski, Mohammad Jahazi, and Mamoun Medraj. Erratum: structure, texture and phases in 3d printed in718 alloy subjected to homogenization and hip treatments. metals 2017, 7, 196. *Metals*, 7(8):315, 2017.

[126] Wakshum M Tucho and Vidar Hansen. Characterization of slm-fabricated inconel 718 after solid solution and precipitation hardening heat treatments. *Journal of Materials Science*, 54(1):823–839, 2019.

[127] Eslam M Fayed, Mohammad Saadati, Davood Shahriari, Vladimir Brailovski, Mohammad Jahazi, and Mamoun Medraj. Effect of homogenization and solution treatments time on the elevated-temperature mechanical behavior of inconel 718 fabricated by laser powder bed fusion. *Scientific Reports*, 11(1):1–17, 2021.

[128] Shang Sui, Jing Chen, Zuo Li, Haosheng Li, Xuan Zhao, and Hua Tan. Investigation of dissolution behavior of laves phase in inconel 718 fabricated by laser directed energy deposition. *Additive Manufacturing*, 32:101055, 2020.

[129] Yunhao Zhao, Kun Li, Matthew Gargani, and Wei Xiong. A comparative analysis of inconel 718 made by additive manufacturing and suction casting: Microstructure evolution in homogenization. *Additive Manufacturing*, 36:101404, 2020.

[130] Xiaoming Zhao, Jing Chen, Xin Lin, and Weidong Huang. Study on microstructure and mechanical properties of laser rapid forming inconel 718. *Materials Science and Engineering: A*, 478(1-2):119–124, 2008.

[131] Judy Schneider. Comparison of microstructural response to heat treatment of inconel 718 prepared by three different metal additive manufacturing processes. *JOM*, 72(3):1085–1091, 2020.

[132] E Chlebus, K Gruber, B Kuźnicka, J Kurzac, and T Kurzynowski. Effect of heat treatment on the microstructure and mechanical properties of inconel 718 processed by selective laser melting. *Materials Science and Engineering: A*, 639:647–655, 2015.

[133] Hae-Jin Lee, Han-Kyu Kim, Hyun-Uk Hong, and Byoung-Soo Lee. Influence of the focus offset on the defects, microstructure, and mechanical properties of an inconel 718 superalloy fabricated by electron beam additive manufacturing. *Journal of Alloys and Compounds*, 781:842–856, 2019.

[134] GD Janaki Ram, A Venugopal Reddy, K Prasad Rao, G Madhusudhan Reddy, and JK Sarin Sundar. Microstructure and tensile properties of inconel 718 pulsed nd-yag laser welds. *Journal of Materials Processing Technology*, 167(1):73–82, 2005.

[135] Nickel Alloy. Corrosion and heat resistant, bars, forgings, and rings 52.5 ni 19cr 3.0 mo 5.1 cb 0.90 ti 0.50 al 18fe, consumable electrode or vacuum induction melted 1775 f (968 c) solution heat treated, precipitation hardenable. *SAE International*, 1965.

[136] So-Yeon Park, Kyu-Sik Kim, Min-Cheol Kim, Michael E Kassner, and Kee-Ahn Lee. Effect of post-heat treatment on the tensile and cryogenic impact toughness properties of inconel 718 manufactured by selective laser melting. *Advanced Engineering Materials*, 23(3):2001005, 2021.

[137] Anatoly A Popovich, Vadim Sh Sufiiarov, Igor A Polozov, and Evgenii V Borisov. Microstructure and mechanical properties of inconel 718 produced by slm and subsequent heat treatment. In *Key Engineering Materials*, volume 651, pages 665–670. Trans Tech Publ, 2015.

[138] Special Metals et al. Inconel alloy 718. *Publication Number SMC-045. Special Metals Corporation*, 2007.

Appendix A

Post-process microstructure evolution and mechanical properties

The influence of heat treatment on the microstructure are discussed in this annex, considering both chemical and morphological heterogeneities. A tailored heat treatment is investigated and an evaluation of the tensile and toughness properties are briefly discussed.

A.1 Homogenization of equiaxed grain zones

The presence of equiaxed grains induces heterogeneous grain morphology and Laves phase distribution, therefore different grain sizes that has an impact on homogenization and phase precipitation kinetics. Figure A.1 shows the time-temperature-transformation (TTT) diagram of the alloy Inconel 718 showing the different phase stability domains. Such diagrams led to construct conventional heat treatment for chemically homogenising the microstructure in order to dissolve the brittle Laves phase C14 at 1100°C for 1h, annealing at 920°C for 1h precipitating δ at the grain boundaries and then precipitating hardening phases γ' and γ" in the matrix [16] at 720 °C for 8h followed by 625°C for 8h. Such heat treatment should avoid precipitation of oxides as well as Laves phase liquation.

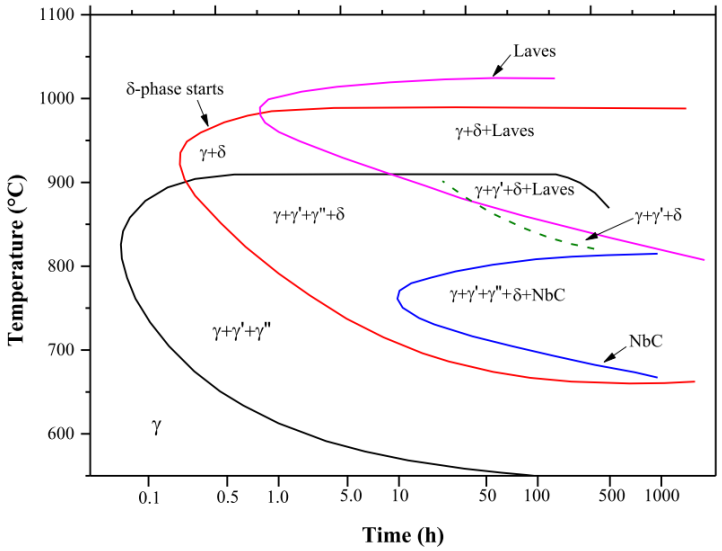

Figure A.1: Time-temperature-transformation (TTT) diagram of Inconel 718, taken from [125].

Figure A.2a shows an example of the hardening phase γ" formed after heat treatment in Inconel 718 processed by SLM. Figure A.2b shows the Laves phase C14 eutectic to dissolve in order to homogenize

the Nb content in the matrix and form homogeneously γ' and γ" in the fcc Ni matrix. With recent new AM processing techniques, phase fraction and grain size differs from those from conventionally obtained and changes for each AM technology used.

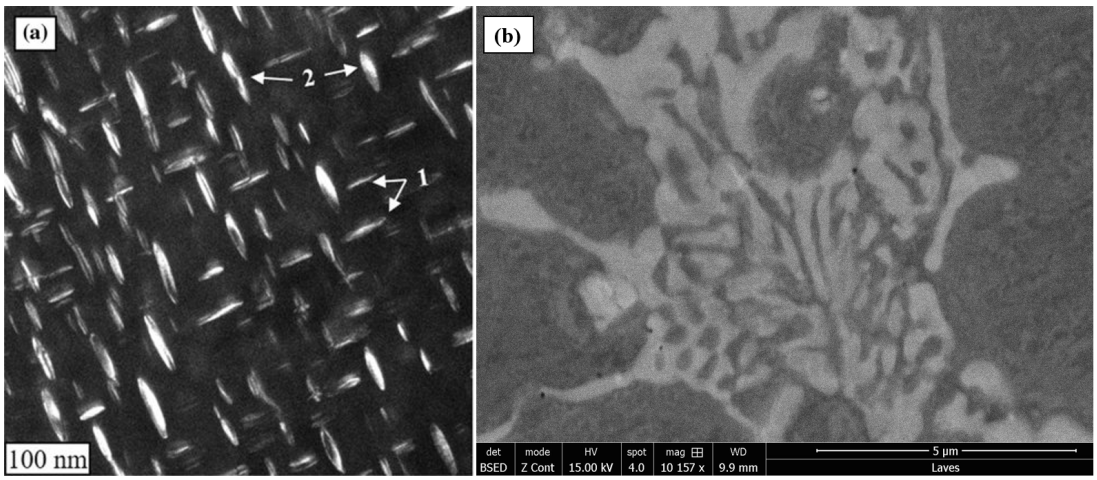

Figure A.2: (a) Example of precipitation of γ" with different orientations, in TEM dark field in the [100] zone axis, taken from [126] (b) Laves phase C14 eutectic in equiaxed grain region, obtained from laser and wire processed Inconel 718 from this work.

Figure A.3 illustrates the standard heat treatment for the alloy in larger dark line. Several studies have pointed out the need to adapt homogenization treatment to the microstructure, i.e. smaller microstructure requires shorter time to homogenize. Seow Cui *et al.* [16] have modified both the time and temperature and they found to achieve dissolution of Laves phase without precipitating δ phase, but noticed recrystallization and important grain growth (3 times the initial grain size). Fayed *et al.* [127] limited the recrystallization and grain growth with short solution time as shown in Fig. A.3 but did not modify the homogenization, and noticed precipitation of δ being already present at 980 °C for 15 min. Another heat treatment was studied by Sui *et al.* [73] composed of a homogenization treatment of 30 min at 1100°C before precipitation. They observed less recrystallized grains then at 1100°C for 1h, especially in the equiaxed grain regions. Such results seem to indicate that Laves phase dissolution could be faster in microstructures induced by AM. Laves phase could also be dissolved through δ precipitation treatment before solution treatment, in order to fragment the Laves phase and reduce their sizes [18]. Sui *et al.* [128] studied the Laves phase dissolution kinetic through different time and temperature treatments, combine with different models. They show the higher the temperature, the less time needed to dissolve the Laves phase in interdendritic regions. From 15 to 30 min at respectively 1100 and 1150 °C, the Laves phase fraction reached is almost null. They do not observe full Laves dissolution at 5 or 15 min. A similar study was done comparing the NbC/Laves phases fraction and grain size processed with SLM and casting for different times at homogenization temperature of 1180°C [129]. The Laves phase fraction dropped to almost 0 % after 20 min of holding for both processed conditions, while the grain size increased notably and then stabilized after 1h for the SLM condition.

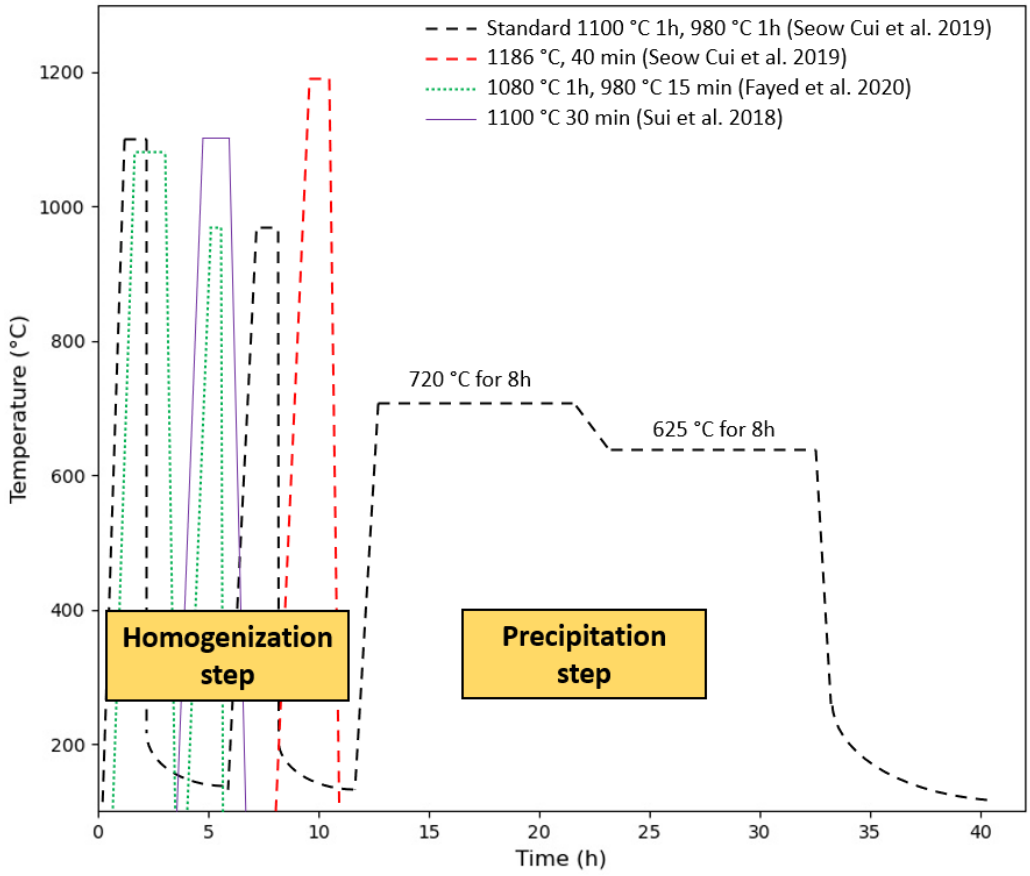

Figure A.3: Comparison of different homogenization heat treatments optimizations. Standard AMS 5383 heat treatment is represented in larger dotted dark line 1100°C 1h, 980°C 1h, 720°C 8h and 625°C for 8h. Modified homogenization of 40 min at 1186 °C [16] in red dotted line. Optimization studied for 1h at 1080 °C and 980 °C for 15 min [127]. Heat treatment time reduction by Sui *et al.* [73] represented by purple line.

To prevent grain growth and loose hardening benefit effect of equiaxed grain size in microstructure obtained with LMD-W in this study, a designed heat treatment must be achieved with limiting both the temperature and time during homogenization and by reaching sufficient Laves phase dissolution.

A.1.1 Experimental methods

Heat treatments were performed using a rapid cycle dilatometer, for heating, holding and quenching conditions in homogenization treatments with different times to follow the NbC and Laves phase fractions. The dilatometer is composed of a vertical chamber under a primary vacuum (5.10^{-4} mbar). The samples are holded by quartz push-hollow rods that also helps to follow deformation of the samples. The heating is performed using 4 lamps of 1000 W with mirrors in the chamber. Quenching was performed using helium gas to 300 °C and then air cooling. Resistivity of the sample can be followed as well as temperature with K-type thermocouples that are spot welded on the samples surface. The investigation of variation of homogenization time was performed on samples taken from a multitrack wall processed with condition A from table A.1.

Figure A.4a provides two processed multi-track walls from processing conditions in table A.1. The pyramidal shape of the walls is due to start and stop sequences of wire feeding that were not optimized when manufacturing the walls. The manufacturing conditions of samples A and B from table A.1 can therefore be compared in tensile and toughness properties, in order to see the effect of input energy on the mechanical properties. Heat treating these built multi-track walls was performed on a B. M. I. industrial furnace B53T 2012 with partial vacuum and inert gas (Ar), the volume capacity is 1 m^2 and maximal temperature of 1200 °C. Such furnace reproduce industrial conditions for heat treatments with non-vacuum atmosphere.

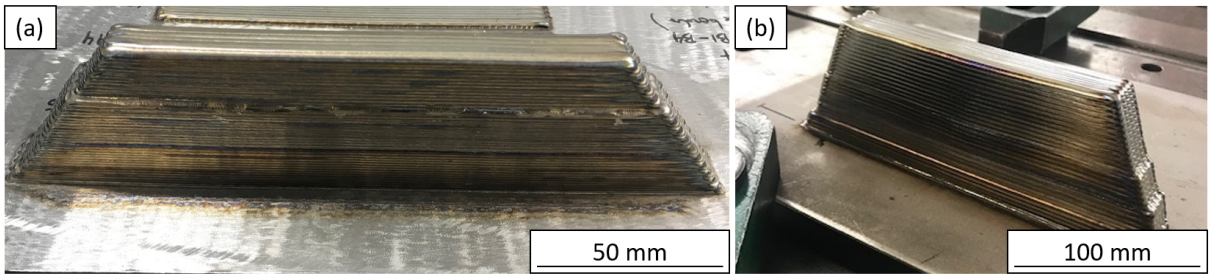

Figure A.4: Multi-track built walls (a) A processing condition and (b) B condition from table A.1, for heat treatment and mechanical characterization.

Table A.1: Processing conditions of multi-track walls for heat treatment and mechanical characterization.

Sample	P (W)	V (m/min)	Wf (m/min)	Energy density (J/mm^3)
A	2200	1.2	1.8	366.7
B	1700	0.6	1.5	515.5

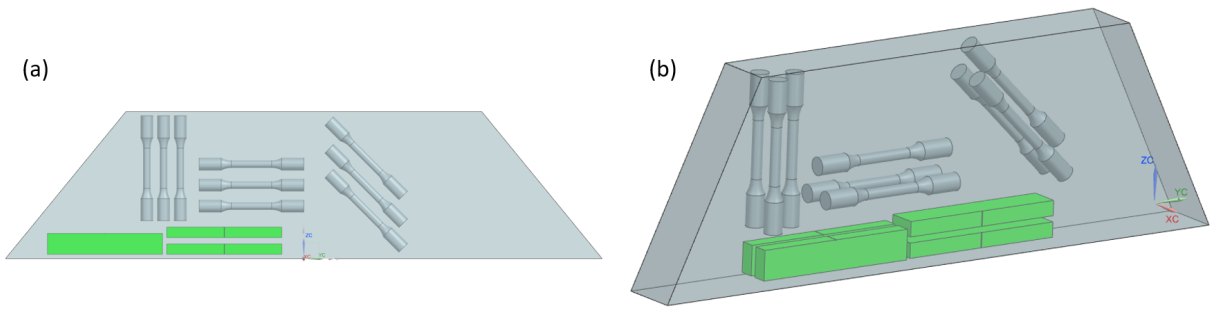

Figure A.5: Tensile and toughness specimens sampling in both multi-track walls (a) A and (b) B. Different orientation is present for tensile specimen: horizontal, vertical and 45°.

A.1.2 Results and discussion

Figure A.6 shows the resistivity signal of the as-deposited alloy during a standard homogenization treatment of 1 h at 1100°C. An acceleration of the signal is observed at the beginning of the treatement, in the first 5 min, then the rest of the linear curve is considered as variation of volume. The fraction of Laves phase present in the microstructure at start being very little (3.2 %). At the end of the treatment the Laves phase fraction drops to 2 %. It seems difficult to have a clear signal of this phase dissolution, but it is worth noticing an important resistivity variation at the beginning of the homogenization step. Therefore, lower time/temperature homogenisation steps can be investigated.

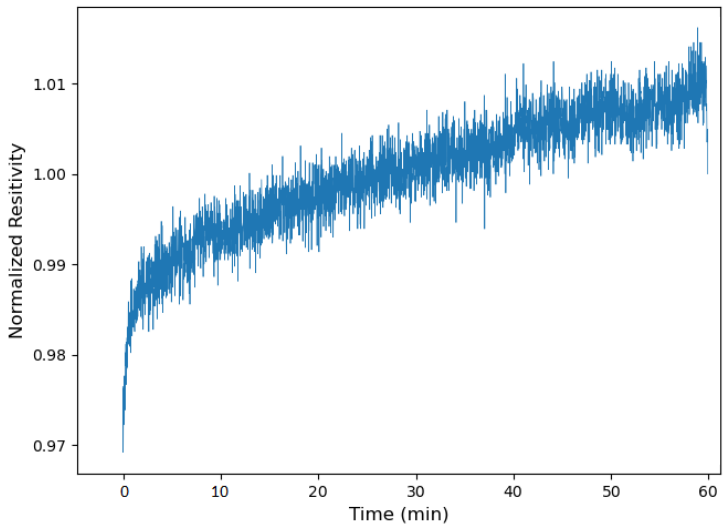

Figure A.6: Resistivity signal normalized over time during standard homogenization step treatment of 1h at 1100 °C.

Figure A.7 provides the evolution of Laves phase and NbC fraction over time for an annealing at 1070 °C, analysed by contrast on the BSE images on blocks of built samples in same conditions of 2200 W, advance speed of 1.2 m/min and wire feeding rate of 1.8 m/min. The fraction starts at 4.1 % for as built material in the equiaxed grain zone, the microstructure is shown in Figure A.8, and drops already at 2.2 % after 5 min of holding time. The fraction is decreasing slightly after 25 min to 2%. Such tendency seem to be similar to the high resistivity variation previously discussed in Fig. A.6, in the first minutes of the heat treatment, as Liu *et al.* also observed during solution treatment [18]. The stagnation of the fraction from 5 to 25 min is curious, most probably indicating the presence of NbC carbides that needs higher and longer time to dissolve and some residual Laves phase.

The corresponding evolution of the microstructure is shown in Figure A.9 for 5 (a-d), 15 (b-e) and 25 min (c-f) respectively. It can be seen that the Laves phase has dissolve importantly at 5 min, while the NbC carbides are remaining in both columnar and equiaxed grain zones (Fig. A.9a). δ phase is identified where large eutectic regions used to be, in Fig. A.9b. Local enrichment of Nb can lead to an increase of the kinetic and temperatures formation of the secondary phases [19]. The same observation can be made for the holding time at 15 min, as shown in Fig. A.9b-e. But for 25 min of holding time, precipitation at grain boundaries of oxides is present, due to slight presence of oxygen in the dilatometer, representative of industrial conditions. The holding time of 15 min seem to be a good compromise between the efficient Laves phase dissolution and limiting the time for both grain growth and oxides formation. It should be stressed that some residual Laves phase can most probably remain in the equiaxed region compared to

the columnar zones. Both of the processed walls with A and B conditions were subjected to the heat treatment provided in Figure A.10 with 15 min at 1070 °C of homogenization step and respectively precipitation steps for 8h each, in an industrial furnace.

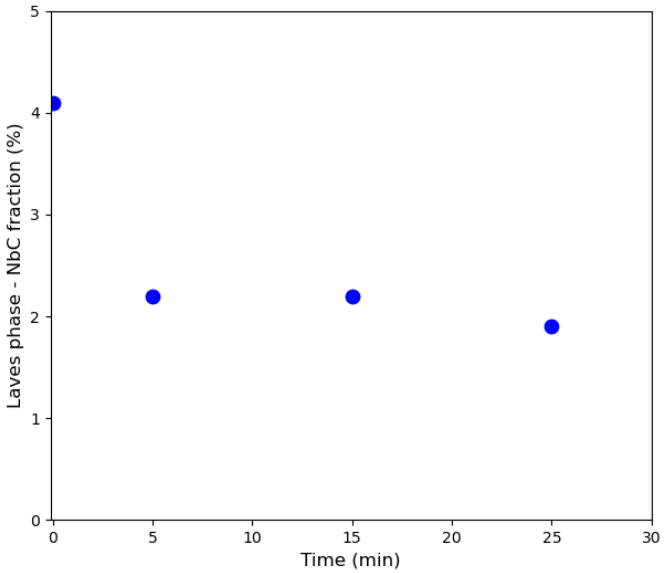

Figure A.7: Laves phase and NbC measured fraction depending on holding time variation during homogenization at 1070°C.

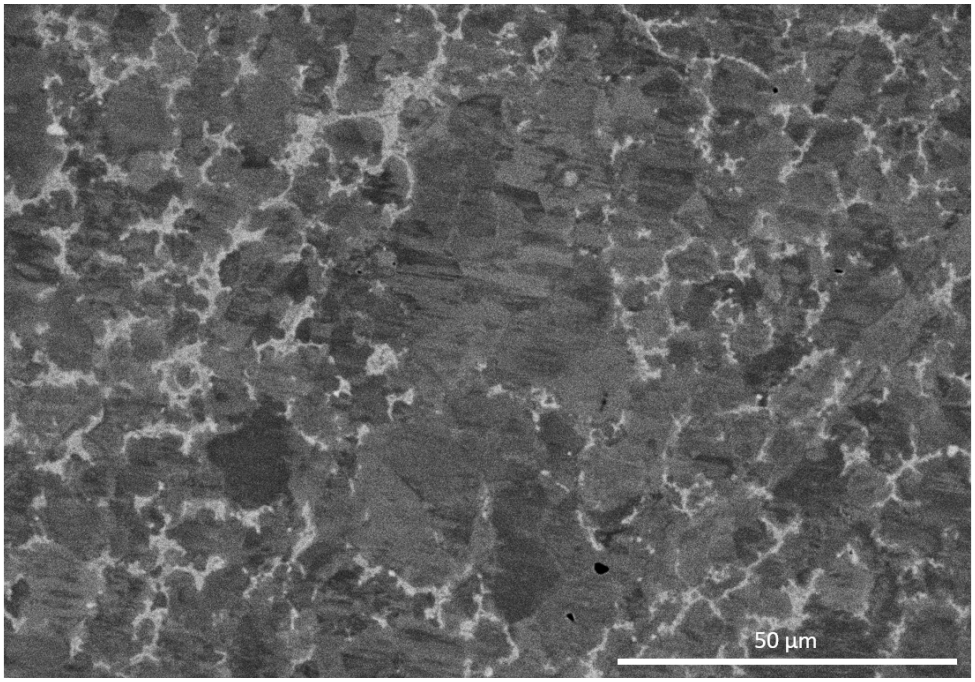

Figure A.8: BSE image of the as-built microstructure. Laves phase are light grey contrast.

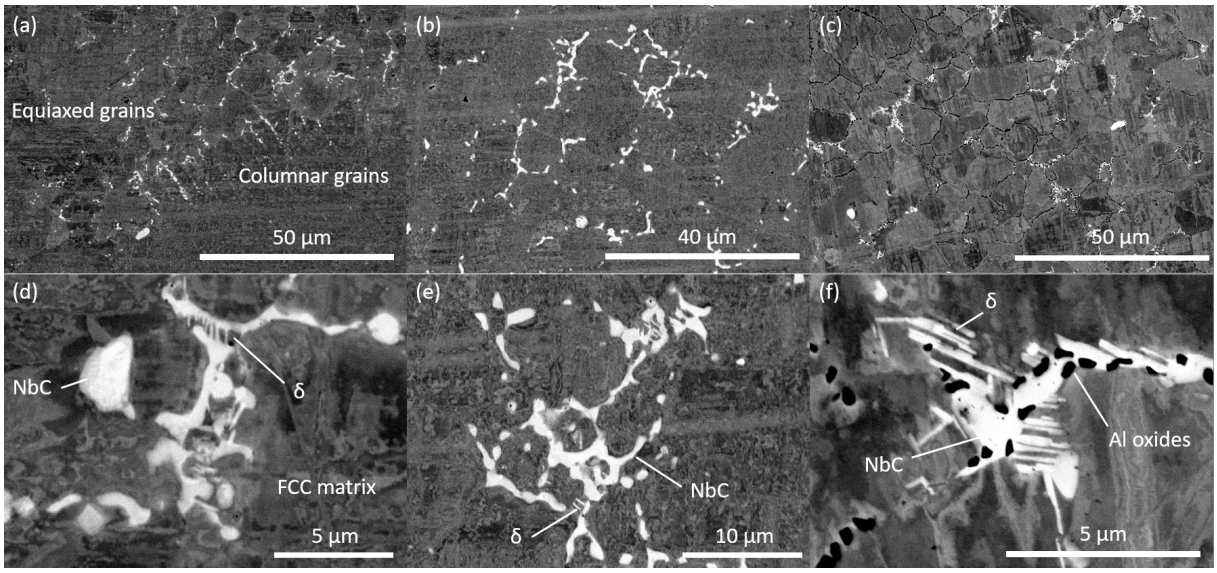

Figure A.9: BSE images of samples homogenized at 1070 °C for (a-d) 5 min (b-e) 15 min (c-f) 25 min.

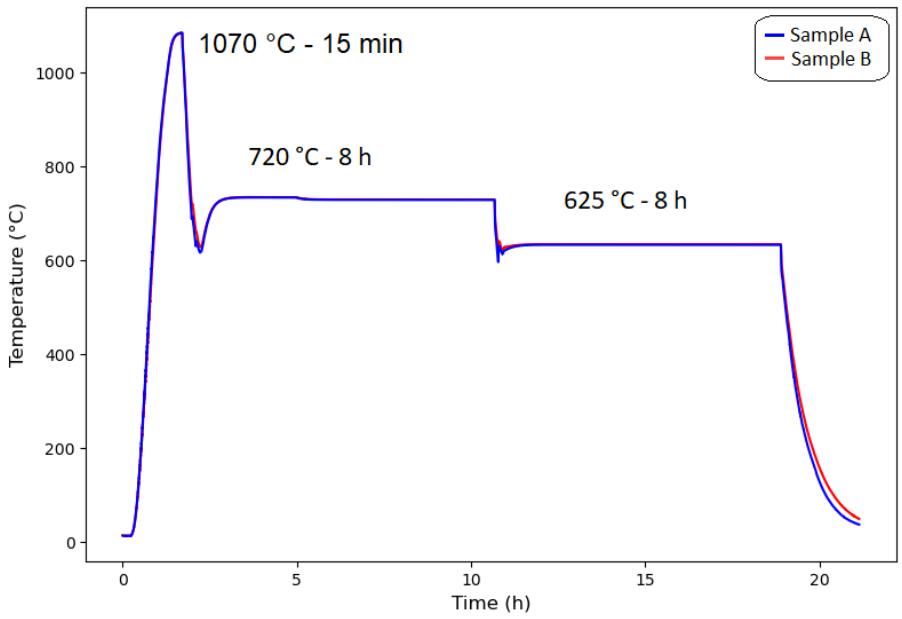

Figure A.10: Heat treatment of the manufactured walls for mechanical characterization: 15 min at 1070°C, 720°C for 8h and 625°C during 8h.

A.2 Mechanical properties

A.2.1 Results

Tensile properties

The different tensile specimens taken from both samples A and B from previous table A.1 enable us to show the effect of texture and building strategy on the tensile properties.

Figure A.11 provides an example of resulting tensile stress-strain for specimens taken in horizontal direction from samples A and B. Differences such as in yield strength, ultimate strength as well as strain are regularly visible between the specimen. In this specific example, the horizontal specimen taken from B present higher yield and ultimate strength than A, but 10 % less in strain.

The different tensile properties can be compared separately depending on the orientation of specimens. Figure A.12 present the evolution of (a) yield strength (MPa), (b) ultimate strength (MPa) and (c) strain (%) separately depending on the orientation of specimens. The yield strength is respectively 1172 MPa and 1174 MPa, that are the same for both samples A and B in the vertical direction. Same statement can be made for the ultimate strength, that is 1315 MPa for sample A and 1305 MPa for sample B. But the elongation is more 10 % more important for the sample A. The horizontal properties are much different. The sample B has superior strength properties, since its yield strength increase up to 1277 MPa and an ultimate strength of 1464 MPa. The elongation is again more important for the sample A, and as well for the specimen at 45 degree. For this direction of 45 degree, the sample A present higher tensile properties.

Such properties are averaged per sample and presented in table A.2 for comparison with literature findings for AM and conventional processes. The yield strength from this work is similar to the SLM and laser weld after heat treatment which is is higher than wrought and other processes. The ultimate strength is more homogeneously distributed among results. The ultimate strength for LMD-W is inferior to SLM and laser weld, but is already achieving the higher values from literature. The elongation shows the important difference of behaviour between samples A and B. The higher input energy leads to coarser microstructure as well as increasing potential defects in the microstructure, which could explain the lower elongation for sample B and therefore shows the importance of processing parameters. This makes the lower energy input for sample A a good example of processing condition since the elongation is close to LMD-P, SLM and EBM processes with high cooling rates involved. Grain refinement in equiaxed zones largely present in the layers induces heterogeneous microstructure and lower texture, which contribute to increase the tensile properties to the rank of SLM and other high cooling rate processes.

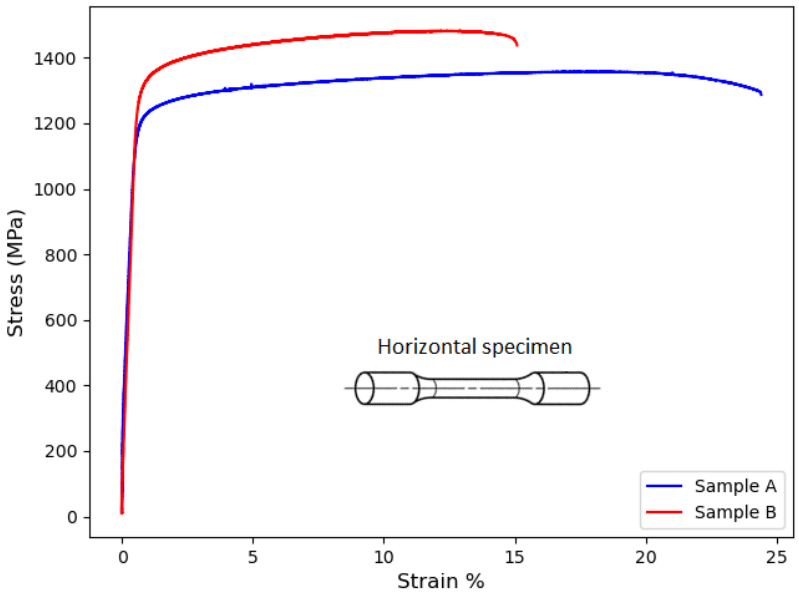

Figure A.11: Example of comparison of tensile stress-strain evolution for 2 horizontal specimen from sample A and sample B.

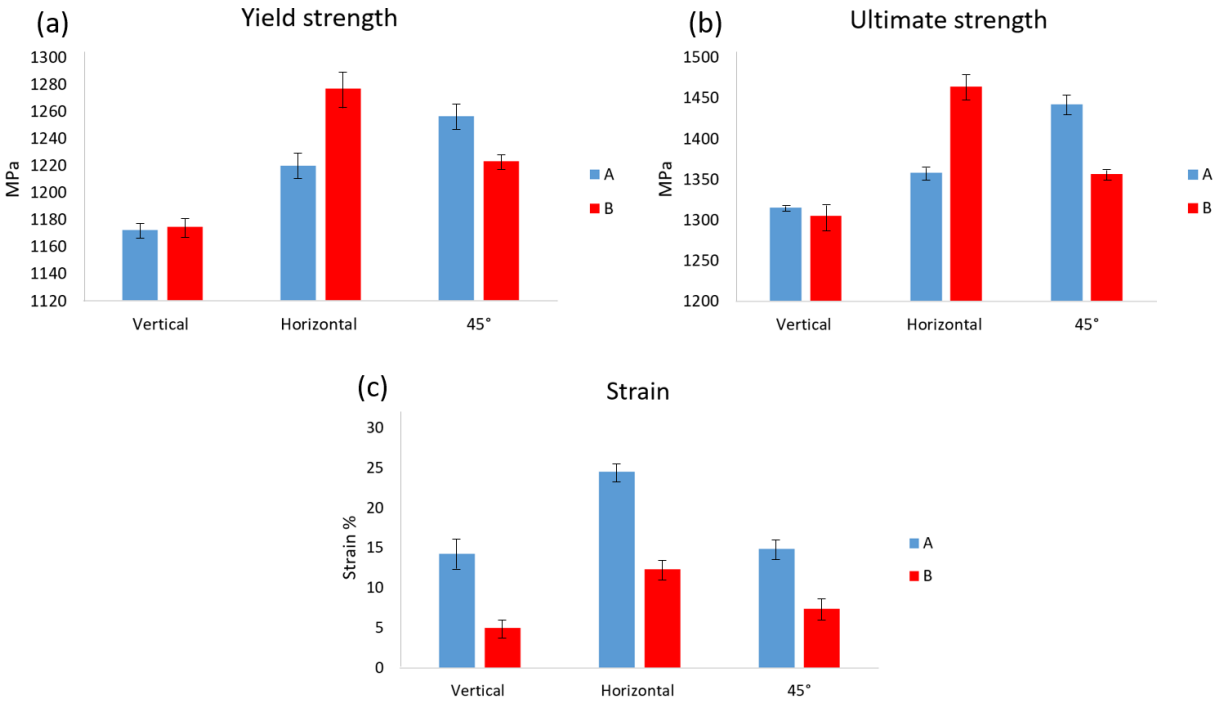

Figure A.12: Evolution and comparison of tensile properties for vertical, horizontal and 45° specimen: (a) yield strength (MPa) (b) ultimate strength (MPa) and (c) strain (%).

Table A.2: Tensile properties of the LMD-W specimen and literature findings after heat treatment for Inconel 718.

	Yield strength (MPa)	Ultimate strength (MPa)	Strain (%)	Ref.
LMD-W Sample A	1216 ± 21	1372 ± 32	18 ± 3	this work
LMD-W Sample B	1225 ± 25	1375 ± 40	8 ± 2	this work
LMD-P	992 ± 4	1245 ± 2	15 ± 3	[73]
LMD-P	1170	1360	18	[130]
SLM	1087 ± 8	1385 ± 6	23 ± 1	[131]
SLM	1241 ± 68	1457 ± 55	14 ± 5	[132]
EBM	1122 ± 17	1300 ± 22	25	[133]
WAAM	1081 ± 26	1245 ± 23	12 ± 3	[131]
Laser weld	1237	1460	16	[134]
Wrought	1034	1241	12	[135]

Toughness

The table A.3 shows the toughness properties of the LMD-W specimen from sample A and B. Previously, the yield and ultimate strength were higher for sample B, and the same tendency is observed for the toughness. The sample B present higher toughness and can achieve wrought strength values while the Sample A is rather similar to SLM findings.

Table A.3: Toughness of the LMD-W specimen and literature findings after heat treatment.

	Toughness	Ref.
LMD-W Sample A	28	this work
LMD-W Sample B	33.4	this work
SLM	25	[136]
SLM	28.8 - 31.9	[137]
Wrought	33 - 38	[138]

Appendix B

Determination of the icosahedral symmetry from EBSD grain-to-grain analysis

Figure B.1 shows the EBSD map used to perform the grain-to-grain analysis as this area contains a high twin frequency. The area of interest is circled in the Figure and the grain presented in the chapter 4 can be seen. The following will detail precisely on how the icosahedral symmetry was determined from the grain-to-grain EBSD analysis and compared to the theoretical orientation of the icosahedron.

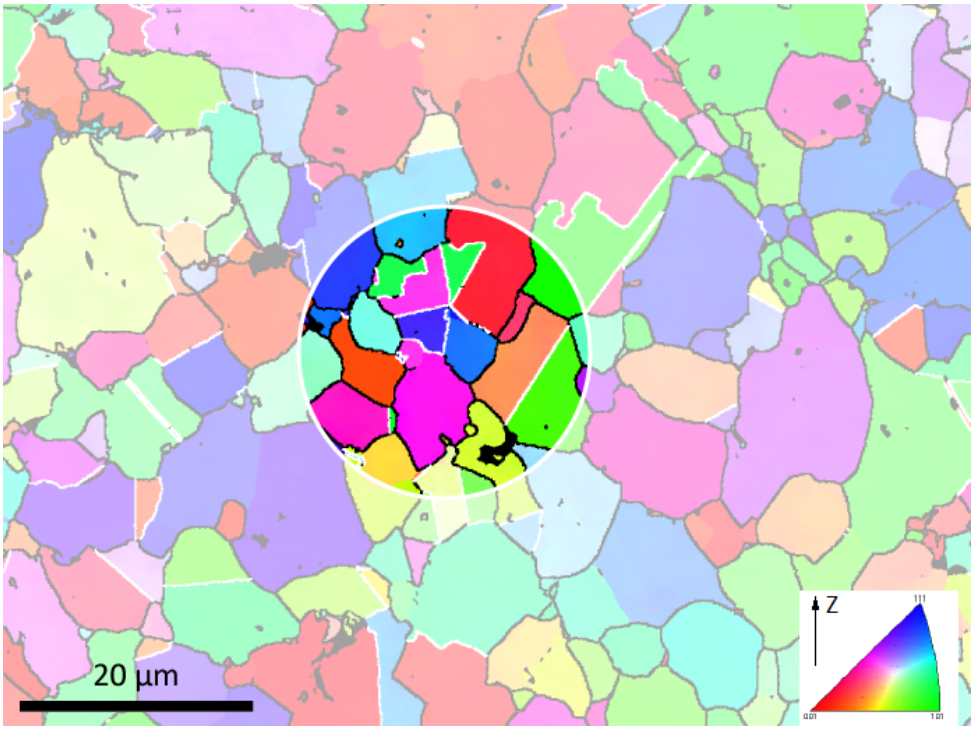

Figure B.1: EBSD map with IPF colouring in the Z direction of the equiaxed zone showing the grains analyzed in the following (circled zone). The twin grain boundaries are white lines and regular grain boundaries are black lines.

For sake of clarity and in order to visualise more easily the different orientations between grains, a change of the reference frame will be done to align the common ⟨110⟩ axis with the Z axis of the pole figure and one of the ⟨111⟩ common plane with the X axis of the pole figure. This change is shown in Figure B.2 for the grains labelled 1-5. The common ⟨110⟩ direction is now centered in the ⟨110⟩ pole figure. The analysis presented in the chapter 4 is given in the new reference frame in Figure B.3 and B.4. As can be seen from Figure B.3, each twin plane has a 72.5 deg. rotation through the common ⟨110⟩ direction: the twin plane between grain 2 and 3 is rotated by 72.5 deg. compared to the twin plane between grain 1 and 2, and so on for 3 and 4, 4 and 5, 5 and 1. As demonstrated by Kurtuldu *et al.* in Al and Au based alloys [2, 1], the common ⟨110⟩ directions correspond to the 5-fold axis of the icosahedron if the ISRO-mediated nucleation mechanism is involved. The results presented so far are compatible with the symmetry of a decahedron; which is necessary but not sufficient to prove an icosahedral symmetry. This is shown is Figure B.4(b) where an icosahedron is represented and coloured with the same colour code as in Figure B.2(a) and B.4(a). To demonstrate the icosahedral symmetry, it is neccesary to identify other grains that are in twinning OR with grains 1, 2, 3, 4 or 5 (and would correspond to the greyed facets in Figure B.4(b)) and share common ⟨110⟩ directions with the neighbouring grains.

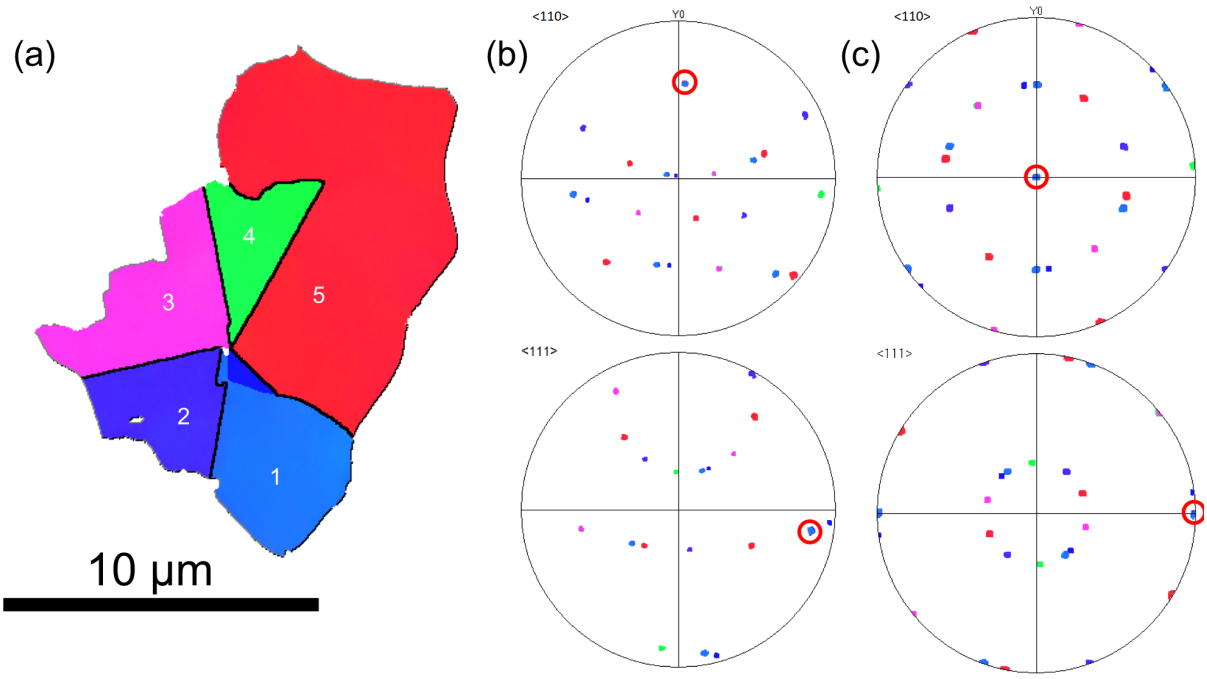

Figure B.2: (a) Grains in twin relationship displayed from fig.B.1 with IPF coloring, (b) ⟨110⟩ and ⟨111⟩ pole figures in the sample reference frame and (c) in the new reference frame. The red circle in the ⟨110⟩ pole figures corresponds to the ⟨110⟩ direction which is common to grains 1 to 5 and the red circle in the ⟨111⟩ pole figures corresponds to the common plane between grains 1 and 2.

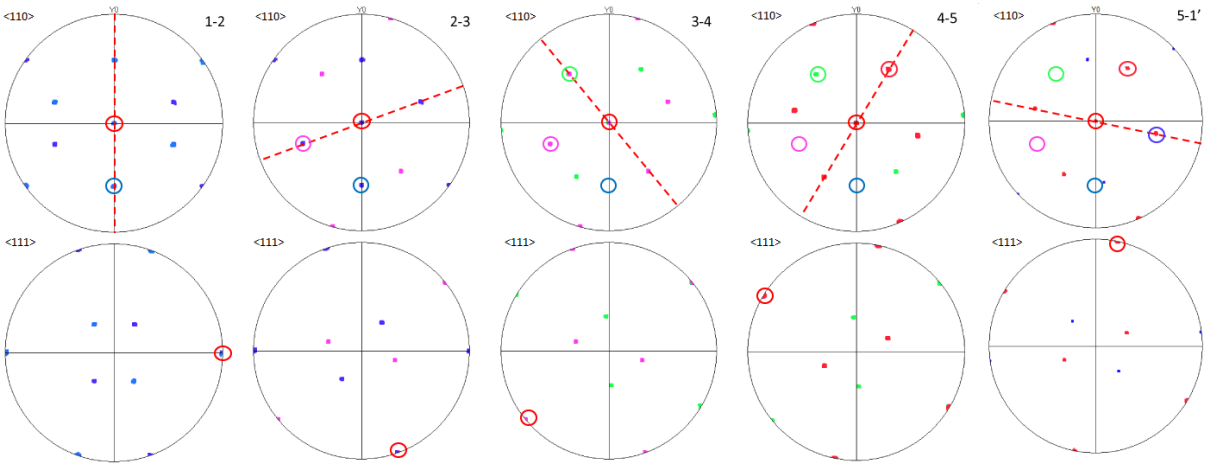

Figure B.3: ⟨110⟩ and ⟨111⟩ pole figures for grain 1-2, 2-3, 3-4, 4-5 and 5-1. The red dashed lines shows the common {111} planes and the coloured circles shows common ⟨110⟩ axis.

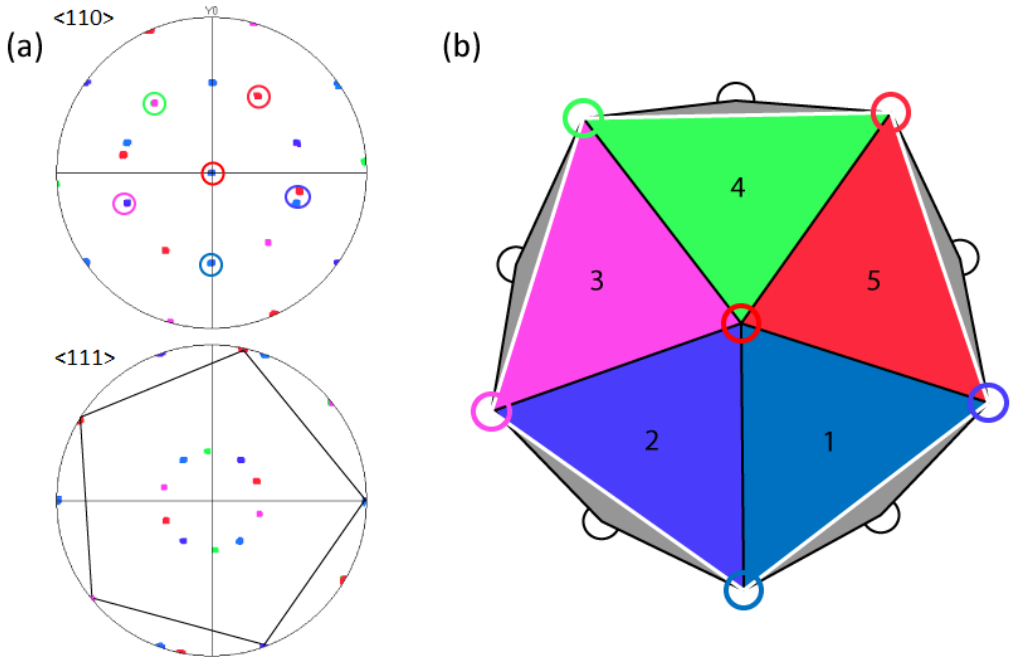

Figure B.4: (a) Summary of the common ⟨110⟩ directions and common ⟨110⟩ poles taken from Figure B.3, (b) Schematic representation of an icosahedron with respect to the determined common ⟨110⟩ axis.

Two grains fulfilling these conditions where found and labeled 6 and 7 in the chapter 4. Their ⟨110⟩ pole figures are presented in Figure B.5(a-c):

- Grain 6 has a twinning OR with grain 2, and also share a common ⟨110⟩ direction with grains 1 and 3.
- Grain 7 has a twinning OR with grain 4, and also share a common ⟨110⟩ direction with grains 3 and 5.
- Grains 6 and 7 have a near-twin OR.

It allows to update Figure B.4(b) to obtain Figure B.6: while 3 grains are missing to characterise fully the icosahedral symmetry, the seven grains that have been analysed give 5 out of 6 possible of the 5-fold symmetry axis and the OR between all the grain are compatible with the icosahedral symmetry only. In Figure B.6, the common ⟨110⟩ directions have been labelled from *g* to *l*.

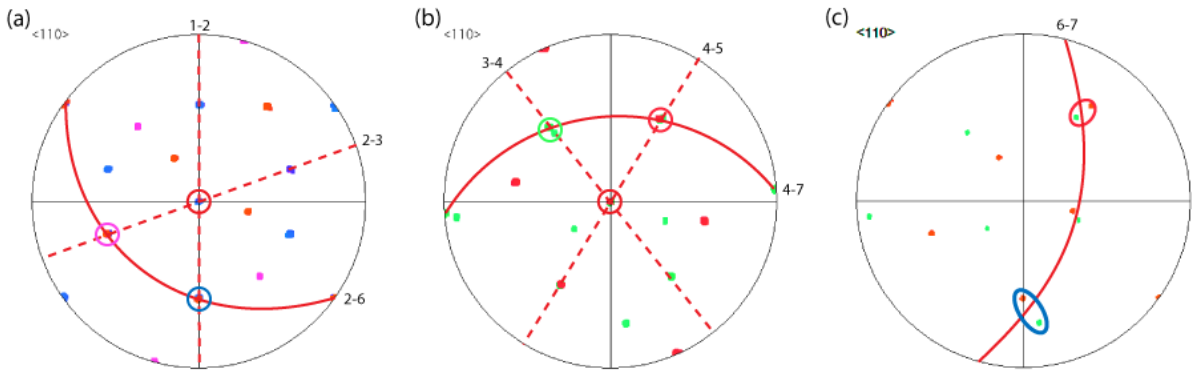

Figure B.5: ⟨110⟩ pole figures showing (a) the common planes and direction between grains 1-2, 2-3, and 2-6, (b) grains 3-4, 4-5 and 5-7 and (c) the near-twin orientation relationship between grains 6 and 7.

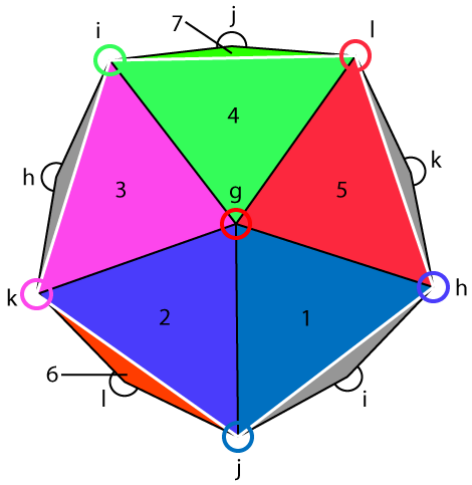

Figure B.6: Schematic representation of an icosahedron with respect to the analysis made for grains 1 to 7.

Figure B.7 shows the ⟨110⟩ pole figures back in the sample reference frame, as shown in the main text. All the common ⟨110⟩ direction determined from at least 3 grains are indicated with circles, with the same colour code as previously. Only the ⟨110⟩ axis labelled *h* is not represented, since it can be determined from only two grains (1 and 5). The last pole figure summarize the position of all the common ⟨110⟩ directions compatible with the symmetry of the icosahedron.

In order to give an additional proof that the nickel fcc grains originate from an icosahedral template, the theoretical pole figure that would be obtained from an icosahedron has been calculated. An icosahedron can be build from 3 orthogonal golden rectangles (whose side lengths are in the golden ratio) as shown in Figure B.8(a), in which a cartesian coordinate system has been defined. As shown in Figure B.8(b), all the 5-fold symmetry axis correspond to the vector between the center of the icosahedron and the vertex of the rectangles; it is then easy to express these 5-fold axis in cartesian coordinate system and plot them as stereographic projections. After having rotated the theoretical icosahedron to have the same orientation as the one determined from EBSD analysis, the obtain stereographic projection is given in Figure B.9(a) (including ⟨110⟩ directions connecting the 5-fold axis) and the experimental ⟨110⟩ pole figure obtained for grains 1 to 5 is given in Figure B.9(b). The match between the two figures is excellent.

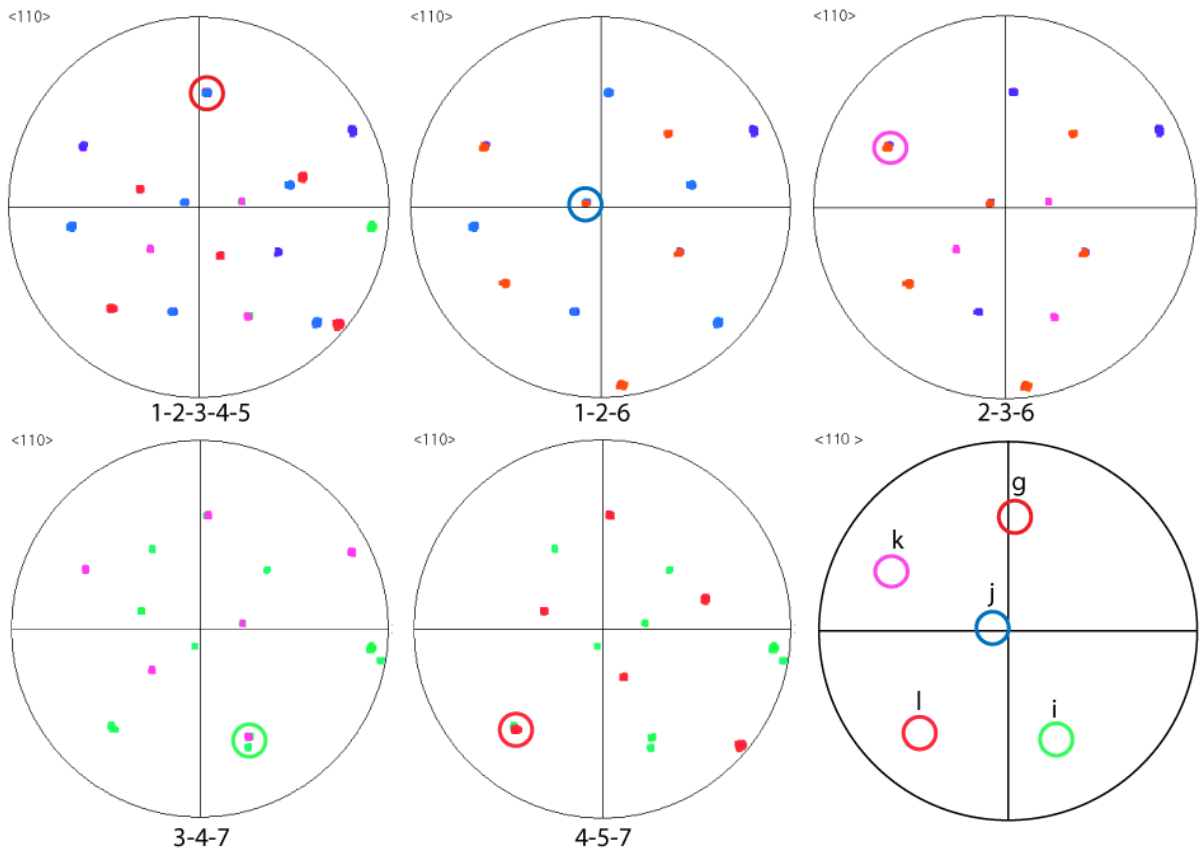

Figure B.7: ⟨110⟩ pole figures in the sample reference frame showing the ⟨110⟩ directions common to at least three grains. The last pole figure summarise the common ⟨110⟩ direction that are labelled from g to l.

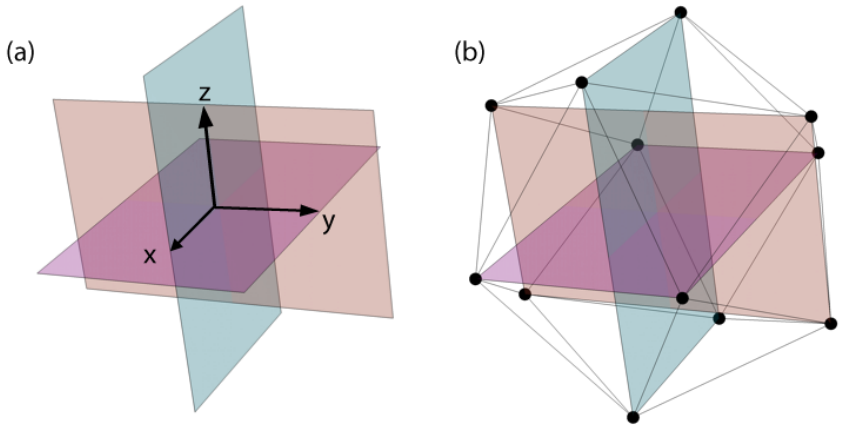

Figure B.8: (a) Construction of an Icosahedron with 3 planes in the X-Y-Z reference (b) each corner of the equidistant planes represents a 5-fold symmetry axis of the icosahedron and are connected with ⟨110⟩ directions.

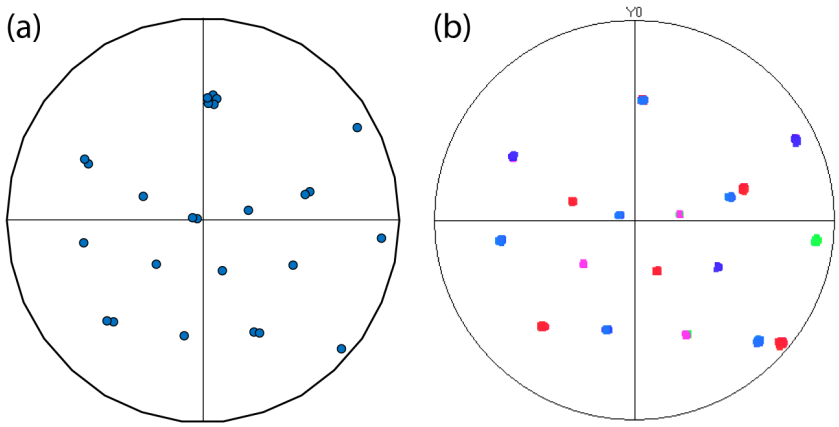

Figure B.9: (a) Simulated stereographic projection of the 5-fold axis of a theoretical icosahedron in the sample reference frame (b) experimental pole figure obtained for grains 1 to 5.

Appendix C
Characterization of the Laves phase C14

C.1 X-ray diffraction characterization

An eutectic between the Laves phase Ni_2Nb C14 and the Ni fcc was processed using a cold crucible with the chemical composition measured from Laves phase encountered in the processed alloy, presented in table C.1. Figure C.1 shows a BSE image of the C14-fcc eutectic, where a C14 grain can be taken for further analysis.

Table C.1: Chemical composition of the processed eutectic C14-FCC (wt.%).

Ni	Nb	Cr	Fe	Ti	Al	Mo
44	22	14	13	2	0.5	4.5

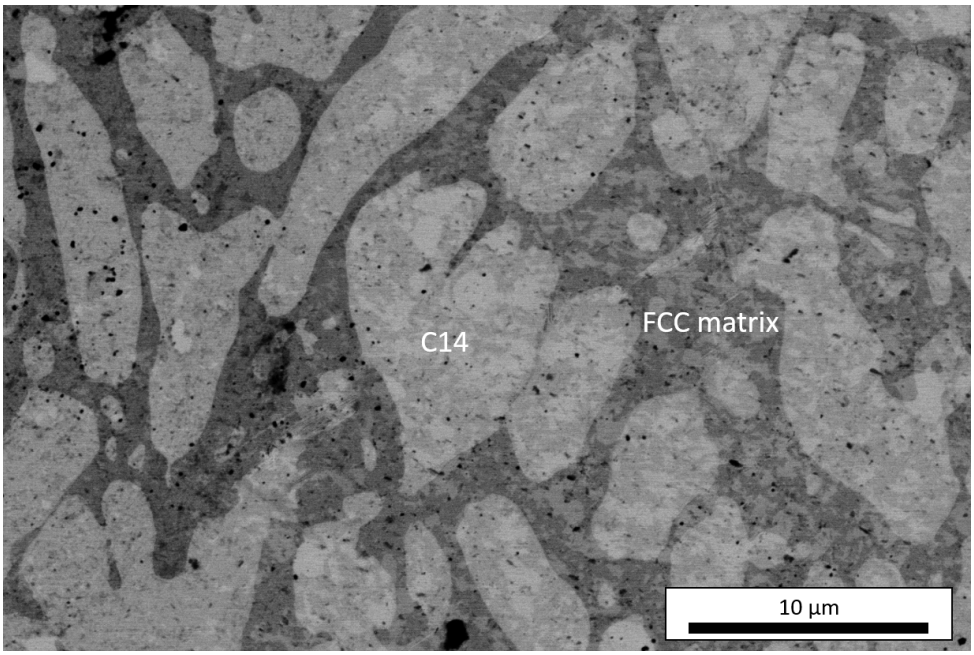

Figure C.1: BSE image of the eutectic C14-FCC.

Figure C.2 is the X-ray diffraction patterns of a single C14 grain, where the hexagonal structure can clearly be observed. From X-ray measurement, the following lattice parameter could be determined:

a = 0.481nm and c = 0.738nm, equal to literature findings [13] with the space group $P6_3/mmc$. The determined $(Ni,Cr,Fe)_2(Nb,Mo,Ti)$ structure possess 95% Ni and 5% (Fe,Cr) at the Ni atomic sites in the lattice structure, that are Wyckoff positions $6h$ and $2a$ indicated in Fig. C.3. On the other hand, the Nb sites $4f$ are occupied with 60% Nb, 38% Mo and 2% Ti. Such substitution is possible due to the close atomic sizes. Figure C.3 show the lattice structure with the different atomic positions.

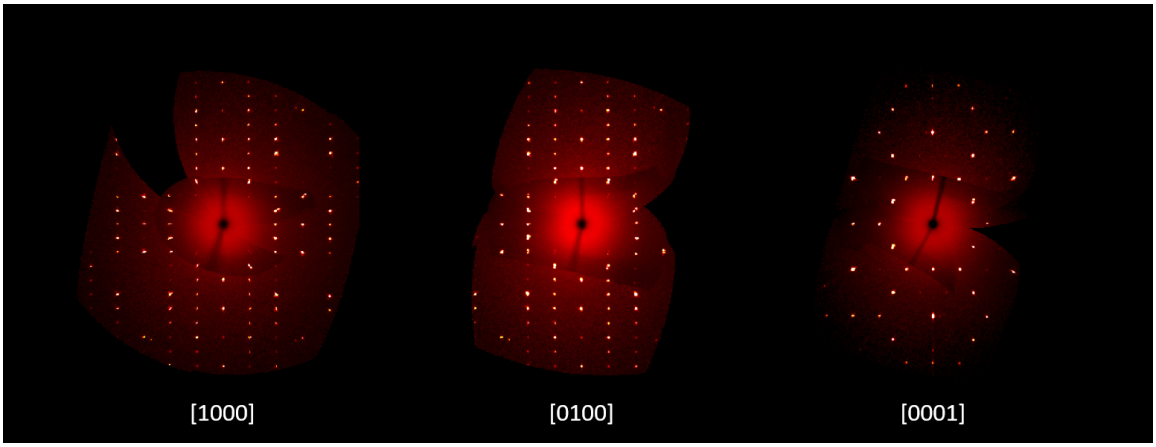

Figure C.2: X-ray diffraction patterns of a monocrystal of C14 illustrating the hexagonal symmetry of the structure.

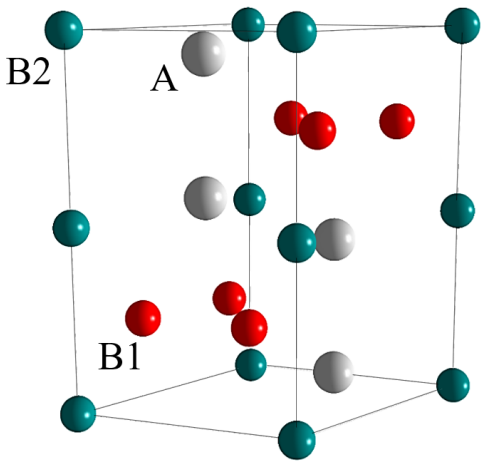

Atom	Wyckoff position	x	y	z	Ideal	Figure symbol
$B1$	$6h$	x	$2x$	$1/4$	$x = 1/6$	
A	$4f$	$1/3$	$2/3$	z	$z = 9/16$	
$B2$	$2a$	0	0	0		

Figure C.3: Lattice structure of the Laves phase C14 with atomic sites labelled with their corresponding positions. Table taken and modified from [117].

C.2 TEM characterization

A thin foil can be extracted from the eutectic region presented in Fig. C.1 and observation can be done using TEM. Figure C.4 shows a TEM image of the zone of interest. It can be noted that an isolated grain was identified in the matrix to be a Frank-Kasper phase with an orthorhombic lattice structure (Cmmm) with $a = c = 0.45$nm and $b = 1.75$nm from its diffraction pattern in Fig. C.4a. The Laves phase C14 can be identified through its [0001] zone axis as shown in Figure C.4b with lattice parameters of $a = 0.48$nm and $c = 0.78$nm as determined using XRD. It is uncommon to observe such needle-like growing phase in the fcc, that seem to form on the edge of the fcc grains.

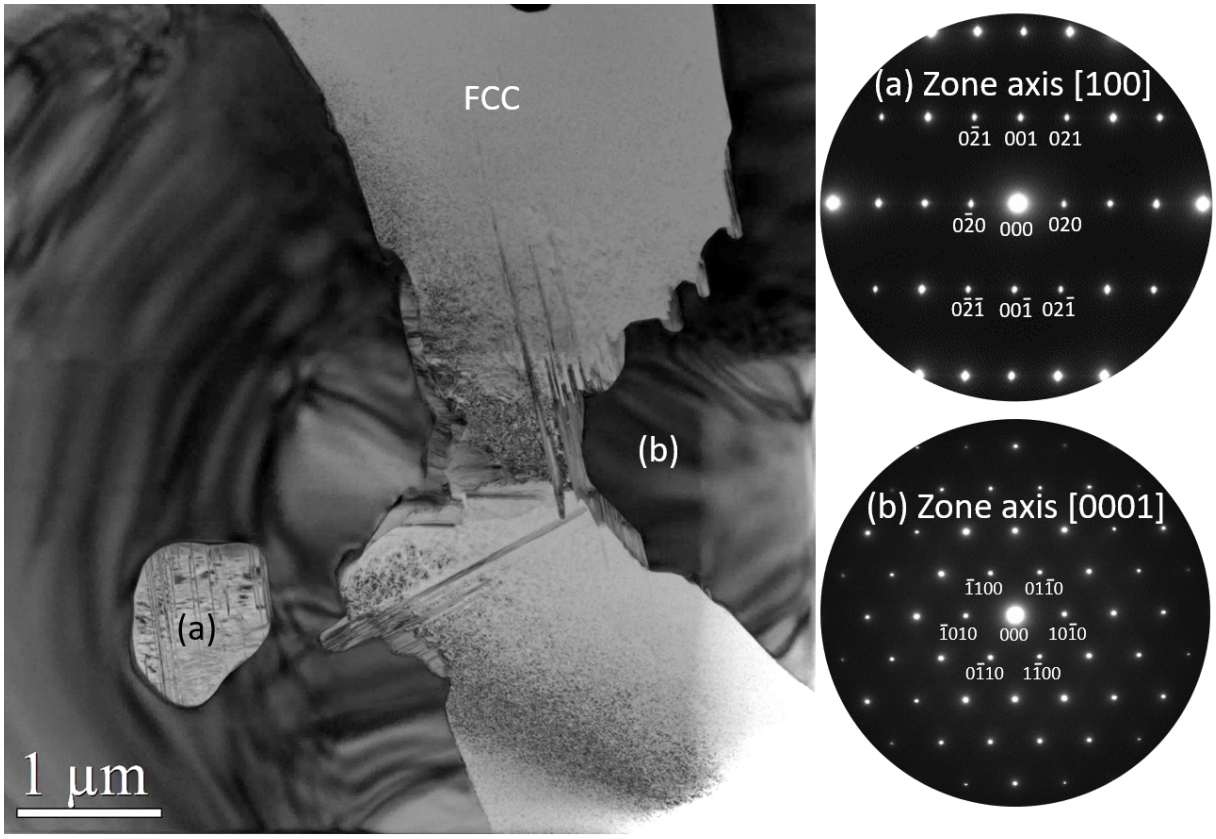

Figure C.4: TEM micrograph of the eutectic zone between the fcc matrix and the Laves phase C14. Diffraction patterns of (a) [100] zone axis of isolated Frank-Kasper phase showing the orthorhombic structure (b) [0001] zone axis of the C14 Laves phase.

Figure C.5 shows a STEM micrograph of the thin foil with the corresponding EDS map of selected area. It shows that the matrix is depleted of Mo and Nb, while the identified Frank-Kasper phase is enriched with Ni and Ti. The needle like phase is also present within the fcc matrix with similar chemical contrast as the Frank-Kasper identified phase.

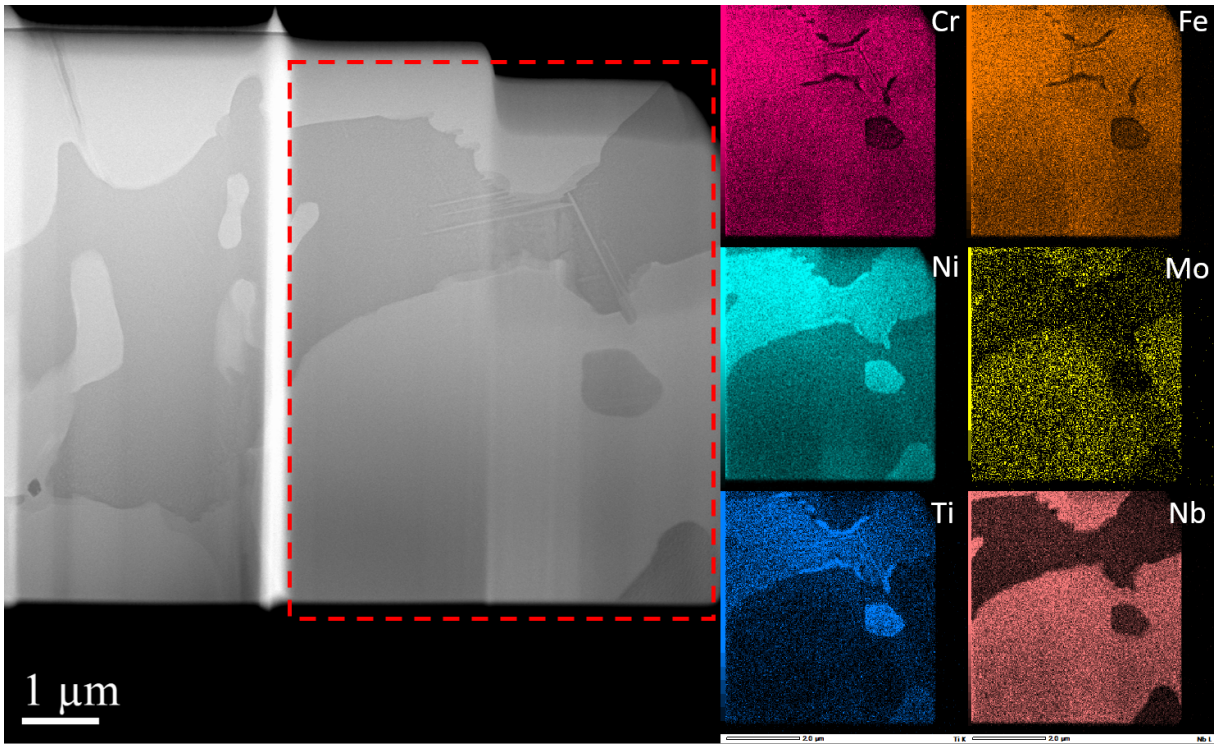

Figure C.5: STEM micrograph of the eutectic fcc/Laves (C14) region with EDS map of the indicated zone (dashed line).

Figure C.6 present the theoretical C14 structure along [0001] zone axis with Nb-Mo-Ti in orange and Ni-Cr-Fe in blue atoms. The corresponding STEM HAADF image along [0001] is shown in Fig. C.6, where the Nb/Mo enriched atomic columns appears more intense and Ni/Cr/Fe are harder to observe (darker contrast). Same observation can be made in Fig. C.7a where the intensity of the selected area is represented in Fig. C.7b. The intensity is proportional to the atomic number, therefore the higher peaks corresponds to the heavier atomic columns (Nb/Mo) while the lighter corresponds to lighter atoms (Ni-Cr-Fe). It is worth noticing that the intensity of the peaks is varying within the lighter elements and more importantly also at the positions of Nb-Mo. For the Nb-Mo peaks, the squared ones are lower then the others meaning less Nb-Mo atoms are present. On the other side, some lighter element peaks seem higher, showing perhaps presence of heavier elements. This information indicates that the element distribution seem to vary and is also observed for other atomic columns.

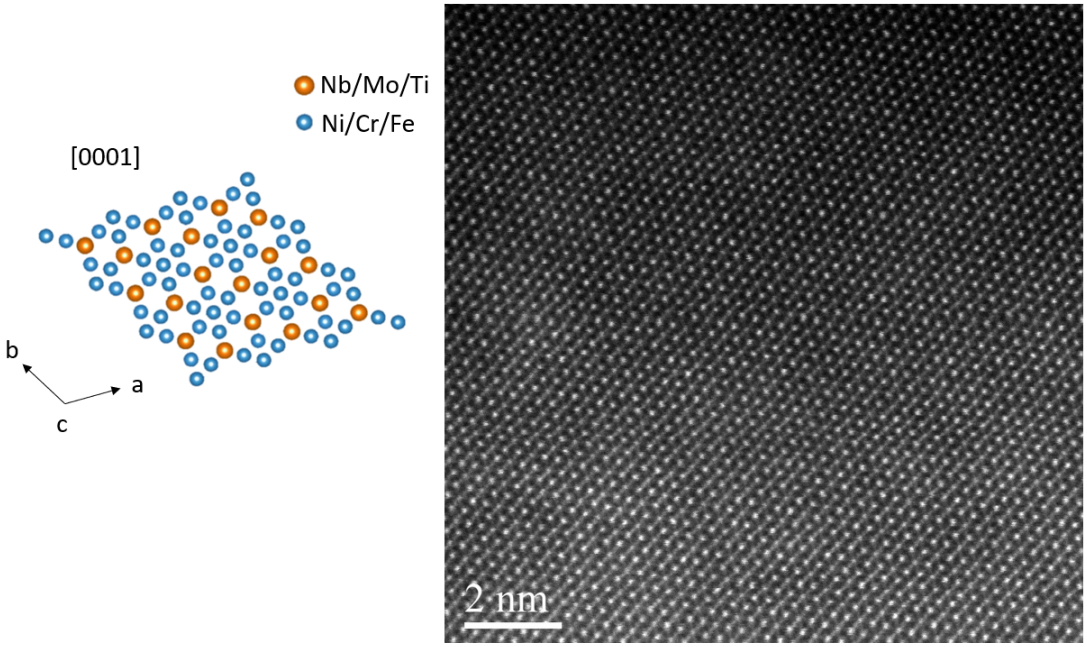

Figure C.6: Theoritical representation of the structure of Laves phase C14 along zone axis [0001] and STEM HAADF micrograph of the atomic columns along [0001].

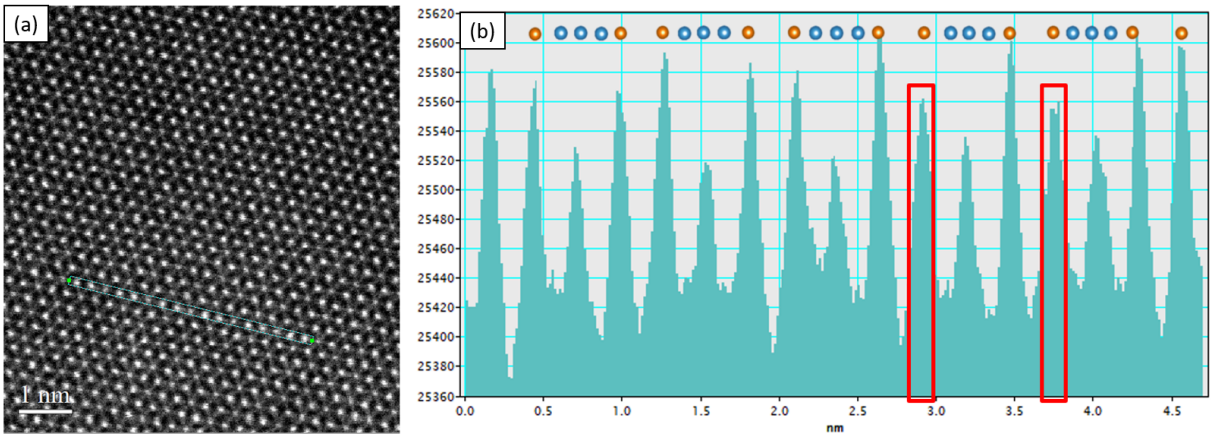

Figure C.7: (a) STEM HAADF micrograph along [0001] with (b) corresponding intensity per atomic column for the selected area line. Higher intensity pics corresponds to heavier atoms such as Nb/Mo. Pics that have lower intensity are squared in red.

Figure C.8 shows an Electron energy loss spectroscopy (EELS) map of Cr-Fe-Ni-Ti in order to see which columns contains these enumerated elements. The Mo-Nb could not be identified with EELS technique due to their higher atomic number. The limit of the technique can be observed through deviation and highly sensitive to vibration during acquisition, that can be observed for the Ti map that is overestimated. Such maps can be combined, in order to see which positions are shared between the different elements, and is shown in Figure C.9a-b. As expected, the Cr-Fe-Ni shares the same atomic columns. On the other hand, the Ti position seem to vary since it is isolated in Fig. C.9a and sharing

common positions with the other elements in Fig. C.9b, that are encircled in red. It is logical that the Ti shares common positions with the Nb/Mo due to its close atomic radius and the results from XRD characterization, but unexpectedly it can be seen also present on the other element sites randomly. The inverse phenomenon could also be possible since of the important variations observed in Fig. C.7 at the Nb/Mo atomic columns. Such observation also shows the present polyhedra in the lattice structure C14 as shown in Fig. C.10a-b are composed of atoms varying their positions opening new possibilities of icosahedral configurations, as schematically illustrated in Fig. C.10c.

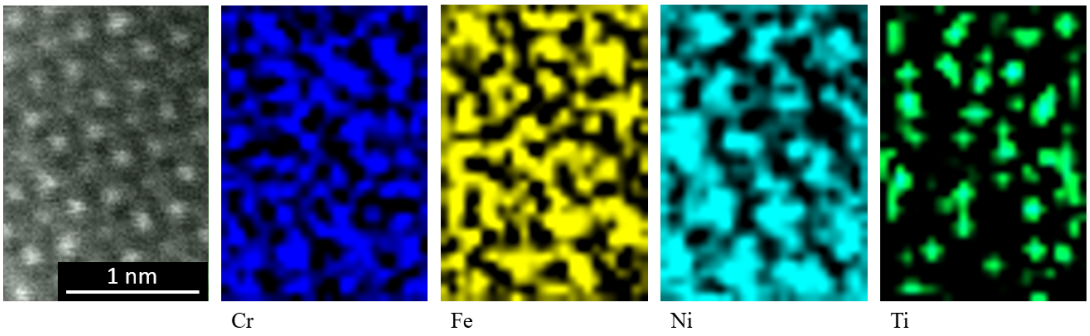

Figure C.8: EELS map showing the partition of Cr-Fe-Ni-Ti elements in the atomic columns, with smooth mask applied.

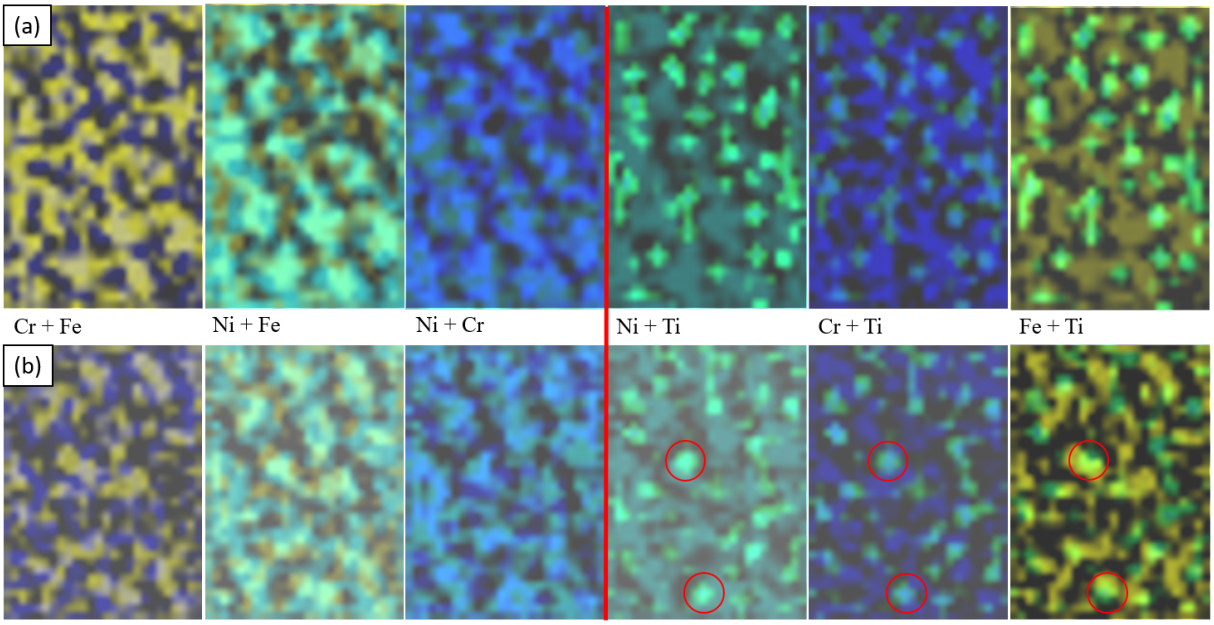

Figure C.9: Combination of the different elemental EELS maps for 2 different zones (a-b), where the elements Cr-Fe-Ni seem to share the atomic positions while for Ti in (a) separating from the other elements and (b) shares common positions (encircled in red).

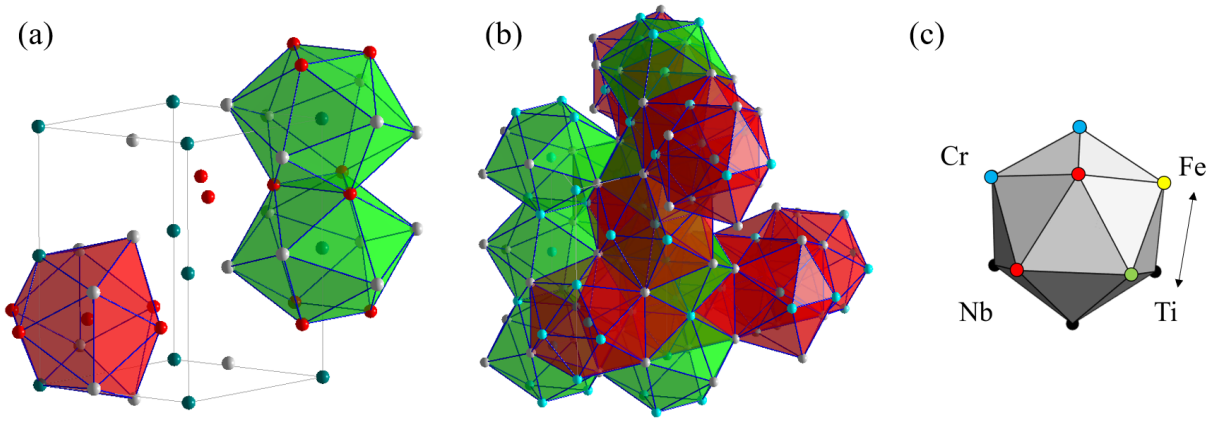

Figure C.10: (a) C14 Laves phase lattice structure with the two different types of icosahedra polyhedra (b) icosahedra network in the structure (c) Schematic example of substitution of Fe and Ti atoms in a icosahedron polyhedron.

Abstract

The use of Inconel 718 alloy in additive manufacturing has been the subject of numerous studies in recent years. It has appeared early that the control of the morphology and size of the grains forming during solidification is a formidable challenge. Our work aims to address this challenge in the case of coaxial laser wire technology by providing a better understanding of the formation of microstructures, including the conditions for the appearance of fine equiaxed grains observed at the bottom of the melt pools. First, the stability of the process as well as the thermal aspects have been investigated. Thanks to fast imaging and thermal imaging, we have been able to estimate the solidification conditions at the bottom of the bath. In a second step, we have analysed by EBSD the equiaxed zones and we have observed that they are very often clustered with twin relations compliant with some icosahedral symmetry. It is proposed that this particular organization is the signature of an "Icosahedral Short-Range Order mediated nucleation" (ISRO) mechanism, which would be favoured by the high cooling rates imposed by the process on the one hand, and by local enrichments of the liquid at the bottom of the melt pool during the melting of the previous layer on the other hand. We have therefore characterized the equiaxed zones by SEM and TEM. We have identified TiC carbides in the grain clusters and we have highlighted a strong local enrichment in Nb around the TiC by EDS. We have been able to identify Nb2Ni at the surface of a TiC carbide which requires a high local Nb composition to appear. From these observations we propose a possible scenario for the appearance of fine equiaxed grains in Inconel 718 deposited by the coaxial laser wire technology. TiC would play an important role by capturing minority elements during remelting, and by promoting local appearance of icosahedral clusters in the liquid that would favor the nucleation of grains whose relative orientations would reflect this icosahedral order.

Keywords : Solidification, Inconel 718, Laser - wire, Additive Manufacturing

Résumé

L'utilisation de l'alliage Inconel 718 en fabrication additive a fait l'objet de nombreuses études au cours des dernières années. Il est rapidement apparu que le contrôle de la morphologie et la taille des grains se formant durant la solidification constitue un véritable défi. Notre travail s'attache à le relever dans le cas de la technologie laser-fil coaxial en apportant une meilleure compréhension de la formation des microstructures, notamment des conditions d'apparition de grains équiaxes fins observés en fond de bain de fusion. En premier lieu, la stabilité du procédé ainsi que les aspects thermiques ont été étudiés. Ainsi, grâce à l'imagerie rapide et l'imagerie thermique, nous avons pu estimer les conditions de solidification en fond de bain. Dans un second temps, nous avons analysé par EBSD les grains équiaxes et révélé qu'ils sont très souvent regroupés en amas multi-maclés présentant une symétrie icosaédrique. Cette organisation est la signature d'un mécanisme «Icosahedral Short Range Order mediated nucleation» (ISRO), qui serait favorisé par les vitesses de refroidissement élevées imposées par le procédé d'une part, et par des enrichissements locaux du liquide en fond de bain lors de la fusion de la couche précédente d'autre part. Nous avons donc caractérisé finement les zones équiaxes par MEB et MET. Nous avons identifié la présence de carbures TiC au sein des amas multi-maclés et nous avons mis en évidence un fort enrichissement local en Nb autour des carbures par EDS. Nous avons pu identifier la phase Nb2Ni à la surface d'un TiC qui requiert une composition locale importante en Nb pour apparaître. À partir de ces observations nous proposons un scénario possible pour l'apparition des grains équiaxes fins dans l'Inconel 718 déposé par la technologie laser-fil coaxial. Les TiC y joueraient un rôle important en capturant les éléments minoritaires lors la refonte, et en promouvant l'apparition locale d'amas icosaédriques dans le liquide qui favoriseraient la germination de grains dont les orientations relatives reflèteraient cet ordre icosaédrique.

Mots-clés : Solidification, Inconel 718, Laser - fil, Fabrication Additive